An Investigation of the Particle Dynamics of a Multi-component Solid Phase in a Dilute Phase Pneumatic Conveying System

Yong Lu

Institute for Materials and Processes
School of Engineering and Electronics

Thesis submitted for the degree of Doctor of Philosophy
The University of Edinburgh
March 09

Abstract

In order to mitigate the risk of global warming by reducing CO_2 emissions, the co-firing technique, burning pulverized coal and granular biomass together in conventional pulverised fuel power station boilers, has been advocated to generate “greener” electricity to satisfy energy demand while continuing to utilize existing rich coal resources. A major problem is controllably distributing fuel mixtures of pulverized coal and granular biomass in a common pipeline, thus saving much investment. This is still under development in many co-firing studies. This research into particle dynamics in pipe flow was undertaken in order to address the problem of controllable distribution in co-firing techniques and gain an improved understanding of pneumatic conveying mechanisms.

The objectives of this research were, firstly, to numerically evaluate the influence of various factors on the behaviour of particles of the different materials in a horizontal pipe gas-solid flow, secondly, to develop an extended technique of Laser Doppler Anemometry in order to determine cross-sectional characteristics of the solid phase flow in the horizontal and vertical legs of a pneumatic conveying system, and, thirdly, to develop a novel imaging system for visualizing particle trajectories by using a high definition camcorder on a cross-section illuminated by a white halogen light sheet. Finally, a comparison was made of cross-sectional flow characteristics established by experiments and those simulated by using a commercial Computational Fluid Dynamics code (Fluent) and the coupling calculations of Fluent & EDEM (a commercial code of Discrete Element Method) respectively.

Particle dynamic behaviour of the solid phase in a dilute horizontal pipe flow was investigated numerically by using the Discrete Phase Model (DPM) in Fluent 6.2.16. The numerical results indicate that the Saffman force plays an important role in re-suspending particles at the lower pipe boundary and that three critical parameters of the critical air: conveying velocity, the critical particle size and the critical pipe roughness, exist in pneumatic conveying systems. The Stokes number can be used as a similarity criterion to classify the dimensionless mean particle velocity of the different materials in the fully developed region.

An extended Laser Doppler Anemometry (LDA) technique has been developed to measure the distributions of particle velocities and particle number over a whole pipe cross section in a dilute pneumatic conveying system. The first extension concentrates on a transform matrix for predicting the refracted laser beams’ crossing point in a pipe according to the shift coordinate of the 3D computer-controlled traverse system on which the probes of the LDA system were mounted. Another part focussed on the proper sampling rate of LDA for measurements on the gas-solid pipe flow with polydispersing particles. A suitable LDA sampling rate should ensure that enough data is recorded in the measurement interval to precisely calculate the particle mean velocity or other statistical values at every sample point. The present study explores the methodology as well as fundamentals of measurements of the local instantaneous density of particles as a primary standard using a laser facility.

The extended LDA technique has also been applied to quantitatively investigate particle dynamic behaviour in the horizontal and vertical pipes of a dilute pneumatic conveying system. Three kinds of glass beads were selected to simulate the pulverized coal and biomass pellets transported in a dilute pneumatic conveying system. Detailed information on the cross-sectional spatial distributions of the axial particle velocity and particle number rate is reported. In the horizontal pipe section, experimental data on a series of cross-sections clearly illustrate two uniform fluid patterns of solid phase: an annular structure describing the cross-sectional distribution of the axial particle velocity and a stratified configuration describing particle number rate. In the vertical pipe downstream of an elbow R/D=1.3, a horseshoe-shaped feature, which shows that the axial particle velocity is highest in wall regions of the pipe on the outside of the bend for all three types of glass beads on the section 0D close to the elbow outlet. The developments of cross-sectional distributions of particle number rate indicate that the horseshoe-shaped feature of particle flow pattern is rapidly dispersed for particles with high inertia.

A video & image processing system has been built using a high definition camcorder and a light sheet from a source consisting of a halogen lamp. A set of video and image processing algorithms has been developed to extract particle information from each frame in a video. The experimental results suggest that the gas-solid flow in a dilute pneumatic conveying system is always heterogeneous and unsteady. The parameter of particle mass mean size is superior to particle number mean size for statistically describing the unsteady properties of gas-solid pipe flow. It is also demonstrated that the local data of particle number rate or concentration are represented by a stratified structure of the flow pattern over a horizontal pipe cross-section.

Finally, comparisons of numerically predicated flow patterns and experimental ones show that there is reasonable agreement at pipe cross-sections located at horizontal positions less than half the product of particle mean velocity and mean free fall time in the pipe from the particle inlet. Further away from the inlet, the numerical results show flow patterns which are increasingly divergent from the experimental results along the pipe in the direction of flow. This discrepancy indicates that particles' spatial distribution in the pipe is not accurately predicted by the Discrete Phase Model or Fluent coupled with EDEM.

Declaration

I declare that this thesis describes work carried out in the Institute for Materials and Processes, School of Engineering and Electronics, the University of Edinburgh. It is the original work of the author except where otherwise stated. This thesis has been composed by myself and was not submitted in any form at another university.

Signed

Yong Lu
Edinburgh, 17 March 2009

Acknowledgements

I would like to express my deepest gratitude to my supervisors, Dr. Donald H. Glass and Professor William J. Easson. Their dedication and enthusiasm to scientific research, their brilliant idea and encouragement were essential to built up this thesis. Without their precious help, I would have never come to Edinburgh and started my Ph.D.

I also want to thank Dr. Martin Crapper, who has advised and guided me for numerical simulations by using EDEM. Here I am grateful to DEM Solutions Limited, Edinburgh for their assistance with this numerical work.

Many thanks to Mr. Bobby Hogg, Mr. Neil Wood and Mr. Roby, who gave much helps of providing technical support for experiments. And also many thanks to my friends near and far for their friendship and the happy moments we shared together, especially to Dr. Hao Wang with whom I shared the flat and encouraged each other in past two years.

I am extremely grateful to the committee of 2005 UK/China Youth Scholarships for Excellence, University of Edinburgh and Southeast University for the financial support. These supports have made my study at Edinburgh possible.

Finally, I dedicate this thesis to my parents, Minlong Lu and Lichun Wang, my parents in-law, Jitang Fan and Fenghua Shen, my wife, Shisen Fan and my lovely daughter, Zixin Lu, who have always been there to support me and give me strength and motivation to accomplish this work.

Dissemination

This work has been presented in several conferences and meetings, and has written in papers that have been published and are in the process of being published, given as follows.

Publications

Lu Y., Glass H. D., Easson J. W., (2009). An investigation of particle behaviour in gas-solid horizontal pipe flow by an extended LDA Technique. Fuel. Accepted (JFUE-D-08-00741).

Lu Y., Glass D. H., Easson W. J., (2008a). Investigating particles behavior in gas-solid horizontal pipe flow by an extended Laser Doppler Anemometry Technique. In: Proceedings of 7th European Conference on Coal Research and its Applications, September 2nd – 5th, Cardiff, UK.

Lu Y., Glass D. H., Easson W. J., Crapper M., (2008b). Investigation of the Flow Patterns of Gas-solid granular flow in a horizontal pipe by FLUENT & EDEM. In: Proceedings of Particle Systems Analysis 2008, September 1st – 3rd, Stratford, UK.

Lu Y., Glass D. H., Easson W. J., (2007). Investigating Flow Properties of Coal Biomass Blends in Pneumatic Conveying System by Computational Fluid Dynamics. In: Proceedings of 2007 international conference on Coal Science and Technology, August 28th- 31th, Nottingham, UK.

Presentations

Lu Y., Glass D. H., Easson W. J., (2008a). Investigating particles behavior in gas-solid horizontal pipe flow by an extended Laser Doppler Anemometry Technique. 7th European Conference on Coal Research and its Applications, September 2nd – 5th, Cardiff, UK. (Oral presentation).

Lu Y., Glass D. H., Easson W. J., Crapper M., (2008b). Investigation of the Flow Patterns of Gas-solid granular flow in a horizontal pipe by FLUENT & EDEM. In: Proceedings of Particle Systems Analysis 2008, September 1st – 3rd, Stratford, UK. (Oral presentation).

Lu Y., Glass D.H., Easson W. J., (2008c). Visualizing particle characteristics in a horizontal pneumatic conveying system, In: 21st Annual Scottish Fluid Mechanics Meeting, May 22nd, Edinburgh, UK. (Poster)

Lu Y., Glass D. H., Easson W. J., Crapper M., (2008d). A comparison of the Numerical Results Investigated by EDEM & Fluent and the Experimental Data in a Gas-solid Horizontal Pipe Flow. In: Proceedings of EDEM User Group Meeting 2008, April 28th – 30th, Edinburgh, UK. (Poster)

Lu Y., Glass D. H., Easson W. J., (2007). Investigating Flow Properties of Coal Biomass Blends in Pneumatic Conveying System by Computational Fluid Dynamics. 2007 international conference on Coal Science and Technology, August 28th- 31th, Nottingham, UK. (Oral presentation).

Table of contents

Table of figures

Table of tables

Nomenclature

(a, b, c)	The direction vector of a beam
C_p	Particle concentration
(C_{mu}, C_1, C_2)	k-ε model constants
CFD	Computational Fluid Dynamics
d, d_p	Particle diameter
d_f	Distance between the interference fringes
D	Pipe diameter
D_p	Particle diameter
DEM	Discrete Element Method
DPM	Discrete Phase Model
ECT	Electrical Capacitance Tomography
Fs	Saffman force
Fr	Fraud number
g	Gravitational constant, $9.81m/s^2$
I	Chrominance
k	Turbulent kinetic energy
K	The constant in the Saffman force equation, 6.46
L	• Length of horizontal pipe • Length of a particle trajectory • The running distance of a beam
LDA	Laser Doppler Anemometry
(n_i, n_r)	Medium refractive index on incident or refracted side
M_T	Optical translation matrix
MR_1	Optic transform matrix at a pipe outer surface
MR_2	Optical transform matrix at a pipe inner surface
N	Total number of particles
PDA	Phase Doppler Anemometry
Q	Quadratic chrominance
r	The distance between a feeding position at the inlet and pipe centerline
R	• Pipe radius • Lens radius • Curve radius
(R, G, B)	(Red, Green, Blue)
Re	Reynolds number
S	• Optical system matrix • Area of a particle trajectory
St	Stokes number
t	Travel time crossing a stripe of the interference fringes

t_{min}	The minimum temporal interval between two adjacent particles
t_k	Time interval between two adjacent particles
T	Measurement interval
$\bar{u}$	Fluid local time averaged velocity
$\bar{u}_{max}$	The maximum value of $\bar{u}$
$\{u_{pk}\}$	Particle velocity sample space
$\bar{u}_p$	The mean particle velocity
U	Fluid velocity
U_0	Air conveying velocity
U_a	Air conveying velocity
U_p	Particle velocity
$<U'^{2}_{p}>^{1/2}$	Granular temperature
U_{px}	Particle horizontal velocity
U_{py}	Particle vertical velocity
U_t	Particle terminal velocity
UDF	User Defined Function
V_i	Unit vector of an incident beam
V_r	Unit vector of the refracted beam
V_n	The unit vector of the normal ray at a point
(x_0, y_0, z_0)	Reference point of a beam
(x, y, z)	A point coordinate on a line
y_i	• Beam’s height on incident or refracted side • Beam’s initial height
y_0	Beam’s translation height
y_r	Beam’s height after refraction
Y	Luminance

α_0	Angle of an outbound beam
α_r	Crossing-angle between refracted beam and its normal.
α_i	• The crossing-angle between incident beam and its normal vector • Angle of an inbound beam
ε	Rate of dissipation of turbulent energy
δ	Pipe roughness parameter
θ	• Feeding angle • The crossing angle of two beams
Θ	Granular temperature
μ	• Air dynamic viscosity • Mean value of the intensities of a group pixels
σ	Variance of Root-mean-square of the intensities of a group pixels
ν	Air kinematic viscosity
ρ	Fluid density

ρ_p	Particle density
Δ	Pipe roughness height
λ	Beam wavelength

Chapter 1 Introduction

Coal is predicted to remain the dominant energy source in world electricity generation in the near future. Co-firing in power stations is a promising technique to generate enough electricity for the energy demand of a developing economy while simultaneously mitigating the risk of Global Warming by reducing CO_2 *emissions. This chapter is intended briefly to introduce co-firing activities and the current key problems of transporting the blend of granular biomass and pulverised coal in co-firing applications. Then some terms used in pneumatic conveying research are discussed so as to provide a uniform approach to the work referenced in subsequent chapters. The objectives and the main contributions of this research are summarized.*

1.1 GLOBAL WARMING AND CO-FIRING TECHNIQUES

Unprecedented catastrophic climatic anomalies, such as blazing hot summers, brutal winters, hurricanes, typhoons and cyclones have occurred frequently in recent years. These natural disasters have been warning and forcing every nation urgently to tackle the serious problems produced by global warming, which has been confirmed by overwhelming scientific evidence. This shows that the earth's temperature has increased by 0.4°C over the past century due to the greenhouse effect caused by man-made fossil combustion (Baxter, 2005). Six gases, namely carbon dioxide, methane, nitrous oxide, hydrofluorocarbons (HFCs), per-fluorocarbons (PFCs) and sulphur hexafluoride, are considered as greenhouse gases which can trap the heat from the sun or the heat reflected by the earth in the atmosphere and make the earth much warmer. Thus, more than 160 nations ratified the 1997 Kyoto Protocol and committed to make legally binding reductions in their greenhouse gas emissions (Matsuo, 1998). A new global agreement to fight global warming in the post Kyoto Protocol era is expected to be concluded in 2009 at the UN Climate Change Conference in Copenhagen (Harris, 2008).

In 2007, the energy target of the European Union was set to achieve 20% renewable energy by 2020 and the UK's share was supposed to be 15% of the UK's energy from renewables (BERR, 2008). To reach this aim, three legal measures, the Climate Change Levy in 2001, the Renewables Obligation (RO) in 2002 and the European Emissions Trading Scheme (EU ETS) in 2005, have been enacted to move the UK's economy from a high-carbon model to a low-carbon or carbon-neutral one through providing financial benefits for using renewable sources such as solar power, wind power, hydro-electric power, geothermal energy, tidal power, wave energy and biofuels. As a result, the level of RO-eligible renewable generation in UK has been increased from less than 2% in 2001 to around 4.4% in 2006. Especially for power plants, the licensed electricity suppliers will be required to increase annually the fraction of renewable sources in their supplied electricity to 10% by 2010 (AEA, 2006).

Among the eligible renewable sources, utilization of biomass as an alternative energy source instead of fossil fuel has been advocated and is under intense study across the world. One line of enquiry focuses on exploring the technique of generating electricity by using a fuel blend of pulverised coal and biomass in power stations. This combustion of fossil fuel mixed with biomass is named co-firing or co-combustion. In general, co-firing biomass resources can be classified into three categories (IPA, 2006), such as wastes (agricultural production wastes, crop residues, mill wood wastes and urban wastes), forest products (wood, logging residues, trees, shrubs, sawdust and bark) and energy crops (short rotation woody crops, herbaceous woody crops, grasses, starch crops, sugar crops, oilseed crops).

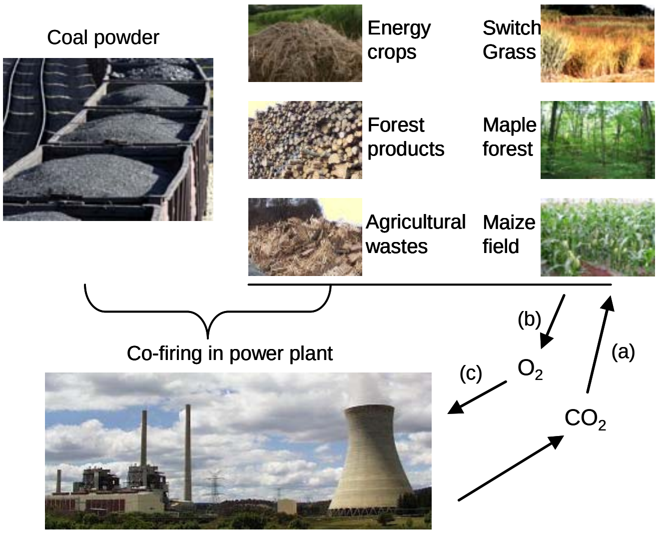

Figure 1. Sketch of CO_2 cycle in co-firing applications

In co-firing applications, not only is biomass utilized as a sustainable alternative energy source which saves the usage of fossil fuel, but also CO_2 emission can be reduced through keeping the net amount of CO_2 from the biomass neutral or zero-emission in the atmosphere. CO_2 emission in a co-firing power plant is shown in Figure 1. Obviously, biomass absorbs CO_2 from the atmosphere in its growing period (a) and releases oxygen back through photosynthesis (b) at the same time. When biomass residuals are co-fired with pulverised coal in power stations, the carbon stored in them will combine with oxygen to produce carbon dioxide, which is emitted back into the atmosphere as an exhaust gas. During the cycle of (a) to (c), the total amount of CO_2 in the atmosphere can be kept constant through continued planting and growth of the biomass.

According to the data of World Energy Outlook (IEA, 2006), fossil fuel provides over three quarters of the UK's electricity generation nowadays and is predicated to remain the dominant energy source utilized for power generation until 2030. The global emission of CO_2 is estimated to be 40 gigatonnes (Gt) in 2030, which is 14 Gt more than the 2004 level. A half of the CO_2 emission increment will be produced by power generation over the projection period. On the other hand, energy demand is substantially increasing under the pressure of rapid urbanization and population explosion. As a result, sustainable energy policy must both tackle global warming and ensure security of the energy supply. Developing co-firing techniques follow this policy, since it is a promising clean way of utilizing abundant coal resources to provide a low-carbon energy supply for economic development.

1.2 CO-FIRING ACTIVITIES AND THE TECHNICAL PROBLEMS OF HANDLING THE FUEL MIXTURE

Basically, biomass co-firing can be categorized as direct co-firing, indirect co-firing or parallel co-firing (DTI, 2006). Direct co-firing, which means burning coal with biofuels in the same boiler using existing or separate mills and transportation systems, is most commonly and widely applied to handle biomass. Conversely, indirect co-firing implies that an on-site gasification or pyrolysis unit can be used to convert biomass materials into a clean fuel gas, which can be fired alone or combusted with coal or natural gas. In parallel co-firing, fossil fuel and biomass are combusted separately and the steam produced by burning biomass is fed to a coal-fired power station where it is upgraded to the higher temperature and higher pressure conditions of the large coal plant.

In the UK, biomass facilities have been developed from two plants in 2002 to sixteen units and the volume of electricity produced by co-fired biomass has increased significantly to an estimated 2.5TWh over 2005/06. So far, most types of boilers, such as cyclone boilers, grate boilers, wall-fired or tangentially fired pulverized-fuel (PF) boilers and circulating fluidized bed (CFB) boilers, have been converted to co-firing biomass with coal. These practical experiences have confirmed that burning biomass with fossil fuels has a positive impact both on the environment and the economics of power generation (DTI, 2007).

Sami et al. (2006) summarized previous co-firing studies in four conclusions:

(1) Co-firing can be performed at moderate and high percentages in cyclone boilers;

(2) Co-firing can be performed at low percentages in PC boilers. The co-firing ratio depends on the pulverizer performance which in turn depends on the type of biomass fuel used. Most biomass fuels have a fibrous structure (e.g. wood, switchgrass) and are difficult to grind to the same sizes as coal used in coal pulverizers. Grinding costs determine the extent to which biomass can be economically pulverized;

(3) Co-firing in PC boilers may require separate fuel feed lines depending upon the capacity of existing pulverizers, type and condition of biomass fuels and the type of pulverizers used;

(4) The potential for successful application of co-firing is site-specific. It depends upon the characteristics of the power plant being considered, the availability and price of biofuels within 50-100 miles of the plant and the economic value of environmental benefits.

However, applying current co-firing technology is also challenged by some technical problems (Biagini, 2005; Baxter, 2005). The first issue is related to combustor fouling and corrosion due to the alkaline nature of the biomass ash. Deposits of ash reduce the heat transfer and may also cause severe corrosion at high temperatures. Secondly, additional studies are needed about the feeding mechanism transporting the fuel mixture to control the co-firing state in a given furnace. This issue is a combination of economics and combustion characteristics. More work is required to be done in this area. Third, practical pulverizer performance needs to be examined.

In current co-firing applications, existing fuel transportation systems can be classified as three types (Sami et al., 2001; Ireland et al., 2004). The first is using separate feed lines and separate burners for dealing with coal and biomass fuels respectively. It has the advantage of better control over fuel flow rates. Thermal output similar to coal-only firing requires higher biomass feed rates. It also increases capital and maintenance costs. Firing low heating value biomass independently of coal also has a risk of poor combustion efficiency. The second is using separate feed lines and a common burner. This method can also be divided into dual inlets and triple inlets on furnaces. In dual inlets, coal is injected in the primary air inlet and biomass is injected in the swirling secondary air inlet (or vice versa). In triple inlets, two primary air inlets are used to feed coal and one swirling secondary air inlet to inject biomass. The third method is that premixed coal/biomass blends are transported in common feed lines to a common burner. Since the fuel blend shares the same pipelines, this method saves much investment in building a new feed system, and is therefore economically advantageous.

Since dilute pneumatic conveying systems are commonly applied to transport pulverised fuel in most coal-fired power plants, our research will focus on investigating the characteristics of transporting biomass/coal blends in a common dilute pneumatic conveying system.

1.3 PNEUMATIC CONVEYING FUNDAMENTALS FOR CO-FIRING APPLICATIONS

Co-firing biomass with coal in the same installation has been proved to be an important renewables technology, and it has the great economic advantage of re-using the existing infrastructure of power stations. Pneumatic conveying, which uses air to convey granular materials through a pipeline, has been used commercially to transport the pulverised coal for many years in coal-fired power stations. The current existing pneumatic conveying systems should be retrofitted to be suitable for transporting the fuel blend. These modifications include fuel handling, storage and feed systems. Since biomass granules have significantly different characteristics from pulverised coal (for instance, biomass has less heating value than that of coals) and are also more fibrous and softer (biomass density varies from 100 to 500 kg/m^3 for forest wood and coal density ranges from 1100 for low-rank coal to 2330 kg/m^3 for high density pyrolytic graphite), these differences in properties mean that there are potential problems in storage, bulk handling, feeding, combustion, slagging, corrosion and gaseous emissions.

According to current technical reports on co-firing in large utility boilers (DTI, 2007), the handling of the fuel mixture is poor because of particle size variation, high fibre and oversize particle content. Additionally, biomass particles may be adherent, corrosive and even abrasive. Moreover, downstream parameters in furnaces, such as combustion efficiency, combustion behaviour and ash products or pollutants, are also related to the conditions of feeding the fuel blend. In view of these factors, it is critical to investigate how to prepare and handle the fuel mixture to ensure the optimum operational performance of a co-firing plant. Therefore, the proposal for 2007-2009 key topics-2 of TASK 32 (Livingston et al., 2007) outlined the optimized biomass technology combinations through a workshop on fuel storage, handling and preparation, as well as systems analysis.

Although pneumatic conveying systems have been widely applied commercially in many industrial fields and there are also numerous experimental and numerical published papers investigating phenomena like gravity setting, roping, erosion, attrition, pressure-wave propagation and gas-solid turbulence modulation in pipes, understanding of the mechanism of pneumatic conveying is still under development due to its complexity. For example, it is still difficult to measure and control the mass flow rate of a solid phase in a pipe and to distribute gas-solid flow from a main pipe to several sub-pipes at an equal mass rate or a specific ratio (DTI, 2003).

In research on co-firing applications, most previous studies focused on combustion issues such as combustion efficiency, pollutant formation, carbon conversion, ash management, corrosion, fuel chemistries associated with blending and other downstream impacts. The relevant literature which focuses on transporting the pulverized biomass and coal fuel supply is particularly sparse.

Before introducing this PhD work in detail, some easily confused definitions in pneumatic conveying research are given here for reference in order to provide a uniform approach to the work in the next subsequent chapters. These terms are cited in the two references (Mills, 2004; Seville et al., 1997).

- ***Air superficial velocity / superficial fluid velocity***. This is the velocity of the air disregarding the presence of the solid particles or porous media. In a pipeline, it is the air velocity based upon the empty cross-sectional area and neglecting the space occupied by the conveyed material. For example, under the condition of fluid flow at volumetric rate Q_f along a pipe of cross-sectional area A, air superficial velocity is defined to be $U_f=Q_f/A$.
- ***Air phase velocity***. It is the same as air superficial velocity.
- ***Air retention*****.** The ability of a bulk material to retain air in the interstitial spaces between particles for a period of time.
- ***Air conveying velocity at pipeline inlet*****.** This is the superficial air velocity at the point where the material is fed into the pipeline. In a single bore pipeline this will be the lowest air velocity in the conveying line and so it must be greater than the minimum conveying air velocity required to ensure successful conveying of the material. In a vacuum conveying system it is approximately equal to the free air velocity.
- ***Air conveying velocity at pipeline exit*****.** This is the superficial air velocity at the end of a conveying line where the material is discharged into the receiving vessel. In a single bore pipeline this will be the highest air velocity in the conveying line. In a positive pressure conveying system it is approximately equal to the free air velocity.
- ***Cross-sectional flow patterns***. These are defined as geometric contours on a pipe cross-sectional characteristic of some parameters like particle velocity, particle number rate and solid phase concentration in a pneumatic conveying system.
- ***Delivered volume concentration.*** This is defined as the ratio of solid phase volumetric flow rate to the mixture volumetric flow rate, which is expressed as $C_{vd}=Q_s/(Q_f+Q_s)$, where Q_s and Q_f are the solid phase volumetric flow rate and air phase volumetric flow rate respectively.

- ***Flow regimes***. These terms are used to describe the state of gas-solid flow by the evidence of its macroscopic appearance along the pipe axial direction. Basically, three major flow regimes: suspension flow (dilute phase), moving bed type flow (dense phase) and slug or plug type flow (dense phase) have been recognized to exist in pneumatic conveying.
- ***Free air condition***. This is specified as the condition at the standard atmospheric pressure ($p=1.013\times10^5$ Pa) and the standard atmospheric temperature ($t=15°C$).
- ***Free air velocity***. This is the superficial velocity of the air when evaluated at free air condition.
- ***Particle velocity / particle actual velocity***. This is defined as the velocity of a particle in a pipe. Here the solid phase is considered as a group of discrete particles immersed in the fluid.
- ***Slip velocity***. This is defined as the absolute difference between air phase velocity and solid phase velocity.
- ***Slip ratio***. This is defined in terms of the solid phase velocity divided by air superficial velocity.
- ***Solid phase velocity / superficial particle velocity***. When solid phase is also considered as a continuous fluid like air and has a volumetric rate Q_s along a pipe of cross-sectional area A, the solid phase velocity U_s is then defined as $U_s=Q_s/A$.
- ***Solid velocity***. This is the same as solid phase velocity.
- ***Void fraction / volume fraction / voidage.*** It means the volume ratio occupied by the fluid.

1.4 OBJECTIVES AND CONTRIBUTIONS IN THIS THESIS

Transporting pulverised coal with biomass in a pneumatic conveying system can be essentially considered as a special case of multi-component gas-solid pipe flow, in which the solid phase consists of two or more particulate materials such as coal powder and sawdust These particles are distinguished by their density and geometric characteristics. The objectives of this thesis are to evaluate the influence of various factors on the particle behaviour of the different materials in a pipe and to investigate local information on the solid phase such as cross-sectional velocity distribution and particle number distribution by numerical simulation and experiments. The results will be of fundamental use in the design of fuel blend transport system.

These aims were met through the following activities:

- Comparing the similarity of the pulverised coal and biomass particles in a pneumatic conveying system by *Computational Fluid Dynamics* (CFD) and the Discrete Element Method (DEM) (Chapter 2; Chapter 7).
- Using *Laser Doppler Anemometry* (LDA) to investigate the local information on the solid

phase at several pipe cross-sections along the fluid direction (Chapter 3; Chapter 4 and Chapter 5).

- Using *a high definition digital camcorder* to visualize and measure the cross-sectional characteristics of the solid phase (Chapter 6).
- *Comparing* the experimental data with the numerical results to study the reasons for any discrepancies (Chapter 7).

Specific contributions outlined in this work are:

- Numerical results indicate that there exists a critical *air conveying velocity*, a *critical particle size* and a *critical pipe relative roughness* in a pneumatic conveying system. *Stokes Number* can be used to classify the similarity of the mean particle velocity of different materials in axial and gravity directions (Lu et al., 2007).
- An algorithm to calculate the spatial optical *transformation matrix* has been developed to calibrate the position of the laser beams' crossing point in a circular pipe for LDA measurements (Lu et al., 2008a; Lu et al., 2009).
- *A video and image processing system* has been developed to visualize and measure the spatial distribution of particle size and concentration over a pipe cross-section (Lu et al., 2008c).
- Experimental data shows *two cross-sectional flow patterns* which can be classified as *an annular structure* of particle velocity contour and *a stratified feature* describing particle number rate contours (Lu et al., 2008a; Lu et al., 2009).
- Comparison of the numerical results and the experimental data indicate that using the current Discrete Phase Model (DPM) can reasonably estimate the cross-sectional flow patterns within *a certain distance* from the inlet. This length is approximately equal to the product of particle mean velocity and its half free-falling time in pipe. In addition, considering the effect of *particle-particle interactions* will improve the accuracy of the particles' spatial distributions in the pipe predicted by numerical simulations (Lu et al., 2008b; Lu et al., 2008d).

Chapter 2

Classifying the Characteristics of Pulverized Coal and Granular Biomass in a Dilute Horizontal Pipe Flow by Computational Fluid Dynamics

Particle dynamic behaviour of the solid phase in a dilute horizontal pipe flow was investigated at the start of the project by using the Discrete Phase Model (DPM) in Fluent 6.2.16. The numerical results indicate that the Saffman force plays an important role in suspending particles at the boundary and that three critical parameters of the air: critical conveying velocity, the critical particle size and the critical pipe roughness, exist in pneumatic conveying systems. Moreover, the Stokes number can be used as a similarity criterion to classify the mean particle dimensionless velocity of the different materials in the fully developed region. Later numerical work appears in Chapter 7.

2.1 LITERATURE REVIEW ON PNEUMATIC CONVEYING IN CO-FIRING APPLICATIONS

In Chapter 1, Co-firing was introduced as a promising technique to mitigate the risk of Global Warming by reducing CO_2 emission, because biomass co-fired with coal can not only utilize the advantages of coal such as abundant resources and high thermal value but also has the great environmental benefit of CO_2 emission neutrality in the biomass life cycle. Biomass particles and pulverized coal can be conveyed into furnaces of a power plant through a separate or common pipeline. Using a common conveying system is much the least expensive option since no separate feed lines and burners are required and existing installations can be used with minor adaptations or retrofitting (Sami M. et al, 2001). But the solution of some technical issues like storing, feeding and pulverizing the mixed fuels may still be required before the widespread adoption of co-firing in power stations.

Despite numerous pneumatic conveyor systems having been built to handle enormous amounts of granular materials in many industrial fields, understanding of the underlying physical process is very limited and there still exist considerable concerns and technical problems due to the complexity of gas-solid flow in pneumatic conveying systems (DTI, 2003). The main challenges lie in the control and measurement of granular pipe flow on-line. Especially, this is a current technical problem (DTI, 2007; Livingston et al., 2007) with different coals and even more so with biomass, since there exist significant differences in density, size, geometric shape and moisture between granular biomass and pulverized coal. All these differences have great influence on the state or properties of the mixture flow. For example, pulverized coal is normally conveyed to the furnace by a distribution pipe network, which is designed to distribute equally or split the pulverized fuel through bifurcations or trifurcations. The evenness of distribution will affect combustion efficiency, pollutant production and flame stability. The majority of pneumatic conveying systems have been designed and calibrated to handle a specific type of granular material. When these conveying systems are retrofitted to convey biomass or fuel blends, the default or designed conveying parameters like minimum pick-up velocity, distribution ratio of a splitter and solid loading ratio . should be re-calibrated and validated.

So far, most co-firing researches in power generation have focused on combustion-related activities such as measuring and modeling the combustion flame, combustion efficiency and NO_x reduction, pollutant formation, ash management, the physical properties of coal-biomass blends and other issues related to combustion. Only a handful of papers have begun to investigate the fundamentals of pneumatic transport of the fuel blends of pulverized coal and granular biomass. Granada et al. (2006) specially designed a hopper for steadily injecting pellets of three forest residues (Eucalyptus, pine and pine bark). His experimental results indicate that pine bark is the most suitable product for co-firing as pellets and that a screw feeder causes higher levels of segregation of fuel mixtures. Wall shear and direct shear experiments were carried out by Zulfiqar et al. (2006) to study shear between the mixture fuels (typical Australian coal and wood chips) and the shear between fuel blends and the wall. The biomass was pine sawdust with equivalent diameter 100 μm or woodchips with average dimensions of 2×3 cm^2 (width by length). Their experimental data indicate that coal-woodchip blends will significantly increase the risk of blockage and flow stoppage. Melander et al. (2004) used the Particle Image Velocimetry (PIV) technique to measure the concentration and velocity of wood fibres in a vertical pneumatic conveying system. Their data confirmed that PIV is a useful tool for measuring the properties of the dilute fibre-gas flows. The measured profiles of air velocity show that they are strongly affected by the volume fraction of wood fibres. Joppich and Salman (1999) studied the steadiness of a screw feeder used to feed wood powder. By using a vibrator feeder mounted at the downstream end of the screw conveyor, the total feeding performance is significantly improved.

In research into dilute particle-laden pipe flow of a single material, Huber et al. (1998) and Sommerfeld (2005) summarized seven important phenomena: particle transport due to turbulence, gravitational settling, wall roughness effect, particle-wall collisions, inter-particle collisions and inertial behaviour in pipe bends. Mills (2004) published a practical book introducing the principles of design of a pneumatic conveying system. In research into the pneumatic conveying mechanism, Fan et al. (1998) addressed the basic principles and fundamental phenomena associated with gas-solid flows, as well as characteristics of selected gas-solid flow systems including dilute transport or pipe flow of gas-solid suspensions. Similarly, Seville et al. (1997) also summarized particle characterization, particle mechanics and solid assembly mechanics in gas-solid flow. With regard to the pneumatic conveying of granular biomass, Cui et al. (2006) reviewed studies into transporting agricultural grains and pulp fibres as well as related flow measurement techniques and modeling.

Although there have been numerous experimental and theoretical studies into pneumatically conveying a single granular material, the corresponding experience and results are not adequate to be used to solve the previously discussed technical issues such as equal distribution of the mixture fuels from a main to several sub-pipes in a pneumatic conveying system. Thus, it is necessary to study local information on the solid phase, such as particle spatial distribution and solid concentration distribution and the microscopic mechanism of pneumatic conveying. Moreover, conveying pulverized coal with biomass can be considered as a special gas-solid flow whose solid phase consists of two or more types of solid particles. The objective of this chapter is to study the different influences on the particle dynamic properties of pulverised coal and granular biomass in a dilute horizontal gas-solid pipe flow and to classify their similarity by analysing the characteristics of the dimensionless parameters.

2.2 NUMERICAL MODEL AND FLUID CONDITIONS

2.2.1 Discrete Phase Model for gas-solid simulations

Recent rapid progress in the theoretical and experimental study of turbulence modulation has led to great progress in understanding some basic mechanisms of gas-solid pipe flow, which can be normally modelled by the Volume of Fluid (VOF) model, Eulerian models and Discrete Phase Models (DPM). There is also a model called CFD-DEM, or the Combined Continuum and Discrete Method (CCDM), in which the motion of the solid phase is described by the Discrete Element Method (DEM). Every particle of the solid phase is tracked by applying Newton’s laws of motion. Correspondingly, the air phase is considered as a continuum fluid by using Navier-Stokes equations in the traditional Computational Fluid Dynamics (CFD) manner. (Tsuji Y., 1993; Crapper M., 2006; Chu K.W. and Yu A.B., 2007).

Since the solid volume fraction in dilute pneumatic conveying is very small (less than 10%), the effect caused by inter-particle collisions is usually ignored in the numerical simulations. Compared with the Eulerian-Eulerian Model, the DPM model considers a solid phase consisting of particles randomly dispersed in an isotropic fluid. Their trajectories are computed by solving the equations governing movement of the solid phase in a Lagrangian frame of reference. In contrast, the conveying air is regarded as a continuous phase whose transport equations are solved in an Eulerian frame of reference. This model is more appropriate for tracking every particle trajectory in the fluid. To deal with phase interactions, three regime types comprising one-way, two-way and four-way coupling calculations between the solid phase and gas phase can be classified by solid volume fraction less than 10^{-6}, larger than 10^{-6} and beyond 0.1% respectively (Elghobashi, 1994). In this work, DPM simulations are used to select the two-way coupling for dilute pneumatic transportation, and two additional forces beside the drag force are to be considered. They are the virtual mass force required to accelerate the fluid surrounding the particle and the Saffman lift force due to shear. The detailed transportation equations of DPM can be found in Fluent User Guide (Fluent Inc., 2006).

2.2.2 The k-ε turbulence model

For single phase flow, no single turbulence model is universally accepted as being superior for all classes of problem. The k-ε model has been widely and successfully applied for single phase turbulent flow (gas or liquid), although there are also other methods like direct numerical simulation (DNS), large-eddy simulation (LES), and discrete-vortex simulation (DVS) under development.

Table 2.1 DPM model setup

Type	Choices
Solver	✧ Segregated solver ✧ Space: 2D or 3D ✧ Steady
Turbulence model(k-ε Model)	✧ Model Constants: C_{mu} =0.0845 C_1 = 1.42 C_2=1.68 ✧ RNG options: Differential viscosity model ✧ Near-wall treatment: standard wall functions ✧ Full buoyancy effects
Discrete phase option	✧ Interaction with continuous phase ✧ Update DPM sources every 15 flow iterations ✧ Saffman lift force ✧ Two-way turbulence coupling
Gravity	✧ the negative direction of y axis ✧ Value: 9.81 m/s^2
Wall collision model	✧ Reflection ✧ Reflection coefficients of normal and tangential directions are 1 ✧ Roughness constant: 0.5 ✧ Roughness height ranges from 0 to 2.32 mm

The modification of the gas turbulence in particle-laden flows is not well understood until now. Many factors, such as particle size, density, and volume fraction, have been identified as having much influence on the turbulence intensity. For example, experimental data (Tsuji et al., 1984; Gore et al., 1989) show that larger particles tend to enhance the turbulence and smaller particles attenuate it. In general, the k-ε turbulence model has been widely used to describe the air phase in gas-solid flow due to this model having been successfully applied for single phase flow (air or liquid).

The k-ε model assumes that the flow is fully turbulent and isotropic, and that the effects of molecular viscosity are negligible. Nowadays the k-ε model has been developed into the Standard k-ε Model, the Realizable k-ε model and the Renormalization Group (RNG) k-ε Model. All these three models have a similar approach, including transport equations for the turbulent kinetic energy (k) and its rate of dissipation (ε). The major differences lie in the equations used for calculating turbulent viscosity and the expression of the generation and destruction terms in the ε equation. Compared with the other two models, the Standard k-ε Model is relatively simple to implement, leads to stable calculations that converge relatively easily, and gives a reasonable prediction for many flows. Its disadvantages are that it gives poor predictions for swirling, rotating and strongly separating flows. Since our studies focus on the properties of dilute phase granular materials in a horizontal pipe, the k-ε model is selected for describing air phase in our numerical simulations. The parameters of DPM setup in Fluent 6.2.6 are briefly listed in Table 2.1.

2.2.3 Numerical convergence criteria

A solution is normally assumed to be convergent when the sum of its normalized residuals (for example, mass, velocity components, turbulent kinetic energies, turbulent and dissipation energies) is less than a specified small tolerance. This tolerance is usually set to 1/1000 by default. In some cases, Kohen et al. (1994) and Huber et al. (1998) found that residuals were not suitable for use as a criterion due to their oscillating at each coupled calculation. For this reason, they advised that the evolution of the stream-wise gas velocity profile at several reference positions should be used as the convergence criterion. In this work, most numerical solutions are used with the standard residuals criterion. In cases where the residuals jump or oscillate, the convergence is determined by the evolution of the stream-wise gas velocity profile at seven specific points.

2.2.4 Model geometry and mesh Grids

In order to provide future comparisons between the numerical results and the experimental data, the domain of our numerical model is similar to the dimensions of the horizontal part of the lab pilot rig, which will be discussed in detail in section 3.2. Figure 2.1 shows both the sketch of the rig and the mesh grids of the numerical model. The rig in Figure 2.1(a) is a pneumatic conveying system with positive pressure including a fan, a cyclone and several glass pipes. Figures 2.1(b) and (c) show the total length of the numerical model and the cross-sectional mesh grid at the model inlet, which are meshed by employing adjustable boundary-fitted coordinate grids respectively. The distance of the first cell adjacent to the wall is set to 0.5mm in order to investigate local fluid behaviour in the pipe boundary region. The whole domain is meshed into 0.6 million cells. The origin point of the reference coordinate is located at the centre of the pipe inlet where y positive axis is opposite to gravity and z axis is along pipe radial direction. The x positive axis is along fluid flow direction,

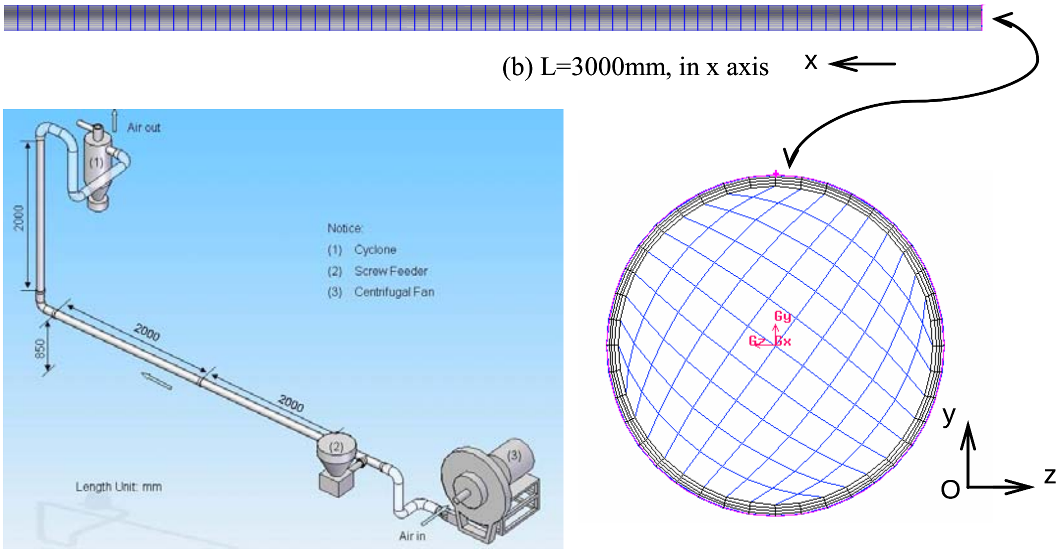

(b) L=3000mm, in x axis

(a) The lab rig

(c) pipe inlet (ϕ80mm) in the plane of Oyz

Figure 2.1 Experimental rig (a) and the mesh grids of the numerical model (b, c).
(Please note that the scale factor of every diagram is different for clarity and the system coordinate is located at the pipe inlet centre.)

2.2.3 Flow Conditions and Selecting Numerical Parameters

In order to be able to extend the experimental results used to meaningful engineering applications, some dimensionless numbers such as Reynolds number, Froude number and Stokes number have been used for characterizing the dynamic similarity between the pilot rig and the large-sale pneumatic conveying system in a power plant. These three essential parameters are individually expressed as

$$\mathrm{Re} = \frac{\rho U D}{\mu}$$
$$Fr = \frac{U}{\sqrt{Lg}} \tag{2.1}$$
$$St = \frac{\rho_p D_p^2 U}{18 \mu D}$$

where ρ, μ and U are density, dynamic viscosity and velocity for air phase separately. D is pipe diameter. L is a characteristic length descriptive of the flow field and is usually defined as being equal to pipe diameter for pipe flow research. D_p and ρ_p are particle diameter and particle density respectively.

Giddings and Aroussi (2004) indicated that keeping the Froude number (based on the pipe inner diameter as the reference length) constant could make the pipe friction behaviour of the experimental rig similar to that of a full-scale power plant pipe. For example, a 25m/s conveying velocity and ϕ330mm (inner diameter) pipe are two normal operating parameters used in the dilute pneumatic conveying systems of a pulverized coal-fired power plant. Our attainable 12m/s air conveying velocity can attain dynamic similarity with the experimental rig with 80mm ID pipes. In addition, a relatively high conveying air velocity must be maintained for dilute phase conveying. The typical order of air conveying velocity is about 10~12 m/s for fine powders like pulverized fuel and wheat flour and 14~16 m/s for fine granular materials like granular sugar and pearlite. If the conveying velocity drops by more than 10 or 20 percent in the pipeline, it is likely to cause a blockage problem (Mills, 2004, p429). Thus the air conveying velocity is to be in the range of 10~48m/s in our simulations.

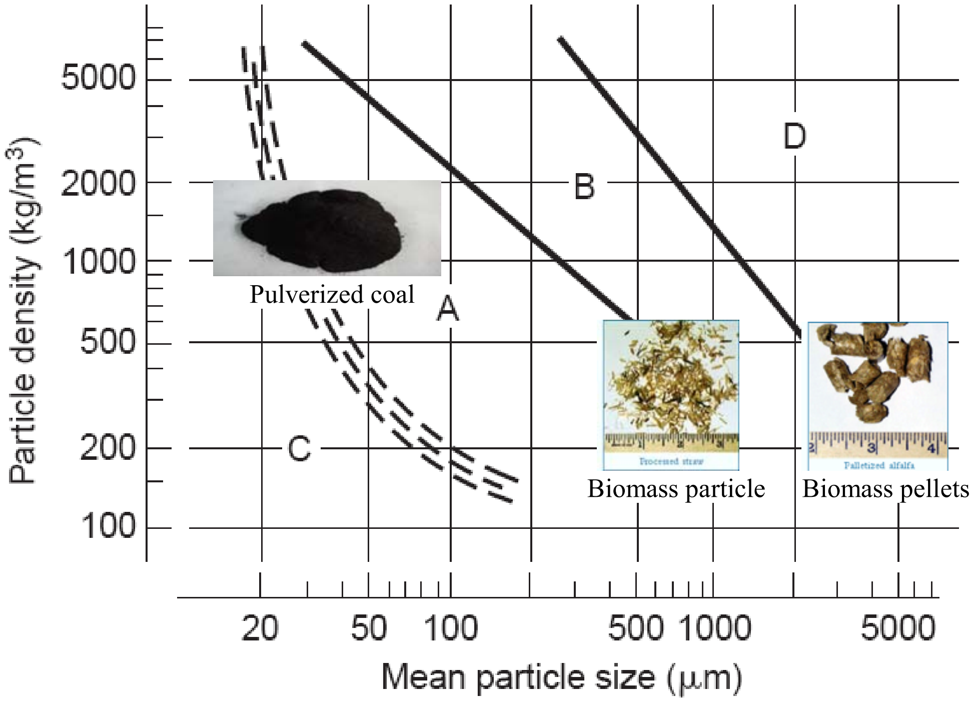

Figure 2.2 Geldart’s classification of fluidization behaviour for fluidization with ambient air (Mills, 2004)

According to their air retention properties, Geldart (1973) classified granular materials into four distinct groups A, B, C and D by using density and average mean diameter in his fluidization research. The experimental results of Mills (2004) confirmed that the materials in group A have very good retention properties and the materials in group C have very good permeability. As such, granular materials of group A and C are suitable to be pneumatically transported either in the dense or dilute phase. Biomass density varies from 100 kg/m^3 for straw to 700 kg/m^3 for forest hard wood and coal density ranges from 1100 kg/m^3 for low-rank coal to 2330 kg/m^3 for high density pyrolytic graphite. The pulverized coal used in modern pulverized coal-fired power stations is normally less than 110μm in size. However, the granular biomass consumed in many demonstration co-firing power plants is usually filtered to be less than 3mm by a 6 mesh sieve before transportation (NETBIOCOF, 2006). Considering the blockage risk due to transporting oversize granular biomass mixed with pulverized coal in a common pipe, a more suitable granular biomass should be less than 1mm in size (equivalent diameter of a sphere) according to Geldart's Chart (Figure 2.2). In addition, glass beads will be used to simulate the gas-solid flow of the mixture fuels in the lab experiments. As such, the numerical simulations will investigate the dynamical properties of three materials (coal, wood and glass beads) of different sizes in a horizontal straight pipe. The detailed numerical parameters are listed in Table 2.2.

Table 2.2 Numerical parameters

Type	Parameters		Value
air	conveying velocity (U_a, m/s)		10,15,18, 20, 24, 30, 48
Pipe	diameter (D, mm)		80
	roughness Height(Δ, mm)		0, 0.08, 0.16, 0.32, 0.67, 1.31, 2.32
	relative roughness(Δ/D)		0, 0.1%, 0.2%, 0.3%,0.83%, 1.6%, 3.3%
loading ratio	(kgs^{-1}/kgs^{-1})		0.01
particle	glass	density (kg/m^3)	2500
		diameter (μm)	20, 40, 60, 100, 200, 300, 450, 500
		shape	Spherical
	coal	density (kg/m^3)	1550
		diameter (μm)	10, 20, 30, 35, 40, 50, 60, 70, 80, 100, 200, 300
		shape	Spherical
	Wood chips	density (kg/m^3)	185
		equivalent diameter (μm)	100,146,204,296,436,581,726,871,1016
		Coal diameter with the same Stokes number (μm)	29, 50, 70, 100, 150, 200, 250, 300, 350
		Shape	spherical
Feeding	position (m)		At the pipe inlet (x=0)
	Initial velocity		Zero (static injection)
	parcels	3D	4500
		2D	200
Discrete phase boundary condition	The elastic model of particle-wall collision		Both the normal coefficient and tangential coefficient are equal to 1.

2.3 RESULTS AND DISCUSSION

Numerical simulations have been performed for different sets of values of the parameters in Table 2.2. All particles are injected homogeneously and statically (zero initial velocities) from the pipe inlet. In some fluid conditions, it was found that the residuals of air turbulent kinetic energy

(k) and its rate of dissipation (ε) may not have been convergent to be less than 1/1000, which is the default convergent value for each residual, although the other four residuals (continuity and three components of air velocity) had met the convergence criteria. For this case, the criteria were modified to determine the evolution of air velocity profile at the nine reference points. The simulations were regarded as being convergent when the velocity profile remained steady after a finite number of iterations. The typical evolution of air velocity profiles at the nine reference points is shown in Figure 2.3(a). These nine points are equally distributed at x=2.0m on the vertical line along pipe radius in y direction. The air velocity profile is observed to be developed steadily after the 60th two-coupling computation, as shown in Figure 2.3(a). The relative error of air velocity relative to its average value at the nine reference points fell close to zero after 800 iterations in Figure 2.3(b). Thus, the numerical computations are considered as being convergent after 800 iterations for the current fluid conditions.

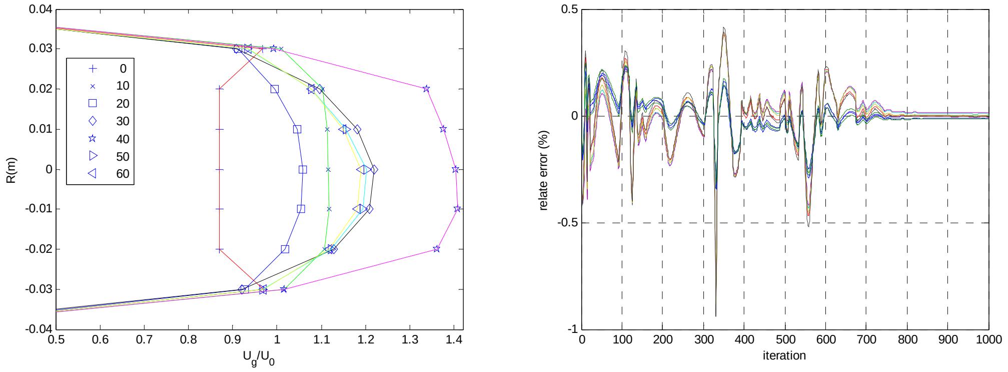

(a) (b)

Figure 2.3 The convergence behaviour of numerical simulations. (a) the evolution of the stream-wise air velocity profile across the pipe at x=2.0m on seven selected iteration numbers of two-coupling computations (b) the development of the relative error of the velocity to its average value versus numerical iteration on nine reference points.

2.3.1 Particle trajectories in the pipe

Numerical simulations were firstly performed to explore particle trajectories in the pipe. Figure 2.4 only shows trajectories of glass beads (100μm) injected along the y axis in a smooth pipe (ϕ80mm) under air conveying velocity 24m/s. Here, R means pipe radius and y stands for the feed position of a particle. Both figures in Figure 2.4 clearly display the phenomenon of gravity settling. It shows that the peak positions of particles gradually decrease along the pipe due to the gravity force. When they hit the pipe surface, particles will bounce and move along the pipe by saltation. Since particles are injected at different positions on the pipe inlet, the trajectories of the particles will not have any axial symmetry property at the particle impact point on the wall due to the curved surface of the pipe, even though an elastic particle-wall collision model is applied in the calculations. In Figure 2.4(b), we can clearly observe that particles injected close to the wall have a jumping path from their feed positions distinct from others in the mainstream region. This indicates that a particle close to the wall must be acted on by an additional force in the y direction, and that this force is larger than the gravity force on the particle. In the boundary region, this additional force is the Saffman lift force induced by flow velocity gradients in the y direction. It can be expressed as (Fan L.S., 2003).

$$\vec{F}_s = \frac{K\mu}{4}\left|\vec{U}_a - \vec{U}_p\right| d_p^2 \sqrt{\frac{1}{\upsilon}\left|\frac{\partial\left(\vec{U}_a - \vec{U}_p\right)}{\partial y}\right|} \qquad (2.2)$$

where F_s is the Saffman force, the constant K is 6.46 (kgm^3s^{-3}), U_a is the air velocity and U_p is the particle velocity, μ is the air absolute viscosity and ν is the air kinematic viscosity. The influence of the Saffman force on particles will be discussed in the following three sections (2.3.2-4) in terms of variations of air conveying velocity, pipe roughness and particle size.

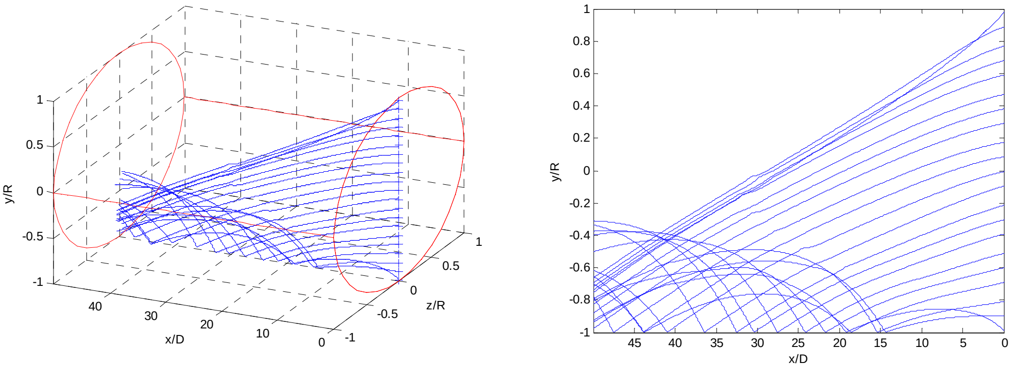

(a) 3D trajectories (b) Trajectories in y direction

Figure 2.4 **Particles trajectories (running direction from right to left)**
(Glass beads, d_p=100μm, U_a=24m/s, ϕ80mm smooth pipe, solid loading mass ratio 1% kgs^{-1}/kgs^{-1})

Figure 2.5 shows the trajectories of two particles injected at two points of y/R equal to -0.90 and -0.99 respectively, which are close to the pipe bottom. These trajectories were selected from those in Figure 2.4 for clearly visualizing particle trajectories in the boundary region. Observing two selected trajectories in the y direction (Figure 2.5a), we can see that the particle injected at the position of y/R=-0.99 has a distinct jump at the start point, which is due to its Saffman force being larger than its gravity force. On the contrary, the particle injected at the position of y/R=-0.90 does not have such a feature. Behind the first particle-collision point, the Saffman force acting on particles should be decreased since particles have been accelerated in the distance, which is more than x/D=15. However, the second peak in the y direction is higher than the first one on each particle trajectory, which indicates that the reflected U_{py} (particle velocity in the y direction) is larger than the impacted U_{py} at the collision point. On the other hand, the trajectories of two particles in the z direction (Figure 2.5b) displays the fact that their positions in the z direction begin to be away from their feeding positions of z=0 behind the first particle-wall collision point. The above phenomena can be also explained by the variations of U_{px} (the axial particle velocity) and U_{py} (the vertical particle velocity) in Figure 2.5(c) and (d) for two selected particles separately. According to the trajectory before the first particle-wall collision point Figure 2.5 (c) and (d), the similarity for both particles lies in that they are accelerated to have an increasing U_{px} in the x axis from the static state at the feeding positions. In contrast, the difference between two particles is that the particle injected at the point r/R=-0.99 has obtained a positive U_{py} which makes it suspended in the y direction (as shown in Figure 2.5 (c)). The particle injected at the point r/R=-0.9 falls down due to gravity force in the y direction. When a particle hits the pipe wall, we can clearly see that not only the sign of U_{py} is changed from the negative to the positive but also the magnitude of U_{py} in the rebound direction is larger than that in the impact direction. Consequently, the second peak in a particle trajectory is higher than the first peak in the y direction. In addition, compared with that in the impact direction, the magnitude of U_{px} decreases a little after particle-wall collision. This indicates that some particle momentum on the x axis has been transferred to that in the y direction during particle-wall collision, since the normal line of the particle-wall elastic collision is along a pipe radius rather than the y axis.

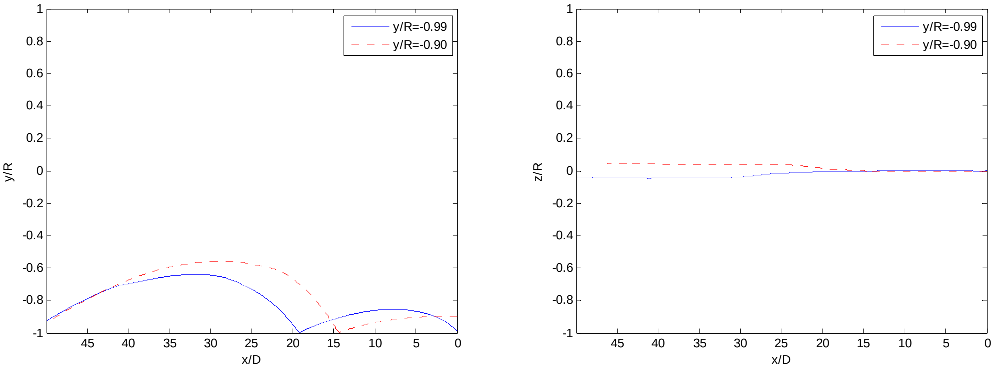

(a) Trajectories in y direction

(b) Trajectories in z direction

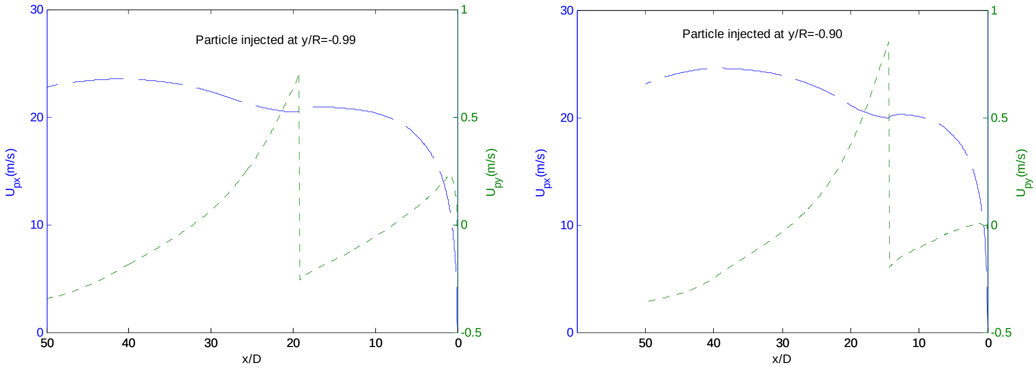

(c) For the particle injected at y/R=-0.99

(d) For the particle injected at y/R=-0.90

Figure 2.5 Trajectories and the variations of (U_{px}, U_{py}) for two selected particles

The above discussions show that both Saffman force and particle-wall collision on pipe wall exert an important influence on particle behaviour at the pipe boundary. In order to only investigate the effect of the Saffman force, the following three sections from 2.3.2 to 2.3.4 will present the numerical simulations in two dimensions for clarity, corresponding to the z=0 section in 3D mode for 100μm glass beads. In this case, the normal line of particle-wall collision is along the y axis and there is no momentum exchanged among three components of a particle velocity during particle-wall collision.

2.3.2 The effect of air conveying velocity

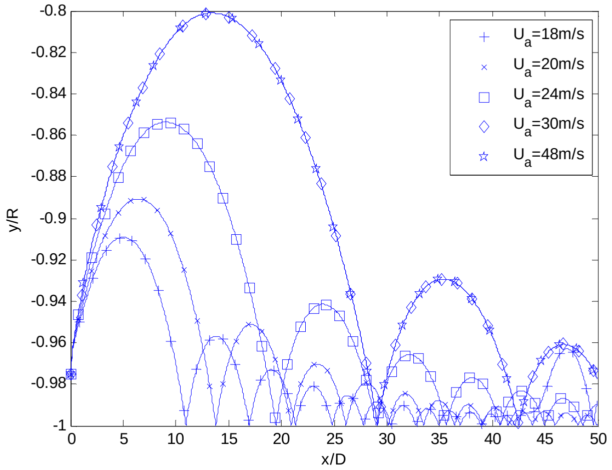

Figure 2.6 Particle trajectories with different conveying velocities
(100μm glass beads, ϕ80mm smooth pipe, solid loading ratio 1%, 2D model)

In the 2D mode just as at the z=0 section in the 3D model, 200 parcels (a parcel means a group of particles with the same diameter injected at the same position) were equally injected over the pipe inlet. The three influences of conveying velocity, wall roughness and particle size are investigated for exploring particle characteristics in the boundary region. Changing only air conveying velocity while keeping other parameters constant, the numerical results of air velocity effects on the boundary region are shown in Figure 2.6. It shows the trajectories of a single particle injected at the position of r/R=97.5% with different air conveying velocities. Compared with other points, an injection point in the boundary region is close to the pipe bottom where the Saffman force should be strong due to the strong gradient of air velocity on the y axis. Observing the first peak of the trajectories in Figure 2.6, we can see that the particle jumps higher and higher when air conveying velocity increases from 16 to 30m/s. However, the particle can jump no higher when the air conveying velocity is more than 30m/s. In this case, it follows the previous highest path. In summary, a stronger air conveying velocity generally benefits by lifting a particle higher from the boundary region toward the pipe mainstream field, but it can not be lifted much higher when air velocity is more than a certain value. This value is defined as the critical air conveying velocity. Here the value of 30m/s is the critical velocity for the current fluid conditions. Note that the numerical simulations have been carried out from 16 to 48 m/s at 2m/s increments and the data of only five typical air velocities are shown in Figure 2.5 for clarity.

2.3.3 The effect of pipe roughness

The effect of pipe roughness, keeping other parameters constant, is now considered. The effect is illustrated in Figure 2.7, under the conditions of transporting 100μm glass beads by a 24m/s air conveying velocity in a ϕ80mm pipe. This figure shows the trajectories of a single particle injected at the position of r/R=97.5% with the different pipe roughnesses. We observe that a particle in the boundary region will be returned to a much higher position for increases in pipe roughness. However, when the pipe relative roughness is more than 1.64%, the trajectories of the particle are the same and the particle can no longer be lifted much higher. We call the value of 1.64% the critical pipe relative roughness for the current fluid conditions.

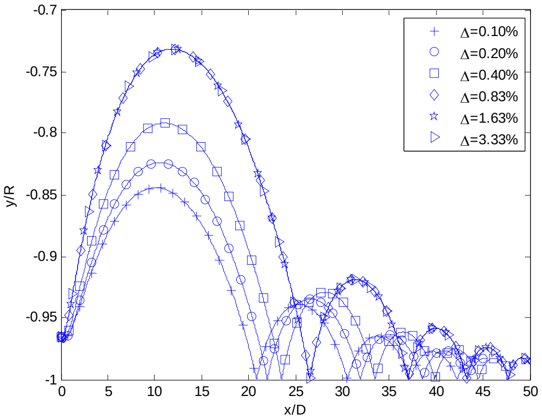

Figure 2.7 Particles trajectories with different pipe roughness heights
(U_a=24m/s, 100μm glass beads, ϕ80mm pipe, solid loading ratio 1%, 2D model))

2.3.4 The effect of particle size

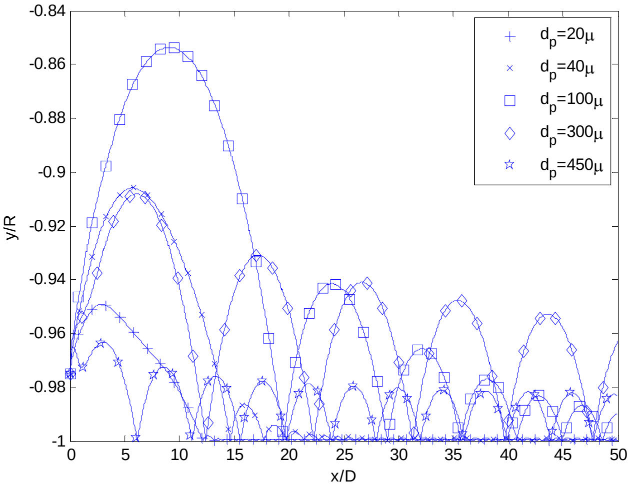

Figure 2.8 Trajectories with different particle sizes
(U_a=24m/s, glass beads, ϕ80mm pipe, solid loading ratio 1%, 2D model)).

In general, the bigger a particle is, the stronger the gravity force acting on it. Also, according to equation (2.2), the larger a particle, the stronger the Saffman force produced. As such, the suspension possibility of a particle in the boundary region is determined by the relative magnitude of the gravity force and the Saffman forces on it. Figure 2.8 shows the effect of particle size under the conditions of 24m/s air conveying velocity in the ϕ80mm smooth pipe. It shows the trajectories of a single particle injected at the position of r/R=97.5% with the different sizes. Particles from 10 to 450μm at an increment of 10 μm have been investigated, but the particle trajectories of only five specific sizes are shown in Figure 2.8 for clarity. Basically, the bigger a particle is, the higher it can be suspended if its size is in the range of 10~100μm. But this phenomenon will no longer exist when a particle is larger than 100μm. As such, the value of 100μm is defined as critical particle size for the current fluid conditions.

As indicated in equation (2.2), the Saffman force in the pipe boundary region will be stronger with increasing air conveying velocity, particle size and pipe roughness. However, the critical values of these three parameters can not be directly deduced from equation (2.2). The three critical parameters explored by the numerical results will benefit in determining the minimum air conveying velocity in dilute pneumatic conveying systems.

2.3.5 The characteristics of particle mean velocity in terms of particle Stokes Number

Table 2.3 Particles Stokes number and terminal velocity

Coal (1550kg/m^3)			Woodchip (185kg/m^3)	Glass (2500kg/m^3)
d (μm)	Stokes Number	Terminal Velocity U_{pt} (m/s)	d (μm)	d (μm)
10	0.072	0.0046	30	8
20	0.287	0.0183	59	16
30	0.645	0.0408	88	24
40	1.147	0.0718	117	32
50	1.793	0.1103	146	40
60	2.581	0.1548	175	48
70	3.514	0.2035	204	56
80	4.589	0.2546	233	63
90	5.808	0.3065	262	71
100	7.171	0.3587	291	79
150	16.13	0.6664	436	119
200	28.68	0.9472	581	158
250	44.82	1.2830	726	197
300	64.53	1.6129	871	237
350	87.84	1.9328	1016	276

Stokes Number (St) is defined as the ratio of particle inertia to fluid drag. It is known that a particle having a small Stokes Number has a good capability of following the fluid. Since granular biomass is usually lighter and larger than pulverized coal, the question whether they have any similar characteristic in pipes is investigated in this section. We will use the Stokes

Number to classify the similarity between pulverized coal and granular biomass characteristics in the direction of fluid flow and apply the terminal velocity (U_{pt}) for the dimensionless analysis of particle velocities in the gravity direction. The detailed equations for calculating the terminal velocity of a particle are listed in the book Processing of Particulate Solids (Seville et al., 1997). Table 2.3 shows values of St and U_{pt} for typical samples of pulverized coal, wood chips and glass beads.

In order to address the similarity of granular biomass and pulverised coal, numerical simulations have been carried out on the transportation of nine kinds of mono-distributed granular woodchips (100~1016μm) and 10 types of mono-distributed pulverised coal (10~150μm) by 10m/s conveying air with solid mass loading ratio 1% in a horizontal smooth ϕ80mm straight pipe. Each kind of particle was released from the pipe inlet with a homogenous distribution across the whole inlet area. The detailed boundary conditions and related numerical parameters are listed in Tables 2.1 and 2.2. Here we have focused our attention on the analysis of the mean particulate velocities of the solid phase, since the mean quantities are of more interest in engineering applications.

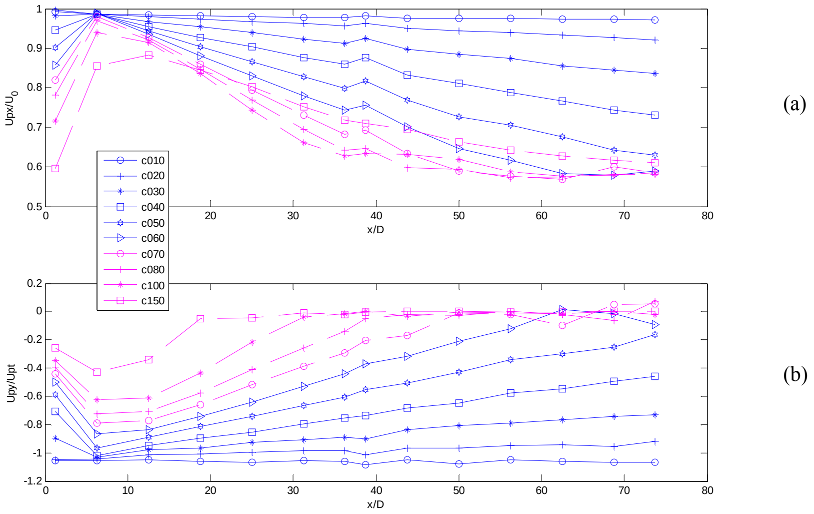

Figure 2.9 The evolution of the mean particulate velocities U_{px} and U_{py} for pulverised coal
(U_a=10m/s; smooth pipe; coal particles size 10~150μm; solid loading ratio 1%, 3D model)

In general, the mean particulate horizontal velocity (U_{px}) on the x axis or fluid direction is rendered dimensionless by the air conveying velocity (U_a) and the mean particulate vertical velocity (U_{py}) on the y axis or gravity direction is made dimensionless by its terminal velocity. The development of these two dimensionless velocities is shown in Figure 2.9 (a) and (b) respectively.

The evolution of the horizontal dimensionless velocity U_{px}/U_a in Figure 2.9(a) shows the progression of the solid phase from the acceleration region into the fully developed state. This process depends on the mean particulate size of the solid phase. The larger the mean particulate size, the longer is the acceleration distance.. In a comparison, fine particles like those of 10μm diameter have almost no obvious acceleration distance before they attain a velocity equal to that of the conveying air (U_a). This agrees with the theoretical prediction of Seville, (1997), that the fine particles have a good ability to follow the fluid. On the contrary, particles with a larger mean size such as 150 μm usually have a longer acceleration distance before attaining their peak velocities in the horizontal direction. Their horizontal mean velocities subsequently begin to decease gradually until they reach a steady value whose dimensionless value is equal to 0.6 (U_{px}/U_a).

With regard to the variation of the vertical dimensionless velocity U_{py}/U_a in Figure 2.9(b), we can see that the mean particulate vertical velocities (U_{py}) of fine coal particles less than 20μm in diameter rapidly develop to their corresponding terminal velocity. However, the mean particulate vertical velocities of larger particles more than 80μm in diameter tend to zero after they enter the fully developed region. This indicates that the vertical velocities of these larger particles have equivalent possibilities of being in the up or down direction with the same absolute velocity on the y axis.

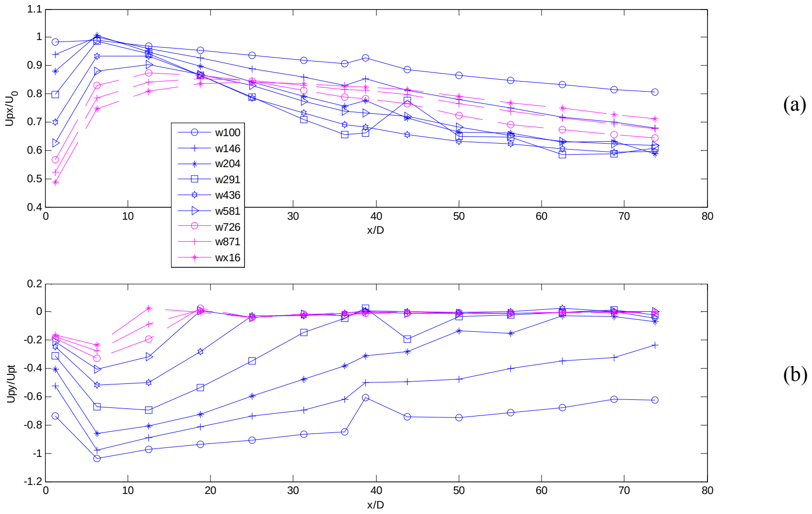

Figure 2.10 Evolution of the mean particulate velocities U_{px} and U_{py} for wood particles
(U_a=10m/s; smooth pipe; Wood chips 100~1016μm; solid loading ratio 1%, 3D model)

Since particles with a low Stokes Number (less than 1) have a good ability to follow the fluid no matter what kinds of materials they are, we only focus on woodchips with equivalent diameter more than 100μm, corresponding to particles with a Stokes number >1 (Table 2.3). Figure 2.10 shows the variation of the dimensionless velocities of the larger wood chips. As with pulverised coal, the larger granular woodchips compared with the smaller ones have a longer acceleration distance to before attaining fully developed flow. Subsequently, their horizontal mean velocity reaches a steady value whose dimensionless value (U_{px}/U_a) is also equal to 0.6. The averaged value of the mean particulate vertical velocities for the larger particles also rapidly reaches zero. Summarizing the foregoing discussions, we can classify the characteristics of the mean particulate velocities in the horizontal and vertical directions into three types by Stokes Number, as listed in Table 2.4. This table indicates that the particles of the different materials have similar dynamic characteristics, such as particulate mean velocities in the horizontal and vertical directions, if their Stokes Numbers are equal.

Empirically, it is reported that the slip ratio, defined in terms of the mean velocity of the solid phase divided by the conveying velocity, is usually around 0.8 (Mills, 2004). This definition is similar to the dimensionless mean particulate horizontal velocity in this chapter if the mean velocity of the particles is considered as the solid phase velocity. According to Table 2.4, the value of $0.8U_a$ is the median value of the mean dimensionless particle velocity in the horizontal direction. Since we use mono-dispersed particles in the numerical simulations, the slip ratio of the poly-dispersed solid phase will vary in the range of $(0.6\sim1)U_a$ depending on its mean particulate size. In the vertical direction, particles with Stokes Number less than 1 can be easily suspended in a fluid since their vertical velocities equal the corresponding terminal velocities. However, for particles with Stokes Number more than 3.5, the averaged value of particle velocity in the y direction tends to be zero. This implies that these particles bounce or slide along the pipe with a high frequency of particle-wall collisions.

Table 2.4 The mean axial particle velocity in the fully developed region

Stokes Number	< 0.6	0.6 ~ 3.5	>3.5
U_{px}/ U_a	1	0.6~1	0.6
U_{py}/ U_t	-1	-1~0	0

2.4 CONCLUSIONS

A detailed analysis of three factors (air conveying velocity, pipe roughness and particle size) that influence particle trajectories in the boundary region has been performed by carrying out numerical simulations using the Discrete Phase Model in Fluent 6.2.16. The numerical results demonstrate that the Saffman Force plays an important factor in a dilute pneumatic conveying system, especially for determining whether a particle will be re-suspended from the boundary region. This analysis shows that there exist three critical parameters: the critical air conveying velocity, the critical particle size and the critical pipe relative roughness. Generally, increasing any one of air conveying velocity, pipe roughness and particle size will improve the chances of a particle being re-entrained from the boundary region, in agreement with equation (2.1) which can be used to calculate the Saffman force. In addition, the numerical results also reveal that the critical values of each of these three parameters will represents a limit beyond which an increase gives no improvement in particle re-entrainment.

The characteristics of the dimensionless mean particulate velocity in the horizontal and vertical directions have also been investigated. The particle mean velocities of the different materials can be classified into three types in the horizontal and vertical directions non-dimensionalising as the Stokes Number or dividing by terminal velocity respectively. The numerical results indicate that particles with Stokes Number less than one have a mean velocity equal to the air conveying velocity in the horizontal direction and a mean vertical velocity equal to the terminal velocity in the fully developed region. Correspondingly, for larger particles with Stokes Number more than 3.5, their mean dimensionless velocity U_{px}/U_a tends towards 0.6 in the horizontal direction and their mean dimensionless velocity U_{py}/U_a essentially zero in the vertical direction. The mean dimensionless velocities of particles with Stokes number between 1 and 3.6 are in the range of 0.6~1 in the horizontal direction and -1~0 in the vertical direction.

The effects of non-spherical particles and inter-particle collisions are ignored in these numerical simulations. The latter effect will be studied by using CFD-DEM (Discrete Element Method) coupling simulations in Chapter 7.

Chapter 3

Extending Laser Doppler Anemometry for particle flow measurement in pipes

An extended Laser Doppler Anemometry (LDA) technique has been developed to measure the distributions of particle velocities and particle number over a whole pipe cross section in a dilute pneumatic conveying system. The first extension concentrates on the transform matrix for predicting the laser beams' cross point in a pipe according to the shift coordinate of the 3D computer-controlled traverse system on which the probes of the LDA system were mounted. The second focuses on the proper LDA sample rate for the measurement of gas-solid pipe flow with polydisperse particles. A suitable LDA sample rate should ensure that enough data is recorded in the measurement interval to precisely calculate the particle mean velocity or other statistical values at every sample point. The present study explores the methodology as well as fundamentals of measurements, using a laser facility, of the local instantaneous density of particles as a primary standard.

3.1 INTRODUCTION

The technique of Laser Doppler Anemometry (LDA) which is also referred to Laser Doppler Velocimetry (LDV) has been developed more than thirty years, since it was invented by Yeh and Cummins in 1964. It is non-intrusive with high accuracy and very high spatial resolution and has been extensively applied for fluid mechanics measurements. Before introducing the extended techniques of LDA, we briefly review the principle of LDA and its applications in gas-solid flow.

3.1.1 The brief principle of LDA

The Laser-Doppler method is based on the measurement of the Doppler shift of laser light scattered from small particles carried along with the fluid. The basic components and a dual beam structure of a LDA system are illustrated in Figure 3.1. This system usually comprises a continuous wave Argon-Ion-laser, fibre optics, a frequency shifter and several lenses to construct an optical probe, which can produce a measurement volume or interference fringes formed by two beams with the same light intensity and a different phase modulated by a Bragg cell. The size and position of this ellipsoidal crossing point is dependent on the focal length of the probe front lens.

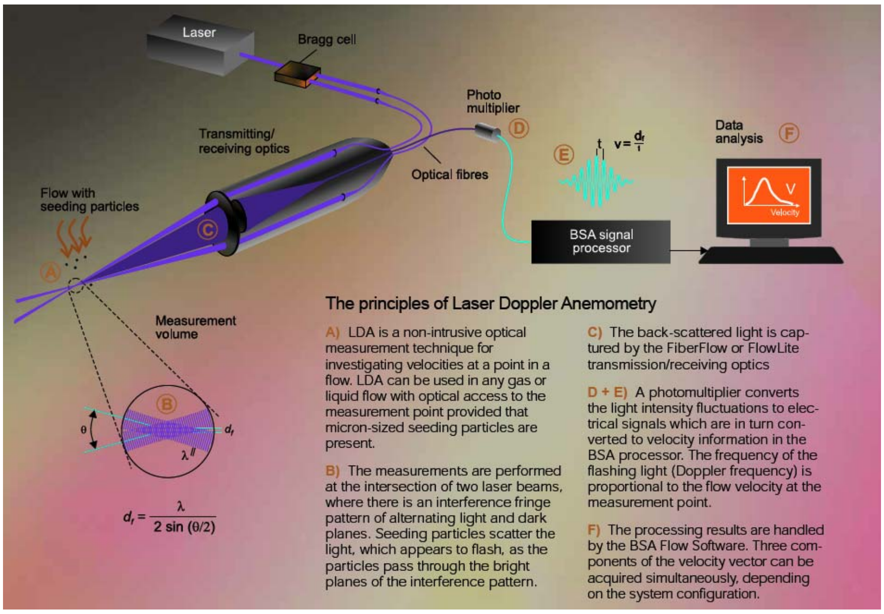

The principles of Laser Doppler Anemometry

A) LDA is a non-intrusive optical measurement technique for investigating velocities at a point in a flow. LDA can be used in any gas or liquid flow with optical access to the measurement point provided that micron-sized seeding particles are present.

B) The measurements are performed at the intersection of two laser beams, where there is an interference fringe pattern of alternating light and dark planes. Seeding particles scatter the light, which appears to flash, as the particles pass through the bright planes of the interference pattern.

C) The back-scattered light is captured by the FiberFlow or FlowLite transmission/receiving optics

D + E) A photomultiplier converts the light intensity fluctuations to electrical signals which are in turn converted to velocity information in the BSA processor. The frequency of the flashing light (Doppler frequency) is proportional to the flow velocity at the measurement point.

F) The processing results are handled by the BSA Flow Software. Three components of the velocity vector can be acquired simultaneously, depending on the system configuration.

Figure 3.1 The schematic diagram of a laser-Doppler anemometry (DANTEC, 2008)

In Figure 3.1, if the two beams with the same wavelength λ intersect at an angle θ, the distance d_f between the interference fringes can be theoretically deduced as:

$$d_f = \frac{\lambda}{2\sin(\theta/2)} \qquad (3.1)$$

When a particle passes through the measurement volume, the scattered light will be distributed over the whole of space. The scattered light is characterized by a Doppler shift, the Doppler frequency f, which is proportional to the velocity component perpendicular to the bisector of the two laser beams. An optical fibre mounted behind the front lens of the probe is used to receive and deliver the scattered light to a photomultiplier. Then the intensity, phase as well as the amplitude fluctuation of the scattered light can be detected and analyzed in the BSA signal processor. If we know the time t which a particle takes to travel the distance between two fringes (it is also called the fringe spacing), its velocity can be directly calculated by equation (3.2).

$$u_p = \frac{d_f}{t} \qquad (3.2)$$

In this way, the task of measuring the velocity of a particle is modified to determine the spent time t or frequency (f=1/ t) of a particle passing through the fringe, which is evaluated in the BSA signal processor by using spectral analysis. The relationship between the frequency and particle velocity is given as equation (3.3).

$$f = \frac{2u_p}{\lambda}\sin\left(\theta/2\right) \tag{3.3}$$

The above explanation is called the Fringe model of LDA in which the Doppler signal is interpreted as several single bursts interspersed with periods of low-power shot noise. Correspondingly, the principle of LDA can be also explained by the frequency demodulator model in which the Doppler signal is considered quasi-continuous. The detailed contents of these two models were reviewed by Buchhave et al. (1979) who deduced the model equations and summarized the physical parameters affecting the Doppler signal, such as Doppler ambiguity, bias correction, refractive index effects and minimizing and eliminating the effects of phase fluctuations on turbulence measurement.

Since a velocity measured by LDA is calculated from the Doppler shift signal produced by a moving particle, this measured velocity is essentially the particle velocity rather than fluid velocity. As a result, Buchhave et al. (1979) suggested a criterion for particle selection for fluid measurement. Empirically, seeding particles with light density should be chosen less than 17 μm for measuring air velocity and 49 μm for water fluid assessment. Consequently, when these particles are used as the seeding particles, the velocities measured by LDA will be regarded as the fluid velocity. Thus, a velocity measured by LDA is considered as particle velocity or fluid velocity depending on the Stokes Number of the seeding particles.

3.1.2 Literature view of LDA applications in gas-solid flow

Gas-solid flow like pneumatically conveyed bulk solids is frequently met in many industrial fields. Instrumentation for detailed gas-solid flow measurements is highly desirable in order to understand physical phenomena and mechanisms for optimum design and operation of gas-solid systems. Since it is a non-intrusive and highly accurate velocity measurement instrument, LDA has been widely applied to investigate characteristics of gas-solid flow individually or combined with other instruments. As a result, there are numerous papers in which some interesting results have been published and some valuable techniques used for extending the functions of LDA have been reported as well.

Since the key function of LDA lies in velocity measurement, papers related to the velocity measurement of a single phase in gas-solid flow are listed in Table 3. From the 1970s, the velocity profiles of a single phase in gas-solid flow in vertical or horizontal pipes (channels) and Circulating Fluidized Bed have been measured along a pipe radius or any specific line by using LDA. The effect of characteristics such as particle velocity, the roughness effect on the development of a stabilized laminar boundary layer, the effect of inter-particle collisions and the effect of particle-wall collisions have been completely or partially explored through analyzing the velocity data measured by LDA. In addition, several papers also used LDA to calibrate other instruments like Electrical Capacitance Tomography (ECT) for velocity measurement.

Since the velocity of a single phase is just one of the basic parameters to characterize gas-solid flow, it is most interesting to obtain the other possible parameters such as solid concentration and particle size as well as their distribution on a cross-section or along the fluid direction. To fully characterize unsteady gas-solid flow, it is important to measure particle velocity and other parameters simultaneously. Table 3.2 lists the previous papers in which LDA was combined with other instruments like a pyrometer and a laser-particle-sizing system to obtain additional information like particle temperature and particle size as well as measuring particle velocity.

Moreover, there have been extensive studies for extending the standard single point velocity measurement of LDA to multifunctional operation, which include multi-point LDA, simultaneous two phase velocity measurement and particle size measurement by using an individual LDA device. For example, several papers describe a similar novel method of setting two threshold amplitude values to classify Doppler signals for measuring velocities of two phases at the same time. The principle of this method is based on the fact that light scattered by a large particle has a large pedestal amplitude of Doppler signal. Additionally, several numerical papers demonstrate how to assess the stability of signal processing in LDA and analyze the possible errors of LDA using a digital method to measure the frequency of Doppler signals. Table 3.3 lists the corresponding principle and the brief results of these papers from the 1980s.

With regard to the optical arrangements in the experiments listed, three general types can be categorized as: in an open environment; in a bounded region with a slot or hole as the measurement window; and in a transparent bounded region without the additional flat window on the wall. Obviously, no light refractive effect occurs in an open environment and there is only a light shift phenomenon on a flat window. But it is necessary to consider the refractive effect which results in changing the direction of a laser beam at a curved surface. As for the refractive effect, Tsuji et al. (1982, 1984) mentioned it in his horizontal and vertical pipe flow measurements. But no detailed information was given for analyzing the deviation of the LDA measuring point from its expected position in pipes. It was assumed that the influence of refraction could be neglected so long as the traversing of the measurement point was within a specific range in a pipe. Most papers give no clear information on dealing with the refraction effect. Many experiments in pipes or channels were carried out to measure particle velocity along a pipe diameter line rather than on a whole cross-section. Thus, it is a basic and essential task to study the refractive effect due to pipe curvature for measuring particle velocity in gas-solid pipe flow.

In the previous section (3.1.1), we have discussed the fact that data recorded by LDA represent the velocity of a particle passing through the measurement volume. With regard to gas-solid measurement, particles of solid phase are directly regarded as the seeding particles. Consequently, the measured results are normally considered as a group of instantaneous particle velocities within a specific interval. The local velocity of the solid phase at this measurement point is usually averaged from this time series data. However, particle size of the solid phase may be distributed widely and particle density may also differ for multi-material solid phases such as pneumatically conveying a fuel mixture of pulverised coal and biomass particles. In these cases, the accurate time-averaged value will be strongly dependent on obtaining enough sample data in the recorded data set of particle velocity. In particular, particle velocity varies with its Stokes Number which is related to particle size, particle density and local air velocity at a sample point. Hence, considering the proper sample rate of LDA is also essential and necessary to gas-solid pipe flow measurement.

For the above discussed reasons, we will study the refraction effect and sample rate in the next two sections.

Table 3.1 The applications of an individual LDA (Single phase measurement)

Reference	Experimental rig	Flow condition	Measurement window type	Results
Birchenough and Mason (1976)	3m long, ϕ49.4mm vertical glass tube	✧ Air conveying velocity, 16-48m/s ✧ Solid loading ratio less than 2.2 ✧ Alumina powder with mean size 21μm	Direct measurement without considering the effect of light refraction on the tube surface	✧ With increasing solid loading, the experimental results display that the particle velocity profiles become flattened ✧ There is negative particle slip at the pipe wall.
Barrent et al. (1995)	An 800mm wide and 1100mm long flat plate with an elliptical leading edge section and porous suction surface mounted in the centre of wind tunnel (800mm width, 600mm height,1600mm length)	✧ Air velocity less than 105 m/s ✧ Seven kinds of particles ranging from 0.5 to 1.5mm	No information about arranging the measurement window	✧ Examining the effect of isolated surface roughness elements on the development of stabilized laminar boundary layers by three- component LDA. ✧ The critical speed at which disturbances are propagated downstream from a surface has been found to be characterized by a constant value of roughness Reynolds number (about 800).
Fan et al. (1996)	A jet (its central ϕ40mm and its annular ϕ68mm) was mounted into a ϕ2000mm cylindrical container	✧ Primary air velocity 20m/s; Secondary air velocity ranging from 30 to 60 m/s ✧ Solid loading ratio, 0.5~1.5 ✧ Silica gel powder (its mean size 50 and 200 μm)	Flat glass measurement window on the wall of the container	✧ The results indicate that the diffusion of the particle phase in the radial direction is much slower than that of the gas phase and the mean velocity profiles of the particle phase are flatter than those of the gas phase.
Tu et al. (1997)	An in-line tube bank consisting of a 6*6 array of carbon steel tube was arranged in a wind tunnel	✧ 11.2m/s air conveying velocity ✧ two kinds of glass beads (66 and 95μm) ✧ solid loading ratio 0.1kg/kg	A glass measurement window of 360*500mm^2 was open on the bank wall.	✧ The collisions between particles and the tube surface had considerably influence on particle motion, which resulted in substantial differences in the flow patterns between two phases through the tubes.
Morsi et al. (2004)	✧ The rig is same as the above one for measuring the instantaneous incident and rebound particle velocities by using two dimensional LDA in the immediate vicinity of the tubes surface.	✧ Air velocity (8~13.7m/s) ✧ Glass beads (means size 35, 66 and 93μm) ✧ Solid loading 0.1kg/kg	No information about arranging the measurement window	✧ For a single tube, the particle rebounding flow pattern in the vicinity of the wall was mainly affected by particle inertia (Stokes Number). The gas flow at high Reynolds number was found to suppress the rebound tendency of the particles. ✧ For tube bundle structure, particles rebounding from the approaching tubes upstream migrated downstream and impinged the tubes in an extremely complex and random disposition.
Parkhomov	A 2500mm long vertical	✧ Reynolds number 15300	No mention	✧ A significant anisotropy of fluctuations of particle

(2007)	stainless steel pipe with ϕ46mm	✧ Glass beads (mean size 50μm) ✧ Tracer particles 2~3μm		velocity has been found. The amplitude of turbulent fluctuations of particle velocity in the axial direction is much higher than that in the radial direction
Datta et. al., (2007)	A 7 m long horizontal pipe section (ϕ57mm) and a 3 m long vertical section.	✧ Air velocity ranging from 1.0 to 5.0m/s ✧ Polyamide chips approximate (3mm long, 3 mm wide and 1mm thick)	No mention	✧ For low solid concentration, the pixel values of the images measured by ECT were low as well, there was not adequate signal to obtain valid velocity measurement from the instantaneous correlation function. This was observed from the velocity distribution profile obtained by ECT compared with the data of LDA

Table 3.2 The applications of LDA combined with other instruments for gas-solid flow measurements

Reference	Experimental rig	Flow condition	Additional instrument and Measurement window type	Results
Fincke et al. (1990)	Powders of a metal (Ni-Al) and a metal oxide (Al_2O_3) were presented for studying the plasma spray-coating process	✧ Air spray velocity 100~300m/s ✧ Particle size within 5~100 μm ✧ Particle mass flow rate within 0.25 to 5 kg/hour	✧ A two-color pyrometer for measuring particle temperature ✧ A scattered-light particle size measurement ✧ No measurement window (in open environment)	✧ Measured particle size, velocity and temperature simultaneously ✧ The particle velocities and temperature were insensitive to the particle injection rate over the loading range. ✧ Particle injection geometry and particle velocity and mass significantly affect the spatial distribution of particle size in the plasma plume and thus can alter the characteristics of the deposited coating.
Huber and Sommerfeld (1994)	In a dilute pneumatic conveying system, the measurements were performed in horizontal and vertical pipes	✧ Air conveying velocity ranging from 10 to 30m/s ✧ Solid loading ratio between 0.2 and 1.0 kg/kg ✧ Glass beads with mean diameter 40μm	✧ Phase Doppler Anemometry (PDA) for particle size measurement ✧ Laser-light sheet technique for measuring the solid concentration within the whole pipe cross-section ✧ No information about the light refractive effect on pipe surface	✧ The experimental results indicated that the pipe wall roughness had a considerable influence on the particle motion after a wall collision and, especially for small collision angles. ✧ An increased conveying velocity reduced segregation in a horizontal pipe due to the higher flow turbulence established. ✧ The motion of large particles (larger than 100μm) was strongly governed by inertial effects and no marked segregation was observed in the different pipe elements considered.

Van de wall and Soo (1994)	A cyclone-standpipe recirculating pipe flow system A horizontal pipe ϕ127mm	✧ Air conveying velocity 20m/s ✧ Glass beads ϕ44-62μm ✧ Solid loading ratio 0.4~2.2 kg/kg	✧ Phase Doppler Particle Analyzer (PDPA or PDA) ✧ No information about the effect of the light refraction on the pipe surface	✧ Determination of instantaneous local particle velocity and density ✧ The experimental data confirmed that PDPA provides a means of determining the instantaneous local particle density when the averaging procedure satisfied the criterion of continuum counterpart of time-averaging and length scale relation. ✧ The local averaging time should include on the order of 102 particles for the continuum approximation and the path length should be smaller than the characteristic dimension of the physical system
Bao and Soo (1995)	The same as the above rig	✧ Air conveying velocity 20 m/s ✧ Solid loading ratio 1.92, 2.04 and 2.5 kg/kg ✧ Glass beads ranging from 0~80μm with the mean size 45μm	✧ PDPA ✧ No detail information about the effect of refraction at the pipe wall	✧ Used a two-dimensional Laser Doppler Velocimeter combined with a phase Doppler particle analyzer to determine average and fluctuating properties and Reynolds stresses. ✧ The traverse of the measuring volume along a vertical diameter gave results showing the gravity effect in the flow of a gas-particle suspension ✧ The instantaneous local particle cloud density and velocity showed the nature of distribution in the particle phase.

Table 3.3 Development of LDA multifunction for gas-solid flow measurement

Reference	Research Objectives and Experimental rig	Flow condition	Multifunction principle and Measurement window	Results
Tsuji et al. (1982)	A horizontal glass pipe (ϕ30.5mm) in a pneumatic conveying system	✧ Air conveying velocity from 6 to 20m/s ✧ Two kinds of plastic particles (1000 kg/m^3) with 0.2 and 3.4mm mean size respectively ✧ Solid loading ratio less than 6 kg/kg. ✧ Ammonium chloride	✧ Principle: determining the pedestal component of the burst signal of LDA, the larger a particle is, the larger the pedestal component is. ✧ Window: considering the refractive effect at the pipe wall, but without	✧ Measured the velocities of air phase and particles simultaneously ✧ As the loading ratio increased and the air velocity decreased, mean-velocity distributions of both phases became more asymmetrical tendency. ✧ The effects of the solid particles on air-flow turbulence varied greatly with particle size. That is, 3.4mm particles increased the turbulence markedly, while 0.2mm ones reduced it.

		(ϕ0.6μm) as tracers	any detailed explanation.	
Tsuji et al. (1984)	A vertical glass pipe (ϕ30.5mm) in a pneumatic conveying system	✧ Air conveying velocity from 8 to 20m/s ✧ Five kinds of glass beads (mean size 3.43, 2.78, 1.0, 0.5 and 0.2 mm) ✧ Solid loading ratio less than 5 kg/kg.	The same as the above	✧ The smaller the particle size, the flatter was the mean air velocity profile for the same mass flow ratio of solids to air. Large particles increased air turbulence throughout the pipe section, while the small particles reduced it. ✧ Both effects of promotion and suppression of turbulence were observed at the same time in the presence of particles of medium size, that is, the turbulence was increased around the pipe centre and reduced near the wall.
Dupont et al. (1991)	A circular cylinder in a wind tunnel for studying the wake developing behind it	✧ Air velocity 4.5 and 61 m/s ✧ No information for tracers	✧ Used spectral analysis method to assess the sample data obtained by LDA ✧ Window: in open environment	✧ A simple model of PSD (power spectral density) was introduced to determine whether the particles used for the seeding were able to follow the characteristic frequencies of the flow ✧ It has been shown that the PSD can be relied on up to frequencies much greater than the mean sampling rate as long as there are well pronounced peaks in the spectrum.
Chao et al. (1992)	The experiments were performed in the shear layer of turbulent jet flow issued from a large 100 and 10 mm nozzle	✧ Seeding particles of paraffin oil with a nominal diameter of 1μm ✧ Air velocity 4m/s for the small nozzle and 1.8m/s for the large nozzle	✧ Used an unequally spaced fractal interpolation method to reconstruct the random, intermittent, low data rate LDA signals for spectral analysis ✧ Window: in open environment	✧ The reconstructed result not only augmented the data points to improve the statistics but also retained the turbulent fractal dimension of the flow. ✧ The results showed that the fractal reconstruction method could properly restore the characteristics of peak frequencies of the flow from low data rate LDA signals or from decimated data, while the conventional sample-and-hold method failed to capture any of the major peak frequencies.
Grechikhin and Rinkevichyus (1993)	Numerical simulation of analyzing the errors of the signal processor of a LDA using digital methods to measure the frequency of the Doppler signal.	✧ Considered the photodetector output represented as the sum of particle velocity signal and noise component of a steady Gaussian process with zero average value ✧ The errors related to the frequency difference of the interfering beams, the period of the interference pattern and the effective radius of the measuring region		✧ Developed a method for evaluating the period of the high-frequency filling of the LDA signal from the coordinates of the “zero” of the process and for estimating the signal frequency from the position of the maximum value of the spectral density. The results reported show that the limiting values of the total error of measurement of the LDA signal

				frequency can be decreased to 0.1~0.3%.
Chen and Kadambi (1995)	A 3.05m long PVC pipe (ϕ25.4mm) connected with a glass test section	✧ Silica gel particles of mean size 40μm ✧ 50% sodium iodide solution as the liquid phase whose refractive index is similar to the silica particles	✧ Used the matched refractive index of the solid and liquid to discriminate the signal amplitude according to the histograms of measured velocity data ✧ Without consideration of the refraction effect on the pipe wall	✧ Discriminated between solid and liquid velocities in a refractive index matched solid-liquid slurry flow by identifying the histogram peaks associated with the solid and liquid velocities respectively. ✧ The experimental data demonstrates that this discrimination technique is suitable to be applied to slurry flows flow of low turbulence intensity (less than 10%) with volumetric concentration as high as 25% in the heterogeneous and saltation flow regimes
Frank et al. (1996)	A horizontal and vertical glass pipe in a heat transfer station	✧ Used the dimensionless parameters without clear data about fluid conditions	✧ Velocity-area methods are characterized by dividing the cross-section into a number of annuli of equal area. ✧ Without information about effect of light refraction on the pipe wall	✧ Developed a multi-point technique of LDA for flow rate measurement in asymmetric and unsteady pipe flow ✧ The uncertainty of flow-rate measurement was decreased less than 1% by using velocity-area methods. The minimum number of radii for slightly asymmetric flow is four, otherwise six or eight radii are used ✧ The design of miniaturized low-cost multi-point sensors with just one laser and signal processor is shown to be possible.
Werther et al. (1996)	A cold model of Circulating Fluid Bed (CFB) with inner diameter of the riser 0.4m and 15.6m height. The measurement region located at a height of 6m above the distributor	✧ Superficial gas velocity 4m/s ✧ Quartz sand with mean size 166μm ✧ Solids volume concentration 1.2%	✧ The LDA probe was contained in a miniaturized measuring head which could be inserted into the CFB ✧ Compared with data measured by fibre-optical probe ✧ Window: no refraction effect due to the Probe being inserted into the CFB	✧ The experimental data confirmed that the LDA technique is a reliable and precise tool for particle velocity measurements in a CFB ✧ It also demonstrated that the results of both LDA and the Fibre-optical probe yielding in the CFB riser were in close agreement
Mathiesen et	A clear PVC riser	✧ Air superficial velocities	✧ The Shape	✧ Developed a modified Shape Discrimination

al. (1999)	(ϕ50.8mm, 2.75 height) in a CFB was used and the test section was located 1.12m over the elbow inlet	0.7 and 1.4m/s ✧ FCC catalyst with density 1700 kg/m^3 and size range from 11 to 180 μm (Sauter mean diameter 55μm) ✧ Solid concentration in CFB 0.5 and 2%	Discrimination technique based on knowledge about Doppler burst signal was used to determine particle size through processing the Doppler signal. ✧ A pair of flat glass measurement windows were mounted on the wall	Technique to extend the LDA technique to measure particle size directly ✧ The experimental results showed that there was no significant agglomeration in the gas-solid flow system. Typical annulus-core flow behavior was observed ✧ The largest particles showed the highest fluctuating velocity. This behavior was caused by significant gas-solid interactions.
Hussainov et al (2000)	A vertical two-phase wind-channel with a closed test section. The test section was made of plexiglass about 2m length. Its initial upper cross section 200×200 mm^2 and its downstream cross-section was 205×205 mm^2	✧ Air conveying velocity 9.5/s ✧ Glass beads with mean size 700μm ✧ Solid loading ratio less than 0.1 kg/kg ✧ TiO$_2$ particles (2μm) as tracers	✧ Used two laser powers of 26 and 10 mw to form two channels for measuring gas (tracers) and particle phase (glass beads) velocities simultaneously ✧ Flat measurement window	✧ The coarse particles considered, attenuated the grid-generated turbulence resulting in an increase of the turbulent energy in the sub-range of the energy containing eddies. ✧ The influence of the Stokes number on the turbulence modulation of the carrier flow is strong.
Hart et. al. (2001)	Developed a seedless equivalent of LDA for use in low-turbulence or supersonic flows or elsewhere where seeding is undesirable or impractical	✧ The principle of Heterodyne Non-resonant Laser-induced Thermal Acoustics (LITA) is to analyze the Doppler shifts of the acoustic waves produced by a short pulse pumped laser in the medium for measuring temperature and velocity. Neither molecular nor particulate seed is added to the flow.		✧ A compact, portable, single-component heterodyne LITA Velocimeter was constructed. ✧ A comparison of the experimental data with Pitot-static probe measurements showed that they agreed with each other. Repeated measurement of various flow profiles showed excellent stability.
Lain et al. (2002)	A horizontal channel of 6m length with the section 35×350mm^2	✧ Air volume flow rate from 507 to 1002 m^3/h and maximum air conveying velocity 30m/s ✧ Solid loading ratio up to 2 kg/kg ✧ Five kinds of glass beads with mean size 60, 100, 195, 625 and 100μm respectively.	✧ Measured two phase velocities simultaneously based on the signal phase discrimination, which was introduced in the paper of Qiu et al. (1991) ✧ A glass plate of measurement window 35 by 350 mm was inserted at the top wall.	✧ The experimental data validated the Reynolds stress turbulence model in conjunction with a wall roughness model and a stochastic inter-particle model, which were introduced by this author. ✧ It also demonstrated that both inter-particle collisions and wall roughness had a very strong effect on the development of the particle phase properties. ✧ A slight enhancement of the turbulent kinetic energy was caused by particle collisions

		✧ Spherical tracer particles with a nominal size 4µm		
Furunich et al. (2002)	A development of a two-component velocity profiler using a fiber multi-point LDA and a CCD area image sensor	✧ A two-dimensional flow channel of 160 by 160mm was used to simulate 0.065m/s water flow ✧ Tracer particles of glass beads with 100µm mean size.	✧ Combined the multi-point LDA system and a CCD area image sensor to measure a two-component velocity profile simultaneously as a function of time	✧ A novel method to measure a two-component velocity profile simultaneously was developed by using combined system of the CCD area image sensor and the multi-point LDA.
Fitzpatrick and Simon (2005)	An isothermal jet at a Mach number of 0.75 Measured the velocities near the end of the potential core of the jet	✧ Air velocity 0.75 Mach ✧ No detail on tracer particles	✧ Used the sample-and-hold reconstruction technique for determining the cross power spectra of turbulence	✧ The results obtained by the proposed method were much better than the mean sample frequency for the low LDA data rates and to the mean sample frequency for the higher rates. ✧ The computational time required for the new approach is significantly less than for the traditional slot correlation method in LDA signal processing
Li et al. (2005)	A development of multi-point LDA	✧ By employing two acoustic optic modulators for both beam splitting and frequency shifting, a multiple measuring volumes could be formed by intersecting the multiple diffraction orders generated by the two modulators. Each measuring volume had its frequency shift, which was proportional to the corresponding velocity at the local point		✧ In contrast to the other multi-detector system, the structure of this multi-point LDA system was significantly simplified. ✧ As the multi-channel information was de-multiplexed by a single-channel signal processor, the processing speed needed to be increased.

3.2. EXPERIMENTAL APPARATUS

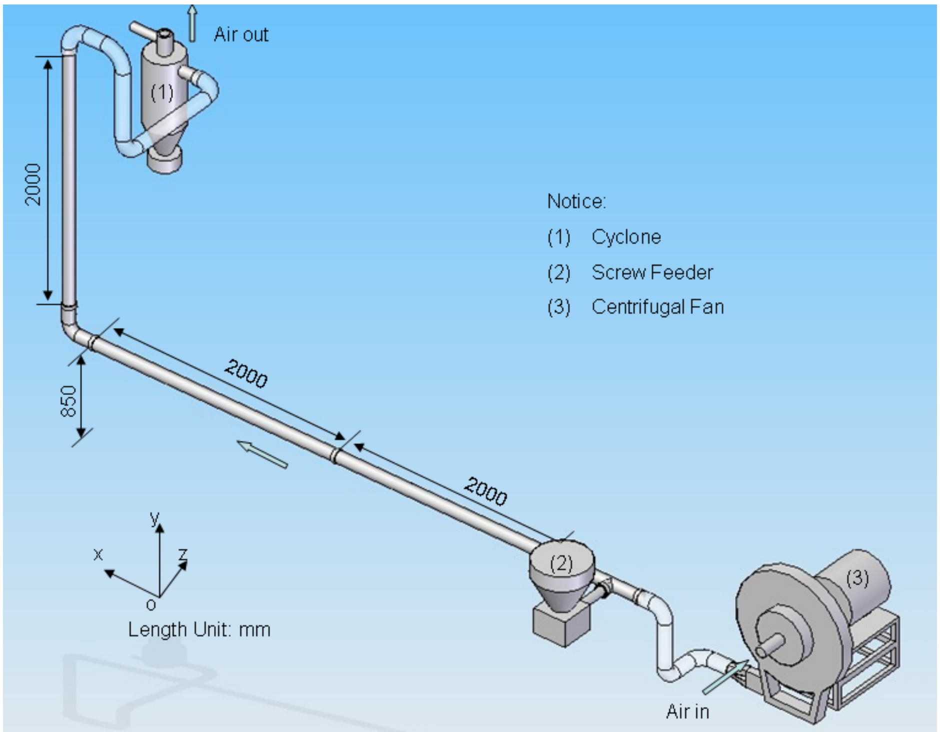

Figure 3.2 Sketch of the experimental rig

In order to characterize the cross-sectional characteristics of the solid phase in different pipe elements of a dilute pneumatic conveying systems, a pilot scale positive pressure dilute pneumatic conveying system was built which involved horizontal and vertical pipes connected by an elbow (R/D=1.3). The schematic diagram of the experimental apparatus is shown in Figure 3.2. The pipe inner diameter and outer diameter are ϕ75 and ϕ85mm respectively. The effective length of the horizontal glass pipes is 4m and the vertical is 2m long. A T-piece is used to connect a screw-feeder with the horizontal pipe and several plastic tubes are used to connect a centrifugal fan and a cyclone. This cyclone is used to separate particles from the air at the end of the system. Then particles separated from air are collected in a storage reservoir for recycling in further experiments. Additionally, every metal connector between the pipes is earthed to reduce electrostatic risk due to particle-wall collisions.

Air flow is provided by a centrifugal fan with a maximum 0.05 m^3/s volume flowrate under against a 2.2kPa back-pressure. Air conveying velocity can vary from 10 to 42m/s by adjusting the pipe back-pressure and the butterfly valve at the inlet of the fan. The maximum particle mass flow rate of the feeder was experimentally determined to be 1.0×10^{-3} kg/s for glass beads with actual density 2550 kg/m^3 and bulk density 1559 kg/m^3.

According to the numerical results of Chapter 2, which states that particles with different materials in gas-solid pipe flow have similar properties at equal Stokes Number (St), three types of glass beads and a smoke are selected in our experiment. Glass beads were used to simulate gas-solid pipe flow and the smoke was used as the seeding particle for air fluid velocity measurement. The manufacturer’s data (Worf Glaskugeln, 2008) indicate that the first type of glass beads range from 0 to 50µm, the second within 70~110µm and the third varied from 180~300 µm.

Since the pipeline is made of glass, the rig can be used to investigate properties of gas-solid flow in a horizontal and vertical pipe as well as in an elbow by using LDA or any other optical imaging system.

3.3 DEVELOPING THE SPATIAL TRANSFORM MATRIX FOR LDA PIPE FLOW MEASUREMENT

The review of LDA applications in gas-solid flow discussed in the section of 3.1.2 indicates that few papers discuss the refraction effect which causes the measurement volume of LDA to deviate from its expected position in the pipe when the crossing point of the laser beams passes through the curved surface of the pipe. In order to access the whole area of a pipe cross section, it would better to evaluate theoretically this deviation. Consequently, a shift coordinate matrix was devised to map actual positions of the measurement volume in the pipe. This is called the transform matrix.

In this section, the basic parameters of LDA used in this study are introduced. Then we will demonstrate how to calculate a spatial coordinate matrix for a given experimental rig and a fixed optical arrangement of the LDA.

3.3.1 Parameters of the LDA system

Two FibreFlow probes with a front lens of f=800mm are used to measure three dimensional velocity in a 3D Dantec LDA system. One probe combines two pairs of beams with wavelengths of 488 nm (blue) and 514.5 nm (green) respectively. The planes produced by the different coloured beams are perpendicular to each other. Another probe was integrated with one pair of 476.5nm beams (violet). As a result, the 3D particle velocity could be measured simultaneously by using these two probes when three pairs of beams focus on the same point. A 40M shifting Hz frequency of a Bragg cell is selected to determine the particle velocity direction. Table 3.4 lists the essential parameters of this three-component LDA.

Table 3.4 LDA parameters

		Blue	Green	Violet
Number of fringes		22	22	22
Fringe spacing (μm)		5.281	5.568	5.672
Beam half angle (deg)		2.648	2.648	2.648
Width of measuring volume (mm)		0.121	0.128	0.122
Length of measuring volume (mm)		2.624	2.767	2.832
Velocity range (m/s)	in the horizontal pipe	6~20	-5~5	-5-5
	in the vertical pipe	-5~5	6~20	-5-5

In order to accurately locate the beams' crossing point, the LDA probes are mounted on a computer-controlled 3-D traversing system whose minimum step is 0.5mm in all three orthogonal directions. A Burst Spectrum Analyser (BSA) is used automatically to process the LDA burst signals. Every record of the experimental data includes particle order number, transient time in the sample volume, three components of particle velocity and the related status. Then statistical values of particle velocity and particle number are calculated from the recorded set in post-processing.

3.3.2 Optic principle of a ray crossing a pipe wall

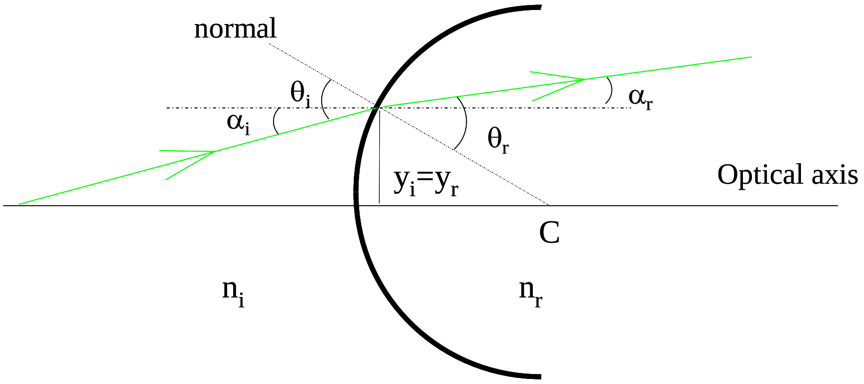

Figure 3.3 Refraction of a ray at a curve

(the incident angle θ_i; the refractive angle θ_r; the curve radius R and the curve centre C; y_i and y_r are equal to the distance from the refractive point to the optical axis; (y_i, α_i) is the coordinate of a inbound ray and (y_r, α_r) is the coordinate of its refraction ray)

It is known that three components of a particle velocity can be measured by using three pairs of laser beams with the same intersection point where the particle crosses. Every velocity component is proportional to the corresponding Doppler frequency originating from the fringe intersected by a pair of laser beams. However, in pipe flow measurement, the crossing point intersected by three pairs of different coloured laser beams may be separated into three crossing points or no crossing point when this point at which the laser beams converge on the outside is shifted inside the pipe. Since a hollow pipe comprises two curved surfaces, refraction occurs at the pipe outer and inner surfaces when a beam traverses the pipe wall. A pair of beams may be convergent dependent on their incident conditions. Before discussing the optical refractive effect on a pipe wall, let us consider the refraction of a beam at a cylindrical surface dividing media of refractive indices n_i and n_r, which is shown in Figure 3.3 (The subscripts of i and r mean incident and refractive respectively).

According to the paraxial form of Snell's law, the optical relationship between the incident beam and its refractive one can be given as (Pedrotti et al., 2007):

$$\begin{bmatrix} y_r \\ \alpha_r \end{bmatrix} = \begin{bmatrix} 1 & 0 \\ \frac{1}{R}\left(\frac{n_i}{n_r}-1\right) & \frac{n_i}{n_r} \end{bmatrix} \begin{bmatrix} y_i \\ \alpha_i \end{bmatrix} \tag{3.1}$$

where the first item on the right side is defined as the refraction matrix M_R.

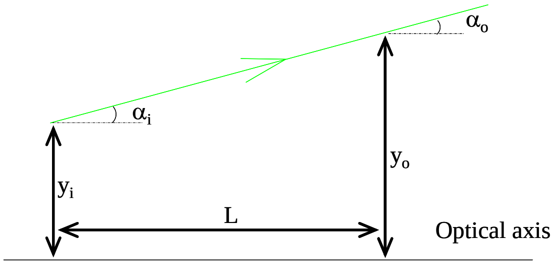

Figure 3.4 The geometric sketch of a beam translating a distance L

With regard to a simple translation in a homogeneous medium (as shown in Figure 3.4), the relationship of a beam passing through two points with a distance L can be described as:

$$\begin{bmatrix} y_o \\ \alpha_o \end{bmatrix} = \begin{bmatrix} 1 & L \\ 0 & 1 \end{bmatrix} \begin{bmatrix} y_i \\ \alpha_i \end{bmatrix} \tag{3.2}$$

where the first item on the right side is called as the transfer matrix M_T.

Consequently, the matrix description of a ray passing through a pipe wall can be simplified as occurring twice (refractions at each surface) with a translation between the surfaces. The optical characteristic of this process is represented by the system matrix of equation (3.3):

$$S = M_{R2} M_T M_{R1} \tag{3.3}$$

where the subscripts of 1 and 2 mean pipe outer and inner surfaces. The matrices are multiplied together from right to left.

The above equations are limited to two dimensional optical calculations and are not directly used in three dimensional optical calculations in pipe flow measurement, for the laser beams of the LDA and the normal line of the pipe surface may not be in an identical plane and their spatial position should be expressed by three dimensional vectors.

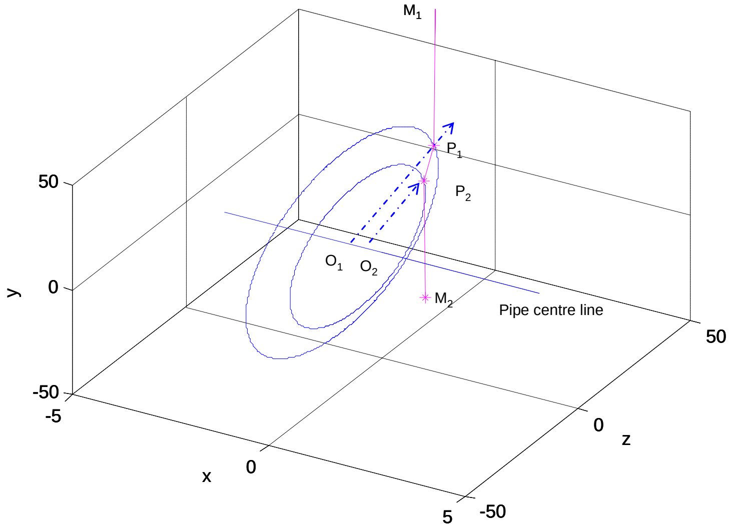

Figure 3.5 The schematic of a ray crossing a pipe

Figure 3.5 illustrates the optical path of a ray crossing a pipe wall. This ray is assumed to originate from the point M$_1$. P$_1$ is its first refraction point at the pipe outer surface and P$_2$ is its second refraction point at the pipe inner surface. O$_1$ and O$_2$ are the circle centres of the pipe outer cross-section through P$_1$ and the pipe inner cross-section through P$_2$. These two sections are perpendicular to the x axis. As such, the vector $\boldsymbol{M_1P_1}$ means the ray outside the pipe. The vector $\boldsymbol{P_1P_2}$ shows the ray crossing the pipe wall and the vector $\boldsymbol{P_2M_2}$ displays the track of the ray inside the pipe. Since a pipe cross-section is a standard circle, the normal vector of a point on its perimeter is the pipe radius pointing outward (we use the Capital Bold Italic to express a vector).

In the Cartesian coordinate system of Oxyz, we introduce three spatial unit vectors ($\boldsymbol{V_i}$, $\boldsymbol{V_n}$, $\boldsymbol{V_r}$) of a ray describing its refraction at the point P$_1$ on the pipe outer surface. P1 is the spatial reference point. $\boldsymbol{V_i}$ is the unit vector of the incident ray. $\boldsymbol{V_n}$ is the unit vector of the normal ray at point P1 of the surface and $\boldsymbol{V_r}$ is the unit vector of the refractive ray. According to Snell's refraction law, these three vectors should locate within the incidence plane formed by the vector product of $\boldsymbol{V_i}$ and $\boldsymbol{V_i}$. The relationship among these three vectors can be expressed as

$$\begin{cases} V_r \cdot \left(-V_n\right) = \cos\theta_r \\ V_r \cdot \left(V_i \times V_n\right) = 0 \\ \left|V_r\right| = 1 \\ n_i \sin\theta_i = n_r \sin\theta_r \end{cases} \tag{3.4}$$

where (n$_i$, n$_r$) are the refractive index of the medium outside and inside the pipe wall. Thus, the unit vector of the refracted ray can be deduced from equation (3.4) when the incident unit vector and the normal unit vector are known. If the refraction point P_1 is also known, the optical path of a beam crossing a pipe wall can be fixed in Cartesian coordinates. This refraction point P_1 is the crossing position of the beam intersecting with the pipe outer surface. Subsequently, the coordinate of this point can be concluded from equation (3.5)

$$\begin{cases} x = x_0 + at \\ y = y_0 + bt \\ z = z_0 + ct \\ y^2 + z^2 = \dfrac{D^2}{4} \end{cases} \tag{3.5}$$

where (a, b, c) are three components of the incident unit vector of a beam and (x_0, y_0, z_0) is its initial position related to a Cartesian coordinate of the origin point on the pipe centre line. The dependent variables (x, y, z) are each given functions of an independent variable t in the parametric form of a beam's mathematic equation. D is the pipe outer diameter.

It is clear that there will be four steps as shown in Figure 3.6 to determine the optical path of each beam of the LDA crossing a pipe wall by using equation (3.5) and (3.4). Then the actual coordinates of the measurement volume formed by a pair of laser beams can be calculated by solving the crossing point of two lines described by the refractive unit vector inside the pipe and the refraction point on the pipe inner surface for each beam.

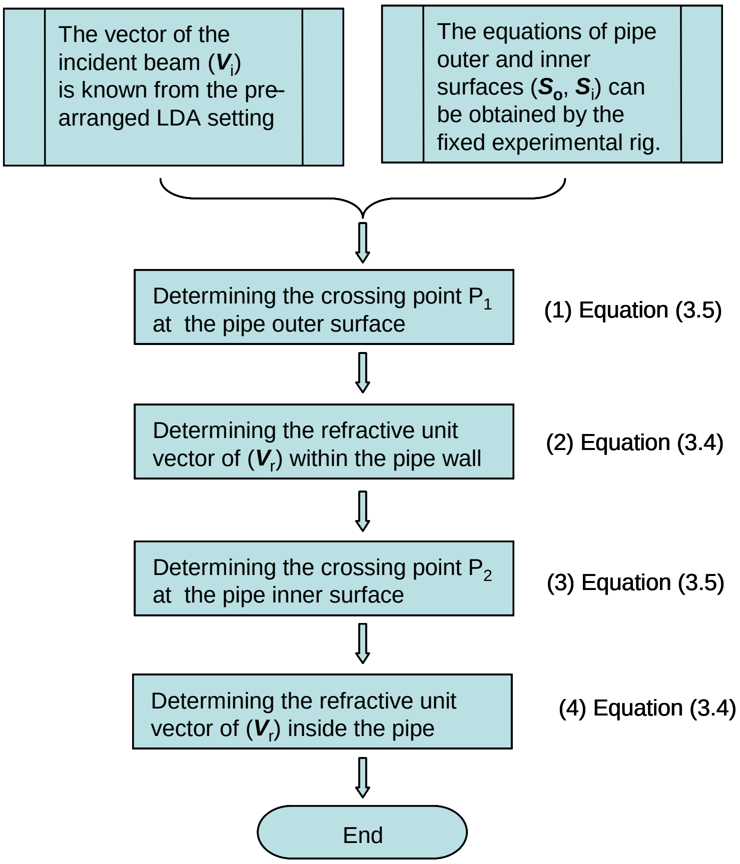

Figure 3.6 Flow chart of determining the optical path of a ray crossing a pipe wall

3.3.3 Optic paths of different colour beams through a pipe

According to the parameters of LDA listed in Table 3.4, the half intersecting angle of each of the pairs of laser beams in the probes of LDA is 2.648°. Now we construct a Cartesian coordinate system with origin at the centre of a pipe cross-section which is the measurement region in our experiments. With regard to the probe combining two pairs of beams, the plane of the probe window and the two planes formed by two pairs of beams are orthogonal with each other. In this case, the probe axis is not only the normal line of the probe window but also the crossing line of two planes formed by two pairs of laser beams. Now the blue beams of the LDA are arranged to measure one velocity component in the x axis or the horizontal direction. The green and violet beams are built for detecting the other two components of velocity in the plane Oyz. Therefore, we can follow the flow chart in Figure 3.6 to calculate the spatial position of each beam of LDA inside the pipe when the angle of the probe axis intersecting with the horizontal plane of Oxz is known and the crossing point of three pairs of laser beams focus on the point of the perimeter curve of the pipe cross-section intersecting with the horizontal plane.

For example, in the horizontal pipe of our experimental rig shown in Figure 3.2, the pipe inner and outer diameters are ϕ75mm and ϕ85mm respectively. Under the condition of the zero probe angle (meaning that the plane formed by the blue beams lies on the horizontal plane of Oxz, the crossing point of the blue beams is initially adjusted to locate at the point (0, 0, 42.5) mm, which is the crossing point of the perimeter curve of the pipe cross-section (x=0) intersecting with the plane Oxz. It is clear that the cross point of the blue beams will arrive at the coordinate origin when the probe is moved about the distance (0, 0, -42.5) mm along z axis if there is no refractive surface. However, considering the refraction effect of the pipe, Figure 3.7 shows the optical paths of two blue beams through the pipe wall and the crossing point is moved to the point (0, 0, -1.67) mm rather than the origin (0, 0, 0) mm. This indicates that there is a deviation of -1.67mm on z axis due to refraction when the cross point of blue beams moves from the point (0, 0, -42.5)mm to the expected point (0, 0, 0) at a probe angle of 0°. The crossing point of the green beams can reach the coordinate origin (0, 0, 0) when the probe is shifted a distance (0, 0, -42.5) mm from the initial point (0, 0, 42.5) mm at the probe angle of 0°. The optical paths of two green beams are shown in Figure 3.8. Comparing Figure 3.7 with Figure 3.8, we can observe that the crossing point of the blue and green beams outside the pipe is separated when it moves into the pipe.

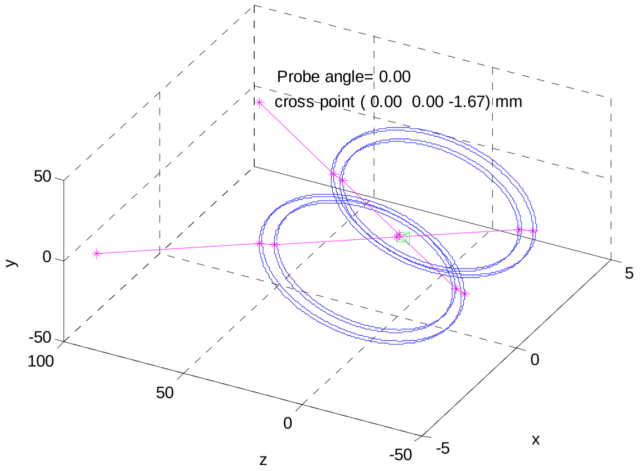

Figure 3.7 Crossing point of blue beams shifting towards the pipe centre line (Units: mm)

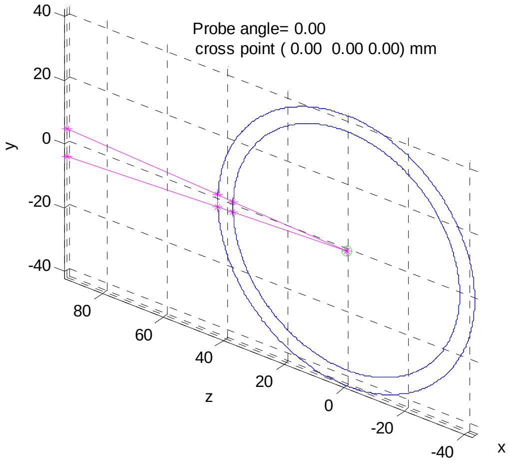

Figure 3.8 Cross point of green beams moving to the pipe centre line (Units: mm)

As a result, the burst-and-coincidence mode of LDA was no longer available for pipe flow measurement due to the different crossing points of the different coloured laser beams. Otherwise, we would need an additional optical arrangement to calibrate or adjust each pair of different colour beams to converge at the same point in the pipe.

3.3.4 Developing the coordinate transform matrix for LDA pipe flow measurement

In the previous section, we demonstrate that there is a deviation between the actual coordinate and the expected position when a crossing point of beams is shifted into a pipe due to the refractive effect at the pipe outer and inner surfaces. The value of this deviation is dependent on probe angle, beams initial conditions and pipe geometric parameters. As for the specific experimental rig shown in Figure 3.2 and the LDA system discussed in the section of 3.3.1, only the probe angle affects the deviations.

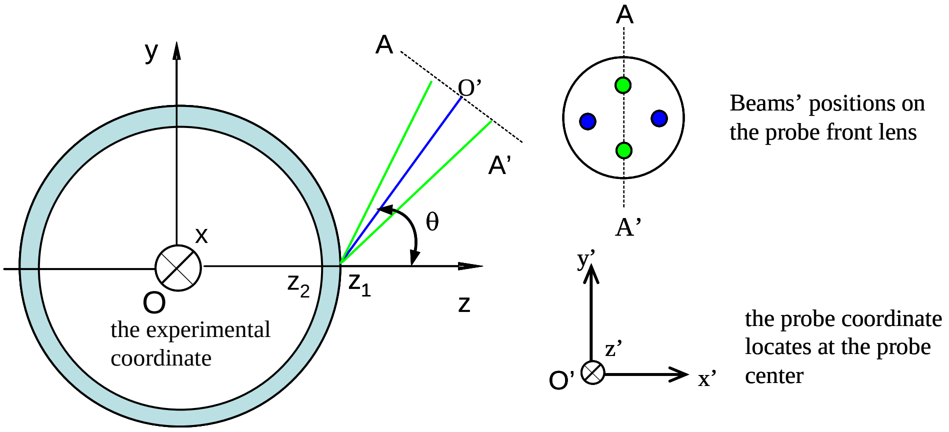

Figure 3.9 The experimental coordinate (Oxzy), the probe coordinate (O'x'y'z') and the initial arrangement of the probe

In Figure 3.9, we construct an experimental coordinate system at the centre of a pipe cross-section and define the x axis along the pipe centre line, the y axis opposite to the gravity direction and the z axis across the pipe. Z_1 is the crossing point of the z positive axis intersecting the pipe outer surface and Z_2 is the point of the z positive axis intersecting the pipe inner surface. Z_1 is also selected as the reference point to locate the beams' spatial coordinates when the probe angle is known. Thus, the initial position of the crossing point of all colour beams locates at z_1. The point O is the origin point of the system coordinate. As such, the angle θ which the plane of blue beams intersects with the horizontal plane Oxz of the coordinate system is defined as probe angle. In other words, the probe coordinate which is formed by two pairs of beams is parallel to the reference coordinate transformed by rotating the experimental coordinate about the probe angle along x axis.

When a three dimensional traverse system carrying the probe moves from Z_1 to Z_2 to cross the cross-section along the z axis (as shown in Figure 3.9), the actual positions of the crossing point of blue beams against the different probe angles are shown in Figure 3.10, which illustrates the deviations of (y'-y) and (z'-z) against z under the different probe angle θ. The variations of (z'-z) show that there always exits a shift between an expected point and its corresponding actual position in the z direction no matter what the probe angle is. But a larger the probe angle results in a larger deviation of the crossing point away from its expected position (y'-y) on the y axis and a smaller shift of (z'-z) in the z axis. This is clearly shown in the pipe centre region. For smaller the probe angles like 0° and 5°, the variation of (z'-z) against z is almost like a straight line which means that the z coordinate of an actual blue beams' crossing point has a -1.67mm shift to its expected z coordinate. In contrast, the variations of (y'-y) clearly display that the larger the probe angle is, the larger the shift between y and y' is. For example, the difference between y' and y is almost equal to zero under the probe angle zero. And at every probe angle, the maximum deviation in y direction occurs at shifting the blue beams' crossing point to the section centre or the coordinate origin point.

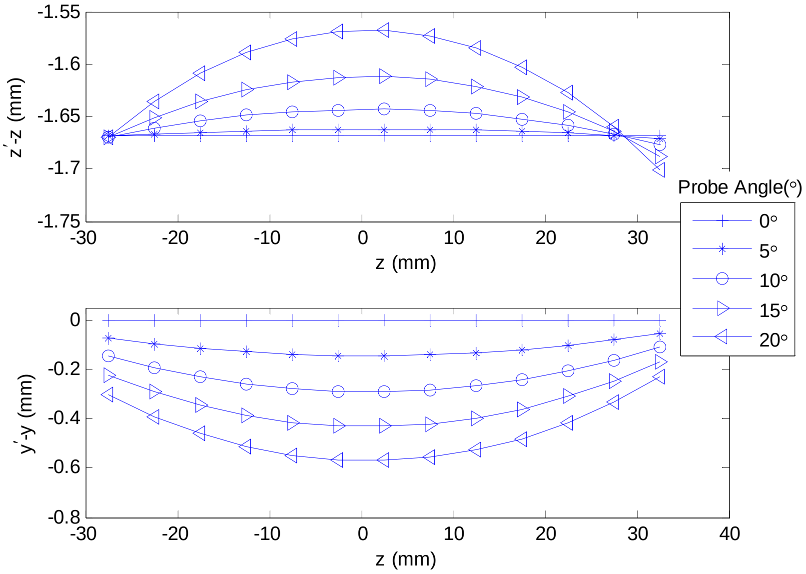

Figure 3.10 Variations of the crossing point of blue beams against probe angle
Note: (y, z) is the expected position and (y', z') is the actual position

Under the same shifting process, Figure 3.11 displays the deviations of (z'-z) and (y'-y) of the green beams at different probe angles when their crossing point moves from Z_1 to Z_2 to cross the pipe along the z axis (as shown in Figure 3.9). In general, the variations of (z'-z) show a similar tendency at the different probe angles, in which the minimum shift occurs in the pipe centre and the maximum shift happens close to the pipe wall in the z axis. By contrast, the variations of (y'-y) show that there is almost no shift between y' and y under smaller probe angles like 0° and 5°. But for probe angles larger than 5°, there exists a large discrepancy between y' and y when the green beams' crossing point is further from the pipe centre. Comparison of Figure 3.11 with Figure 3.10 shows that the identical crossing point of blue and green beams outside the pipe will be separated when the crossing point moves into the pipe.

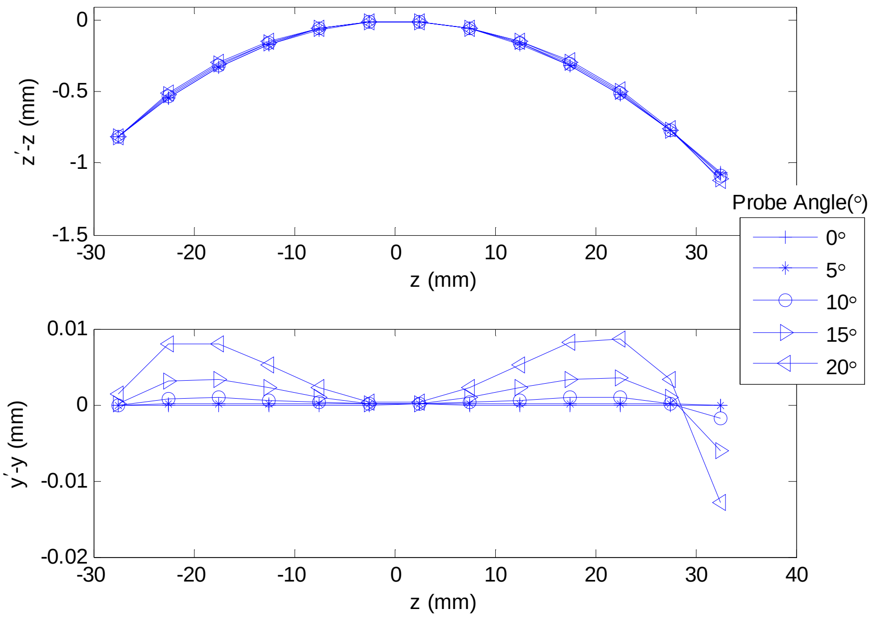

Figure 3.11 Variations of the crossing point of green beams against probe angle
Note: (y, z) is the expected position and (y', z') is the actual position

Considering the probe angle as a constant of -5°, Figure 3.12 (a) and (b) show the actual coordinates of the blue and green crossing points in the horizontal section of the rig respectively, when the traverse system carrying the probe is linearly shifted to access the whole pipe cross section. Generally, two colour crossing points have less discrepancy from their normal positions in the pipe mid part than in the pipe top or bottom regions. All the crossing points lie in the same plane of Oxz. Figure 3.13 (a) and (b) display the spatial positions of blue and green crossing points in the vertical section of the rig pipe separately over the entire cross-section at a probe angle of -5°. Both two colour crossing points have more deviations from their expected position in the right or left region than in the pipe centre. Comparing Figure 3.13 with Figure 3.12, we can see that both colour crossing points in the vertical pipe not only deviate from their normal positions but also are no longer on the same plane of a pipe vertical cross-section, which means that there is a deviation in the y axis, although the movement of the 3D traverse system is limited to the plane of Oxz. Therefore, in order to compensate the deviation in y axis, we should add an additional y value at each sample point for keeping sample points on a pipe vertical cross-section, when setting the shift coordinate of the traverse system.

On the other hand, there also exists a practical over-current problem for the photomultipliers in the LDA, which is caused by the strong intensity of the reflected light on the pipe outer surface. The over-current condition will make the linear scale capability of the photomultipliers worse. In addition, the laser source of the LDA system had to be powerful enough to measure the velocity of a micro particle like smoke (size less than 30 μm), which is used to trace fluid due to its small Stokes number. In our experiments, the trade-off between laser power and the probe angle was tested to select two data sets of (0.8w, 0°) and (1.6w, -5°). A zero probe angle minimizes the crossing point deviation due to the refraction effect.

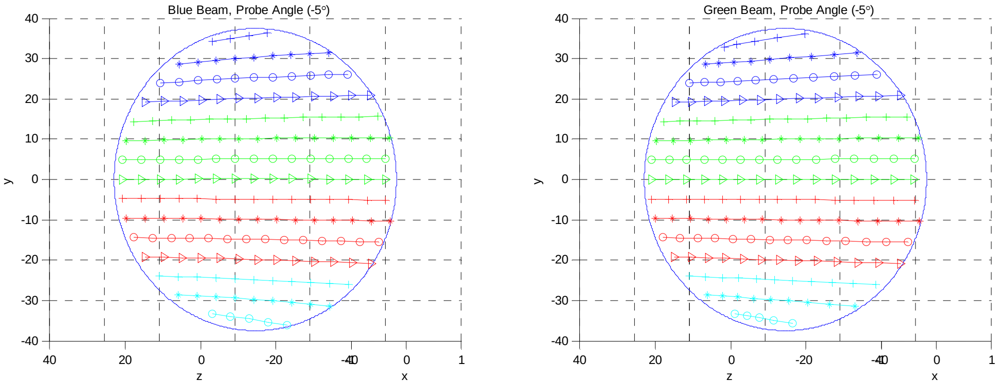

(a) Coordinates of the blue beams' crossing point (b) Coordinates of the green beams' crossing point

Figure 3.12 In the horizontal pipe at the -5° probe angle

According to the above discussions, a total of 1047 sample points are arranged to occupy the whole area of a horizontal or vertical cross section by shifting the traverse system. The spatial resolutions of these sample points were defined as 1mm in the y direction and 2mm in the z direction respectively. Thus a transform matrix can be calculated in advance, which is used to index a shift coordinate of the traverse system with a sample point in pipe.

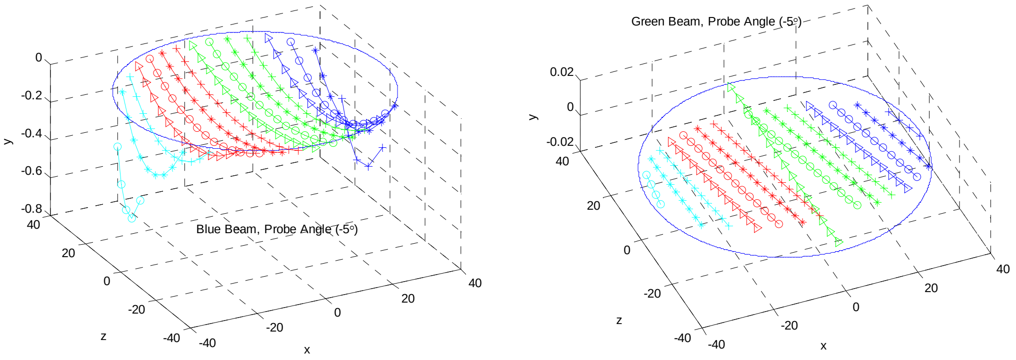

(a) Coordinates of the blue crossing point (b) Coordinates of the green crossing point

Figure 3.13 In the vertical pipe at the -5° probe angle

3. 4 SAMPLE RATE OF LDA FOR GAS-SOLID FLOW MEASUREMENT

According to Shannon's sampling theorem, it is necessary to sample a continuous signal at a rate greater than twice its highest frequency component for measuring it exactly. The twice highest frequency of a continuous signal is also called Nyquist frequency or Nyquist rate (Smith, 2003).

However, particle signals recorded by LDA at a measurement point inside a pipe are discrete with a random fluctuation due to the local fluid conditions and particles impacting states. These signals can be considered as a numerical event like a discrete-time random process which is illustrated in Figure 3.14.

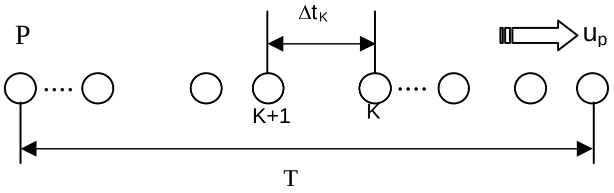

Figure 3.14 The sketch of particle signals recorded by LDA

With regard to LDA measurement, Figure 3.14 shows the signal characteristics of particle velocities recorded by LDA. A total of N particles are assumed to cross the LDA fringe at the sample point P within a time interval T. The parameter u_p expresses a particle instantaneous velocity. The parameter K is used to label the order of particles passing through P and Δt_K means the time interval between particle K and particle (K+1). When these particles are very small, for example, seeding particles like ammonium chloride smoke (mean size 0.6 μm), the measured LDA data represent the local velocity of the air phase at the point P. Since seeding particles are fine with a small Stokes Number and have a good ability to follow the fluid, the time-series signals of $\{u_p\}$ recorded by LDA are similar and only dependent on the local air phase state. In the case of a steady flow measurement, the set of $\{u_p\}$ should have a small deviation. Hence, the total number of signals $\{u_p\}$ would have less influence on calculating its mean velocity. However, for gas-solid flow measurement, particles of solid phase are considered as the seeding particles for LDA measurement and they are different in terms of size and initial conditions, as well as density, for a multi-material solid phase. The signals $\{u_p\}$ recorded by LDA at the point P are not only related to the local air phase state but also dependent on the particle properties. Items in the set $\{u_p\}$ may have large discrepancies. Compared with measuring the air phase velocity, particle signals for solid phase measurement are discrete with an unequal separation distance. Then the local mean velocity of solid phase will be affected by particle number in the velocity set $\{u_p\}$, which can be described as equation (3.6)

$$
\begin{aligned}
&T = \sum_{k=1}^{N-1} \Delta t_k \\
&u_p = \{u_{pk}, k = 1, \Lambda\ , N\} \\
&\bar{u}_p = \sum_{k=1}^{n} u_{pk} \Big/ N
\end{aligned}
\qquad (3.6)
$$

where T is the measurement period and N is the total number of particles crossing the measurement fringes. In the group equation (3.6), the first expression means the sum of the time intervals between particles equals the total measurement time. The second means that the measured instantaneous velocity would be one of the items in the particle velocity countable sample space. The third is the equation for calculating particle mean velocity whose accuracy is obviously related to the total number and the deviation of particle velocity set $\{u_p\}$. Then, if t_{min} is the minimum temporal interval between two adjacent particles crossing the measurement point, it can be described as

$$t_{\min} = \min\{\Delta t_k, k = 1,\ldots, N\} \tag{3.7}$$

Thus, it would be possible to record each item in the sequence of particles shown in Figure 3.9 if the sample frequency of LDA is equal to or greater than $1/t_{min}$ and the other time interval Δt_k can be assumed as $\Delta t_k/t_{min}=n$ (n is an integer). Since the minimum temporal interval at a local point is much affected by the local solid concentration and the corresponding boundaries around the point, it will change point by point on a whole pipe cross-section. In contrast to continuous-time signals, which have a minimum sample rate of twice its highest frequency for avoiding aliasing, there is no Nyquist frequency for a discrete-time signal. As such, we will demonstrate how to determine the suitable sample frequency of LDA for our experiments discussed in Chapter 4.

3.5 SUMMARY

In this chapter, LDA applications for gas-solid flow research have been reviewed, which shows that there is still a lack of papers discussing the refractive effect and the sample rate in gas-solid pipe flow measurement by using LDA in detail. Since the refractive effect due to the pipe's curved surface can not be ignored, we have developed a group of mathematical equations and demonstrated the calculations of the transform matrix for mapping the actual positions of the measurement volume of LDA in the pipe by shifting the traverse system according to probe angle. In addition, particle size in gas-solid flow has a very wide distribution and particle velocity is dependent on many factors like Stokes Number, drag coefficient and local air velocity etc. When LDA is applied to measure the local velocity of solid phase, which is averaged from velocities of particles passing through a sample point, a sequence of discrete-time signals can be recorded. In order to calculate accurately the time-averaged velocity at a local point, the sample frequency of LDA should be experimentally determined. Theoretically, this sample rate should be at least equal to or greater than $1/t_{min}$ which is described in equation (3.7).

Chapter 4

Experimental studies of cross-sectional characteristics of air velocity in pipes using the extended LDA Technique

---

In this chapter, the extended LDA technique was applied to measure the cross-sectional distributions of air velocity on two horizontal pipe cross sections and eight vertical pipe cross-sections behind a horizontal-to-vertical 90º bend (R/D=1.3) in the rig. On the horizontal cross-sections, the experimental contours of the axial air velocity (U_{ax}) show an annular feature. On the vertical cross-sections, each cross-sectional distribution of the axial air velocity (U_{ay}) has been shown to be like a horseshoe. A secondary flow including two circulations has also been shown in the cross-sectional distributions of the radial air velocity (U_{ax}) on the vertical cross-sections close to the bend outlet. At the further downstream sections, both the above features explored by U_{ay} and U_{ax} gradually become weak. A comparison of the experimental data and the numerical results by CFD indicate good agreement.

4.1 INTRODUCTION

In the previous sections, we have discussed how to calculate the transform matrix for mapping the actual positions of the measurement volume of LDA in a pipe according to the shifting coordinate of the traverse system and the importance of a proper LDA sample rate for gas-solid flow measurement. With regard to the experimental rig shown in Figure 3.2, the transform metrics at the 0° and -5° probe angles respectively, which had been calculated in advance according to the principle discussed in Chapter 3, were used to arrange the shift coordinates of the traversing system to make the crossing point of the laser beams able to access a whole pipe cross-section.

At the 0° probe angle, the experimental coordinate is parallel to the orthogonal probe coordinate (as shown in Figure 3.9) which is formed by two pairs of the laser beams (blue and green). The measured signals using the blue beams and the green beams are corresponding to the axial air velocity (U_{ax}) and the vertical air velocity (U_{ay}) in a horizontal pipe respectively. By contrast, the measured signals using the blue beams and the green beams are corresponding to the horizontal air velocity (U_{ax}) and the axial air velocity (U_{ay}) in a vertical pipe. When the probe angle is not equal to 0° (like -5°), this probe coordinate will be parallel to the reference coordinate transformed by rotating the experimental coordinate about -5° along x axis. In this case, the data measured by the blue beams still represents the air x velocity (U_{ax}), but the data measured by the green beams are not directly equal to the air vertical velocity (U_{ay}), for there is the -5° intersection angle between them.

In order to avoid uncertainty due to the separation phenomenon of the crossing points of different colour beams (as discussed in Chapter 3), the 0° probe angle was used to investigate the horizontal and vertical characteristics of air velocity and the -5°probe angle was only applied to study the horizontal characteristics of air velocity in the following sections.

A total of 1047 measurement points were arranged over a pipe cross-section by shifting the three-dimensional traverse system according to the pre-calculated transform coordinates. A suitable sample rate of LDA was selected as the same as that for particle velocity measurement. It was 10K Hz determined by the experiments in Chapter 5. For air velocity measurement, the seeding particles were produced by burning a bundle of incense. The smoke is less than 10μm (Fang et al., 2002).

4.2 MEASURING THE CROSS-SECTIONAL CHARACTERISTICS OF THE AXIAL AIR VELOCITY (U_{ax}) IN A HORIZONTAL PIPE

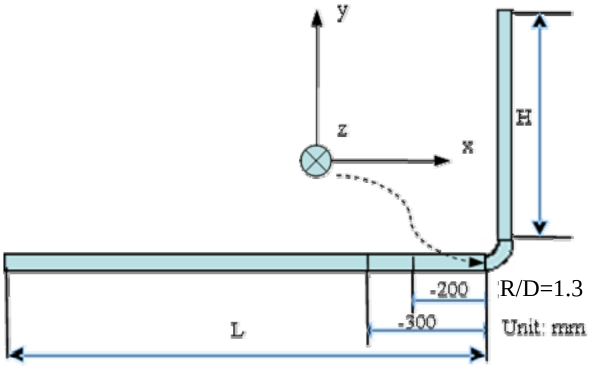

(R/D=1.3, R is the bend radius 100mm and D is the pipe diameter 75mm)

Figure 4.1 2D schematic diagram of two selected cross sections in the rig horizontal pipe

In the horizontal pipe of our rig shown in Figure 4.1, two cross-sections which are 200mm and 300mm away from the elbow inlet respectively were selected as the measurement regions. Here, the experimental coordinate locates at the centre of the elbow inlet. The x positive axis denotes fluid direction on the pipe centre line. The y negative direction is on the gravity direction and the z positive axis signifies inward towards the paper.

It is known that the turbulent velocity profile in a circular pipe can be described by an empirical equation (4.1), which was summarized from J. Nikuradse's experimental data (Schlichting H., 1955).

$$\frac{\overline{u}}{\overline{u}_{\max}} = \left(1 - \frac{r}{R}\right)^{1/n} \qquad (4.1)$$

where $\overline{u}$ is the local time averaged velocity; $\overline{u}_{max}$ is the maximum value of $\overline{u}$,; R is the pipe radius; r is the distance from the pipe centre and n is the empirical exponent factor dependent on Reynolds number. This equation is also called 1/n-th power law of air velocity profile in pipe. According to J. Nikuradse's experimental data, the value of the exponent n is n=6 at the lowest Reynolds number $Re=4\times10^3$; it increases to n=7 at $Re=110\times10^3$. For our fluid condition of air conveying velocity 12m/s in ϕ75mm pipe, its Reynolds number is equal to 56×10^3 for air density 1.12kg/m^3. As such, the n is chosen as 7 in our experiments. In order to compare conveniently the cross-sectional data of air velocity with the empirical profile estimated by equation (4.1), the experimental data and the empirical profile are plotted together.

Under the condition of air conveying velocity 12m/s and the -5° probe angle, the axial characteristics of air velocity were investigated and the experimental data are illustrated in Figure 4.2 and Figure 4.3.

In order to compare conveniently the cross-sectional data of air velocity with the empirical profile estimated by equation (4.1), the experimental data and the empirical profile are plotted together. Figure 4.2(a) shows air velocity profiles along the y axis on two cross-sections at x=-200 and -300mm. Similarly, profiles of the axial air velocity (U_x) along the z axis on the two sections are displayed in Figure 4.2(b). The maximum value of air velocity (U_{max}) which is used to normalize the experimental data of air velocity is selected from the data of air velocity on the cross-section x=-300mm. As such, the maximum normalized value of air velocity on the other cross-section x=-200mm is equal to 0.97 rather than 1. This discrepancy is possibly due to experimental random error, since the measurements on the two cross sections were carried out separately without coincidence. Comparison of the experimental data with the empirical velocity profile indicates that they have a good agreement and a similar shape. The total deviation between the experimental data and the value given by Eq. (4.1) is less than 10%. The maximum discrepancy occurs at the pipe boundary (r/R>0.82). It is also observed that the air velocity profile along the y axis (z=0) is closer to the empirical one-seventh power profile than air velocity profile along the z axis (y=0). Moreover, the air velocity profile on the y axis (z=0) is almost symmetrical along the pipe centre line, but the air velocity on the z axis (y=0) is somewhat skewed. There is a bias in the centre velocity towards the pipe bottom.

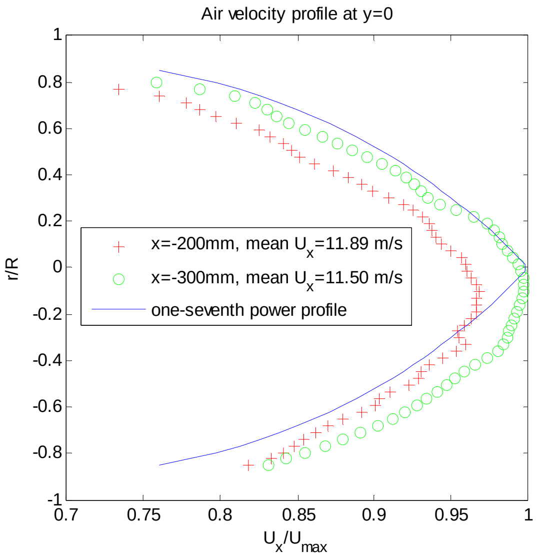

(a)

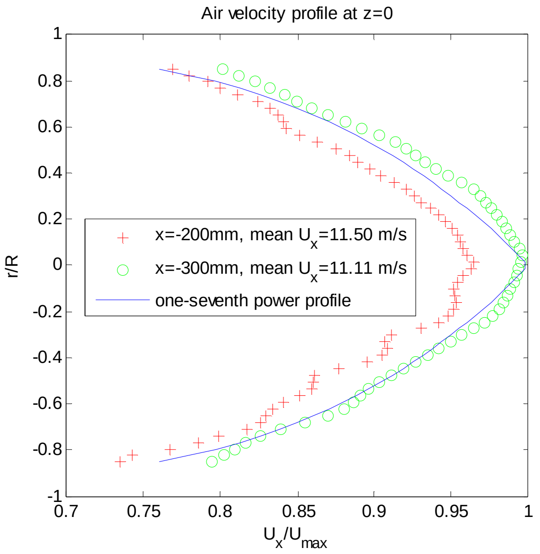

(b)

Figure 4.2 Velocity profiles of the axial air velocity (U_x) at x=-200, -300 mm along (a) y axis and (b) z axis, under air conveying velocity 12m/s

With regard to the cross-sectional distribution of air velocity, Figure 4.3 clearly shows the contours of air velocity on two pipe cross-sections on which two sub contour diagrams display an annular nature of the cross-sectional distribution of the axial air velocity. It is clear that the axial air velocity decreases gradually from pipe centre to pipe wall on each cross section. However, the fastest region of the axial air velocity does not exactly locate at the pipe geometric centre, having a small deviation towards the z-negative direction. But in the y direction, there is no obvious deviation. This kind of deviation indicates that the actual air flow in the rig is not ideal.

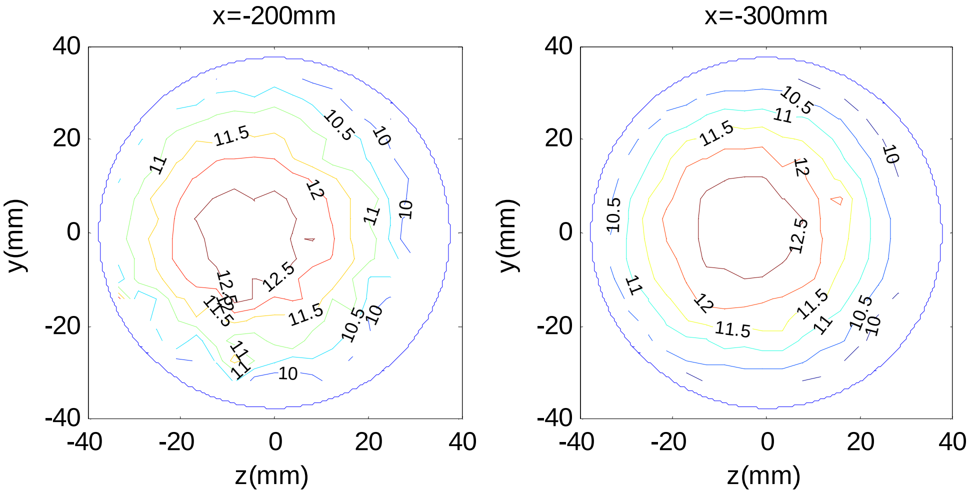

Figure 4.3 Cross-sectional distribution of the axial air velocity distribution (U_x) at two horizontal cross-sections of x=-200 and -300mm from the bend inlet respectively, under air conveying velocity 12m/s)

4.3 AIR VELOCITY IN THE RIG VERTICAL PIPE AFTER A 90º BEND

Since the effect of gravity on air can be ignored, the velocity characteristics of single phase air in a horizontal or vertical pipe should be identical if fluid conditions at inlet are the same. However, large discrepancies will occur when a vertical pipe is mounted downstream of a connecting elbow. So far, there have been many studies to investigate the elbow effect on gas-solid flow. This effect is also called the roping phenomenon. Forkeer et al. (2004) reviewed the related papers. However, there is still lack of experimental air velocity data for single phase flow in a vertical pipe behind an elbow. In this section, we will publish our experimental data of air velocity distribution on a series of cross-sections along the vertical part of the rig.

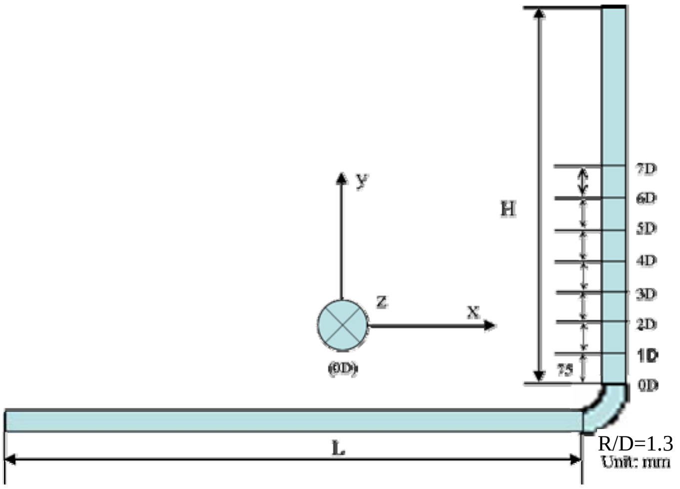

(R/D=1.3, R is the bend radius 100mm and D is the pipe diameter 75mm)

Figure 4.4 2D schematic diagram of cross sections along the vertical pipe behind a 90° bend (R/D=1.3, R is the bend radius 100mm and D is pipe diameter 75mm; 0D is 15mm away from the bend outlet).

In the experiments, air conveying velocity was adjusted to 10m/s and the incense smoke was again used as the seeding particles. A total of eight cross-sections from 0D to 7D downstream of the elbow exit, with a 75mm interval spacing equivalent to one pipe diameter (D), were selected as measurement regions along the vertical leg. The origin of the reference coordinate was chosen to be the centre of the cross-section 0D, as shown in Figure 4.4. The section 0D is about 15mm away from the bend outlet. On each section, a total of 274 sample points with a 4mm interval distance in the x and y directions were selected to grid a whole cross section.

The experimental data on a series of cross-sections along the vertical pipe are illustrated in Figure 4.5 for the axial air velocity U_{ay} and Figure 4.7 for the radial air velocity U_{ax} respectively. The corresponding numerical data, which have been simulated for single phase air by using the standard k-ε model in the commercial Computational Fluid Dynamics software Fluent 6.3.26 (Fluent Inc., 2006), are plotted in Figure 4.6 and Figure 4.8.

Compared with the annular nature of the axial air velocity U_{ax} on a horizontal pipe cross-section shown in Figure 4.3, cross-sectional distributions of the axial air velocity U_{ay} in the vertical pipe do not retain such annular structure due to the bend effect. Especially, on the section 0D, the slowest regions of U_{ay}(the dark blue colour) are located at the pipe centre and the region close to the pipe inner wall (the x negative axis). The fastest region of U_{ay} (the dark red colour) is around the region close to the pipe outer wall (the x positive axis). Generally, a horseshoe-like feature is shown on the cross-sectional distributions of U_{ay} at 0D. This horseshoe can be also observed on cross-sectional distributions of U_{ay} at the further downstream sections. Compared with that at the section 0D, the axial air velocity U_{ay} is gradually accelerated inside the horseshoe and decelerated outside it from the section 1D to 7D. Consequently, the difference of U_{ay} between inside and outside the horseshoe is narrowed. The total scale number of isolines is decreased, which shows the homogenous area within a certain isoline enlarged.

With regard to the numerical simulations of air single phase pipe flow, the evolution of the axial air velocity (U_{ay}) shown in Figure 4.6 is illustrated through cross-sectional distributions of U_{ay} along the vertical pipe behind an elbow (R/D=1.3). Here, the geometric parameters of the numerical model are the same as those of the experimental rig shown in Figure 4.4. Air conveying velocity at the pipe inlet is 10m/s in the smooth glass piping of the rig. The detailed content of numerical equations and the related numerical parameters are those discussed in Chapter 2. It is clear that the elbow apparently affects the axial air velocity distributions in the vertical pipe behind a bend. When the main direction of air flow is changed from x positive axis to y positive axis, the annular structure of the cross-sectional distributions of the axial air velocity (U_{ax}) in a horizontal pipe is also modified into a shape like a horseshoe in the vertical pipe, where air runs faster in the pipe outer wall than in the region of the pipe centre or the pipe inner wall. The slow region of U_{ay} is marked as the blue on the section 0D and the green on the section of 2D. Then its colour is developed as the little dark yellow on the section of 7D. All these colour variations mean increase tendency of U_{ay} in the pipe centre region.

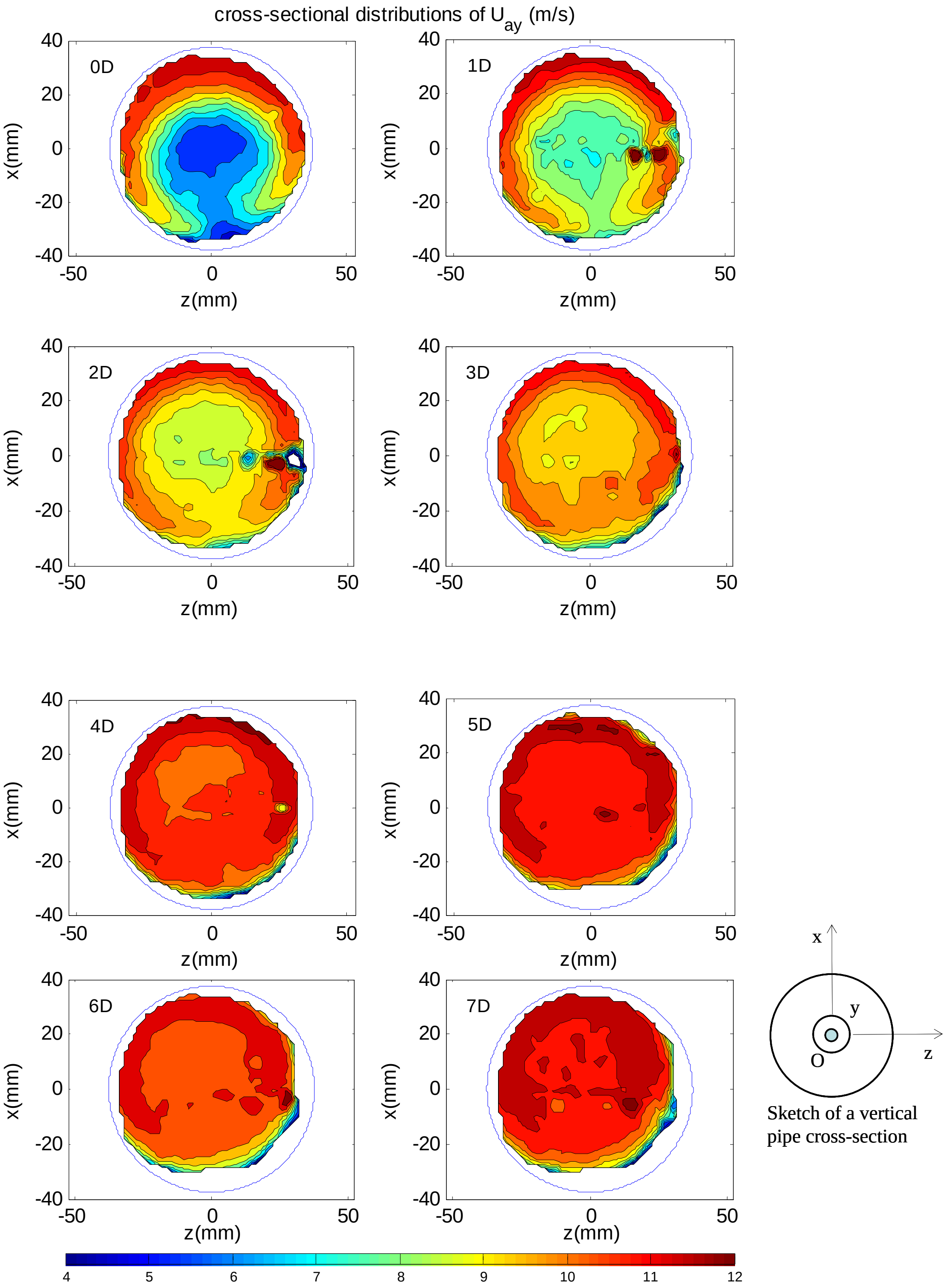

Figure 4.5 Experimental cross-sectional distributions of the axial air velocity (U_{ay}, m/s) along the vertical pipe behind a 90° bend (R/D=1.3, R is the bend radius 100mm and D is pipe diameter 75mm; 0D is 15mm away from the bend outlet).

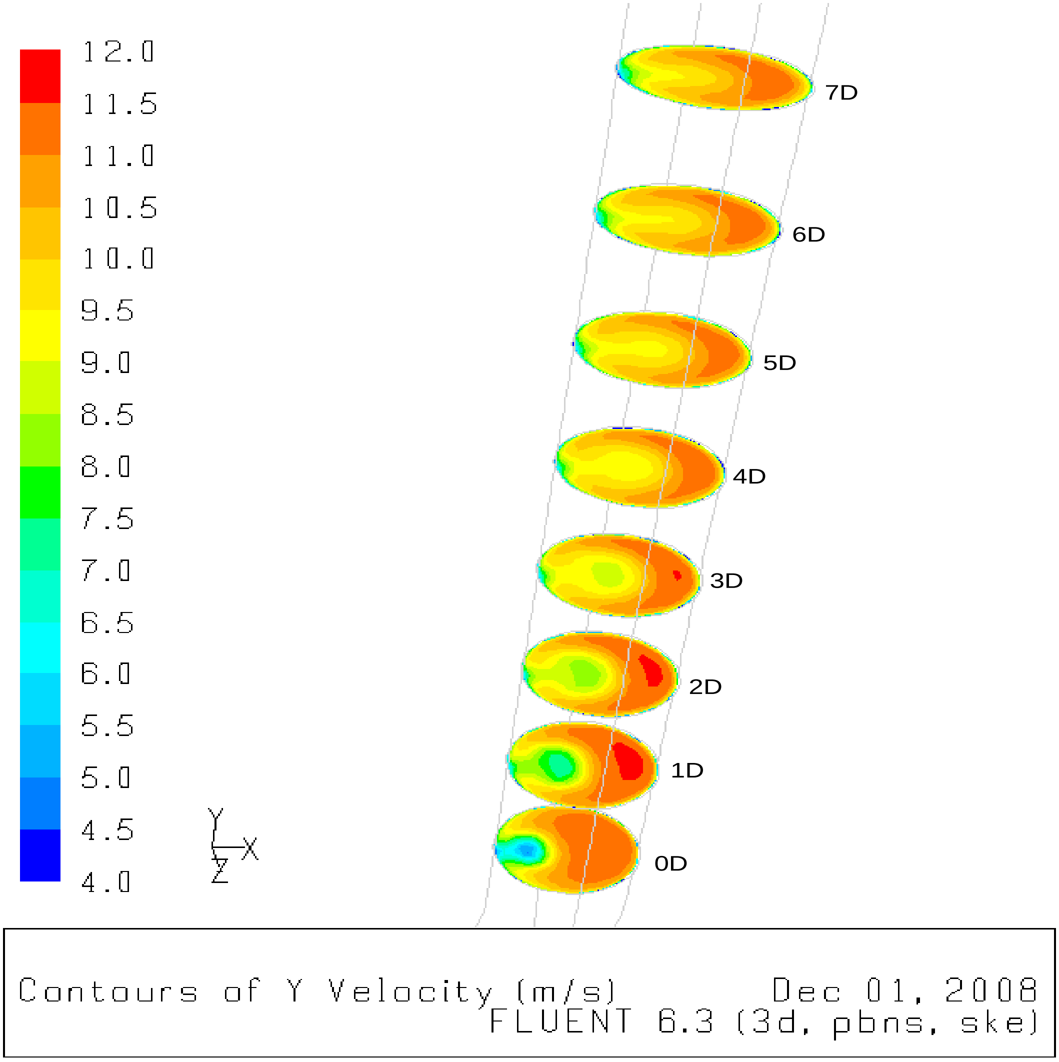

Figure 4.6 Numerical cross-sectional distributions of the axial air velocity (U_{ay}, m/s) along the vertical pipe behind a 90° bend (R/D=1.3, R is the bend radius 100mm and D is pipe diameter 75mm; 0D is 15mm away from the bend outlet).

The comparison of Figure 4.5 and Figure 4.6 not only shows the similar structure of the axial air velocity (U_{ay}) distribution on each section but also illustrates the similar evolution of U_{ay} from 0D to 7D. On each section, the numerical data validate that the axial air velocity is faster on the outside of the horseshoe than inside it. Also, the axial air velocity inside the horseshoe gradually increases and decreases outside the horseshoe. As such, the total scale number of U_{ay} decreases and the difference of U_{ay} between inside the horseshoe and outside it tends to lessen, which shows the cross-sectional distributions of U_{ay} inclining to the homogenous during air flow development further downstream.

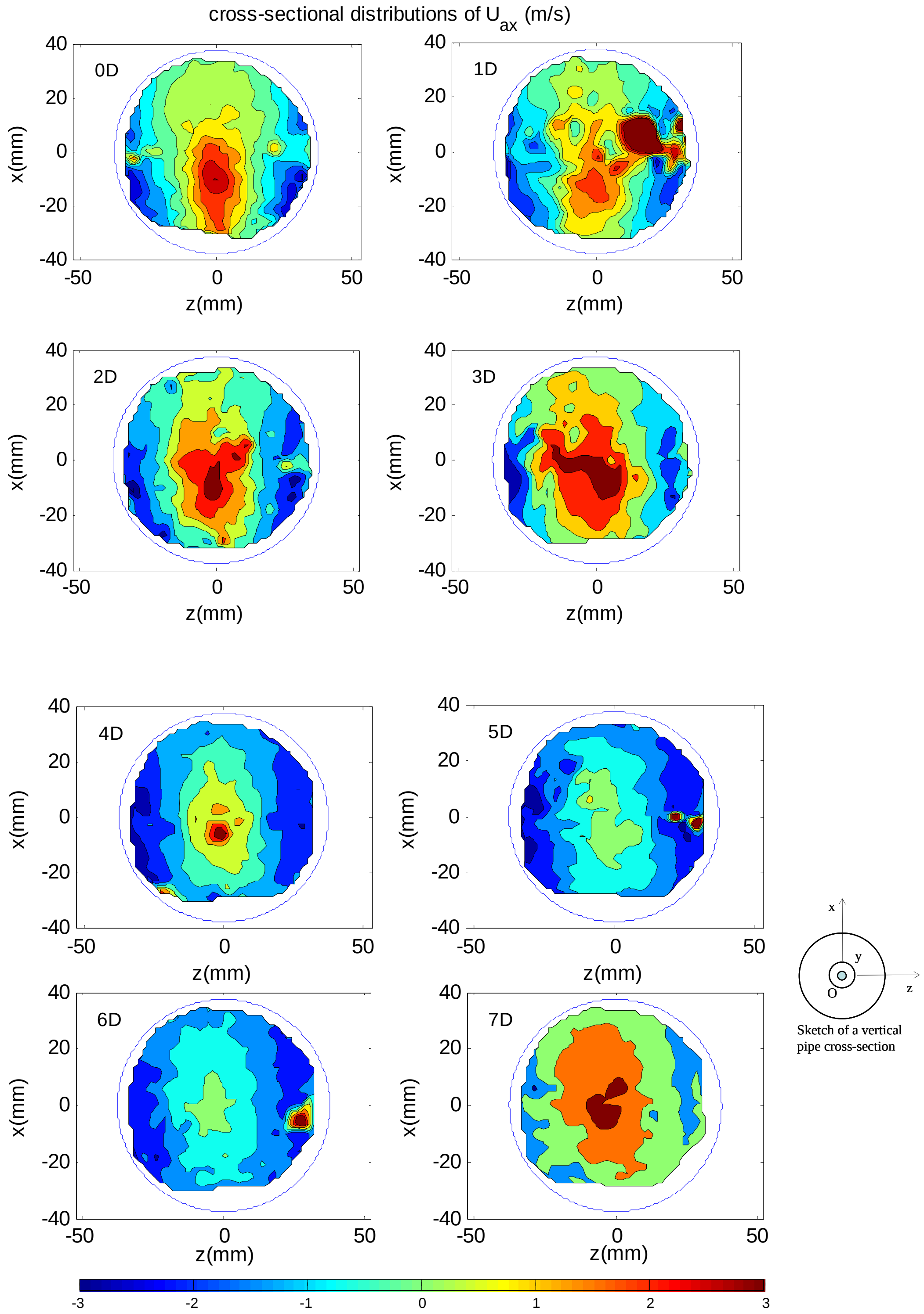

Figure 4.7 Experimental cross-sectional distributions of the horizontal air velocity (U_{ax}, m/s) along the vertical pipe along the vertical pipe behind a 90° bend (R/D=1.3, R is the bend radius 100mm and D is pipe diameter 75mm; 0D is 10mm away from the bend outlet).

As for the radial air velocity (U_{ax}) in the x axis, Figure 4.7 and Figure 4.8 respectively show the experimental and numerical distributions of U_{ax} on the eight cross-sections from 0D to 7D in the vertical pipe behind the 90° bend (R/D=1.3). In Figure 4.7, the experimental cross-sectional distribution of U_{ax} on each section can be classified into three sub-regions according to the direction of U_{ax}. These sub-regions include the mid strip along the x axis and two sectors outside the strip towards the pipe left and right walls. According to the colour bar in Figure 4.7, the mixed colour of yellow-green represents U_{ax} close to zero velocity. The dark blue stands for the fastest U_{ax} in the x negative direction and the dark red indicates the fastest U_{ax} in the x positive direction. As such, U_{ax} is positive or zero in the mid strip and negative in the two sectors.

An interesting phenomenon is shown in the cross-sectional distribution of U_{ax} on the section 0D, where the positive maximum U_{ax} (3m/s) locates on the mid strip close to the pipe inner wall (the negative x axis) and U_{ax} tends to be zero at the pipe outer wall. In two sectors, U_{ax} changes its direction from the positive to the negative when air flow reaches the pipe outer wall. Then U_{ax} is gradually accelerated towards the pipe inner side till it reaches the maximum magnitude of U_{ax} in the negative x axis (-3m/s). This process illustrates a secondary flow resulting from the momentum transfer among three components of air velocity due to the 90° bend at the section 0D. This secondary flow includes two circulations. Each them starts from the pipe outer wall (U_{ax} tends to be zero). Then one is accelerated along the pipe left wall counter clockwise while U_{ax} shows an increasing tendency in the negative x direction By contrast, the other is accelerated along the pipe right wall in the negative x direction clockwise. When both subflows meet at the pipe inner wall, they are mixed and run towards the pipe centre (the positive x direction). U_{ax} reaches its maximum positive value (dark red colour) before the pipe centre. Then U_{ax} gradually decreases to be nearly zero in the mid strip close to the pipe outer wall. These two circulations demonstrate a symmetrical feature in the cross-sectional distribution of U_{ax}. Perhaps, this symmetry is due to air flow coming along the x axis in the horizontal pipe and there being no additional force in the z axis.

On the downstream sections 1D, 2D and 3D, the cross-sectional distributions of U_{ax} can be still observed to be similar to that on the section 0D. But the symmetric feature of U_{ax} shown at the section 0D is skewed. The region with the maximum positive radial air velocity (U_{ax}) shifts from the pipe inner wall towards the pipe centre. Compared with that on the previous sections, the U_{ax} scale number is obviously reduced on the sections from 4D to 6D. The difference of U_{ax} between the mid belt and either of the two sectors becomes smaller and the positive peak of U_{ax} decreases as well. However, on the section 7D, the cross-sectional distribution of U_{ax} shows that U_{ax} in the mid belt becomes positive again and the positive maximum U_{ax} occurs close to the pipe centre. This is unexpected and does not agree with those on the previous cross-sections due to unknown reasons. Overall, variations of cross-sectional distributions of U_{ax} from 0D to 7D indicates that the bend effect on the momentum transfer between the axial air velocity (U_{ay}) and the radial air velocity (U_{ax}) is still active as far as the section 7D.

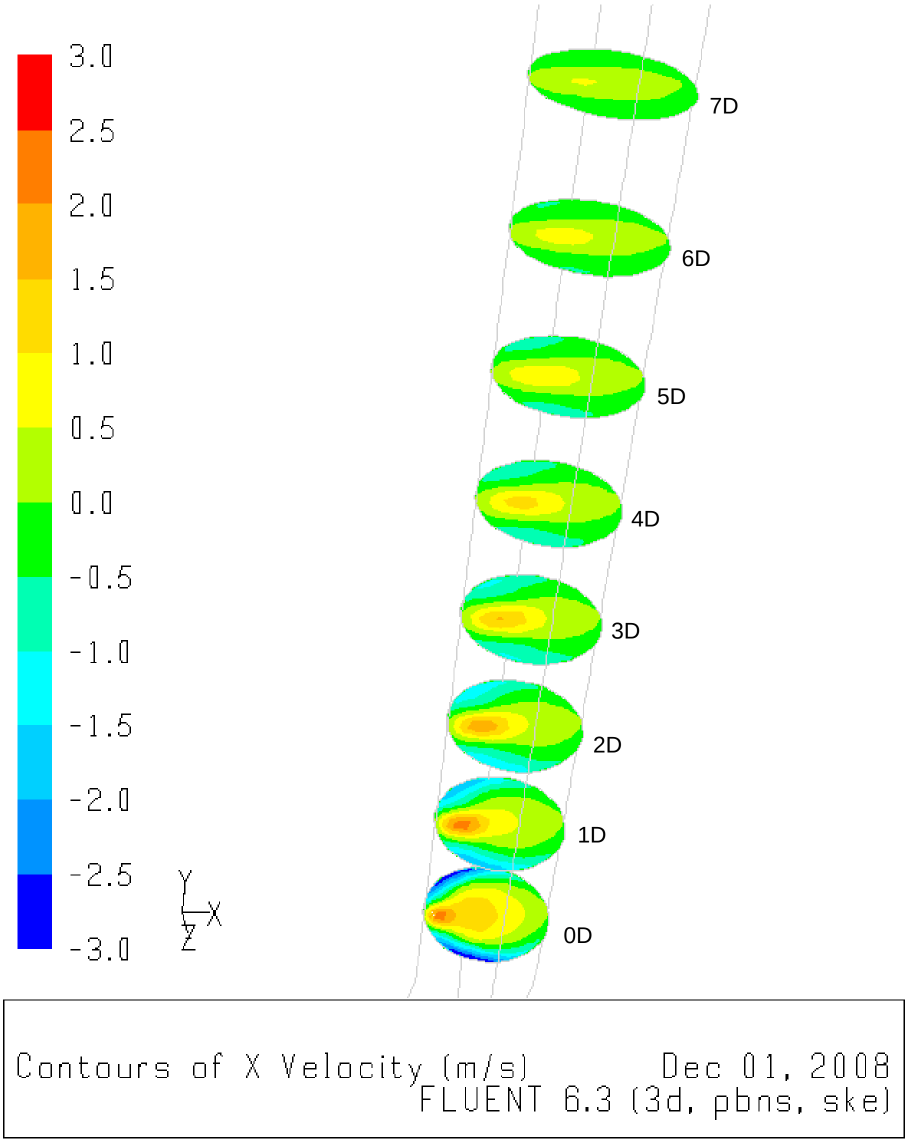

Figure 4.8 Numerical cross-sectional distributions of the horizontal air velocity (U_{ax}) along the vertical pipe behind a 90° bend (R/D=1.3, R is the bend radius 100mm and D is pipe diameter 75mm; 0D is 10mm away from the bend outlet).

Figure 4.8 shows the numerical distributions of U_{ax} on the sections from 0D to 7D. Compared with Figure 4.7, a similar structure of the U_{ax} cross-sectional distribution can be observed, especially on the section 0D. The symmetrical feature along the z axis is clearly shown in the cross-sectional distribution of U_{ax} on each section. However, the symmetrical structure of the experimental data shown in Figure 4.7 is not regular like those predicted by the numerical data in Figure 4.8. In addition, the difference of U_{ax} between the mid strip and its two outsides gradually becomes smaller, for the magnitude of U_{ax} estimated by the numerical data decreases either in the mid strip or in the two sides of the strip. Consequently, the numerical prediction of the secondary flow described by U_{ax} becomes weaker and weaker from the section 0D to 7D. By contrast, the experimental secondary flow shown by U_{ax} is observed to retain a larger magnitude of the negative U_{ax} in the boundary of the pipe left and right walls on the section 6D.

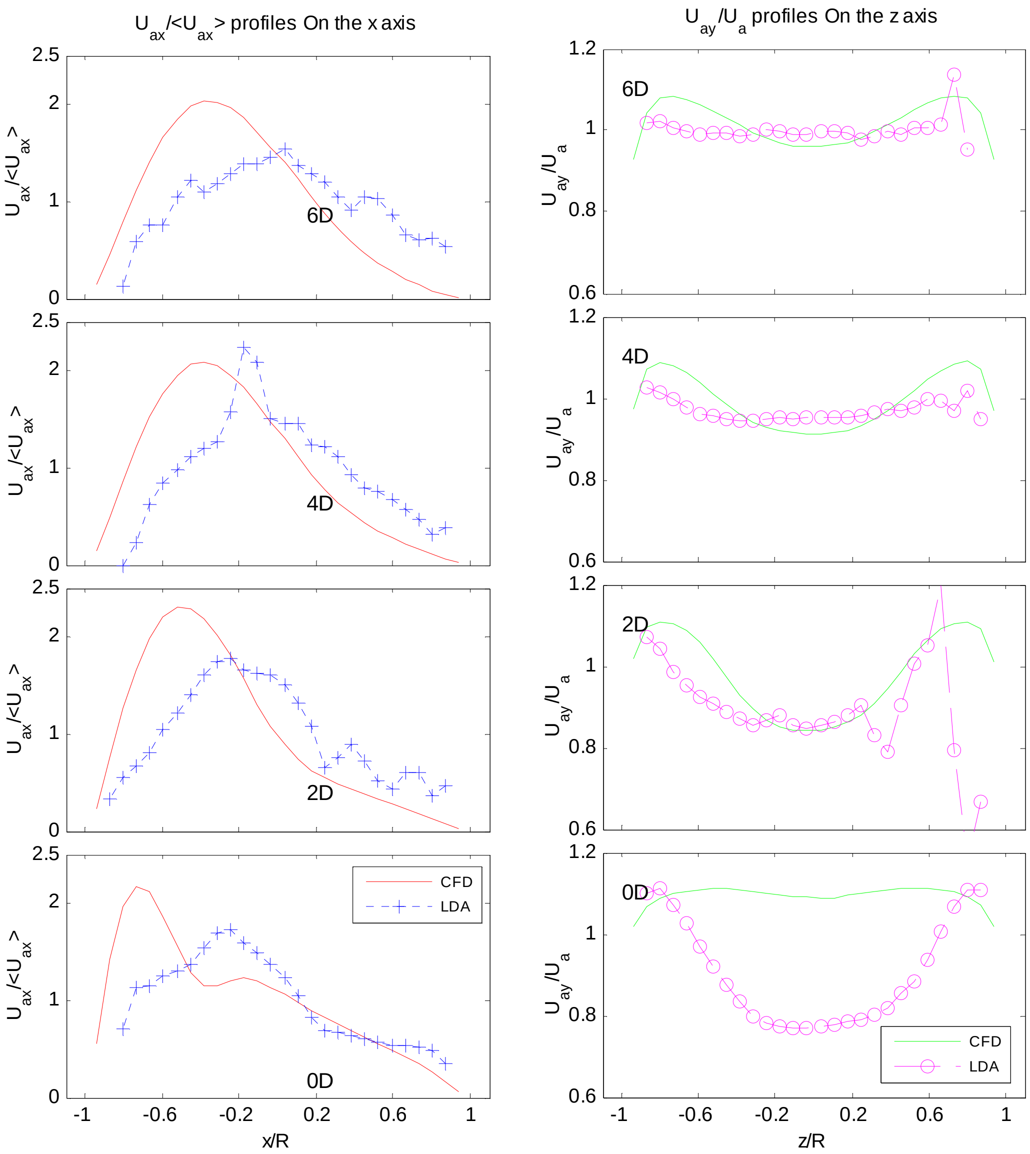

Figure 4.9 Profiles of U_{ax} and U_{ay} along the x axis at four selected vertical cross-sections (<U_{ax}> is the mean absolute value of U_{ax}; U_a is the air conveying velocity 10m/s)

In order to quantitatively and clearly compare the experimental data with the numerical results, the numerical and experimental profiles of U_{ax} and U_{ay} on the x axis and on the z axis are displayed in Figure 4.9 and Figure 4.10 respectively.

Figure 4.9 shows the evolution of profiles of U_{ax} and U_{ay} in the x axis at the four selected cross-sections. With regard to U_{ax}, the numerical U_{ax} profile shape is similar to the experimental one on each section. Both the numerical and the experimental data show that U_{ax} in the negative x axis is faster than in the positive x axis. The width of U_{ax} profile gradually expands from 0D to

6D. However, the peak of each profile estimated by the numerical data is much closer to the pipe inner wall (the negative x direction) than that in the experimental data. For U_{ay} profiles on the x axis, both the experimental and numerical data display a similar decreasing tendency of U_{ay} from the pipe outer wall to the pipe inner wall (along the negative x direction) at each section. The U_{ay} profiles are much flatter, which is shown by the narrowed difference of U_{ay} among the different points on the x axis. However, the numerical profile of U_{ay} has a wider flat top region than the experimental profile of U_{ay} does at the section 0D and 2D, for the experimental cross-sectional distributions of U_{ay} with the fastest velocity in Figure 4.5 are thinner than those of the numerical results in Figure 4.6.

Figure 4.10 shows the experimental and numerical profiles of U_{ax} and U_{ay} in the z axis. The symmetrical feature along the z axis is shown in both the experimental and the numerical profiles of U_{ax} and U_{ay} at each section. The profile peak of U_{ax} and the bottom of U_{ay} are located at the point z=0. Another observed agreement for U_{ax} or U_{ay} is the similar profile shape between the experimental and the numerical profiles downstream of the section 0D. In general, U_{ax} is faster in the pipe centre than in the pipe left (the z negative axis) and right sides (the z positive axis). By contrast, U_{ay} is faster in the pipe two sides than in the pipe centre along the z axis. However, the profile shape of U_{ax} and U_{ay} has much discrepancy on the section 0D, although their experimental and numerical profiles show a similar variation tendency. At the section 0D, the experimental profile of U_{ax} show a sharp peak at the point z=0, where the numerical profile of U_{ax} shows a flat top. And the numerical profile of U_{ay} is very flat with a minor drop from the pipe two sides to the pipe centre along the z axis. In contrast, the experimental profile of U_{ay} shows a deep minimum in the centre region around z=0 where U_{ay} is slowest in the z axis.

Comparing the one-dimensional profiles in Figure 4.9 and Figure 4.10 with the two-dimensional cross-sections distribution in Figure 4.5~4.8, we can see that the discrepancies between the experimental and numerical profiles of U_{ax} and U_{ay} in the x axis and the z axis at the section 0D are mainly caused by the fact that the numerical positions of the highest velocity region of U_{ax} and the horseshoe centre of U_{ay} differ from the corresponding positions measured by experiments.

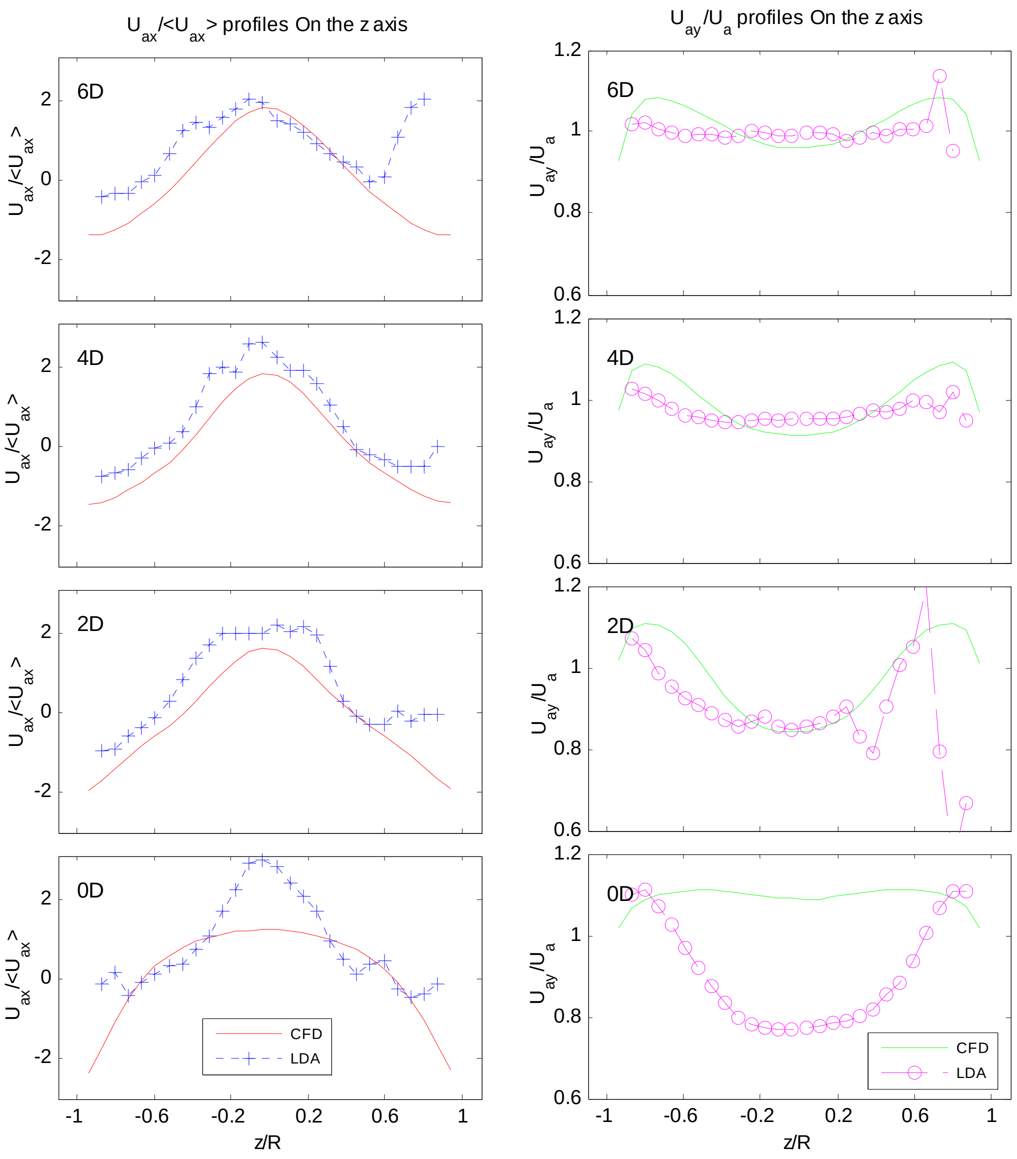

Figure 4.10 Profiles of U_{ax} and U_{ay} along the z axis at four selected vertical cross-sections ($<U_{ax}>$ is the mean absolute value of U_{ax}; U_a is the air conveying velocity 10m/s)

4.3 CONCLUSIONS

The two calculated transform matrices, for the horizontal and vertical pipe flow measurements respectively, were used to arrange the shifting coordinates of the traverse system which carried the LDA probes to access measurement cross-sections in the horizontal pipe and the vertical pipe behind a horizontal-vertical 90° bend (R/D=1.3).

On the two horizontal cross-sections, the experimental data of the axial air velocity (U_{ax}) reveal an annular nature. Both the profiles of U_{ax} on the y axis and the z axis agree with the empirical one-seventh power-law profile. On the eight vertical cross-sections from 0D to 7D, the horseshoe-like feature is displayed on each cross-sectional distribution of the axial air velocity (U_{ay}). U_{ay}, is slower inside the horseshoe close to the pipe inner wall and U_{ay} is faster in the region around the pipe outer wall. The difference of U_{ay} between inside and outside of the horseshoe gradually decreases at further downstream sections from 0D. A secondary flow is revealed in the cross-sectional distributions of the radial air velocity (U_{ax}), especially on the section 0D. This secondary flow includes two circulations symmetrical along the z axis. Hence, a vertical cross-section can be classified into three regions of the mid strip and the two sectors outside the strip, according to U_{ax} directions. On each section, the secondary flow on the mid strip is divided into two at the pipe outer wall. One subflow is accelerated towards the pipe inner wall along the pipe left wall and the other along the pipe right wall. Then two subflows are mixed at the region close to the pipe inner wall. The direction of the mixed flow is changed towards the pipe centre (in the positive x direction). Before reaching the pipe centre, the mixed flow is accelerated to obtain its maximum magnitude of U_{ax} in the positive x direction. Then U_{ax} is decelerated to approach zero at the pipe outer wall. Thus, the left subflow with the mixed flow forms the circulation in the counter-clockwise direction. The right subflow with the mixed flow forms another circulation in the clockwise direction. However, at the further downstream sections of 4D to 6D, the secondary flow becomes weak, for the magnitude of U_{ax} gradually decrease and the difference of U_{ax} between the mid strip and its two sides is narrowed.

A comparison of the experimental data by LDA and the numerical results by CFD indicate that both of them on the x axis and the z axis show a similar shape for the axial air velocity (U_{ay}) and the horizontal air velocity (U_{ax}).

Chapter 5

Experimental investigation of Particle Dynamics in a Dilute Pneumatic Conveying System using the Extended LDA Technique

---

This chapter presents experimental results obtained by using the extended LDA technique introduced in Chapter 3, for the quantitative assessment of particle dynamic behaviour in the horizontal and vertical legs of the dilute pneumatic conveying system shown in Figure 3.2. Three kinds of glass beads were selected to simulate the pulverized coal and biomass pellets transported in a dilute pneumatic conveying system. Detailed information on the cross-sectional spatial distributions of the axial particle velocity and particle number rate is reported. In the horizontal part, the experimental data on a series of cross-sections clearly illustrate two uniform fluid patterns, annulus structure and stratified configuration, which describe the cross-sectional distributions of particle velocity and particle number rate respectively. In the vertical pipe behind an elbow R/D=1.3, a horseshoe shape characterizes the cross-sectional distribution of axial particle velocity for all three types of glass beads on the section 0D, close to the elbow outlet. The development of cross-sectional distributions of particle number rate indicates that particles with high inertia would be de-entrained from the rope formed in a bend.

5.1 FLUID CONDITIONS AND MEASUREMENT PARAMETERS

The objectives of the experimental investigation are particle dynamic properties like particle velocity, particle number rate and their spatial distribution over a pipe cross-section. All of them have been measured by employing the extended technique of Laser Doppler Anemometry (LDA) which was discussed in Chapter3. The experimental tasks included the measurement of the cross-sectional distributions of particle velocity and particle number rate for different particle sizes as well as the assessment of the effect of particle size on the turbulence intensity of the solid phase in the horizontal and vertical parts of the dilute pneumatic conveying system which is displayed in Figure 3.2.

Experiments were performed under the dilute flow regime with three different sizes of glass beads and smoke. Three types of glass beads were selected to be transported in pipes by air, which were to simulate the dilute gas-solid flow of pulverized coal or biomass pellets. According to the criterion of similarity of Stokes Number as introduced in Chapter 2, the first type of glass beads (less than 50μm) and the second (70~110μm) correspond to pulverized coal within 0~110μm, as used in power stations. The third group (180~300μm) represents wood-chips around 1mm size. In addition, smoke was used to track the air phase of the flow in the LDA experiments.

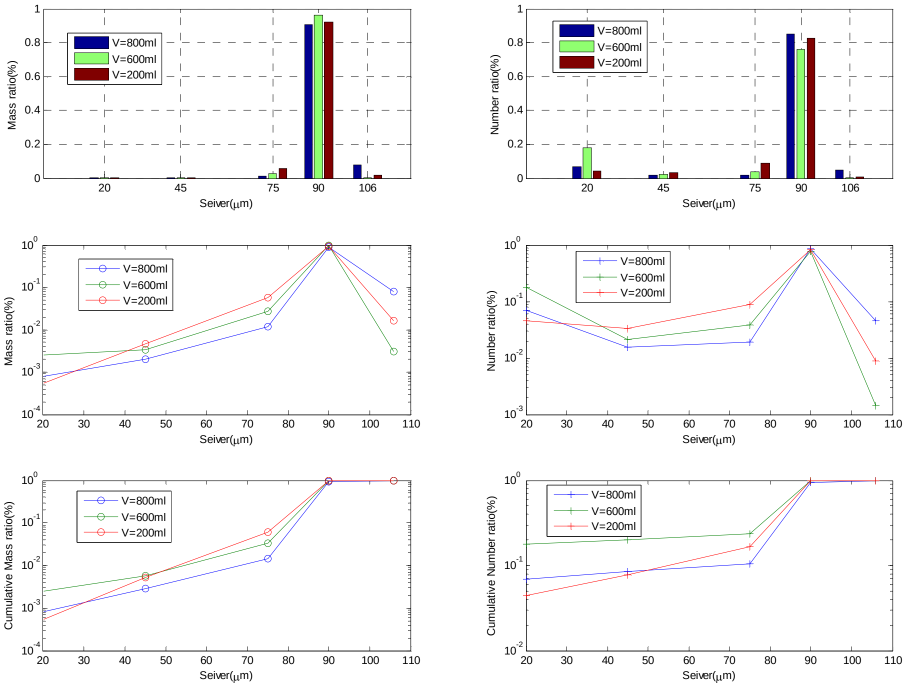

(a) by mass

(b) by number

Figure 5.1 Particle distribution for the second type of glass beads.

As for the second group of glass beads, its real density and bulk density are 2550 kg/m^3 and bulk density 1569 kg/m^3 respectively. These beads were also sorted using 5 different sieve meshes (38, 45, 75, 90 and 106μm) on a high efficient electric-magnetic shaker. The distributions of the mass ratio and particle number are shown in Figure 5.1. In producing these results, three particle sample volumes of 600ml, 400ml and 200ml were sieved over two hours. According to the mass distribution (in Figure 5.1a), most particles are located in the range 90~106μm and the corresponding mass is about 90%. If mesh size was considered as the mean diameter of particles grouped in this mesh, the particle number median diameter should be 90 μm where the particle cumulative number ratio is more than 50% (as shown in Figure 5.1b). These measured results agree with the size precision of 90% in range on the data sheet of glass beads provided by the company Worf Glaskugeln GmbH (2008).

5.2 DETERMINING THE PROPER SAMPLE RATE OF LDA

In section 3.4, we have discussed the reason why the sample frequency of LDA should be at least equal to or greater than $1/t_{min}$ (t_{min} is the minimum temporal interval between two adjacent particles). Since particle signals recorded by LDA are discrete, there is no theoretical Nyquist frequency for a continuous signal and a suitable sampling frequency of LDA must be experimentally investigated under different fluid conditions.

In general, the frequency variation of particles at a point can be described as the local particle number rate, particle velocity or particle mass flow rate. Among these three parameters, particle number rate is the most proper and evident parameter for expressing particle local frequency variation, for it can be directly obtained by counting every available burst signal recorded by LDA according to the LDA principle discussed in section 3.1.1. Subsequently, at a measurement point, particle number rate against the different sample rate of LDA can be deduced from counting burst signals. With regard to a steady gas-solid flow with a constant solid loading ratio, the faster the sample rate of LDA, the larger the available burst signals that can be recorded, which results in a higher particle number rate. If we observe that particle number rate is no longer increased with the sampling rate of LDA beyond a certain value, the current particle number rate shows the maximum frequency variation of particles at the measurement point under the current fluid conditions. Thus, the suitable sample rate of LDA should be selected as larger than this maximum frequency.

To extend the above discussion relating to a point, to the whole space of a pneumatic conveying system, the proper sample rate of LDA for measurement in a horizontal or vertical pipe will be determined when the highest local frequency variation of gas-solid flow is acquired. Due to gravity settling, solid phase concentration in the bottom region of the horizontal parts is higher than in other parts, even ignoring the effect of elbows in the pneumatic conveying system as shown in Figure 3.2. When the proper sample rate of LDA is obtained by experiments at the bottom region of the horizontal leg, this sample rate will be suitable for measurements at other space in the system as well.

In our LDA experiments, the second type of glass beads (70~110μm), which was used to determine the suitable sample frequency of LDA, was conveyed by an air conveying velocity 12 m/s with solid mass loading ratio (1.6% kgs^{-1}/kgs^{-1}) at the maximum injection speed of the screw-feeder. Eleven sample rates of LDA were evaluated at 15 sample points on each y coordinate in the lower half of a pipe cross-section (300 mm away from the elbow inlet). The measured data of particle number rate at each sample point by the different sample rate were shown in Figure 5.2.

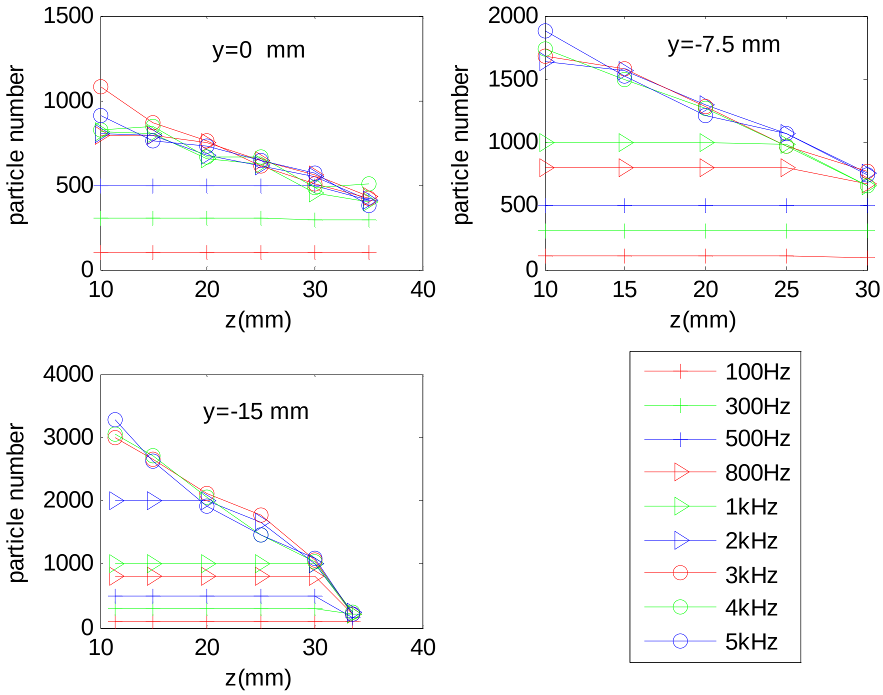

Figure 5.2 Particle number rate against the sample rate of LDA on the section 300mm away from the elbow inlet air velocity 12m/s, solid loading ratio about 1.6%

Comparing these three diagrams in Figure 5.2, we notice that the higher the sample rate is, the more particles are counted. And we also see that particle number rate varies spatially according to the different sample rate of LDA. At a low sample rate equal to or less than 500 Hz, particle number rate is almost the same at 500 counts per second at the different sample points on three different y coordinates as shown in the three sub-diagrams of Figure 5.2. It is clear that a 500Hz sample rate of LDA is too low for experiments. Particle number rate under this sample rate does not display its spatial variation due to gravity settling. Increasing the sample rate, we can see that particle number rate is also increased not only from pipe wall to pipe centre along the z axis but also towards the pipe bottom (along y negative axis). However, particle number rate at each sample point is no longer increased rapidly and its value retains only a narrow fluctuation when the sample rate of LDA is more than 4 kHz. As such, 4 kHz is considered as the maximum frequency variation of particles on the sample line (y=-15mm) under the current fluid conditions.

In practice, 10 kHz was empirically selected as the sample rate of LDA in our experiments with consideration of the possibility of particle number rate (larger than 4000, but less than 10000) at points close to pipe bottom under the fluid conditions of solid mass loading ratio 1.6% kgs^{-1}/kgs^{-1} at a 12m/s air conveying velocity in a ϕ75mm pipe.

In addition, for LDA is a single point instrument, a measurement over each cross-section consumed about 70 minutes for a measurement interval over one second at every sample point. The 10 kHz sample rate of LDA will ensure the recording the maximum 10k number of the data set $\{U_{pi}, i=1, \ldots, N\}$ at each position in one second. Here U_p can be one component of the particle velocity at the measurement position depending on the optical arrangement of the LDA. N is the actual total number of particles crossing the sample point within one second (N<10k), which is defined as the particle local number rate. Thus the particle mean velocity at a sample point (x, y, z) is given by

$$\left\langle U_p(x,y,z)\right\rangle = \frac{1}{N}\sum_{i=1}^{N} u_{pi}, u_p \in \{u_{px}, u_{py}, u_{pz}\} \qquad (5.1)$$

where $\{u_{px}, u_{py}, u_{pz}\}$ are three particle velocity components and < > represents an appropriate average. The particle root-mean-square (RMS) fluctuation velocity is calculated as averaging the squared difference between a time-series of local velocities and its mean value at a sample point. It can be described by

$$\left\langle U'^{\,2}_p\right\rangle^{1/2} = \sqrt{\frac{1}{N}\sum_{i=1}^{N}\left(u_{pi} - \left\langle U_p\right\rangle\right)^2} \qquad (5.2)$$

where $\langle U'^{2}_p\rangle$ is also representative of the granular temperature Θ which is proportional to the square of a random velocity with which the particles oscillate about a mean hydrodynamic velocity (Campbell, 1990). Then particle turbulence intensity is expressed as

$$I = \frac{\Theta^{1/2}}{\left\langle U_p\right\rangle} \qquad (5.3)$$

Using the equations outlined above, the experimental data will be analyzed to display the cross-sectional properties of particle dynamics along the horizontal and vertical parts of the experimental rig.

5.3 EXPERIMENTAL RESULTS ON PARTICLE DYNAMICS IN A HORIZONTAL PIPE

In Chapter 4, we have demonstrated how to measure the cross-sectional velocity of air phase by using the pre-calculated transform matrix to match each shift coordinate of the traverse system with the actual spatial position on the measurement region.

Similarly, the cross-sectional properties of the solid phase like particle velocity, particle number rate and granular temperature were also investigated by means of LDA with a 10 kHz sample rate. On each cross-section, a total of 1047 sample points was designed to represent the distribution over the whole region. These were accessed through shifting the three-dimensional traverse system of the LDA. Consequently, each section has been meshed into the 1047 local subregions. The following subsections will present the experimental results of three types of glass beads (<50μm; 70~110μm and 180~300μm) in the horizontal pipe respectively.

5.3.1 Features of the measured parameters at a typical point

Among the experimental results of the second type of glass beads (70~110μm), Figure 5.3 shows the variations of the three components of the particle velocity measured at a typical position on the cross-section eight pipe diameters (8×75mm) upstream of the elbow inlet. The typical position is located at (0, 25, 0) mm which is marked as the red cross shown in the right hand side of Figure 5.3 and is relative to the reference coordinate located at the section centre. Each velocity component is a discrete time series recorded by LDA and fluctuates around a mean value, for there is no clear increasing or decreasing trend in Figure 5.3. However, the variation of $\{U_{px}\}$ is much stronger with a covariance of 0.32. The covariance values of $\{U_{py}\}$ and $\{U_{pz}\}$ are 0.11 and 0.05 respectively.

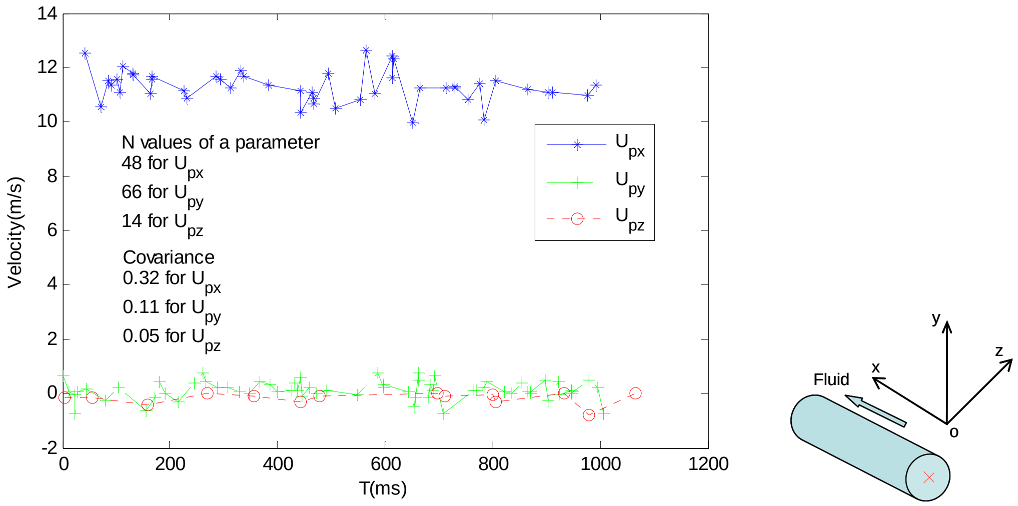

Figure 5.3 The measured particle velocity at a sample point in three axes
(U_a=12m/s; particles within the size range 70~110μm)

In Chapter 3, we have discussed the refraction effect of the curved pipe wall which makes the identical cross-point (at which three pairs of three colour beams of the LDA intersect) separate when the crossing point is moved into the pipe. The measurements of the three components of $\{U_{px}\}$, $\{U_{py}\}$ and $\{U_{pz}\}$ are not coincident in location, since the actual crossing points of the three colour beams are (0, 25.10, -1.67) mm for the blue beams (U_{px}), (0, 24.98, 1.08) mm for the green beams (U_{py}) and (0, 25.01, 0.92) mm for the violent beams (U_{pz}). They are grouped around the typical point (0, 25, 0) within a 2mm distance.

The total number of measured items for each parameter in one second is considered as the particle number rate. Here, the sets {U_{px}}, {U_{py}} and {U_{pz}} over one second consist of 48, 66 and 14 items separately. Thus, the measured particle number rates are defined as 48, 66 and 14 per second.

Therefore, we will use the statistic time-averaged values of {U_{px}}, {U_{py}}, {U_{pz}} and particle number rate N to describe the overall variability of solid phase in a local subregion which is represented by a typical point.

5.3.2 Characterizing the experimental data on a pipe cross-section

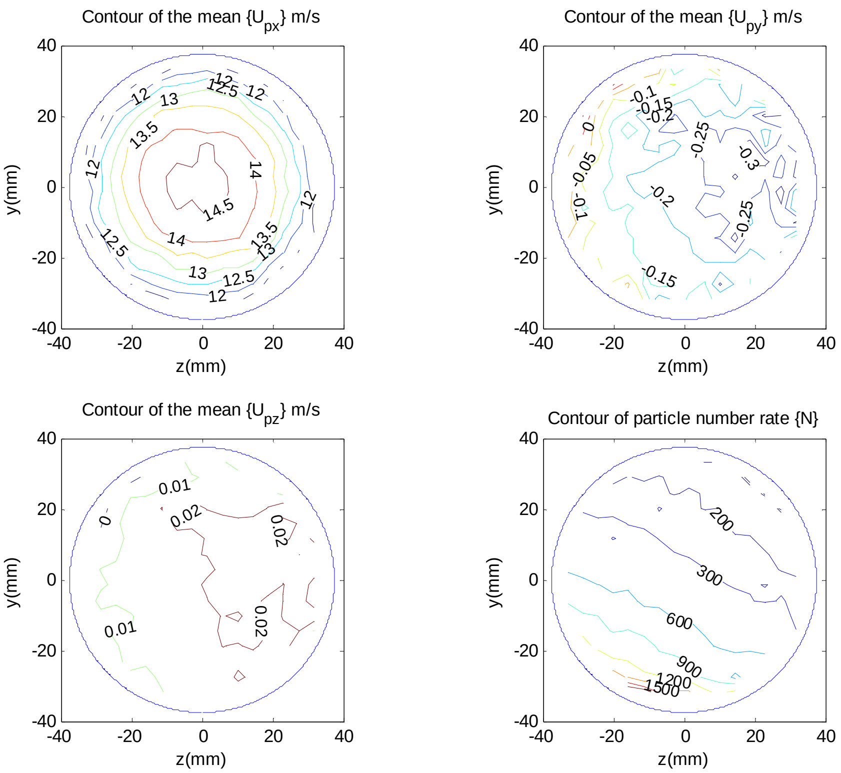

Figure 5.4 Cross-sectional flow patterns described by the distributions of particle mean velocity and particle number rate respectively (U_a=12m/s; particles within the size range 70~110μm)

Figure 5.4 displays the time-averaged values of experimental data on the section eight pipe diameters upstream of the reference point 15mm before the elbow inlet in the horizontal pipe. Among the four diagrams in Figure 5.4, the spatial distribution of the time-averaged particle axial velocity {U_{px}} clearly forms an annular distribution, in which the particle axial velocity decreases from the centre of the section to the wall. We call this kind of fluid pattern an annular cross-sectional pattern. Moreover, for the same gas-solid flow on the section, we also observe that the particle number rate is represented by a stratified distribution layered from the pipe top to the bottom. This stratified configuration clearly expresses the phenomenon of gravity settling due to the gravity force in a horizontal pipe. Aslo an iso-line of the stratification reduces in height along the y axis from the pipe right-hand to left-hand side along the z positive direction, which means that the particle number rate is larger in the z negative field than in the z positive region under the conditions of the identical y coordinate. This inhomogeneous distribution on the z axis may be caused by the particles initial conditions, as in the experiments they were horizontally injected along the z negative direction by a screw feeder. Thus, the particles will possess an initial velocity in the z negative direction after being injected, which results in an initial tendency of the particles to move towards the z negative direction.

As for the other two particle velocity components, $\{U_{py}\}$ and $\{U_{pz}\}$, their cross-sectional distributions do not have any clear pattern, especially for the contour of $\{U_{py}\}$. In general, the time-averaged values of $\{U_{pz}\}$ over the whole section are positive, which shows the overall tendency of particles to move toward the z positive direction. However, the time-averaged values of $\{U_{py}\}$ may be positive or negative and have a random distribution on the section.

Therefore, we will use the parameters of $\{U_{px}\}$, the corresponding granular temperature $\{\Theta\}$ and particle number rate $\{N\}$ to analyze the cross-sectional experimental data along the fluid direction in the following sections.

5.3.3 The development of cross-sectional fluid patterns in a horizontal pipe

Under the conditions of air conveying velocity 12m/s and solid mass loading ratio 1.6% and a sample rate 10 kHz for Laser Doppler Anemometry, the experimental measurements for the second type of glass beads (70~110μm) were performed at a series of pipe cross-sections upstream of the elbow inlet as shown in Figure 5.5. The reference cross-section is defined as 0D which is 15mm before the elbow inlet. The origin point of every local coordinate system locates at the centre of the pipe cross-section.

The experimental results of time-averaged particle axial velocities $\{U_{px}\}$, granular temperature $\{\Theta\}$ and particle number rate $\{N\}$ on each cross sections are visualized in the same row in Figure 5.6. The cross-sectional evolution of these three parameters is subsequently displayed from the section 7D to 1D along the fluid direction. With regard to cross-sectional fluid patterns, on every section from 7D to 1D, the annular contour structure of $\{U_{px}\}$ and the stratified contours of $\{N\}$ are also clearly observed, resembling the results shown in Figure 5.4. Thus, gas-solid pipe flow for solid phase with Stokes number less than 3.6 could be treated as either annular flow or stratified flow, describing contours of particle axial velocity or particle number rate respectively.

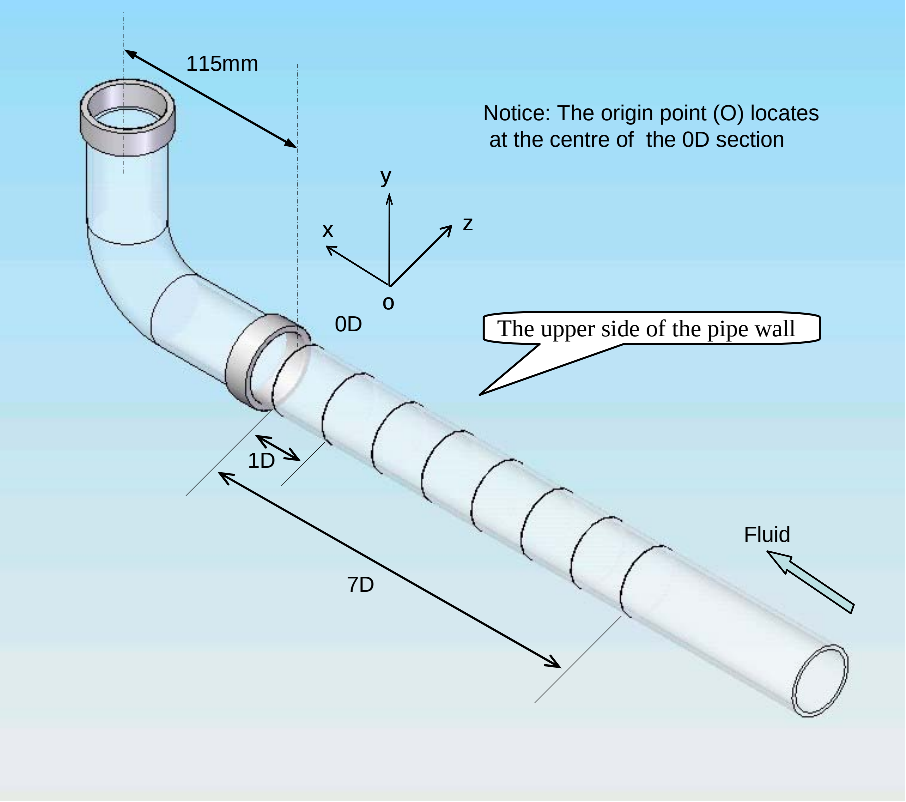

Figure 5.5 The sketch of eight measurement cross-sections along the horizontal pipe

Despite the general similarity of fluid patterns among the cross-sections, the shape, area and centre of the annular core (the fastest region) for $\{U_{px}\}$ vary along the fluid direction. Moreover, the centre of each core is obviously not situated at the corresponding cross-section geometric centre of the cross-section, which results in axial asymmetry for the $\{U_{px}\}$ cross-sectional distribution. Considering the development of the variance of $\{U_{px}\}$ or granular temperature $\{\Theta\}$, we can see an analogous shape on each section. Basically, the variance of fluctuation of $\{U_{px}\}$ is smaller in the right-up region of a cross-section, which means a steadier gas-solid flow than in the other parts. For the development of particle number rate $\{N\}$, a similar layered configuration is observed for the cross-sectional distribution of particle number rate on each section. But an iso-line of particle number rate varies in actual position with a decreasing trend from the left to the right (along the z axis) of each cross-section. This phenomenon shows the effect on the behaviour of the downstream gas-solid flow caused by the manner of feeding particles, since the particles have minor initial velocities on the z negative axis when they are injected by the screw feeder from the pipe right side to the pipe centre.

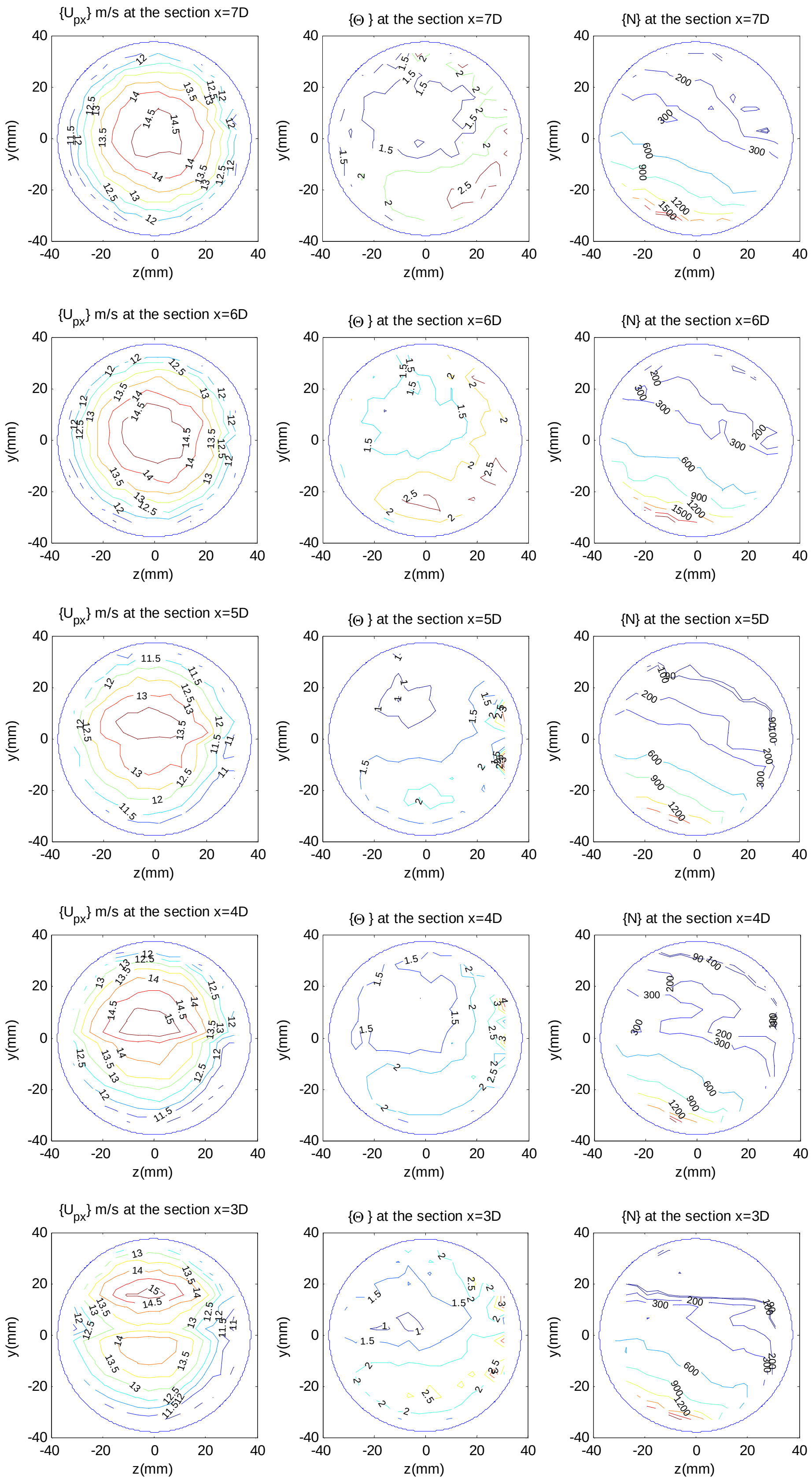

(Figure 5.6 Continue)

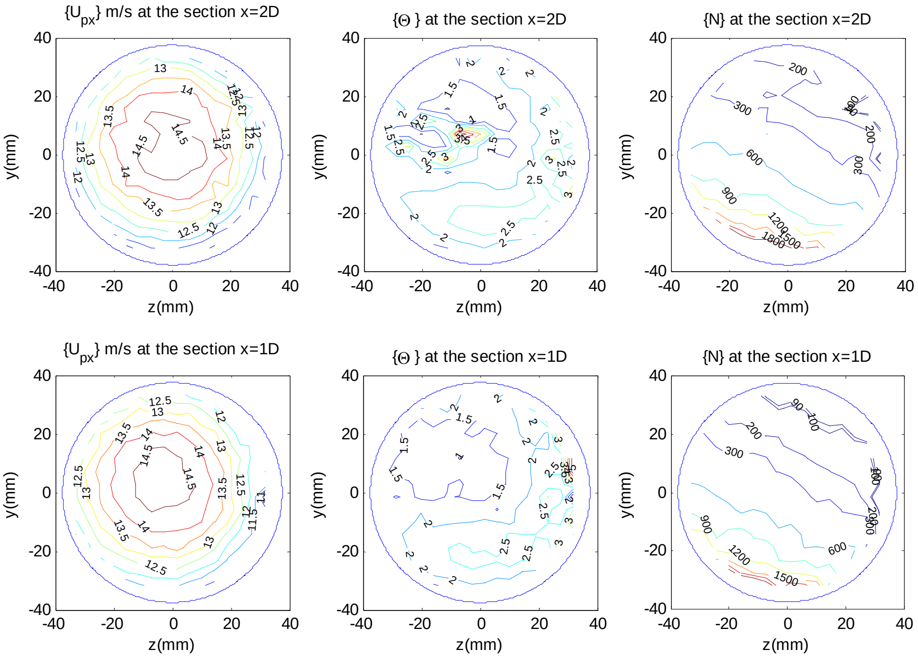

Figure 5.6 Cross-sectional distributions of the mean values of {U_{px}} and the granular temperature {Θ} (unit: m^2/s^2) as well as particle number {N} at an air conveying velocity 12m/s

According to the chart of Geldart for classification of fluidization behaviour (as shown in Figure 2.2), the three kinds of glass beads used in the experiments can be characterized by their retention properties. The first type is less than 50μm, within which glass beads less than 20μm or within 20~50μm respectively, correspond to Group C materials (with very good permeability) or Group A materials on the Geldart chart. The second type of glass beads within 70~110μm also corresponds to Group A materials, which have good retention properties and are suitable for dense phase pneumatic conveying as well. As for the third type of glass beads ranging from 180 to 300μm, they are equivalent to Group B materials with very poor air retention capability and can de-aerate rapidly when the supply of fluidizing air is shut-off. The empirical minimum conveying air velocities in dilute phase suspension flow are about 10~12m/s for transporting Group A materials, 13~16m/s for Group B materials and around 3~4m/s for Group C materials (Mills D., 2004).

Since the three kinds of glass beads (density 2550 kg/m^3) have been used to simulate the flow of pulverised coal (0~110μm, density 1550 kg/m^3) and biomass pellets (size<1.0mm, density<800 kg/m^3) , these pulverised coal and biomass pellets are effectively Group A materials. But for high density and larger granular biomass, the classification is Group B. Here, our experiments mainly focus on Group A materials. It is very meaningful to study particle dynamic behaviour in dilute phase pneumatic transportation under the minimum air conveying velocity. In this way, it can be seen whether the two cross-sectional fluid patterns in the above discussions represent the regime of dilute phase pneumatic conveying in low air velocity. There follows a set of experimental results on the same series of cross-sections (as shown in Figure 5.5) under an air conveying velocity of 10m/s in the horizontal pipe.

5.3.3.1 Glass beads less than 50μm (the first type)

Glass beads of the first type are less than 50μm in diameter and their Stokes Numbers are also less than 3.6. On the whole, these kinds of particles have a good ability to follow the air flow. For these fine particles, the corresponding particle number rate is drastically larger than the other two types under the same solid mass loading. In order to keep the same sample rate 10 kHz of LDA for the three types of glass beads, the solid mass loading ratio for the first type is only 1/10 that of the other two types whose solid mass loading ratios are about 1.9% under an air conveying velocity of 10m/s in ϕ75mm pipe.

Figure 5.7 and 5.8 visualize the cross-sectional experimental data of the first type of glass beads on the sections from 7D to 0D. In order to make these experimental data on different sections comparable, the axial particle velocity and the particle number rate are separately normalized by air conveying velocity (U_a) and the total number rate ($\sum N$) on each cross-section.

In Figure 5.7, the development of the cross-sectional distributions of the dimensionless axial particle velocity $\{U_{px}/U_a\}$ is illustrated along the fluid flow direction. The contours of $\{U_{px}/U_a\}$ apparently display a similar annular form, especially on the sections from 7D to 1D. In these contours, each annular core with an iso-line value of 1.2 is around the section centre with a slight deviation towards the z positive axis. The iso-line value of $\{U_{px}/U_a\}$ shows clearly decreasing tendency from pipe centre to pipe wall. But the area within an iso-line may be different dependent on the detailed cross-section. Although the annular form is also shown in the contour of $\{U_{px}/U_a\}$ on the section 0D, the key difference with those on the other sections lies in that the annular core is shifted beyond the pipe centre and its iso-line value is increased as 1.3 on the section 0D. This difference must be caused by the effect of the bend on the upstream fluid flow, for the section 0D is 15mm upstream from the bend inlet. On the whole, in terms of the similarity among the cross-sectional distributions of $\{U_{px}/U_a\}$, the dilute suspension flow of glass beads of the first type can be treated as being fully developed and steady in the horizontal pipe before one pipe diameter of the bend.

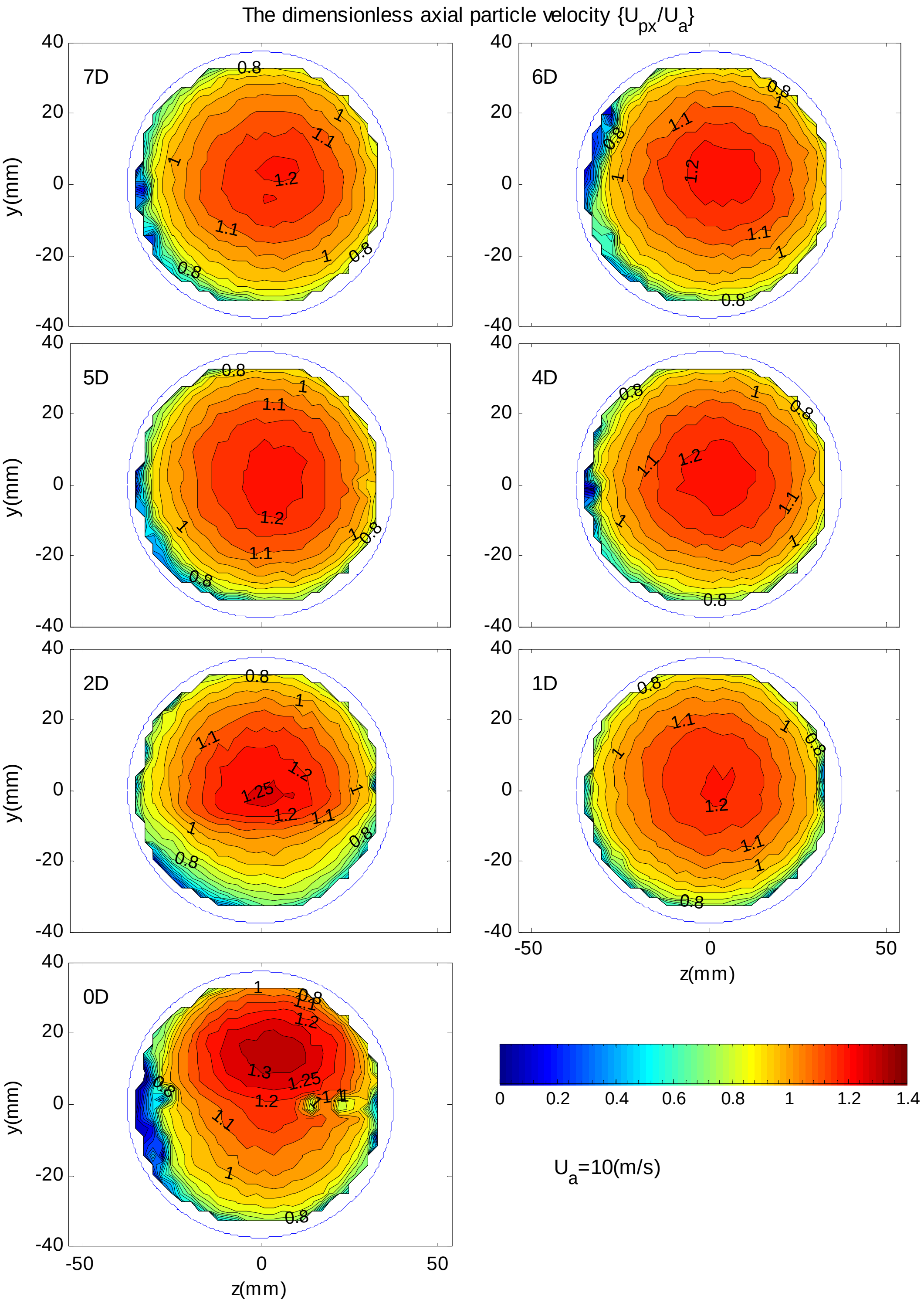

Figure 5.7 Development of cross-sectional distributions of the dimensionless axial particle velocity {U_{px}/U_a} of the first type of glass beads (<50µm) under an air conveying velocity U_a=10m/s and the solid mass loading ratio 0.19%.

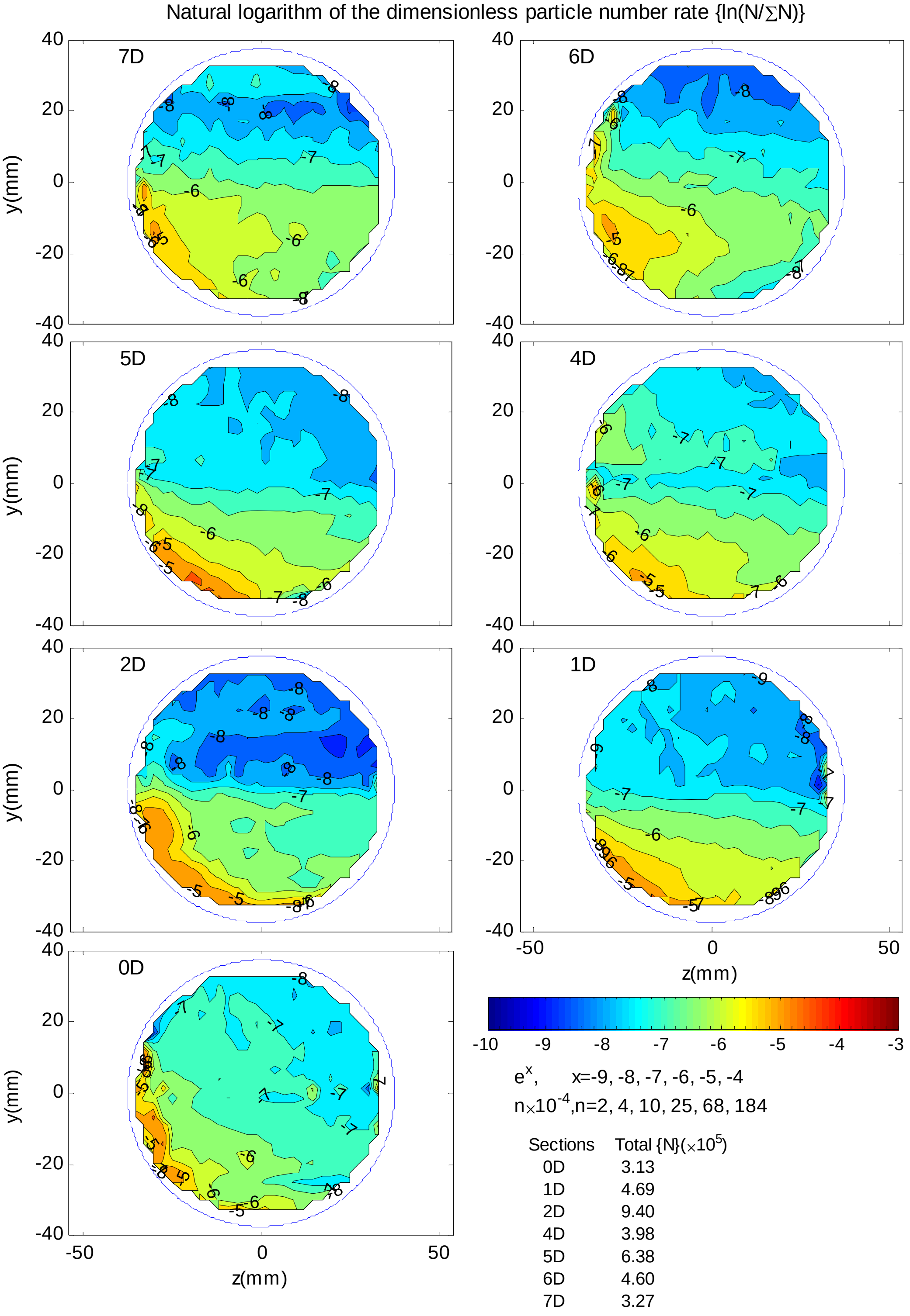

Figure 5.8 Development of cross-sectional distributions of the dimensionless particle number rate {ln(N/ Σ(N))} of the first type of glass beads (<50μm) under an air conveying velocity U_a=10m/s and the solid mass loading ratio 0.19%.

By contrast, Figure 5.8 shows the cross-sectional distributions of the natural logarithm of the dimensionless particle number rate {ln(N/ Σ(N))} from the section 7D to 0D. The contours of particle number rate {N} in Figure 5.8 not only generally illustrate the stratified configuration on each section, but also clearly show the different layered shape of each contour varying along fluid direction. On the section 7D, the largest value of particle number rate is in the region close to the bottom-left of the section. Then this region gradually expands towards the section bottom until the section 5D. The contour iso-line of -7, which is corresponding to 10×10^{-4} of the total particle number rate, remains near the centre (y=0) of the pipe until the section 1D. But the regions layered by iso-lines show some fluctuations. This fluctuation indicates the different frequency of particle-wall collision on each section. Due to gravity, particles with small Stokes Number still have a falling tendency. As such, the larger the region with maximum particle number rate means the more the particles are concentrated, which may cause a higher frequency of particle-wall collision. When particles are re-suspended towards the pipe centre due to the Saffman force and the effect of particle-wall collision, the region with the maximum particle number rate on the next adjacent section will be decreased. This variation also shows that the gas-solid pipe flow of the first type of glass beads is heterogeneous and unsteady, which is contrary to the result deduced by the variations of {U_{px}/U_a}. Therefore, the gas-solid flow formed by the first type of glass beads shows steady and unsteady state simultaneously dependent on which parameters are used to view it.

5.3.3.2 Glass beads within the range 70 to 110 μm (the second type)

The second type of glass beads range from 70 to 110 μm and the corresponding Stokes Number varies within 10~28. Compared with the first type, glass beads of the second type have higher inertial properties and they usually keep their own track rather than following fluid like the particles of the first type. Under an air conveying velocity of 10m/s and solid mass loading ratio 1.9%, the measured experimental data on the sections from 7D to 1D (as shown in Figure 5.5) are illustrated in Figure 5.9 and Figure 5.10.

In Figure 5.9, an annular form is also observed on each cross-sectional distribution of the dimensionless axial particle velocity {U_{px}/U_a} of the second type of glass beads (70~110μm). Overall, this annular form, in which the axial particle velocity decreases from the annular core to the pipe wall, resembles that shown in Figure 5.7. But the iso-line value and position of the annular core are different in the two figures. From the section 7D to 1D, each centre of the annular cores with an iso-line value of 1.35 in Figure 5.9 is beyond the pipe centre, which is different from the observation that every centre of the annular core with an iso-line value of 1.2 is shifted towards the z positive axis in Figure 5.7. In the main stream region of each cross-section, the values of iso-lines from pipe centre to pipe wall are larger in Figure 5.9 (1.35~1.0) than those in Figure 5.7 (1.2~0.8). Thus, the area-averaged axial particle velocity of the second type of glass beads should be faster than that of the first type of glass beads on the sections from 7D to 1D.

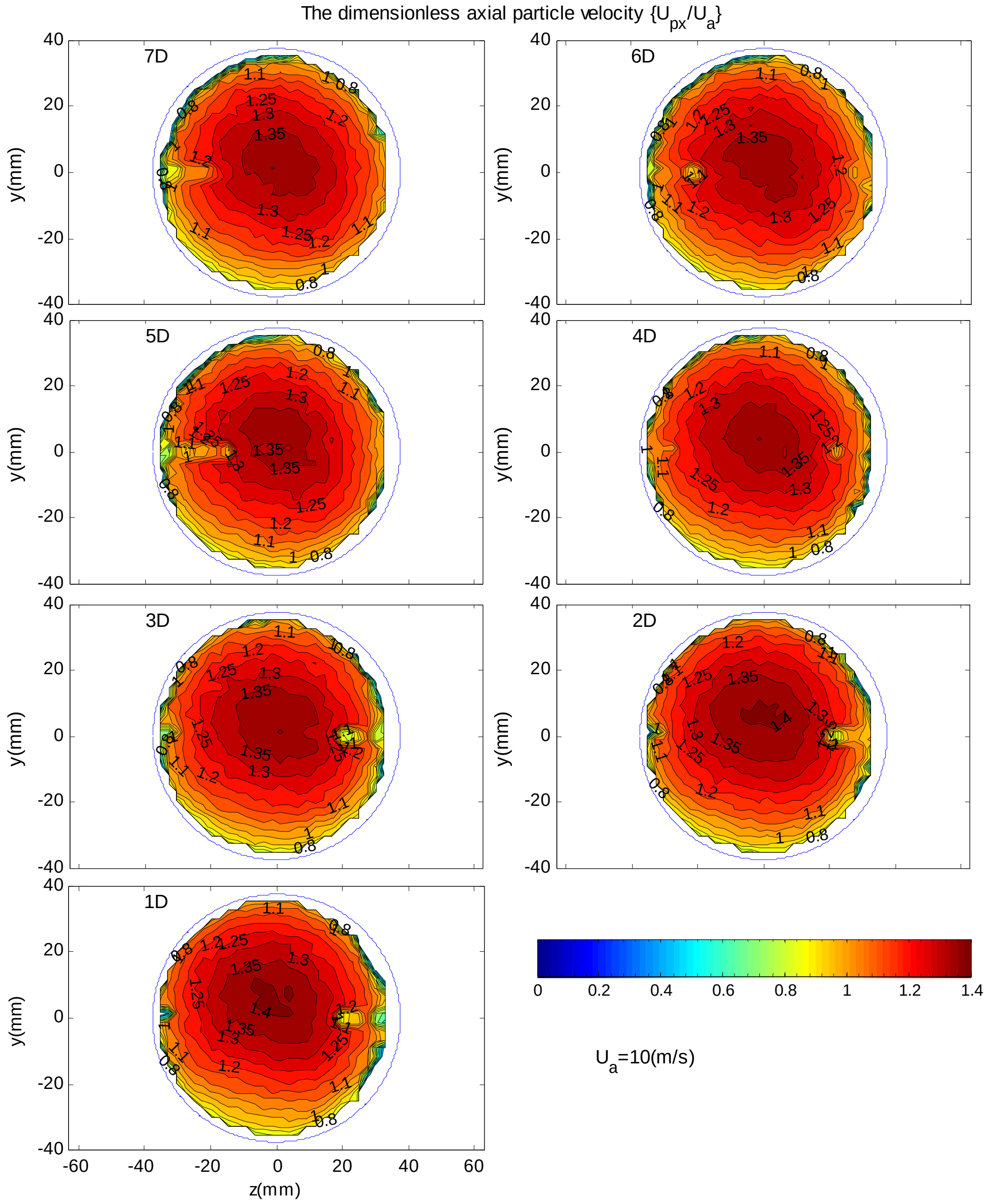

Figure 5.9 Development of cross-sectional distributions of the dimensionless axial particle velocity {U_{px}/U_a} of the second type of glass beads (70~110μm) under an air conveying velocity U_a=10m/s and the solid mass loading ratio 1.9%.

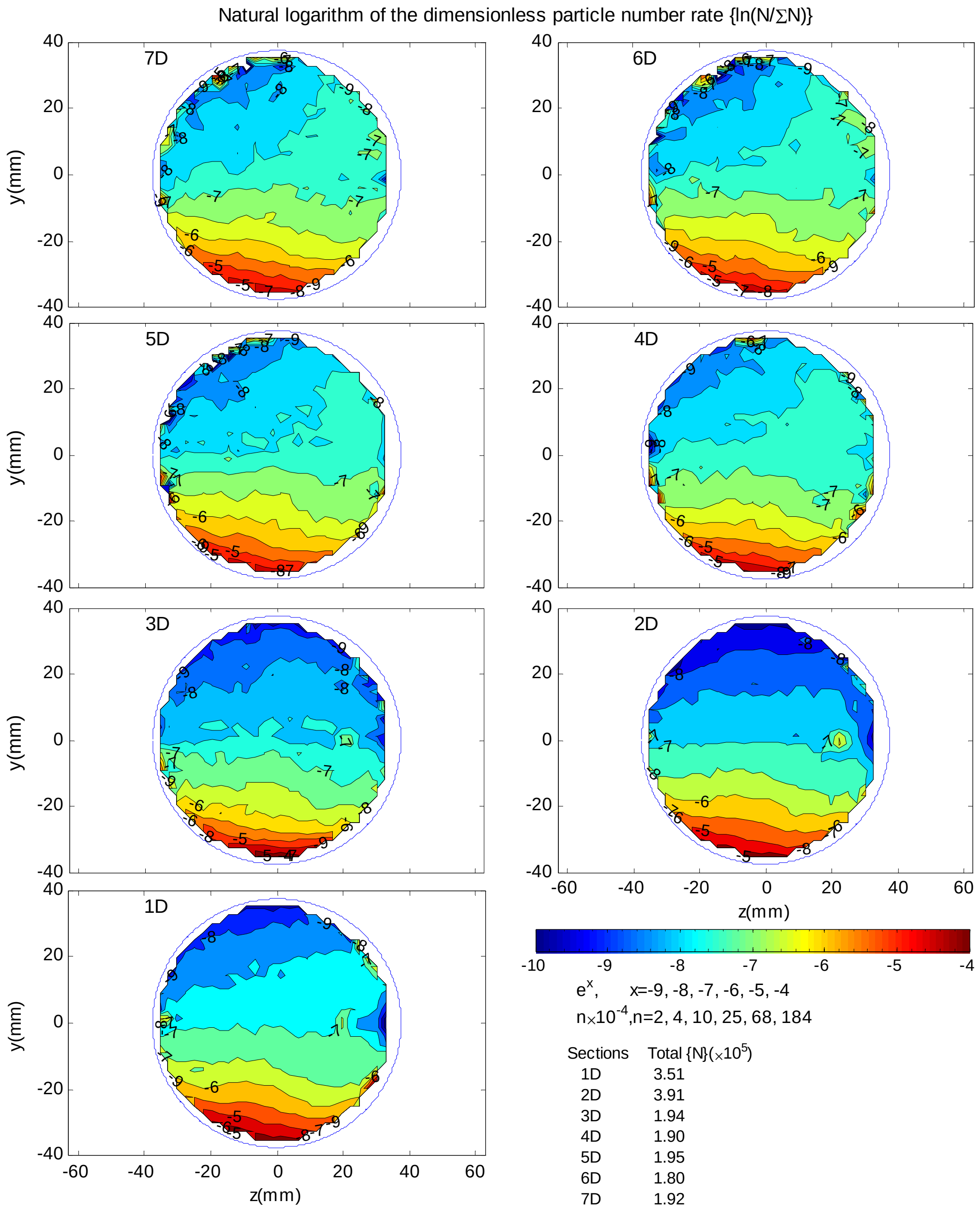

Sections	Total {N}(×10^5)
1D	3.51
2D	3.91
3D	1.94
4D	1.90
5D	1.95
6D	1.80
7D	1.92

Figure 5.10 Development of cross-sectional distributions of the dimensionless particle number rate {ln(N/ Σ(N))} of the second type of glass beads (70~110μm) under an air conveying velocity U_a=10m/s and the solid mass loading ratio 1.9%.

Similarly, the stratified configuration observed in Figure 5.7 can be also found in Figure 5.10, which displays the development of cross-sectional distributions of the dimensionless particle number rate {ln(N/ Σ(N))} for the second type of glass beads (70~110μm). This layered feature demonstrates the phenomenon of gravity settling due to gravity force which makes particles concentrate close to the bottom region in a horizontal pipe. On the sections from 7D to 1D, the stratified iso-lines of each cross-sectional distribution of {ln(N/ Σ(N))} in Figure 5.10 are different from those in Figure 5.8. A comparison of them shows that the total number of layers in Figure 5.10 is more than that in Figure 5.8 with the same interval of 0.5. And the maximum value of $\{\ln(N/\Sigma(N))\}$ occurs at the left-bottom of each section in Figure 5.8. In contrast, the maximum value of $\{\ln(N/\Sigma(N))\}$ in Figure 5.10 is nearly close to the bottom centre of each section with little deviations towards the left-hand side. Third, the iso-line with the value of –7, which is corresponding to 10×10^{-4} of the total particle number rate of each section, varies around the pipe centre line of y=0mm from the section 7D to 1D in Figure 5.7. This corresponding iso-line in Figure 5.10 is below but close to the pipe centre line of y=0mm.

5.3.3.3 Glass beads within the size range 180~300μm (the third type)

Glass beads in the third type vary within the size range 180~300μm. Figure 5.11 shows the experimental data measured by LDA on the cross-sections from 7D to 1D (as shown in Figure 5.5) under an air conveying velocity of 10m/s and solid mass loading ratio 1.9%.

As for cross-sectional distributions of the dimensionless axial particle velocity $\{U_{px}/U_a\}$, the annular feature is not apparently shown in Figure 5.11, which is compared with that in Figure 5.7 or Figure 5.8. With the same interval value of 0.5, the spatial distribution of $\{U_{px}/U_a\}$ on each section in Figure 5.11 can be divided into the inner circle and the outer ring by the iso-line of 1.2. Unlike the other two types of glass beads, there is no annular core with the maximum value of $\{U_{px}/U_a\}$ for the third type of glass beads in Figure 5.11. The areas bounded with the value of an iso-line larger than 1.2 are just randomly distributed within the inner circle of each section.

Since the maximum values of $\{U_{px}/U_a\}$ are separately 1.2, 1.35 and 1.4 for the first, the second and the third types of glass beads, this denotes an interesting phenomenon that larger glass beads have obtained faster maximum axial particle velocity under the same air conveying velocity. According to the experimental results of Tsjui et al. (1982), air flow turbulence was reduced by plastic particles of a mean size 210μm (the range 100~400μm; density 1000kg/m^3). As such, the kinematic energy of air flow or air velocity may be increased due to the lessening turbulent energy. Thus, an increasing air velocity would also make the second and the third type of glass beads accelerate faster.

Nevertheless, the above explanation need to be confirmed by the further experimental data, especially the simultaneous measurement data of two phase velocities in gas-solid pipe flow with different particle size.

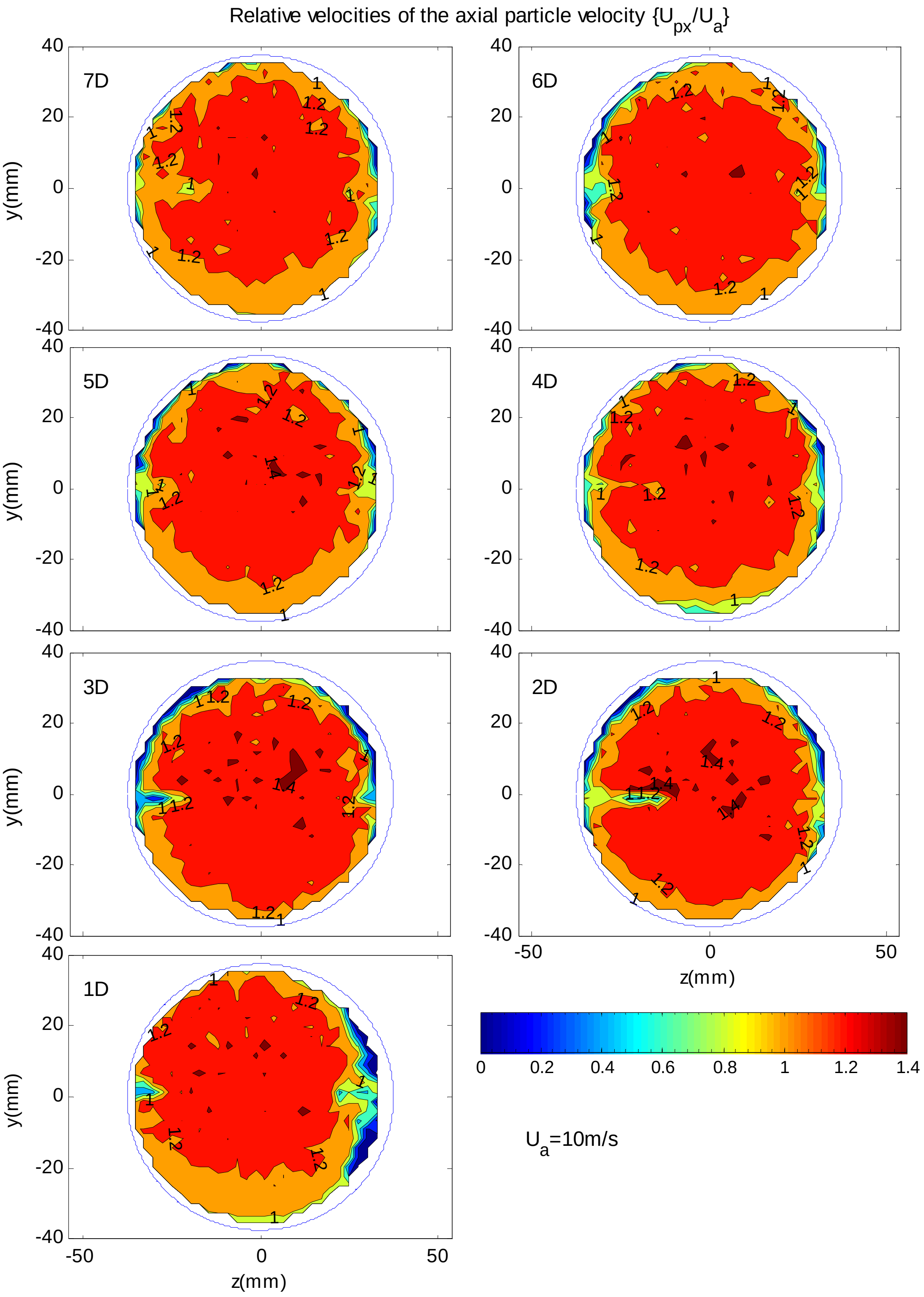

Figure 5.11 Development of cross-sectional distributions of the dimensionless axial particle velocity {U_{px}/U_a} of the third type of glass beads (180~300μm) under an air conveying velocity U_a=10m/s and the solid mass loading ratio 1.9%.

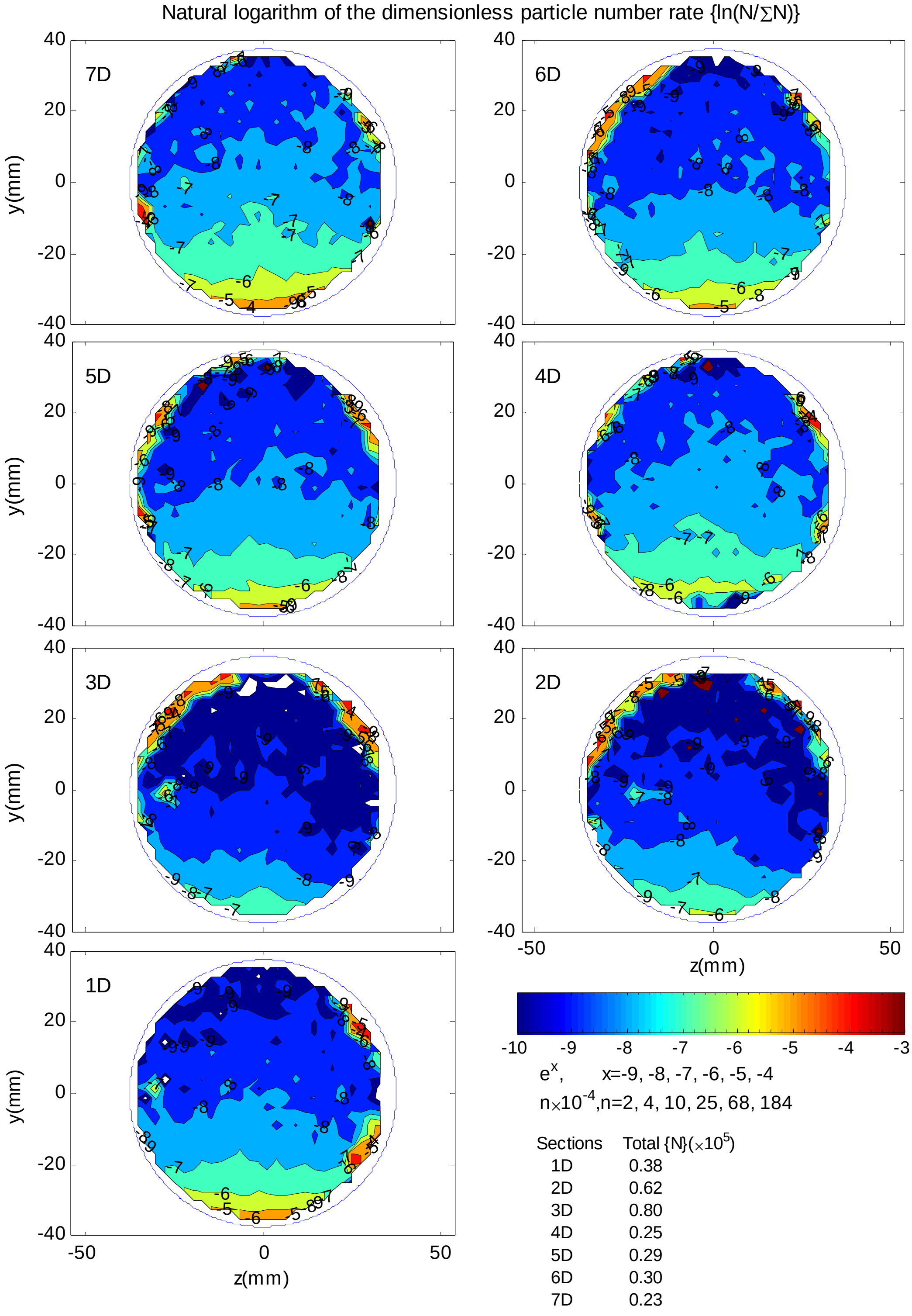

Sections	Total {N}(×10^5)
1D	0.38
2D	0.62
3D	0.80
4D	0.25
5D	0.29
6D	0.30
7D	0.23

Figure 5.12 Development of cross-sectional distributions of the dimensionless particle number rate {ln(N/ Σ(N))} of the third type of glass beads (180~300μm) under an air conveying velocity U_a=10m/s and the solid mass loading ratio 1.9%

As for the third type of glass beads, Figure 5.12 shows the development of cross-sectional distributions of the dimensionless particle number rate {ln(N/ Σ(N))} from the section 7D to 1D.

Compared with that in Figure 5.8 and Figure 5.10, the stratified configuration can be still observed on each section in Figure 5.12. With the same interval of $\{\ln(N/\Sigma(N))\}$, the total layer in Figure 5.12 (the third type of glass beads) is larger than that in Figure 5.8 (the first type of glass beads), but less than that in Figure 5.10 (the second type of glass beads). The iso-line with the value of –7, which is corresponding to 10×10^{-4} of the total particle number rate of each section, is away from the pipe centre line of y=0mm and varies around the height of 1/4 pipe diameter from the pipe bottom. In addition, the distribution of iso-lines of $\{\ln(N/\Sigma(N))\}$ does not strictly decrease from the top to the bottom on each section in Figure 5.12. The regions with the relative larger values, close to the maximum value of $\{\ln(N/\Sigma(N))\}$, is not only located in the pipe bottom but also found around the pipe top wall. This phenomenon is not shown in Figure 5.8 or Figure 5.10. Moreover, there exists some symmetry along the pipe vertical centre line of z=0mm in Figure 5.12. This symmetric property is different from the experimental results observed in Figure 5.8 and Figure 5.10. It indicates that the inertia effect on dynamic behaviour of glass beads in the third type is much stronger.

5.4 PARTICLE DYNAMIC BEHAVIOUR IN A VERTICAL PIPE DOWNSTREAM OF A 90° ELBOW

The roping phenomenon is one of great interest in pneumatic conveying research. It occurs in a bend and results in particles being concentrated within a small portion of one pipe cross-section at the bend, as well as in the pipe downstream of the bend, due to particle inertia. Consequently, it is very important to study the Rope disintegration processing after a bend before dual or triple branches are used to deliver particles in a controllable way to the various burners in a pulverized fuel (PF) boiler. Furthermore, the extended technique of Laser Doppler Anemometry has been applied to determine not only the spatial change in the particle velocity distribution but also to characterize the particle segregation, as shown by particle number rate, in a bend.

As for the characteristics of air flow in a vertical pipe downstream of a bend, experimental and numerical data of cross-sectional distributions of the axial air velocity $\{U_{ay}\}$ and the horizontal air velocity $\{U_{ax}\}$ have been discussed in Chapter 4. The cross-sectional distribution of the axial air velocity $\{U_{ay}\}$ on the section 0D displays a horseshoe shape, where $\{U_{ay}\}$ is slower inside (pipe inner wall) and faster outside (pipe outer wall). This feature can be still observed on the further downstream sections. But the difference of $\{U_{ay}\}$ between inside and outside the horseshoe tends to be lessened. Moreover, a secondary flow described by $\{U_{ax}\}$ is formed on the section 0D and gradually becomes weak till it has completely disappeared.

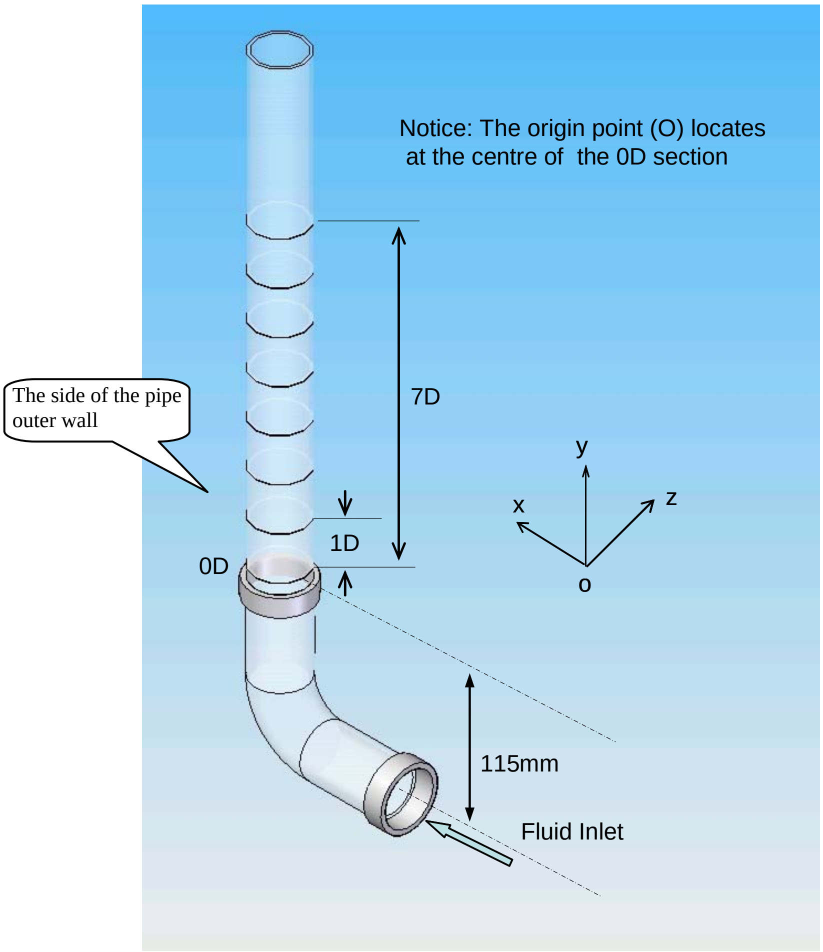

Figure 5.13 The arrangement of measurement cross-sections in the vertical pipe

In the following sections, the experimental data of three types of glass beads, pneumatically transported from a horizontal pipe section through an elbow (R/D=1.3) into a connecting vertical pipe, have been measured by the extended technique of Laser Doppler Anemometry discussed in Chapter 3. A total of seven cross-sections along the vertical pipe are schematically illustrated in Figure 5.13 and the reference cross-section (0D) is about 15mm away from the elbow outlet. The distance between two adjacent cross-sections is equal to one pipe diameter.

5.4.1 Glass beads less than 50μm (the first type)

With regard to the first type of glass beads (<50μm), the experimental data measured by LDA on the cross-sections from 0D to 6D in the vertical pipe are illustrated in Figure 5.11, Figure 5.12 and Figure 5. 13 for the dimensionless axial particle velocity $\{U_{py}/U_a\}$, the dimensionless horizontal particle velocity $\{U_{px}/\max(\mathrm{abs}(U_{px}))\}$ and the dimensionless particle number rate $\{\ln(N/\sum(N))\}$ respectively, under an air conveying velocity 10m/s and solid mass loading ratio 0.19%.

In Figure 5.14, the horseshoe shape can be found on each contour of $\{U_{py}/U_a\}$ from the section 0D to 4D. This feature is similar to that shown in contours of the axial air velocity $\{U_{ay}\}$ in Figure 4.5. Generally, the axial particle velocity $\{U_{py}\}$ is faster on the outside portion of the horseshoe (towards pipe outer wall) than that on the inside portion of the horseshoe (towards pipe inner wall). At the further downstream sections of 5D and 6D, the horseshoe-shaped feature no longer exists and the cross-sectional distributions of $\{U_{py}/U_a\}$ have developed into another pattern where a small region with the slower $\{U_{py}\}$ is surrounded a ring with the faster $\{U_{py}\}$. In addition, the region with the slowest $\{U_{py}\}$ on a section is close to the pipe right wall (the z positive direction) behind the section 1D and its area is gradually enlarged from the section 1D to 5D. A similar distribution can be found between the contour of $\{U_{py}/U_a\}$ on the section 5D and that on the section 6D. Also the maximum value of $\{U_{py}/U_a\}$ on both sections is decreased as 1 from 1.3 on the section 0D. The similarity suggests that gas-solid flow of the first type of glass beads begin to be steady from the section 5D.

With regard to the dimensionless horizontal particle velocity $\{U_{px}/max(abs(U_{px}))\}$ of the first type of glass beads (<50μm), Figure 5.15 shows the development of the cross-sectional distribution of $\{U_{px}/max(abs(U_{px}))\}$from the section 0D to 6D in the vertical pipe downstream of a bend. It is very clear that the secondary flow of the first type of glass beads shown in Figure 4.7 (for the single air phase) can be also observed in Figure 5.15. On each section, we assume the pipe inner wall as the start position, where the secondary flow runs towards the pipe outer wall with a decreasing tendency of $\{U_{px}\}$. When the secondary flow reaches at the pipe outer wall, $\{U_{px}\}$ is close to zero. Then this secondary flow changes its fluid direction from the x positive axis to the x negative axis and it is developed into two subflows which run towards the pipe inner wall with an acceleration along the pipe left wall and the pipe right wall respectively. As such, the secondary flow forms two subcirculations of one counter-clock-wise and one clock-wise separately. From the section 0D to 6D, the key difference between secondary flows is that the region with the positive maximum $\{U_{px}/max(abs(U_{px}))\}$ is gradually shifted from the pipe inner wall to the pipe centre and the total number of iso-lines is reduced.

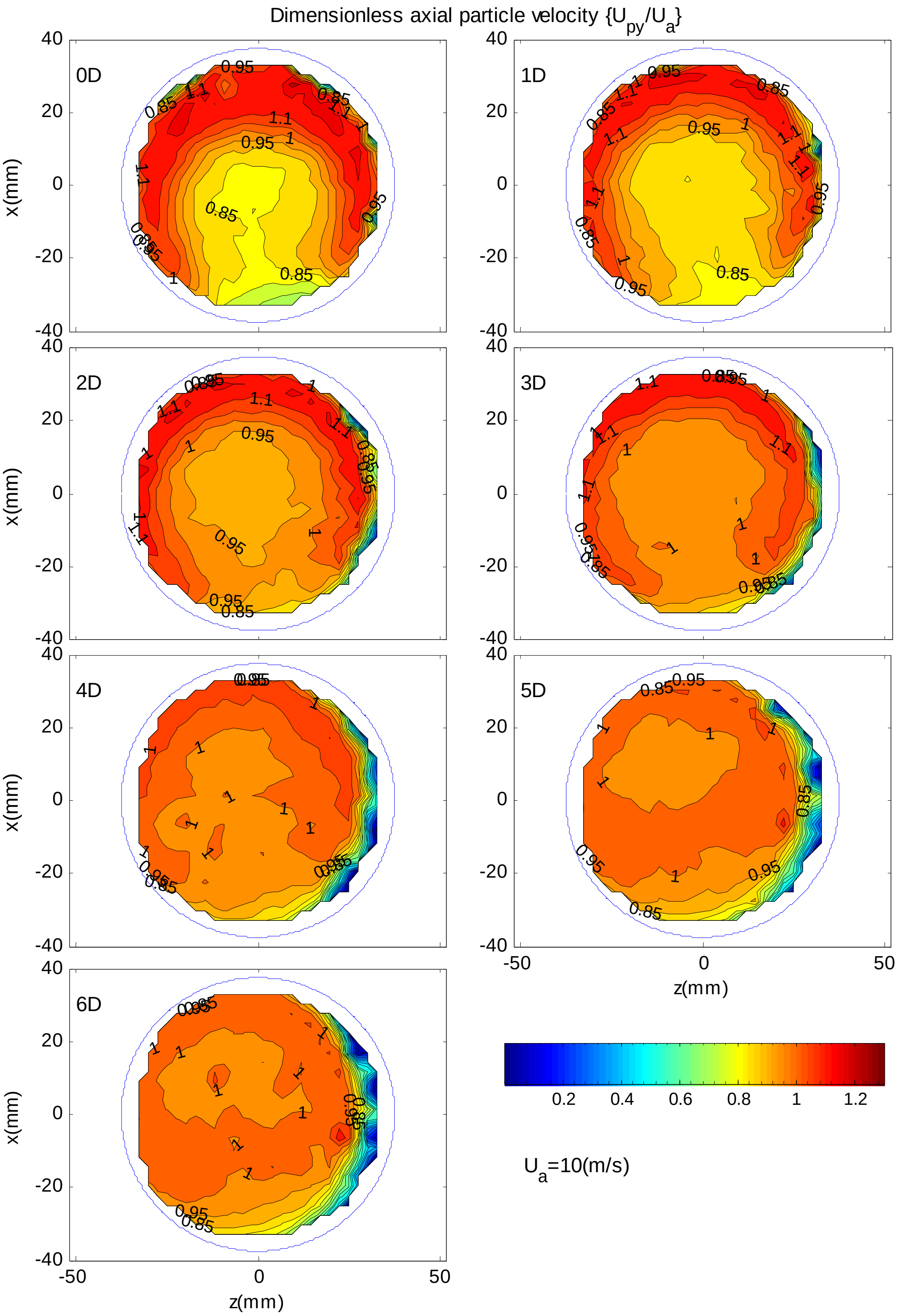

Figure 5.14 Development of cross-sectional distributions of the dimensionless axial particle velocity $\{U_{py}/U_a\}$ of the first type of glass beads (<50μm) under an air conveying velocity U_a=10m/s and the solid mass loading ratio 0.19% in the vertical pipe behind an elbow (R/D=1.3)

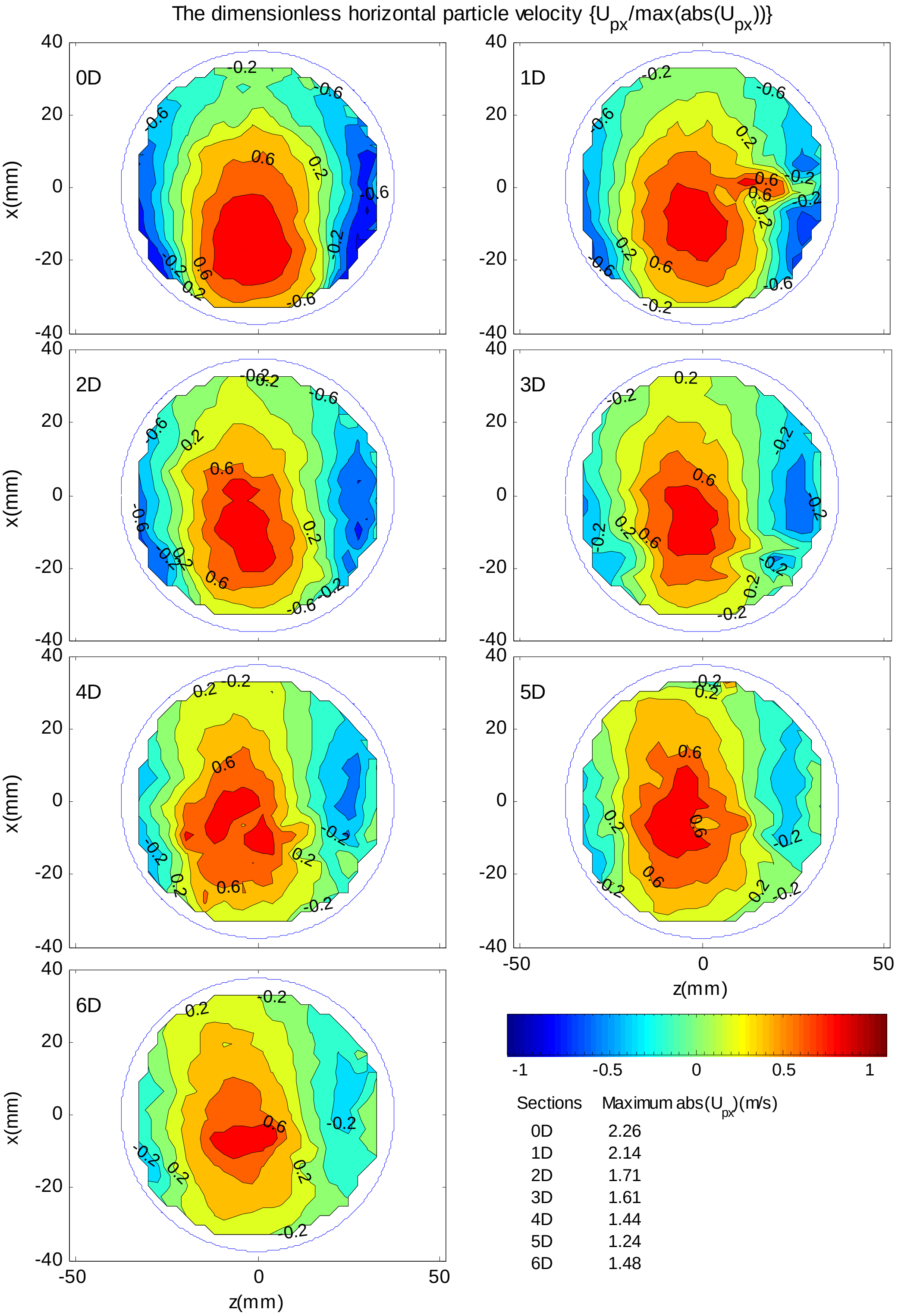

Sections	Maximum abs(U_{px})(m/s)
0D	2.26
1D	2.14
2D	1.71
3D	1.61
4D	1.44
5D	1.24
6D	1.48

Figure 5.15 Development of cross-sectional distributions of the dimensionless horizontal particle velocity {U_{px}/max(abs(U_{px}))} of the first type of glass beads (<50μm) under an air conveying velocity U_a=10m/s and the solid mass loading ratio 1.9% in the vertical pipe behind an elbow (R/D=1.3)

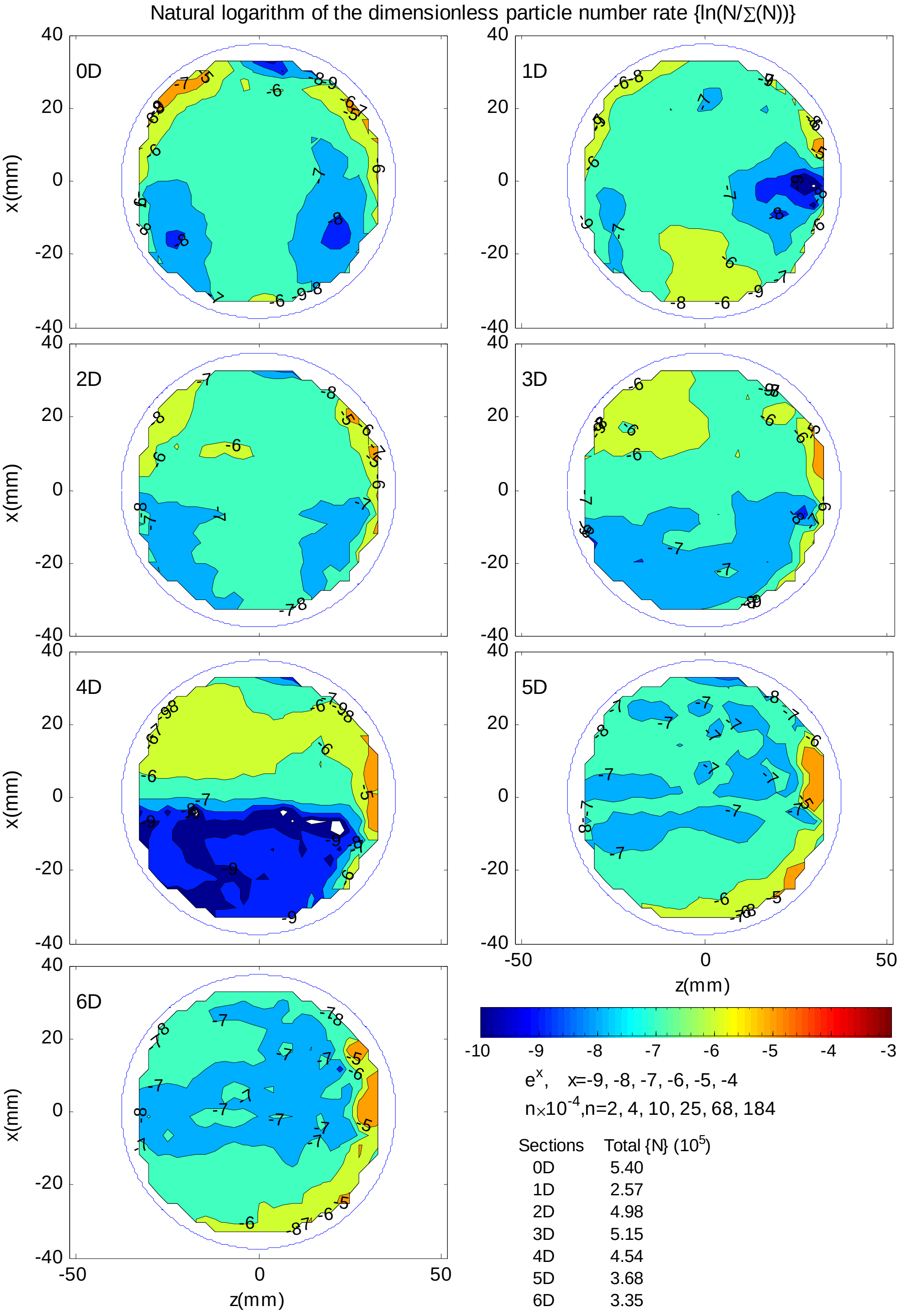

Sections	Total {N} (10^5)
0D	5.40
1D	2.57
2D	4.98
3D	5.15
4D	4.54
5D	3.68
6D	3.35

Figure 5.16 Development of cross-sectional distributions of the dimensionless particle number rate {N/∑(N)} of the first type of glass beads (<50μm) under an air conveying velocity U_a=10m/s and the solid mass loading ratio 1.9% in the vertical pipe behind an elbow (R/D=1.3)

Figure 5.16 displays the experimental data of the dimensionless particle number rate {ln(N/ Σ(N))}, which is normalized by the summation of particle number rate on each section, from the section 0D to 6D in the vertical pipe. Overall, the feature of stratified configuration or any other uniform pattern can not be observed on cross-sectional distributions of {ln(N/ Σ(N))} in Figure 5.16. On the section 0D, referring to the horseshoe shape of {U_{py}/U_a} as shown in Figure 5.14, we can see that the relatively dense particle number rate with the iso-line value of -6 is positioned closed to the outside portion of the horseshoe (the pipe outer wall). In contrast, the region with the smaller value (-7) of {ln(N/ Σ(N))} is located in either the pipe left-inner or right-inner wall. On the section 1D, the contour of {ln(N/ Σ(N))} resembles with that on the section 0D. But the area within an iso-line may be shifted. At further downstream sections, the contours of {ln(N/ Σ(N))} are developed to be randomly distributed with no clear shape. On the section 5D or 6D, the region with the higher relative density {ln(N/ Σ(N))} is shown at the pipe right-inner wall with the smallest value of {U_{py}/U_a}. On the whole, the rope of relative dense particle number rate formed in the bend has still not dispersed by the section 6D for the first type of glass beads transported by a 10m/s air conveying velocity and solid mass loading ratio 0.19% .

5.4.2 Glass beads within the size range 70~110μm (the second type)

Experiments using the second type of glass beads were performed to measure cross-sectional distributions of the axial particle velocity{U_{py}}, the horizontal particle velocity {U_{px}} and particle number rate {N} on the same series of cross-sections as discussed in the proceeding section. Under fluid conditions of air conveying velocity 10m/s and solid mass loading ratio 1.9%, the experimental data on cross-sectional distributions of three parameters from the sections 0D to 6D are shown in Figure 5.17, Figure 5.18 and Figure 5.19

As for the dimensionless axial particle velocity {U_{py}/U_a}, Figure 5.17 shows the development of its cross-sectional distributions in the vertical pipe downstream of the bend. The horseshoe-shaped feature can be also observed on the contours of {U_{py}/U_a} from the section 0D to 4D, but it is no longer apparent on the contours of {U_{py}/U_a} at the further sections of 5D and 6D. However the contour shape of {U_{py}/U_a} is identical to that on the section 6D, which indicates a steady state of gas-solid flow for the second type of glass beads after the section 5D. All the above observations have a good agreement with those observed in Figure 5.14 for the first type of glass beads. At a point on each cross-section, the axial particle velocity of the first type in Figure 5.14 tends to be the corresponding local axial air velocity in Figure 4.5. But it is less than that of the second type in Figure 5.17. This phenomenon shows the inertia effect on particle dynamics, since the first type (<50μm) has a smaller Stokes Number than the second type

(70~110μm) does. As such, after being accelerated by the fastest air flow, the second type of glass beads would retain its state with a high velocity and the first type tends to follow the current local air flow when both glass beads enter into a region with lower air velocity.

Figure 5.18 shows the development of cross-sectional distributions of the dimensionless horizontal particle velocity $\{U_{px}/U_a\}$ from the section 0D to 6D. Clearly, the characteristic of secondary flow is also shown in Figure 5.8, especially at the sections of 2D to 6D. Compared with those in Figure 5.15, the feature of secondary flow is not clear in the contours of $\{U_{px}/U_a\}$ on the section 0D and 1D in Figure 5.18. But we can still see the increasing tendency of the magnitude of $\{U_{px}/U_a\}$ towards the x negative axis along the pipe left-hand wall and the pipe right-hand wall respectively. In addition, for the second type of glass beads, the magnitude of $\{U_{px}/U_a\}$ in Figure 5.18 is generally larger in the x negative direction than in the x positive direction. But the magnitude of $\{U_{px}/U_a\}$ in the x positive direction obviously increases from the section 0D to 6D. By contrast, for the first type of glass beads, the magnitudes of $\{U_{px}/U_a\}$ in both x directions are nearly equal on each cross-section (as shown in Figure 5.15).

With regard to the dimensionless particle number rate $\{N/\sum(N)\}$, Figure 5.19 shows the development of its cross-sectional distributions from the section 0D to 6D. On the section 0D, the rope of the region with the maximum $\{N/\sum(N)\}$ is shown at the pipe outer wall. Additionally, a stratified configuration shows that $\{N/\sum(N)\}$ decreases from the pipe outer wall to the pipe inner wall. This stratification feature was not found in the behavour of the first type of glass beads in Figure 5.16. At the further sections downstream of 0D, the total contour number of $\{N/\sum(N)\}$ gradually decreases while both the dense region with the maximum $\{N/\sum(N)\}$ of -6 and the dilute area with the minimum $\{N/\sum(N)\}$ of -9 are smaller and smaller. In particular, downstream of the section 4D, the dense region with the iso-line value of -6 is lessened like a curved strip located around the pipe left-inner wall and the cross-sectional distributions of $\{N/\sum(N)\}$ are developed into a simple pattern in which a relatively dilute region with the iso-line value of -8 is surrounded by a relatively dense region with the iso-line value of -7 over the main area of the section 5D and 6D.

Therefore, the gas-solid flow of the second type of glass beads can be considered as being steady downstream of the section 4D, according to the similarities of cross-sectional distributions of $\{U_{py}/U_a\}$ and $\{N/\sum(N)\}$. In addition, the development of the cross-sectional distributions of $\{N/\sum(N)\}$ indicates that the rope of the second type of glass beads is still retained until the section 6D, where a dense region with the maximum $\{N/\sum(N)\}$ is located at the pipe left-inner wall.

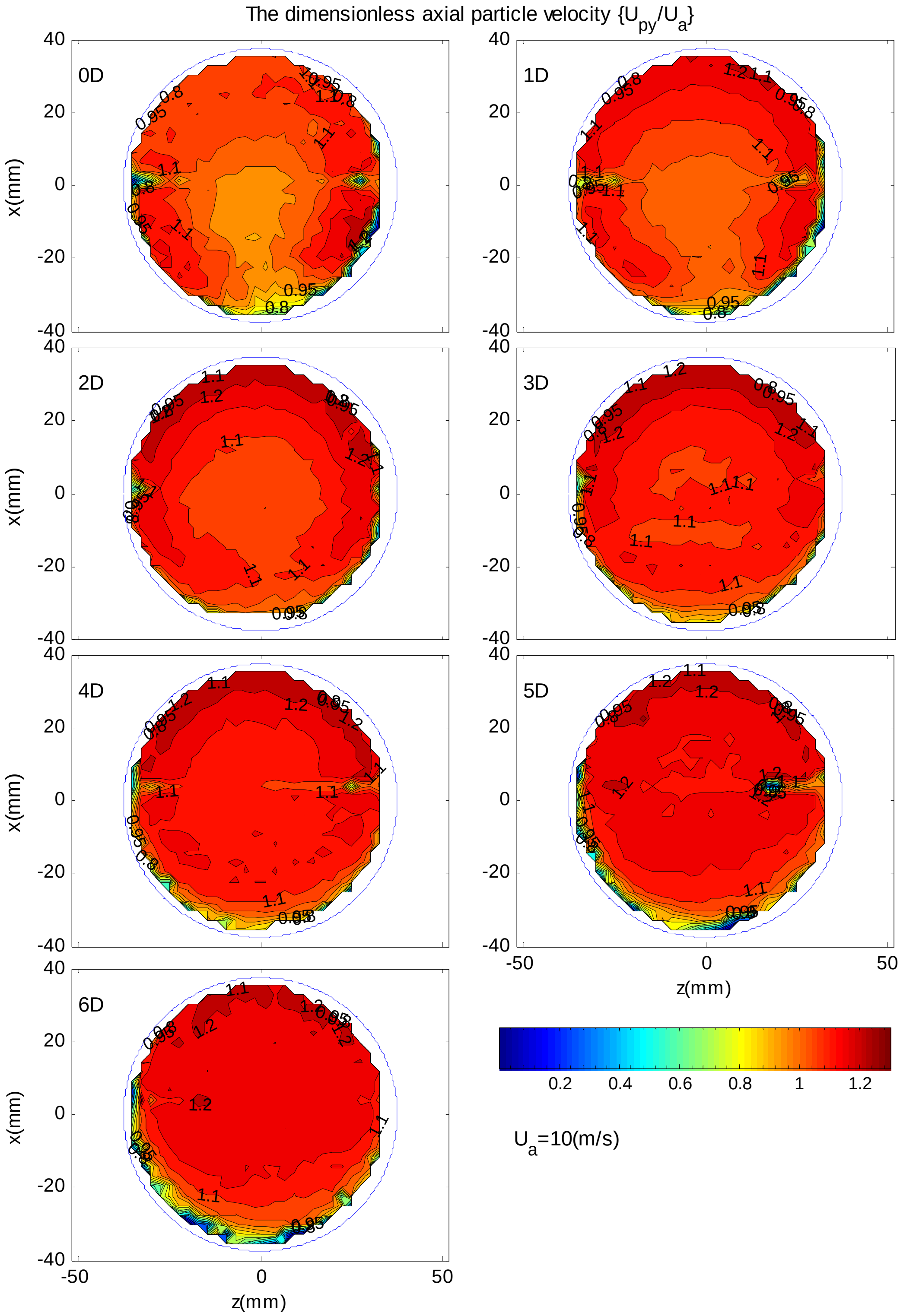

Figure 5.17 Development of cross-sectional distributions of the dimensionless axial particle velocity {U_{py}/U_a} of the second type of glass beads (70~110μm) under an air conveying velocity U_a=10m/s and the solid mass loading ratio 0.19% in the vertical pipe behind an elbow (R/D=1.3)

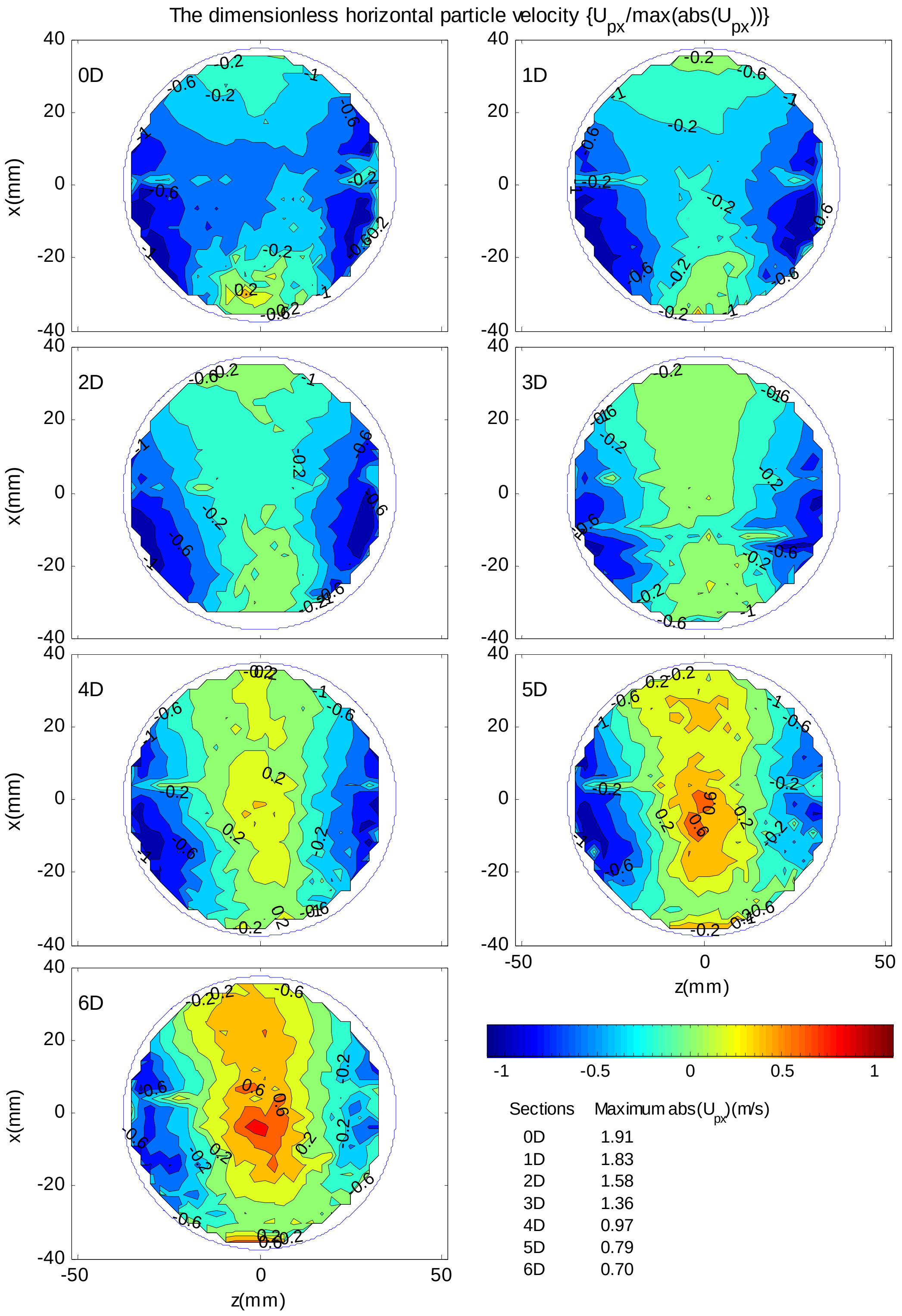

Sections	Maximum abs(U_{px})(m/s)
0D	1.91
1D	1.83
2D	1.58
3D	1.36
4D	0.97
5D	0.79
6D	0.70

Figure 5.18 Development of cross-sectional distributions of the dimensionless horizontal particle velocity {U_{px}/max(abs(U_{px}))} of the second type of glass beads (70~110μm) under an air conveying velocity U_a=10m/s and the solid mass loading ratio 1.9% in the vertical pipe behind an elbow (R/D=1.3)

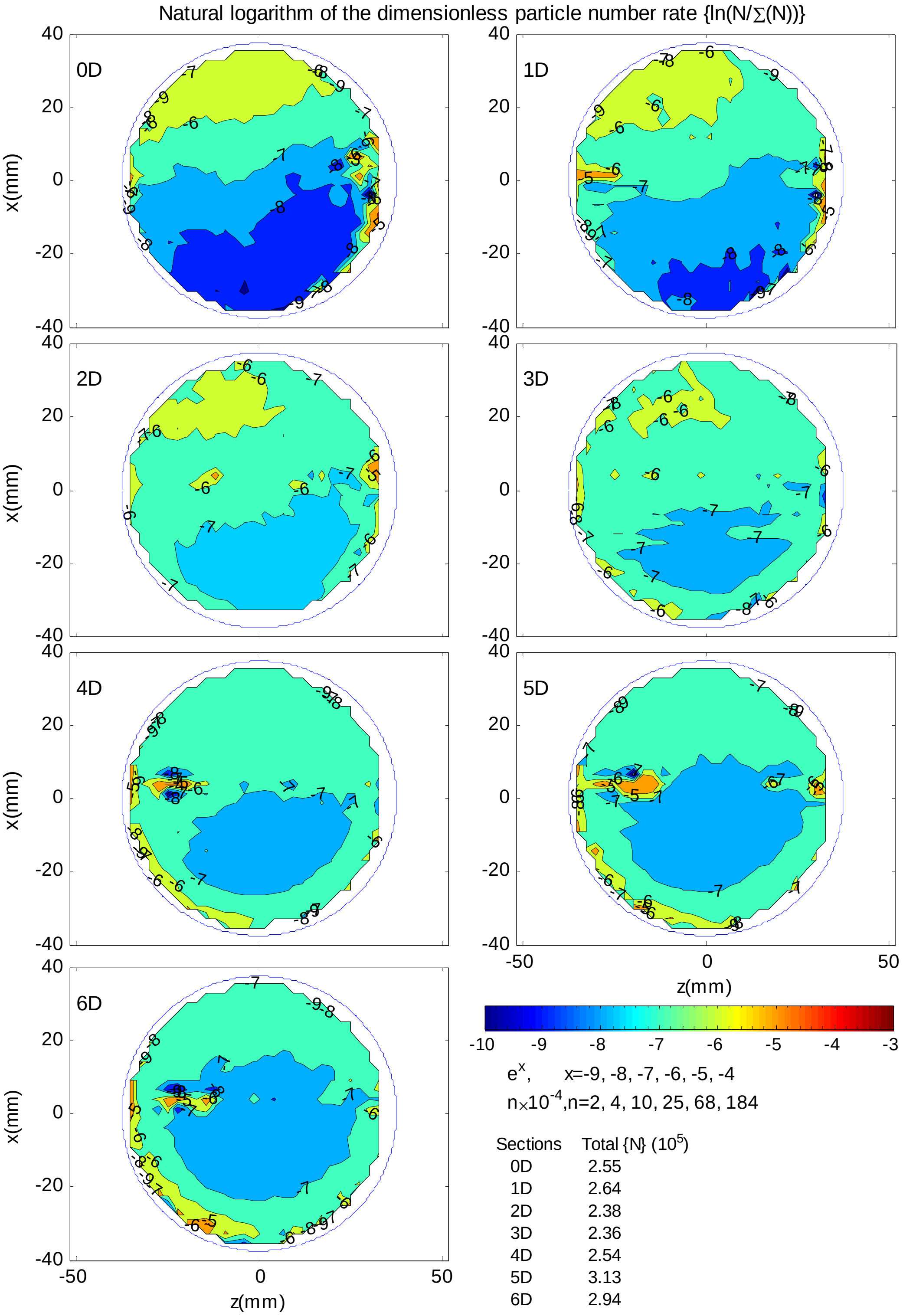

Sections	Total {N} (10^5)
0D	2.55
1D	2.64
2D	2.38
3D	2.36
4D	2.54
5D	3.13
6D	2.94

Figure 5.19 Development of cross-sectional distributions of the dimensionless particle number rate {N/∑(N)} of the second type of glass beads (70~110μm) under an air conveying velocity U_a=10m/s and the solid mass loading ratio 1.9% in the vertical pipe behind an elbow (R/D=1.3)

5.4.3 Glass beads within the size range 180~300μm (the third type)

The experiments were performed using the third type of glass beads within the size range 180~300μm, which were transported in the pipe by an air conveying velocity 10m/s with a solid mass loading ratio 1.9%. The experimental data are plotted in Figure 5.20, Figure 5.21 and Figure 5.22 respectively.

As for the dimensionless axial particle velocity $\{U_{py}/U_a\}$, Figure 5.20 shows the development of its cross-sectional distributions from the section 0D to 6D in the vertical pipe downstream of the bend. In general, the horseshoe-shaped feature is observed in contours of $\{U_{py}/U_a\}$ before the section 3D. Further downstream, a clear shape can no longer be observed on contours of $\{U_{py}/U_a\}$ on the sections of 4D to 6D, where $\{U_{py}/U_a\}$ is much more randomly distributed and has a larger value (more than 1) in the main area of a cross-section. Comparing Figure 5.20 with Figure 5.14 (the first type glass beads) and Figure 5.17 (the second type of glass beads) as well as Figure 4.5 (air flow), we list their key difference and similarity in Table 5.1.

Table 5.1 Comparisons of the axial velocity distributions in a vertical pipe downstream of a bend among three types of glass beads and air flow

		Air flow ($\{U_{ay}/U_a\}$)	Glass beads ($\{U_{py}/U_a\}$)		
			The first type (<50μm)	The second type (70~110 μm)	The third type (180~300 μm)
Stokes Number		-	<3.5	10~28	>35
Horseshoe-shaped feature observed on the sections		from 0D to 7D	from 0D to 4D	from 0D to 4D	from 0D to 2D
on the section 6D	Region with the smallest axial velocity close to	the pipe right-inner wall	the pipe right wall	the pipe left-inner wall	the pipe left wall
	The values of iso-line in the main area of the section 6D	>=1	>=0.95	>=1.1	>=1.2

Obviously, the horseshoe-shaped feature is a common characteristic in contours of the axial velocity $\{U_{ax}/U_a\}$ or $\{U_{ay}/U_a\}$ in the vertical pipe downstream of a bend for both air flow and gas-solid flow of three types of glass beads. This feature is still observed at the section 7D for air flow. By contrast, it disappears at the downstream of the section 4D for the first and second types of glass beads and at the downstream of the section 2D for the third one. Therefore, this horseshoe-shaped feature must be formed due to the bend effect which changes a horizontal flow of air or gas-solid into the vertical one. The different dispersion positions of the horseshoe indicate that particle Stokes Number influences the cross-sectional patterns of $\{U_{ay}/U_a\}$ in a vertical pipe behind an elbow. In addition, for the axial particle velocity of three types of glass beads on the main area of the section 6D, it shows that a larger glass bead has a higher axial velocity which is closer to the maximum axial air velocity. This denotes that particle inertia is also important, for larger glass beads have higher inertia.

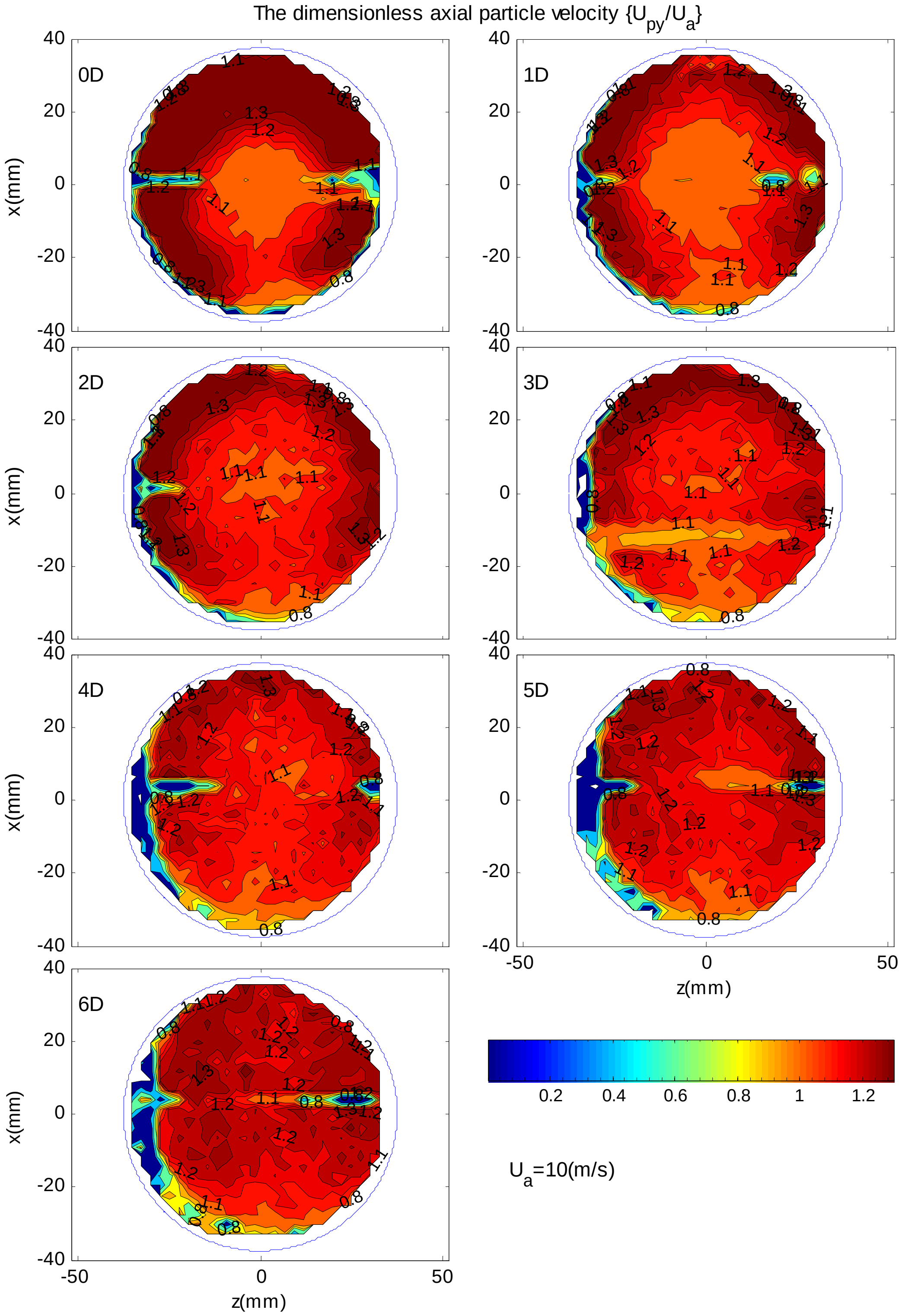

Figure 5.20 Development of cross-sectional distributions of the dimensionless axial particle velocity $\{U_{py}/U_a\}$ of the third type of glass beads (180~300μm) under an air conveying velocity U_a=10m/s and solid mass loading ratio 0.19% in the vertical pipe behind an elbow (R/D=1.3)

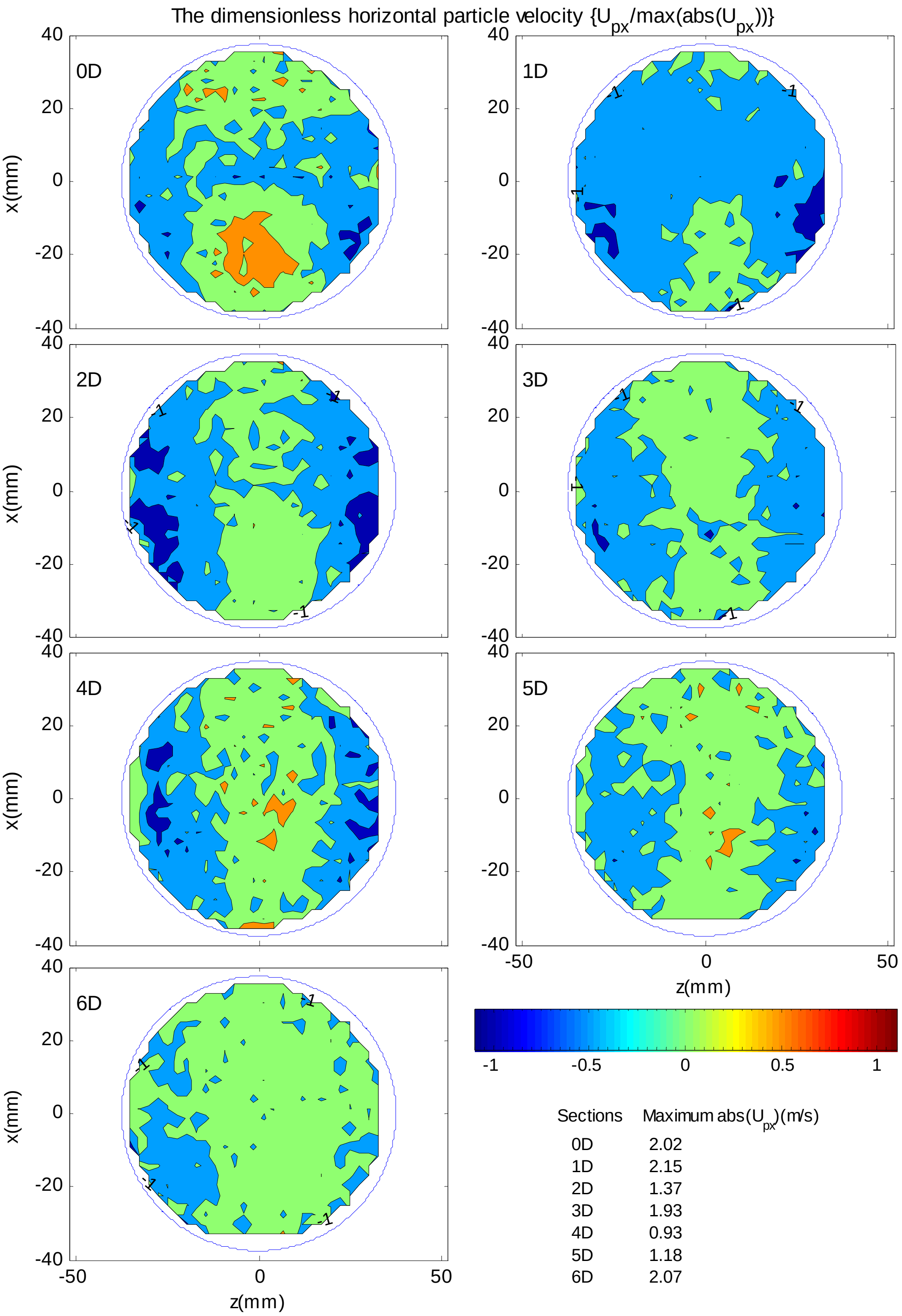

Sections	Maximum abs(U_{px})(m/s)
0D	2.02
1D	2.15
2D	1.37
3D	1.93
4D	0.93
5D	1.18
6D	2.07

Figure 5.21 Development of cross-sectional distributions of the dimensionless horizontal particle velocity {U_{px}/max(abs(U_{px}))} of the third type of glass beads (180~300μm) under an air conveying velocity U_a=10m/s and the solid mass loading ratio 1.9% in the vertical pipe behind an elbow (R/D=1.3)

Contours of the dimensionless horizontal particle velocity $\{U_{px}/\max(\mathrm{abs}(U_{px}))\}$ from the section 0D to 6D are displayed in Figure 5.21. Unlike those of the other two types of glass beads, each contour of the third type does not show the feature of secondary flow in the vertical pipe downstream of the bend. Overall, there is no clear form shown in contours of $\{U_{px}/\max(\mathrm{abs}(U_{px}))\}$ on the sections of 0D, 1D and 6D. But a similar structure can be seen on the sections from 2D to 4D. Contours of $\{U_{px}/\max(\mathrm{abs}(U_{px}))\}$ on these sections illustrate that a strip in the middle of the section divides it into three parts along the x axis. Basically, $\{U_{px}/\max(\mathrm{abs}(U_{px}))\}$ is almost zero in the strip and negative in both sides of the strip. Moreover, the magnitudes of $\{U_{px}/\max(\mathrm{abs}(U_{px}))\}$ have no significant discrepancy on all sections, especially on the section 6D, where $\{U_{px}/\max(\mathrm{abs}(U_{px}))\}$ is almost homogenously distributed with a value of zero over most of the area of the section. Compared with Figure 5.15 and Figure 5.18, the key difference lies in the lack of structure of secondary flow in Figure 5.21. This indicates that air secondary flow (the horizontal air velocity) has much more influence on the first and the second types of glass beads than on the third one.

The evolution of cross-sectional distributions of the dimensionless particle number rate $\{N/\sum(N)\}$ is shown in Figure 5.22. Generally, there is no uniform or clear pattern in any contours of $\{N/\sum(N)\}$ from the section 0D to 6D. In most regions of a whole section, $\{N/\sum(N)\}$ has a relative small value of -7 or -8, which are corresponding to 10 or 4×10^{-4} of the total particle number rate on this section. The rope, which is formed by the region with the maximum particle rate, is the most frequently but sporadically located along the pipe left wall and each region only occupies a small fraction similar to several discrete circles on the whole section. This is different from the experimental results observed in Figure 5.16 and Figure 5.19 for the first and the second types of glass beads, for both types of glass beads at least have a clear form shown in the contours of $\{N/\sum(N)\}$ on the section 0D. This difference among three types of glass beads also indicates that particle inertia plays an important influence on particle dynamic properties in a vertical pipe downstream of a bend, for the third type of glass beads with the largest Stokes Numbers tends to retain their previous state at the elbow outlet, when they enter into the vertical pipe from the elbow. And the other two types will be easily influenced to follow the current local air flow in the same process from the elbow to the vertical pipe. .

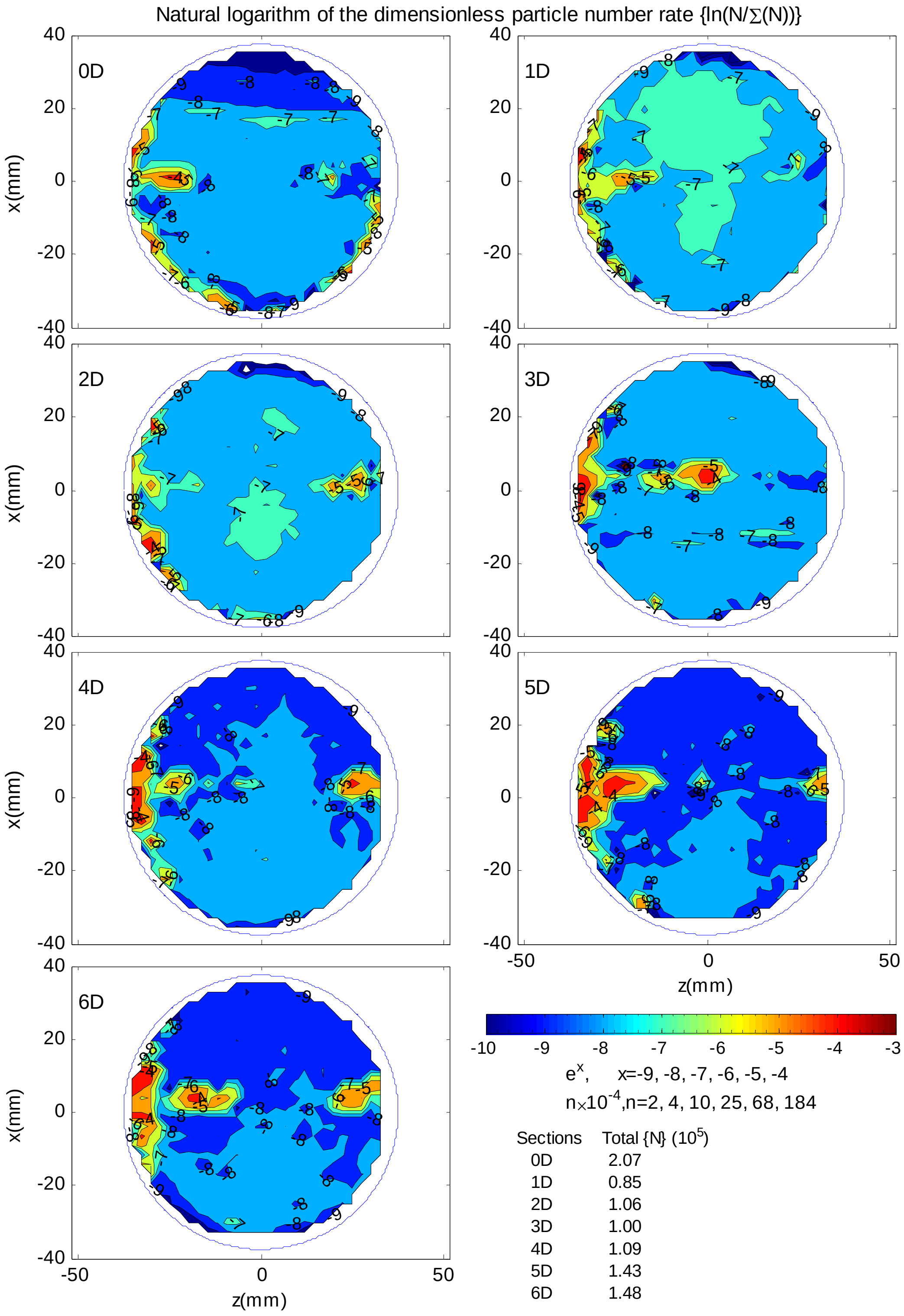

Sections	Total {N} (10^5)
0D	2.07
1D	0.85
2D	1.06
3D	1.00
4D	1.09
5D	1.43
6D	1.48

Figure 5.22 Development of cross-sectional distributions of the dimensionless particle number rate {N/∑(N)} of the third type of glass beads (180~300μm) under an air conveying velocity U_a=10m/s and the solid mass loading ratio 1.9% in the vertical pipe behind an elbow (R/D=1.3)

5.5 DISCUSSION AND COMPARISON

5.5.1 The discrepancy between air velocity and particle velocity in the horizontal pipe

David Mills (2004b) stated that the particle velocity would typically be about 80% of the air conveying velocity in a horizontal pipeline in dilute phase conveying and about 70% in vertical upward flow in a pipeline, which can be expressed in terms of a slip ratio of particle velocity over air conveying velocity. This statement is based on the concept that particle velocity should be lower than that of the conveying air, since the mechanism of conveying is one of drag force in dilute phase conveying. However, he did not describe the related methods for particle velocity measurement or experimental data.

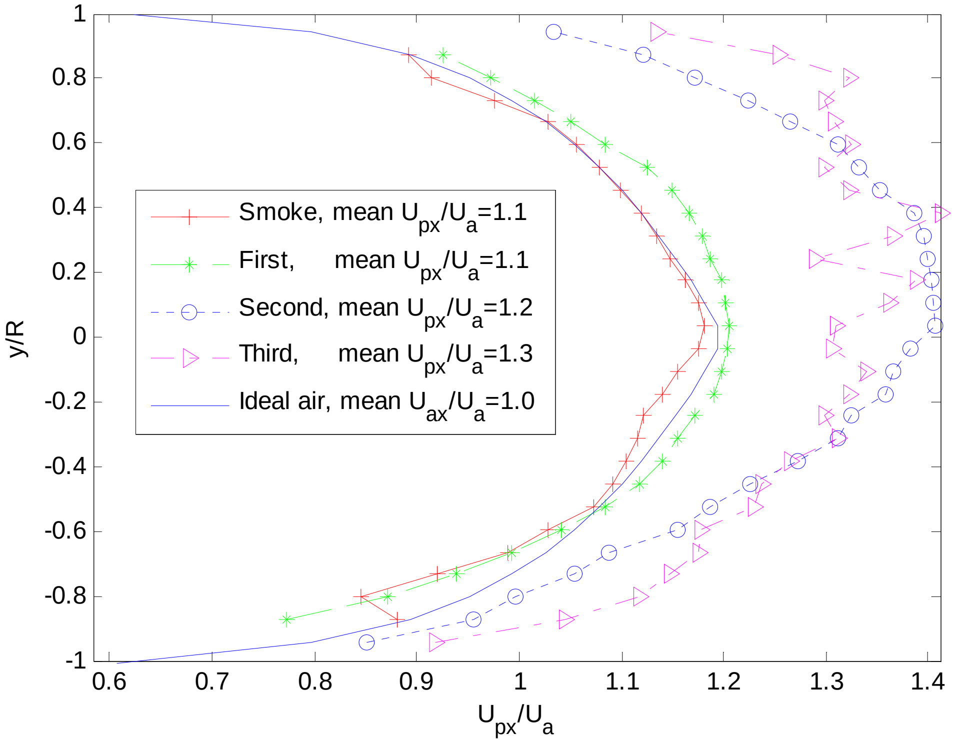

Figure 5.23 The vertical profile of axial mean velocity for four types of particles at the section 1D in the horizontal pipe (U_a=10m/s, air conveying velocity; First: glass beads less than 50µm; Second: glass beads within 70~110 µm; Third: glass beads within 180~300 µm).

So far, most cited experimental data of particle velocity in horizontal pipes are expressed as a one-dimensional profile along the gravity force direction (y axis). In order to make a convenient comparison with other related work, we re-plotted the experimental data on the horizontal section 1D for three types of glass beads as well as smoke in the one-dimensional profiles shown in Figure 5.23. Compared with the one-seventh power profile of ideal turbulent flow (Rober et al., 2004), we can obviously see that both profiles of smoke and the first type of glass beads have a good agreement with that of ideal gas flow and they are nearly identical only with minor discrepancies, since both the first type of glass beads (<50μm) and smoke particles have a small Stokes number (<3.6) which gives a good ability to follow the flow of the transporting air. By contrast, the profiles of the second (70~110μm) and the third (180~300μm) types of glass beads show a significant discrepancy. The mean value of U_{px}/U_a, is 1.1, 1.1, 1.2 and 1.3 for smoke, the first, the second and the third types of glass beads respectively. This indicates that the mean axial particle velocity of particles with larger size is greater than that of the smaller particles, which must result from high inertia of the larger particles. Since the empirical one-seventh power law states that the ratio of the average velocity to the centreline velocity varies from 0.79 to 0.87 in a fully developed flow in a smooth pipe, this means that fluid velocity at the pipe centre is about 1.3 or 1.2 times larger than the mean velocity. Consequently, particles with high inertia would retain their original velocities when accelerated in the fastest region of fluid or due to particle-particle collisions. We can in fact see that the axial particle velocities for the second and third types of glass beads are faster than that of air phase at a local point, especially in the region close to the pipe wall. In addition, we also notice that the maximum ratio of the axial particle velocity to air conveying velocity measures about 1.4, which is larger than that of 1.3 estimated by the one-seventh power law. The possible reason may be the kinematic energy of air flow increased due to turbulent energy lessened by larger micro-particles like the third type of glass beads.

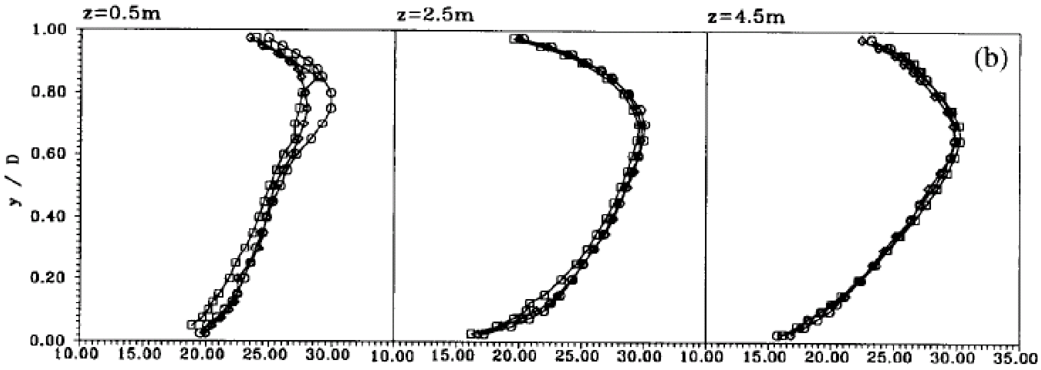

Fig. 7. Development of vertical profiles of particle phase properties along a horizontal glass pipe for different particle mass loadings [μ=(○) 0.3, (◇) 0.5 and (□) 0.7, superficial gas velocity U_s=23 m/s]. (a) Particle concentration in kg/m³; (b) axial mean particle velocity in m/s; (c) axial particle velocity fluctuation in m/s; (d) number mean particle diameter in μm.

Figure 5.24 Experimental data of Huber and Sommerfeld (1994) for flow in a horizontal pipe by Phase Doppler Anemometry under air conveying velocity 23m/s for glass beads with a mean size 40μm

With regard to particle velocity measurements in a horizontal pipe, Figure 5.24 shows the experimental data of Huber and Sommerfeld (1994) using Phase Doppler Anemometry (PDA). Apparently, the maximum particle velocity is about 30m/s, which is 1.3 times faster than the air conveying velocity 23m/s. They did not give any explanation. Then Kussin and Sommerfeld (2002) published their experimental data obtained by measuring the particle velocity of glass beads with mean size 100μm in a horizontal channel using PDA, as shown in Figure 5.25. Here, particle velocity is clearly slower than air velocity except for the boundary region and the maximum ratio of particle velocity to air conveying velocity is about 1.0.

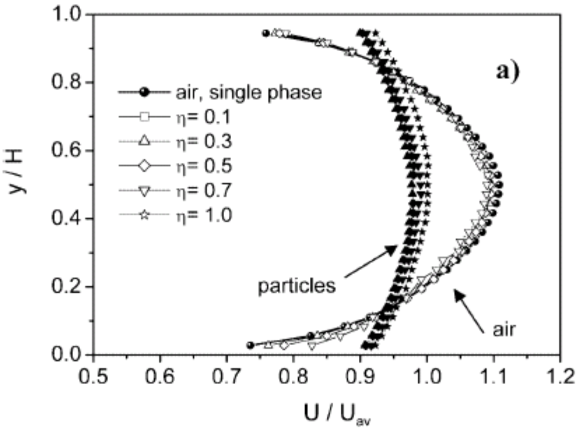

Fig. 6a–c. Vertical profiles for air and 100-μm particles with U_{av}=19.7 m/s for the low roughness case (R1): a horizontal mean velocities of air and particles; b horizontal component of rms velocity fluctuation; c vertical component of rms velocity fluctuation (*open symbols*: air; *closed symbols*: particles)

Figure 5.25 The experimental data obtained by Kussin and Sommerfeld (2002) in the horizontal channel using PDA.

Figure 5.26 shows the experimental data of Tsuji et al. (1982) for flow in a horizontal pipe under an air conveying velocity of 15m/s and at different solid loading ratios. They extended the standard technique of LDA to measure simultaneously the velocities of air phase and solid phase by discerning the amplitudes of Doppler Signals scattered by the particles (plastic pellets with mean size 200μm and density 1000 kg/m^3) and the seeding particles (ammonium chloride with mean size 0.6μm). Their experimental data show that the profiles of particle velocity are close to those of the air phase at the different solid loading ratios. The values of particle horizontal velocity to air conveying velocity are less than 1.3.

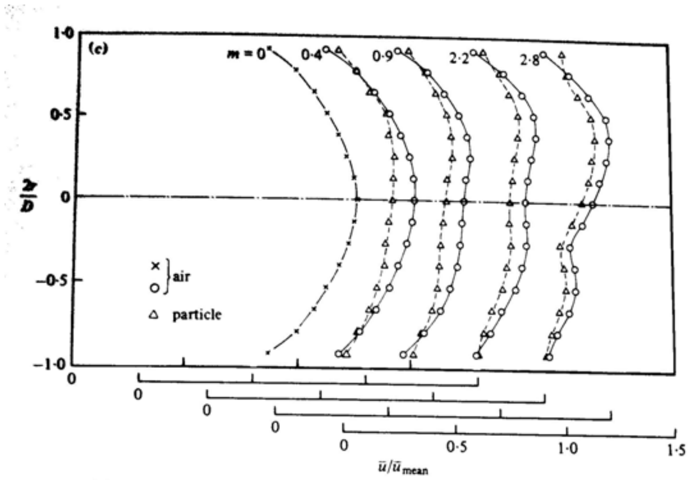

FIGURE 11. Mean velocity distributions of air and 0·2 mm particles: (*a*) $\bar{u}_{mean}$ = 6 m/s; (*b*) 10 m/s; (*c*) 15 m/s.

Figure 5.26 Tsuji's experimental data (1982) by LDA in a horizontal pipe

Figure 5.27 shows one set of the experimental data measured by Yilmaz and Levy (2001) who used a fibre-optic probe to measure time-averaged local particle velocities, concentrations and mass fluxes for pulverised-coal particles (90% less than 75μm) in a horizontal pipe. Their experimental data show that the maximum ratio of particle velocity to air conveying velocity is less than 1.2.

According to the experimental data in the figures of 5.15, 5.16, 5.17 and 5.18, the previous experiments of measuring particle velocity in a horizontal pipe mainly focused on a single type of particle with varying different air conveying velocities or changing solid loading ratios. Under the same fluid conditions, experiments using the same materials with different sizes like our experiments are still scarce.

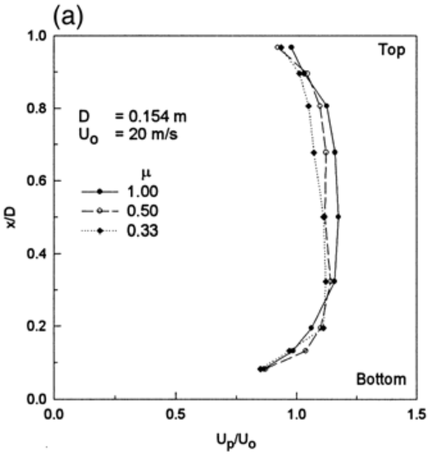

Fig. 4. Effect of solids loading ratio (μ): (a) particle velocity profiles

Figure 5.27 Experimental data of Yilmaz and Levy (2001), obtained by using Optical-Fibre velocimetry

5.5.2 Particle dynamics in the vertical pipe downstream of a right angle elbow

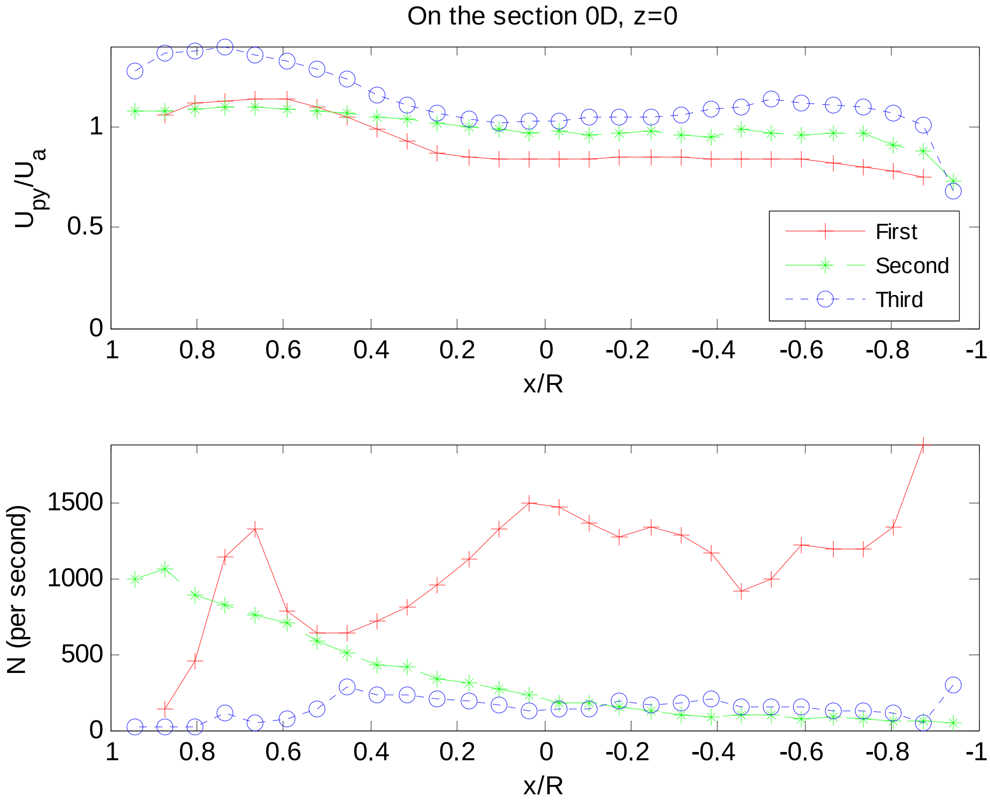

Figure 5.28 **Profiles of the axial particle velocity {U_{py}} and particle number rate {N} along the x axis on the section 0D in the vertical pipe downstream of the right angled elbow. (U_a=10m/s, air conveying velocity; First: glass beads of size less than 50μm; Second: glass beads within the size range 70~110 μm; Third: glass beads within the size range 180~300 μm; R: pipe radius 37.5mm).**

In order to compare with the previous works, Figure 5.28 shows profiles of the axial particle velocity and particle number rate for three type of glass beads along x axis (z=0) from the section 0D of the vertical pipe. The profile data of {U_{py}} were extracted from Figure 5.14, Figure 5.17 and Figure 5.20. The profile data of {N} were obtained from Figure 5.16, Figure 5.19 and Figure 5.22. Here the x positive axis points to the pipe outer wall. The section 0D is about 15mm away from the elbow outlet.

Compared with contours of {U_{py}/U_a} and {ln(N/Σ(N))} in Figure 5.14 to Figure 5.22, the {U_{py}}profile does not illustrate the horseshoe-shaped feature in cross-sectional distribution on the section 0D for three kinds of glass beads. But the profile of each {U_{py}} shows the decreasing tendency from the pipe outer wall to the inner wall (along the x negative axis), which is similar to that observed in the corresponding cross-sectional distributions. In addition, the axial particle velocity of the third type of glass beads is larger than that of the other two types, which indicates the inertial effect on particle velocity, since particles with high inertia should keep their initial velocities rather than easily follow the carrier fluid. As for the profiles of particle number rate {N}, the profile of the second type of glass beads reveals that the dust rope formed in the bend is close to the pipe outer wall. But we can not clearly see the rope from the profiles of the first and third types of glass beads. However, the regions with a high density of particles of the first and third types can be observed on their cross-sectional distributions of {N}.

So far, three previous papers which experimentally study particle dynamics in a vertical pipe behind a pipe bend have been searched. Figure 5.29 shows the profiles of the axial particle velocity and particle concentration at the position 0.1m away from the elbow outlet. These data were measured by Huber and Sommerfeld (1994) who used PDA to study the degree of segregation of glass beads with mean size 40μm under 14 and 21m/s air conveying velocity with solid loading ratio 0.5 in a vertical pipe behind an elbow. Here the pipe outer wall locates at z=0mm. Their experimental data of particle concentration profile display the rope located at the region close to the pipe outer wall and the minimum velocity at the pipe outer wall corresponds to the velocity of the dust rope sliding along the wall. They thought it might be caused by momentum losses from particle-wall and inter-particle collisions. However this is different from that observed in Figure 5.12, which shows that particles within the rope region not only have the maximum particle number rate but also have the higher velocities. The region with the maximum axial particle velocity locates at the inside of the horseshoe shape of the cross-sectional distribution of $\{U_{py}\}$ on the section 0D. This feature is also observed in both Figure 3.20 and 3.21 for air phase experimental data and numerical results. Moreover, glass beads with mean size 40μm or less than 50μm have a low Stokes Number, which indicates that their profiles should show the features of the air phase.

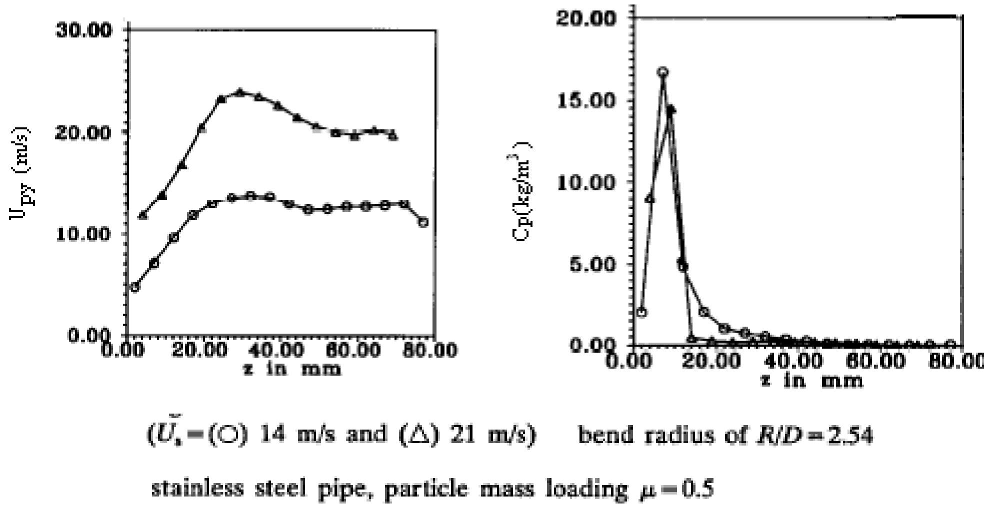

Figure 5.29 Profiles of the axial particle velocity and particle mass concentration (Huber and Sommerfeld, 1994)

Another two experiments were performed by Yilmaz and Levy (1998, 2001). They used a fibre-optic probe to measure time-averaged local particle velocities, concentration and mass fluxes over cross-sections in a vertical pneumatic conveying line following a horizontal-to-vertical elbow under a range of conveying air velocities and solids mass loadings. In their experiments, pulverized coal with mean diameter 75μm and true density 1680 kg/m^3 were conveyed with solid loading ratio 0.33 to 1 under air velocities from 15 to 30m/s. Since their latest experimental data in 2001 included the old results, Figure 5.30 shows their measurement results at the position close to the elbow outlet (z/D=1). Compared with Huber's data in Figure 5.29, the profiles of particle concentration in Figure 5.30 show a high particle mass concentration close to the outer wall (along the x negative axis) for four different fluid conditions. Obviously, this finding is close to our experimental data of particle number rate shown in Figure 5.19. But the profiles of the axial particle velocities are only limited within a short distance x/D less than 0.3 and there is no data for the left space. The authors did not present any reason for this.

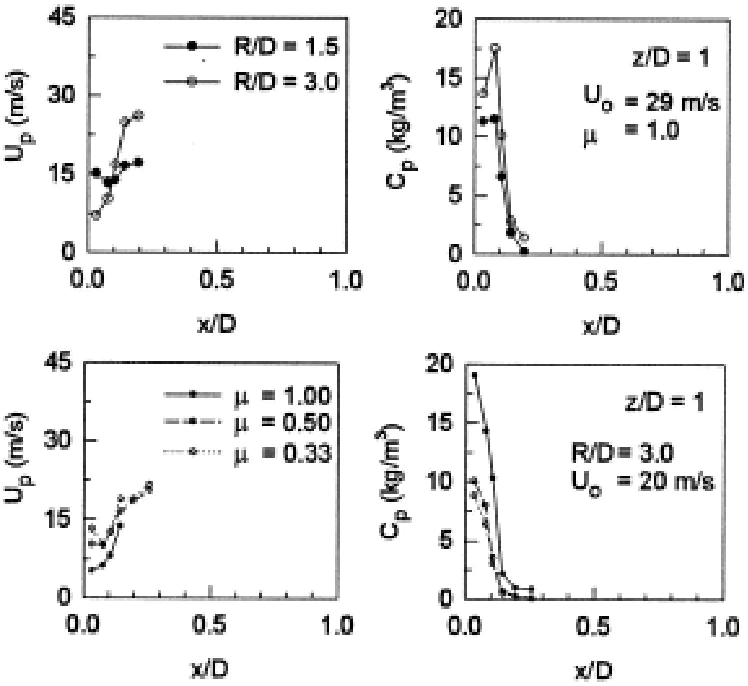

Figure 5.30 Profile of the axial particle velocity and particle concentration at the position of z/D=1 under different fluid conditions (Yilmaz andLevy, 2001)

5.6 SUMMARY AND CONCLUSIONS

Pneumatic conveying of granular materials is one of the most important applications in many industries. It is essential and necessary to characterize particle dynamics in different components of a pipeline to explore the mechanism of pneumatic transport. In this chapter, the extended LDA technique discussed in Chapter 3 was applied to study cross-sectional features of three types of glass beads in a horizontal pipe and in a vertical pipe behind an elbow.

In the horizontal pipe, the experimental data show that the cross-sectional flow patterns of the solid phase in the gas-solid pipe flow (glass beads less than 110μm) can be classified by annular flow describing the axial particle velocity contours and stratified flow characterising particle number rate distribution over a cross-section. However the position of the annular core and the values of iso-lines are dependent on particle size and vary along the fluid streamwise direction. By contrast, these two flow patterns can be still observed for the third type of glass beads (180~300μm), but their characteristics are not clear like those for the other two types of glass beads.

In the vertical pipe after an elbow (R/D=1.3), a horseshoe shape feature has been found on cross-sectional distributions of the axial particle velocity for all three types of glass beads on the section 0D close to the elbow outlet. At the further downstream sections, the horseshoe-shaped feature is gradually distorted until it completely disappears. The distance for total disintegration is about 4D for the first type of glass beads, 2D for the second type and 1D for the third one. As for particle number rate, its cross-sectional distribution on the section 0D shows that a rope is formed at the pipe outer wall where the maximum particle number rate occurs. On the whole, the rope formed by the first type of glass beads can be still observed at the section 6D. For the second type of glass beads, the rope will disintegrate from the section 4D according to the similarities between cross-sectional distributions of $\{U_{py}/U_a\}$ and $\{\ln(N/\Sigma(N))\}$. Overall, the roping characteristic is not obviously shown in the gas-solid flow of the third type of glass beads after the section 0D. All of these indicate that ropes formed from larger particles disperse more easily, for reasons perhaps related to their higher inertia.

Moreover, the current experimental data have been compared with several previous experimental publications. These comparisons reveal that there exists much discrepancy between them. This discrepancy may be caused by possible factors of different instruments and different fluid conditions as well as different experimental rigs. Consequently, further experimental studies will be necessary to measure more granular materials under a range of fluid conditions for understanding the mechanism of pneumatic conveying.

Chapter 6

Visualization and Measurement of Cross-sectional Characteristics of Solid Phase in a Dilute Pneumatic Conveying System

In applications of dilute pneumatic conveying, the two important parameters of particle diameter and solid volume fraction have been intensively studied in numerous experiments and numerical simulations. But local information on their spatial distribution in pipes has scarcely been reported to date, especially over horizontal pipe cross-sections. This chapter presents a video & image processing method of measuring particle diameter and solid volume fraction through analyzing particle tracks and positions in frames of a video. Using a high definition camcorder, the behaviour of the solid phase is recorded when particles cross a pipe cross-section which is highlighted by a light sheet produced by a halogen lamp. On every frame in a video, the instantaneous particle positions, particle diameter and the local solid fraction over the pipe cross section can be extracted. The corresponding time-averaged values can also be calculated through averaging data on all frames in a specific interval. The experimental results suggest that the gas-solid flow in a dilute pneumatic conveying system is always heterogeneous and unsteady. The parameter of particle mass mean size is superior to particle number mean size for statistically describing the unsteady properties of gas-solid pipe flow.

6.1 INTRODUCTION

Pneumatic conveying systems are widely applied to process granular materials in many industrial fields. A pneumatic conveying pipeline system typically consists of horizontal and vertical sections as well as connecting elbows. Consequently, there exist different physical phenomena in different parts of a pipe line. For example, gravity settling occurs in horizontal pipes. Roping happens in an elbow due to a centrifugal force which makes particles concentrate into a rope. Obviously, gas-solid pipe flow is so complicated that understanding of its mechanism is still under development. Many features have still to be investigated, especially local information on solid phase velocity and particle diameter and frequency distribution over the pipe cross-section. These parameters are important in the design of systems to ensure even solid distribution between a main duct and the branches into which it divides. For example, in Co-firing applications, estimating the spatial distributions of pulverized coal and biomass granular before a splitter is an essential step in determining how to split mixed fuel in a common transportation pipeline.

In Chapters 3, 4 and 5, we extended the current Laser Doppler Anemometry (LDA) technique for pipe flow measurement and used it to explore particle behaviour over a series of cross-sections along the horizontal pipe. The experimental results demonstrated two kinds of cross-sectional flow patterns: annular structure and a stratified configuration, described by particle velocity and particle number rate respectively. Since LDA is a mono-point instrument with a high sample rate, it only provides information at a single spatial point in a flow field. Consequently, the measured cross-sectional patterns of solid phase measurements represent particle time-averaged characteristics with the assumption that gas-solid pipe flow is steady in time. However, this assumption ignores flow phenomena dominated by spatial structure, which must be determined by measuring fluid parameters on a whole field simultaneously. It is a cumbersome task to measure a parameter over a whole field by using a point-wise instrument. In order to investigate simultaneous particle behaviour over a pipe cross-section, using a light-sheet technique with image processing is a good choice. This is a common flow visualization method. In this technique, a light beam (laser or other light source) is formed into a sheet using cylindrical lenses. This light sheet is used for sectioning and illuminating flow to form a planar measurement region where fluid characteristics can be extracted from analyzing videos or photos recorded by a CCD or camera.

The aim of flow visualization is to make flow patterns visible by adding smoke, oil or fine particles to trace fluid motion. This kind of technique has had a long development history. For example, Reynolds demonstrated that pipe water flow could be classified as laminar or turbulent by its Reynolds Number. This result was deduced through observing the dye streak when some dye was injected into a pipe flow. Another well known experiment was conducted by Ludwig Prandtl, who investigated unsteady separated flows behind wings and other objects in a water tunnel by utilizing flow visualization techniques (Sabersky et al, 1999). However, results obtained by early flow visualization techniques were qualitative descriptions of the flow field rather than quantitative data such as flow velocity. With progress in the hardware of optics and electronics as well as novel theories or algorithms in fluid mechanics and signal processing over the past two decades, some traditional visualization techniques have been developed or are under development into newer advanced instruments like Particle Image Velocimetry (PIV), Particle Track Velocimetry (PTV) and Electrical Capacitance Tomography (ECT). which can be employed for quantitative measurement of complex instantaneous velocity fields not only in a single phase flow but also in multiphase flows (Dyakowski et al., 2000; Datta et al., 2007).

In previous literature related to flow visualization applications in gas-solid pipe flow, Hesselink et al. (1998) reviewed the influence of digital computers on the classical methods of flow visualization. He thought that the most striking and promising of these techniques were optical tomography and gradient imaging, which allowed the interior of flows to be probed and visualized using line-of-sight techniques applied from different directions. On the other hand, sheet-illumination techniques provided powerful means to visualize the interior of flows. Particle tracking was an intuitively attractive method for making velocity measurements, but care should be exercised when attempting to determine derivative data.

So far, developing and applying tomography techniques by using different image media, such as ultrasonic, nuclear magnetic resonance, γ-ray/X-ray, electric capacitance/resistance, are still current topics in fluid measurement. As for ultrasonic tomography, Brown (1996) developed a laboratory device to identify the gas-solid flow mode in a pipe. His experimental results indicated that a measurement frequency in excess of 1 MHz and particle diameter greater than 1mm were necessary. Warsito et al. (1999) and Utomo et al. (2001) also used this technique for measuring the time-averaged cross-sectional distribution of gas and solid holdups in a slurry bubble column. A doughnut-shaped macroscopic flow scheme was observed to represent the cross-sectional distributions for the gas holdup. Particles mainly distributed to the centre of the doughnut in the column. Correspondingly, Dyakowski et al. (2000) overviewed the principle of electrical tomography methods and their applications for investigating, monitoring and controlling wet and dry granular conveying systems. Using electrical capacitance tomography (ECT), Rao (2001) investigated instantaneous and time-averaged concentration distributions of large particles over a pipe cross-section under different flow regimes. Even in homogeneous air flow, the contour of particle concentration is like a stratified flow. In his experiments, polyethylene particles (mean size 2.8mm with 1123 kg/m^3 density) were transported in a 40.4mm PVC pipe by conveying air at 28.6m/s velocity. Laurent et al. (2002) proposed a direct approach to discriminating annular from stratified flow through analyzing capacitance data rather than processing the images recorded by ECT. Its general idea for flow pattern classification relied on finding geometrical properties in a frame corresponding to a set of capacitance measurements. Azzopardi et al. (2008) used a twin-plane ECT system to monitor the flow rate of pulverised coal (mass median diameter 61μm) transported by air in 36.8mm diameter pipe. The experimental results indicated that there were two types of systematic fluctuations in the time series of mass flow rate and concentration and the cross-sectional distribution of solid showed that the coal was concentrated around the pipe wall. There are also many other papers investigating the influence of factors such as wall roughness, pipe diameter and solid mass loading on cross-sectional particle concentration profiles, which are summarized by Fokeer et al. (2005) and Fuchs et al. (2007) . Since reconstruction algorithms used for inverting a set of measured data to map material distribution inside a sensor are a group of nonlinear equations, results deduced from linear approximations to the nonlinear equations would result in poor accuracy.

As well as tomographic techniques, there are also many studies of gas-solid pipe flow using digital imaging methods, which can be applied to directly extract information like particle diameter, particle concentration and their distribution from one or series of gas-solid flow images. Among these studies, Huber et al. (1994) introduced a laser-light sheet technique to measure particle concentration distribution over a whole pipe cross-section through analyzing the light intensities scattered by particles on images taken by CCD. Since the light sheet intersected the pipe at 45º with respect to the pipe axis, the experimental data were not over a right angled cross-section. Kadamibi et al. (1998) extended the Particle Imaging Velocimetry (PIV) technique for particle diameter measurement and studied the Gaussian distributed intensity variation across the depth of the light sheet and the optical depth of field. For a given PIV light sheet illumination setup, the point spread function of the optical system should be less than 10% of the imaged particle diameter. Additionally, it is essential to ensure an imaged particle occupies at least 3 pixels to obtain an accurate size estimate. Similarly, Miyazaki et al. (1999) also used PIV to study particle motion (glass beads, 2.9~3.9mm) in gas-solid spiral flow in a horizontal tube and Li et al. (2000) investigated particle behaviour (polyvinyl chloride and polyethylene particles with mean size 3.13mm and 4.26mm respectively) in a horizontal dilute swirling pipe flow. His experimental results indicate that the particle concentration profiles exhibit symmetric distributions with respect to the pipe axis and a higher particle concentration appears near the wall in the acceleration region. Morimoto et al. (2003) proposed a tuft grid method combined with a image processing technique to visualize the characteristics of a pneumatic type ultra fine powder classifier. Caicedeo et al. (2003) studied bubble characteristics as function of the gas velocity in a two-dimensional fluidized bed by using digital image analysis. Cater et al. (2005) introduced a method of using low-cost CCD combined with an electrostatic velocity meter to measure particle diameter, size distribution and mass flow rate in a dilute pneumatic conveying system. The features of particle-wall collision and the bouncing of particle during pneumatic conveying in the dilute phase have been visually analyzed by means of digital image techniques (Sommerfeld et al. 1999; Vasquez et al. 2008).

According to the above discussions, it is clear that only a few studies have been dedicated to measuring cross-sectional characteristics of the solid phase in gas-solid pipe flow, especially there is a lack of papers describing the measurement of particle spatial distribution of the solid phase over a whole pipe cross-section. In this chapter, a video & image processing method that instantaneously measures particle diameter and particle concentration over a horizontal pipe cross-section as well as the characteristics of their time-averaged values by using a high definition camcorder and a powerful halogen light box, is introduced.

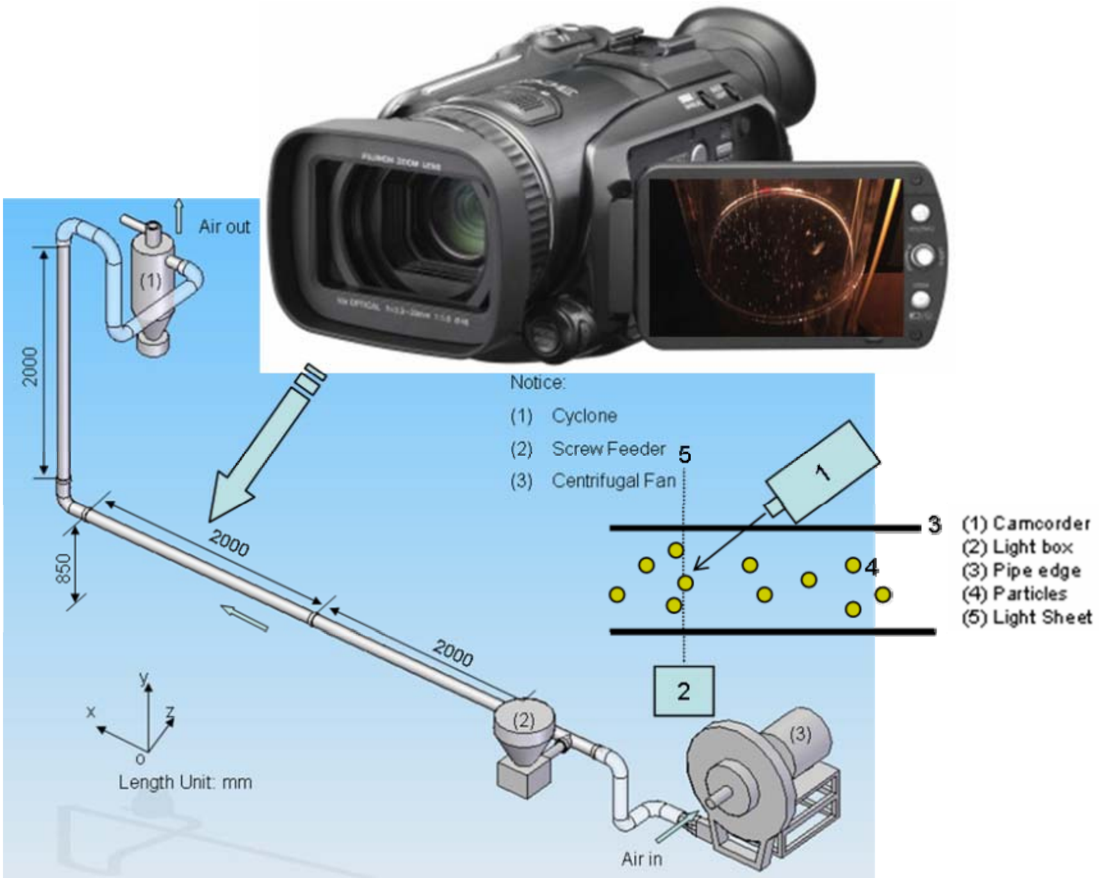

Figure 6.1 Sketches of experimental rig and optical arrangement for experiments

6.2 EXPERIMENTAL SETUP AND FLOW CONDITIONS

Figure 6.1 sketches the experimental rig in which all the experiments were performed. The pipeline of the apparatus includes a 4m long horizontal section connected to a 2m long vertical pipe through a horizontal-to-vertical elbow. One T-type piece was installed to connect a screw feeder with the pipeline. In order to lessen the effect of electrostatic charging, all pipe metal connectors are earthed.

The air flow provided by a centrifugal fan varies from 5~42m/s. Under the condition of 10 m/s air conveying velocity, the maximum value of solid loading ratio is about 1.6% for glass beads (size within 180~300μm, density 2550 kg/m^3) injected by the screw feeder. The measurement region is located on a horizontal pipe cross-section 240mm upstream of the elbow's inlet or 3.60m downstream from the screw feeder injection position. When gas-solid flow passes through this section, particles of the solid phase are illuminated using a sheet of light approximately 2mm thick produced by a 500w quartz halogen lamp box. The light rays are arranged to be perpendicular to the pipe axis with the sheet cutting across the pipe. Particles within the light sheet are imaged using a high definition JVC GZ-HD7 camcorder, which is mounted on a tripod to focus on the measurement region centre. The camcorder axis intersects the light sheet at about a 45° angle, which is depicted in the sub diagram of Figure 6.1.

The JVC GZ-HD7 is a tapeless camcorder and has the features of 10× optical zoom, 1/5 inch CCD sensor, optical image stabilizer and 2.7 inch colour LCD It can record 25 high quality frames (1920×1080 pixels) per second. Its shutter speed varies from 1/2 to 1/4000th of a second and the aperture from f/1.8 to f/8.0. It has also a 60GB unit hard disk which can store five hours video at full high definition. The video is stored in extended MPEG-2 transport stream files, commonly known as M2TS, which is defined as a TOD file extension in JVC GZ-HD7. Here, MPEG stands for Moving Pictures Expert Group, the committee of industry which created the standard. Transport stream (M2TS) is a communication protocol for audio, video and data which is specified in MPEG-2, and which makes extensive use of motion compensated prediction to eliminate redundancy. The most significant extension of MPEG-2 over MPEG-1 is an improvement in options within a picture that can be used to perform motion compensated prediction of interlaced signals. MPEG-1 treats each picture as a collection of samples from the same moment in time (known as frame-based coding). MPEG-2 has modes in which the data can either be predicated using one motion vector to give an offset to a previous frame or two vectors giving offsets to two different fields (Digital TV Group, 2008). Therefore, using JVC GZ-HD7 will obtain more raw video data with high spatial resolution.

In this study, f1.8 aperture and 1/250s shutter speed was empirically selected for our experiments. When particles passed through the exposed area, a two-minute video of their behaviour was recorded for every flow condition. Instantaneous or time-averaged local information on particle diameter and particle concentration was extracted from these videos. In the following sections, we will discuss the related video & image processing algorithms and the experimental results.

6.3 VIDEO & IMAGE PROCESSING SYSTEM

Since data rate is one of the key parameters in transmitting a series of high definition frames, the format of Moving Picture Experts Group-II (MPEG2) is implemented to code the particle videos in the JVC GZ-H7 camcorder. The procedure of data processing in this study will be divided into two main routines of video decoding processing and image processing respectively, which are sketched in Figure 2. Once the experimental videos have been obtained, the first step is to decode the MPEG2 videos into Audio Video Interface (AVI) format (Clarke et al. 1995). An AVI video consists of series of uncompressed bitmap frames (BMP images) in which the coordinate of a pixel is directly matched to the corresponding point in the measurement region. Then an individual frame or several consecutive frames in a video can be extracted for further image processing at the next stage.

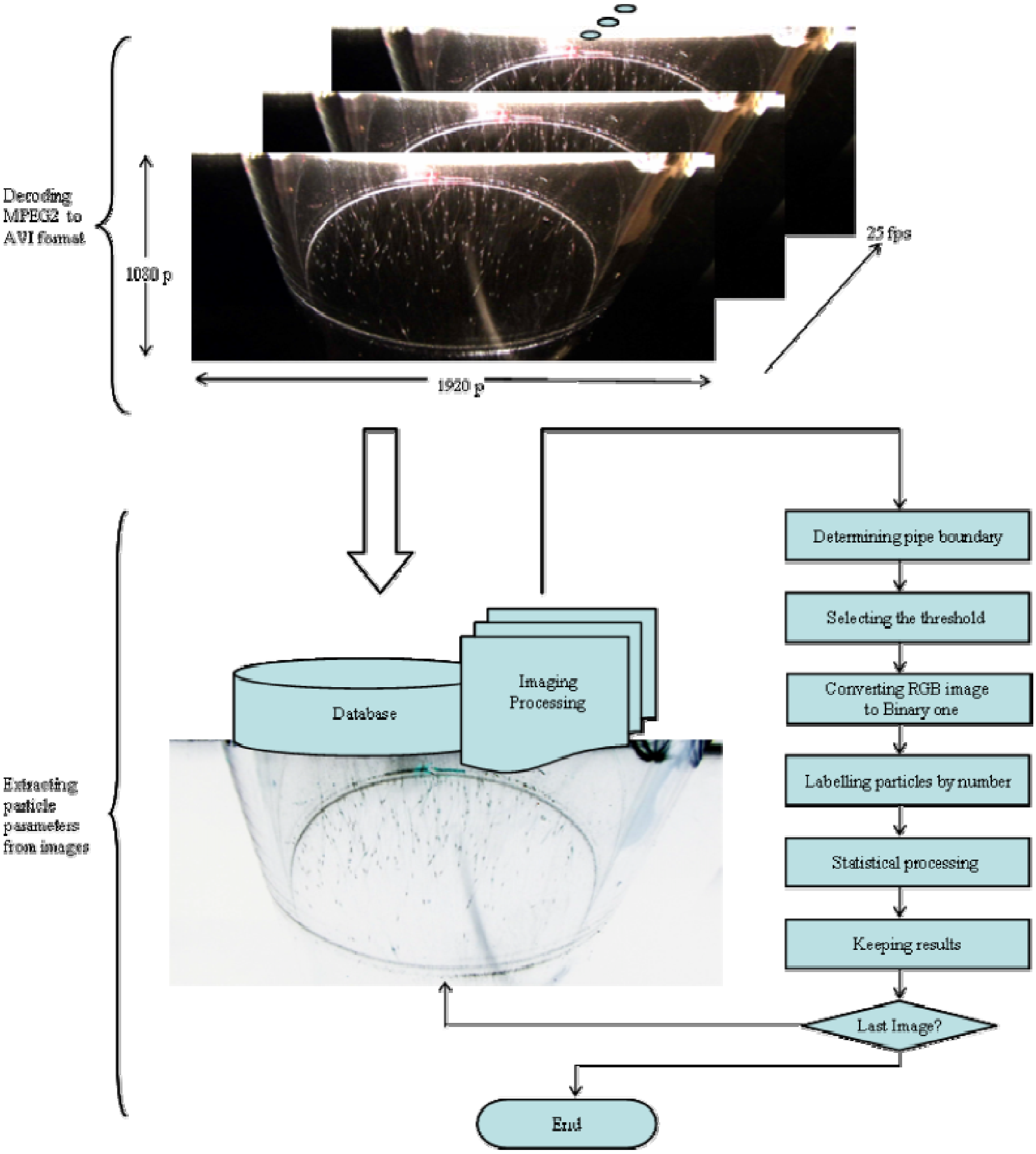

Figure 6.2 Flow chart of video and image processing

In general, all video & image algorithms used in this research are implemented using

MATLAB7.0 with Image Processing Toolbox, also incorporating some routines described in Nixon (2002). In the procedure of processing a single image, the first step is to determine the boundary or pipe wall so as to reduce the noise caused by the data outside the pipe, since the measurement region is only one part of a frame. Then much of the other unwanted noise can be filtered by subtracting a reference image, which is taken before injecting particles into the pipe. In this way, only the data within the boundary or inside the pipe is kept and the rest is set to be background. According to Otsu's method (1979), the greyscale image converted from an original true colour frame is changed into a binary image by implementing Otsu's operator. This produces a binary image (white particle regions on a black background) which contains particle information ready for sizing and counting. In order to identify every separate particle, each region of white pixels will be labeled with a different number. The number of pixels contained in each labeled region is equivalent to the projected track of a particle's motion in the measurement region over 1/250s.

6.3.1 Principle of decoding a MPEG-2 video

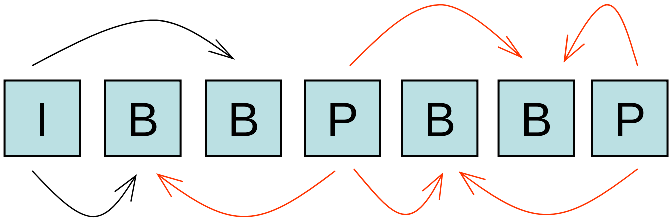

Figure 6.3 Three types of pictures in a video stream (red colour arrow means bidirectional)

The format of the high definition video recorded by JVC GZ-HD7 conforms to MPEG-2 high profile and is stored in extended MPEG-2 transport stream files. JVC provides the software called Cyberline PowerDirector 5 NE, which is used to convert transport stream files to program stream files in standard MPEG-2 format, which can be replayed and edited by using common algorithms for MPEG-2. This is a popular coding and decoding standard for digital compression or decompression of audio and video signals. A MPEG-2 video removes both spatial and temporal redundancies by using compression algorithms based on the Discrete Cosine Transform for motion estimation and compensation. There exist three kinds of frames in a MPEG-2 video stream (as shown in Figure 6.3), which are Intra-coded (I), Predicative-coded (P) and Bidirectionally predicated-coded (B) pictures. I-pictures are coded without reference to other pictures. This is periodically applied to provide access points where decoding can begin. P-pictures represent the difference between the current picture and the reference picture and are usually compressed for reducing video stream redundancy. In addition, B-pictures can use the previous and next I- or P-pictures for motion-compensation, and offer the highest degree of compression (Tudor, 1995).

In a MPEG-2 video, its stream is organized as a Group of Pictures (GOP) which are composite of I-, P- and B-pictures. A typical I:P:B picture ratio in a GOP is 1:3:8, and a typical display order of GOP is:

$$B_1\ B_2\ I_3\ B_4\ B_5\ P_6\ B_7\ B_8\ P_9\ B_{10}\ B_{11}\ P_{12}$$

where the subscripts mean positions in the original video. The encoder reorders the pictures into the following sequence:

$$I_3\ B_1\ B_2\ P_6\ B_4\ B_5\ P_9\ B_7\ B_8\ P_{12}\ B_{10}\ B_{11}$$

Under this configuration, if the decoder encounters a P-picture, its motion prediction is with respect to the previously decoded I- or P-picture; if the decoder encounters a B-picture, its motion prediction is with respect to the previously two decoded I- or P-pictures.

In an encoding process, each picture in a video stream is divided into 16×16 macroblocks, which consist of a 2×2 array of blocks (each of which contains an 8×8 array of pixels). Macroblocks specify colours using a luminance channel to represent saturation (colour intensity), and two chrominance channels to represent hue. A red, green and blue (RGB) signal can be equivalently expressed as luminance (Y) and chrominance (UV) components. For a standard definition video, MPEG-2 streams are encoded in the common sampling structure of 4:2:0, which means a macroblock using four blocks for the luminance channel and one block for each of the two chrominance channels. Each of the I-, P- and B-pictures are processed by a 2-dimensional Discrete Cosine Transform (DCT), which can separate a picture into parts with varying visual importance. The DCT coefficients are quantized to reduce the number of bits needed to represent them. The run-length encoder scans the DCT matrix in a zig-zag order to consolidate the zeros in the matrix. Finally, the output of the run-length encoder, motion vector data, and other information, are Huffman coded to further reduce the average number of bits per data item. The compressed stream is sent to the output device (Drake et al. 2005).

Correspondingly, the process of decoding a MPEG-2 video is essentially performed using the inverse encoding process. The input stream is Huffman and run-length decoded, resulting in quantized Discrete Cosine Transform (DCT) matrices. From the coded video stream, it reconstructs the I-pictures. Then P- and B-pictures are reconstructed by using the corresponding I-pictures, additional coded data and motion vectors. As a result, each pixel in an uncompressed frame in a decoded MPEG-2 video has a clear relationship with a spatial position. These uncompressed frames can be extracted from the AVI video file for further image processing.

6.3.2 Strategy for processing large volume of uncompressed frames (AVI files)

With the dramatic volume expansion of uncompressed frames in a video file, technology is needed to effectively extract or browse a specific segment in a short time. The first strategy is to eliminate audio information for increasing video rate during decoding a MPEG-2 video. The second strategy performed is to cut a thirty-seconds part in a two-minute video for each set of fluid conditions, which is carried out during converting a JVC TOD file into the standard MPEG-2 video. The file size of a 30s MPEG-2 video is usual about 90 Mbytes. Its corresponding decoding file size is about 900 Mbytes. Such a large volume uncompressed file would consume much time in being loaded into computer memory and being indexed by frame number or a specific time or interval. The third strategy is to split a thirty-second uncompressed AVI file into 30 sub files kept in Matlab mat data format, which will benefit in quickly and conveniently loading a video data file for the imaging process. Each sub-file will only accommodate one second worth of data of 25 frames according to the JVC GZ-HD7 recording rate of 25 frames per second. Thus, we will obtain about 750 frames with high definition (1920×1020 pixels) at each measurement section within thirty seconds.

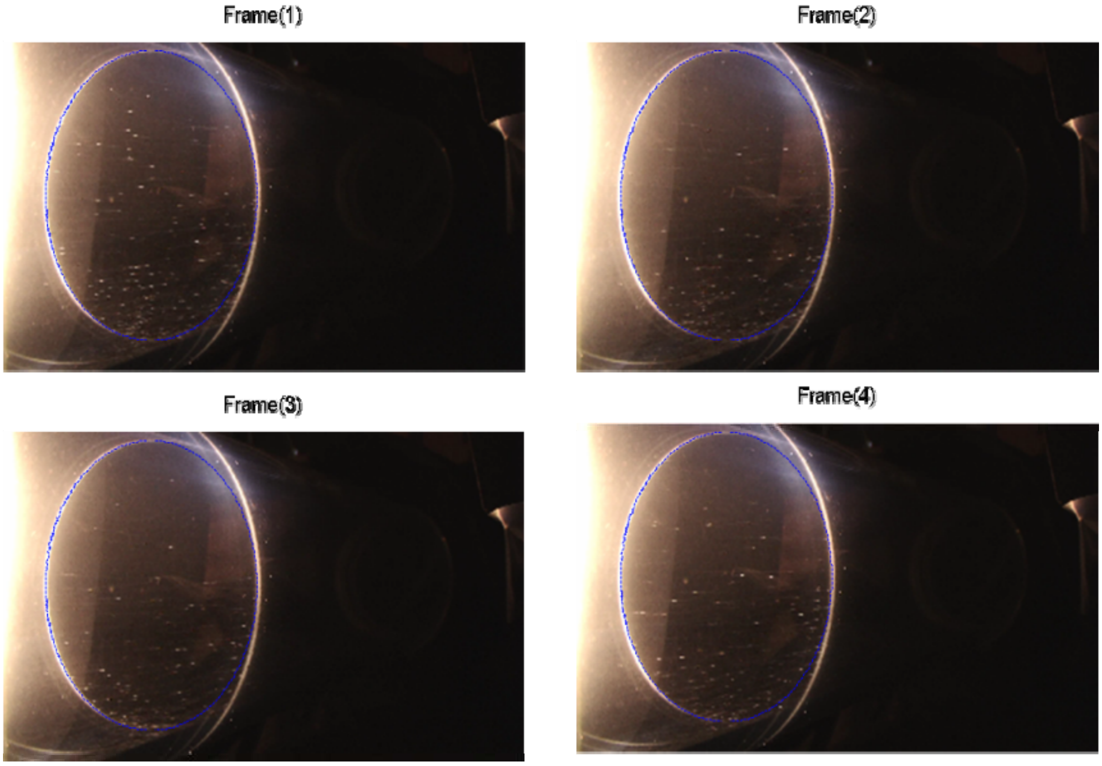

Figure 6.4 Four specific frames in an AVI video

In these experiments, all measurements were conducted in the rig shown in Figure 6.1. Glass beads within the range 180~300 μm (manufacturer's specification) were conveyed in ϕ75mm glass pipes by an air superficial velocity of 10m/s. Figure 6.4 shows four typical frames (5th, 10th, 15th and 20th) in a one-second video consisting of 25 frames on the pipe cross-section 3.70 m away from the feed position. All four frames clearly display the instantaneous spatial distribution of solid phase over the cross-section. Comparing the four frames with each other, we clearly observe that particle number is greater in the pipe lower half than in its upper half. This is the gravity settling phenomenon in horizontal pipes. However, there are still some particles in the pipe upper half, which indicates that the particles are in a state of dynamic suspension rather than irreversibly depositing on the pipe bottom after 3.70m (which would happen if they were simply settling under gravity.). Consequently, these pictures show the heterogeneous nature of solid phase flow over a pipe cross section. In addition, the total particle number is also observed to be apparently different from frame to frame. This denotes the unsteady characteristic of gas-solid flow in time over the pipe section. All of these qualitatively demonstrate the heterogeneous spatial and unsteady temporal nature of gas-solid pipe flow in a dilute pneumatic conveying system. In the next section, we will show the extraction of quantative information from these uncompressed frames.

6.3.3 Particle diameter and spatial position measurement

In the above section, we have discussed how to decode a MPEG-2 video and obtain the corresponding uncompressed frames which are high definition pixel pictures. Each pixel in a frame is mapped to a spatial position on the pipe cross-section which is illuminated by the light sheet. Figure 6.4 shows four sample uncompressed frames in an AVI video. Before extracting particle information from these pictures, it would be better to manually determine the pipe inner surface edge which forms the boundary of measurement region. With regard to the cross-section on each frame of Figure 6.5, it is clear that the white colour curves which are highlighted by the light sheet are the pipe edges. Since we use a halogen light rather than a laser light source, there exists a small divergent angle for the light sheet, which results in two white curved segments rather than one continuous oval curve encircling the section boundary. In order to eliminate noise from outside the pipe, a boundary template is created manually through setting data as zero for each pixel outside the pipe and setting data as 1 for each pixel inside the pipe. In this way, an uncompressed frame like frame (1) in Figure 6.4 multiplied by the boundary template results in the picture as shown in Figure 6.5. Thus the measurement region of 850×950 pixels can be separated from the entire picture of 1920×1080 pixels under the current optical arrangement in our experiments. Each frame in a video will be implemented by a logic AND with the boundary template to obtain the data only within the measurement region box.

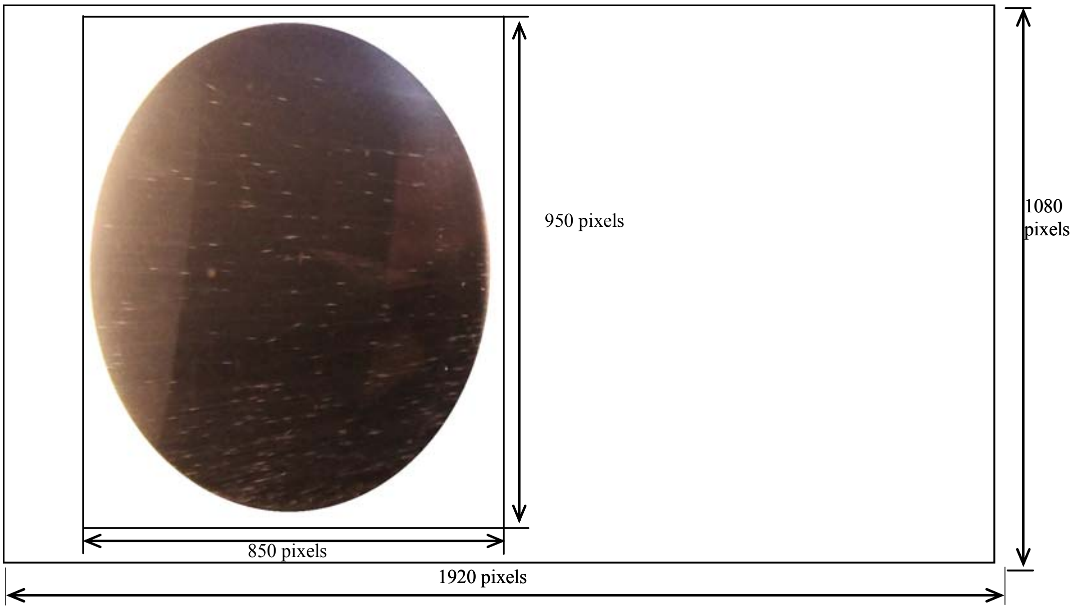

Figure 6.5 The region of the pipe cross-section on a frame

With respect to the sub image within the measurement region in Figure 6.5, it is a true colour picture which is stored in MATLAB as a three dimensional array that defines red (R), green (G), and blue (B) colour components for each individual pixel. The colour of each pixel is determined by the combination of the red, green and blue intensities stored in each colour plane at the pixel's location. Observing particle images in Figure 6.5, we can see that particle images are much brighter and close to white. In contrast, the colour of the positions with no particle tends towards black. Therefore, it is convenient to separate particles from the background in the picture according to their luminance information rather than their colour data. The matrix of the colour picture in RGB space will be converted into the space of luminance (Y) and in-phase chrominance (I) as well as quadratic chrominance (Q) by using equation (6.1) (Bovik Al, 2000).

$$\begin{bmatrix} Y \\ I \\ Q \end{bmatrix} = \begin{bmatrix} 0.299 & 0.587 & 0.114 \\ 0.596 & -0.275 & -0.321 \\ 0.212 & -0.523 & 0.311 \end{bmatrix} \begin{bmatrix} R \\ G \\ B \end{bmatrix} \tag{6.1}$$

If all the components of the I and Q matrixes are set to zero while retaining the luminance matrix Y, the true colour sub-image will be converted to a greyscale one. Figure 6.6 shows the colour sub-image of the measurement region and its corresponding grayscale picture converted by using Equation (6.1).

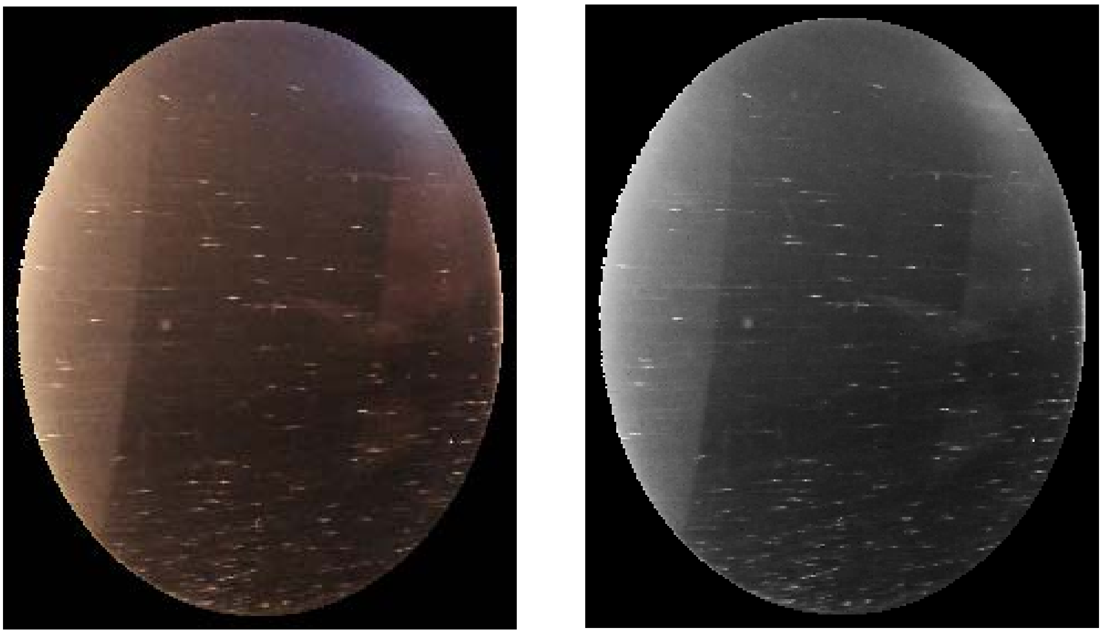

(a) color image (b) gray image

Figure 6.6 Particle images on the pipe cross-section

Since digital images are prone to a variety of types of noise due to electronic transmission or other processes, enhancement algorithms like the Wiener filter (Lim et al. 1990) have been used to reduce image noise and increase particle contrasts in the picture for facilitating the extraction of particle information. The Wiener filter is an adaptive filter which uses a pixelwise adaptive method based on statistics estimated from a local neighbourhood of each pixel. Its algorithm can be described as

$$\begin{aligned} \mu &= \frac{1}{NM} \sum_{n_1, n_2 \in \eta} a(n_1, n_2) \\ \sigma^2 &= \frac{1}{NM} \sum a^2(n_1, n_2) - \mu^2 \end{aligned} \qquad (6.2)$$

where η is the N-by-M local neighbourhood of each pixel in the image A in which a is one element. Using the estimates of equation (6.3), a pixelwise Wiener filter can be created.

$$b(n_1, n_2) = \mu + \frac{\sigma^2 - \upsilon^2}{\sigma^2} (a(n_1, n_2) - \mu) \qquad (6.3)$$

where ν^2 is the noise variance. Its value is calculated from averaging all the local estimated variances in a frame. Figure 6.7 (a) shows the results of the gray image in Figure 6.6(b) denoised by a Wiener filter.

Observing the raw images in Figure 6.6 as well as the denoised image and Figure 6.7(a), we still notice that the background of each image is heterogeneous and is divided into a three striped regions with different brightness. On the left and right side of the images, the brightness of the background is much higher than that in the field between two sides. This results from the optical arrangement for the measurement system in practice. Consequently, we must reduce the effect of an inhomogeneous background on converting a greyscale image to the binary one. In other words, the heterogeneous background should be separated from the particles in an image, which can be realized by using a Median Filter (Lim et al., 1990). The Median Filter is a nonlinear operation which is more effective than convolution for reducing "salt and pepper" noise while preserving edges. Since fine particles are pneumatically transported in the dilute phase, their images in a picture can be considered as some kind of noise like "salt and pepper". When an m-by-n Median Filter is performed on an image matrix in two dimensions, each output pixel contains the median value in the m-by-n neighborhood around the corresponding pixel in the input image (Nixon et al., 2002). As a result, Figure 6.7 (b) shows the corresponding result of processing the denoised image (Figure 6.7 (a)) by using a 25 × 25 Median Filter. Using this filter, we have obtained a separated background through removing particle images in the denoised picture of Figure 6.7(a). It is clear that the separated background image still keeps its original features.

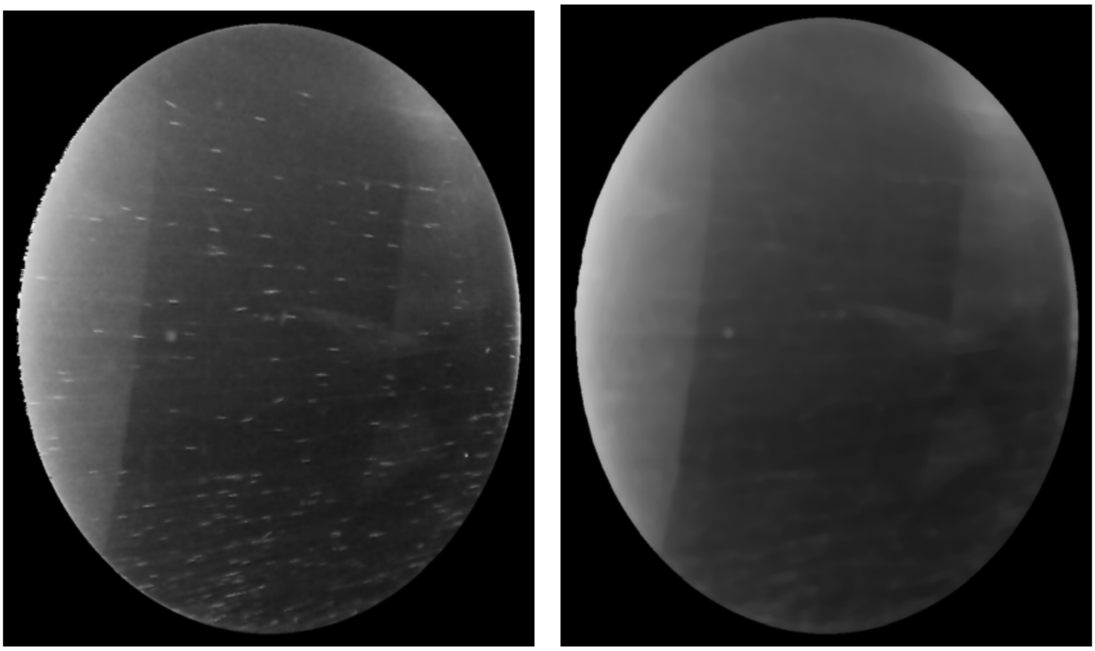

(a) The denoised image (b) The separated background

Figure 6.7 Denoising the image (a) and separating the background (b)

Subsequently, when the denoised image of Figure 6.7 (a) has its separated background image Figure 6.7(b) separated, the subtraction residue is shown in Figure 6.8 (a) in which, while the heterogeneous background was removed, we have obtained most of particles with some segments of the pipe edge or the boundary of the cross-section. Since the noise resulting from shadows and variant illumination in Figure 6.7 (a) has been eliminated through the above subtraction process, the entire image of Figure 6.8 (a) can be converted from a greyscale image to the binary one by using an optimal thresholding process. Otsu’s method (Otsu, 1979) is one of the most popular techniques of optimal thresholding to automatically perform histogram shape-based image thresholding or reduce a greyscale image to the binary one. Essentially, this technique maximizes the likelihood that the threshold is selected so as to separate the image between an object and its background. This is achieved by choosing a threshold level that gives the best separation of classes, for all pixels in an image. The image to be thresholded is assumed to include two kinds of pixels which are classified as foreground and background respectively. Then it calculates the optimum threshold separating those two classes so that their combined spread (within-class variance) is minimal. Figure 6.8 (b) shows the corresponding binary image of Figure 6.8 (a) thresholded by Otsu’s method. Comparing Figure 6.8 (b) with Figure 6.8 (a), we can see that particle images are highlighted in a homogeneous black background.

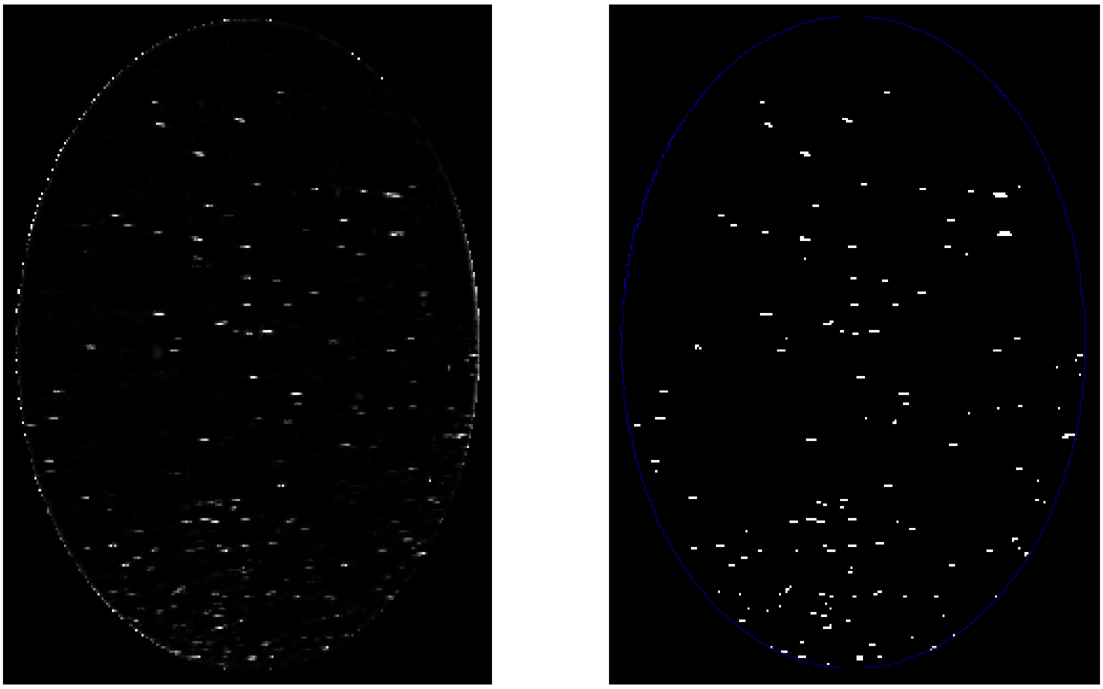

(a) Eliminating the background

(b) The binary image

Figure 6.8 The image with its background subtracted (a) and its binary image (b)

So far, the binary image as shown in Figure 6.8 (b) has been obtained and is suitable for applying quantification algorithms to extract essential particle features such as shape, size and spatial positions. Since a particle taken by CCD is represented as a collection of bright pixels in an image, it can be classified by object descriptors which are used to describe the properties of the group of pixels forming a particle image. Two object descriptors of Region and Shape, which characterize the arrangement of pixels within the area and the configuration of pixels in the perimeter or boundary respectively, are used to describe an object. A region usually describes interior points which are surrounded by a boundary or perimeter which is also often called the region's contour or shape. A shape can be traced by quantifying the relative position of consecutive points on the boundary of a region. Thus, the key point for two descriptors lies in obtaining particle contour or shape.

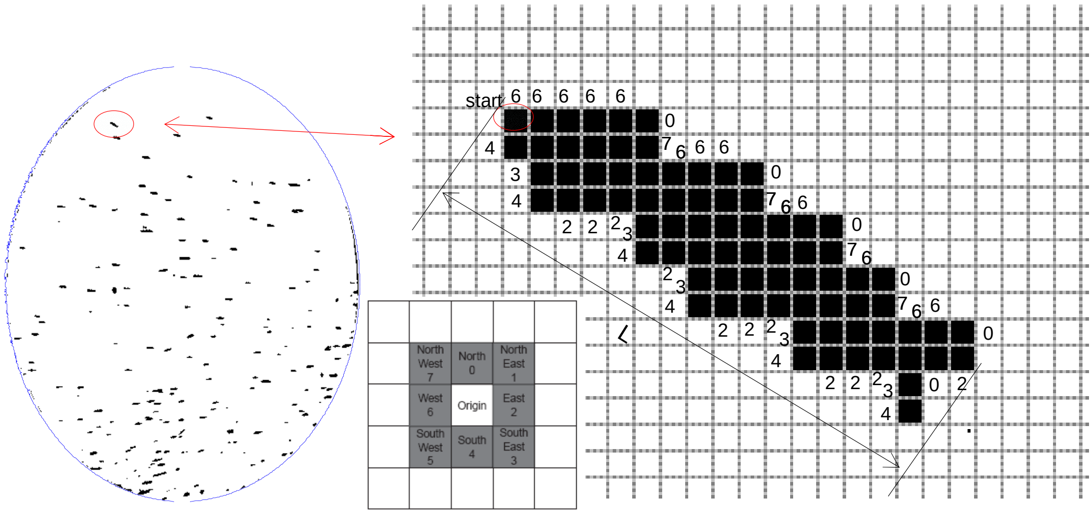

(a) Particle raw image (b) Connectivity in Chain Codes (c) Particle scaled image

Reference point: start (x, y)

Chain codes =

{4,3,4,2,2,2,3,4,2,3,4,2,2,2,3,4,2,2,2,3,4,0,2,0,6,6,7,0,6,7,0,6,6,7,0,6,6,6,7,0,6,6,6,6,6}

Figure 6.9 Particle sample chain codes with 8-way connectivity template

The method called the chain code technique, which stores the relative co-ordinates between consecutive pixels, achieves the shape of a region by analyzing each point on the boundary in sequence and assigning a code to denote the spatial direction between two adjacent points. For 8-way connectivity, one pixel has eight possible relative relationships with its neighbors. The relationship template is shown in Figure 6.9 (b) where each number of 0~7 is encoded as one of the major compass directions. Given a complete border which is equivalent to knowing a set of connected points, if we define the first left-top point of a particle as the start position or the reference point, the chain code of the particle border is formed by concatenating the number that designates the direction of the next adjacent points along an anti-clockwise direction. That is, given a pixel, the successive direction from one pixel to the next pixel becomes an element in the final code. This is repeated for each point until the start point is reached again, when the shape is completely analyzed. For example, the image of a particle track taken by CCD in Figure 6.9 (a), which is inverted from Figure 6.8 (b), is enlarged for visualizing its pixel group as shown in Figure 6.9 (c). The particle's first pixel (P_0) on the left top position is marked as "start" which is the reference point of encoding the particle border chain. According to the 8-way connectivity template shown in Figure 6.9 (b), the direction from the start point (P_0) to the next (P_1) is south (i.e. code 4) on an anti-clockwise loop, so the first element of the chain code describing the shape is 2 . Then the direction from point (P_1) to the next anti-clockwise adjacent point (P_2) is southeast (code 3), hitherto the next element of the code is 3. This coding is repeated until the 44th point (P_{44}), which is connected westwards to the starting point (P_0), so the last element (the 45th element) of the code is 6. Subsequently, the total area, perimeter and geometric centre bounded by the Chain Codes can be deduced.

In Figure 6.9 (c), the group of black pixels forms the area of the sample particle trajectory within 1/250s (CCD shutter speed) projected on the pipe cross-section. In order to simplify the question and avoid more complicated morphological analysis, the shape of a particle trajectory is an approximate rectangle whose area (S) is equal to the product of the trajectory length (L) and particle diameter (D_p). It can be defined as

$$S = L \times D_p \qquad (6.4)$$

For example, the total area (S) of the particle trajectory in Figure 6.9 (c) is counted as 78 square pixels. If the coordinate of the start point is assumed as (0, 0) pixel, the point at the right bottom of particle trajectory locates at (17, 9) pixel. Thus the length of the particle trajectory is figured out by equation (6.5)

$$L = \sqrt{(17-0)^2 - (9-0)^2} \approx 19.24 \qquad (6.5)$$

Thus, the particle diameter is equal to

$$D = {}^{S}\!/_{L} = {}^{79}\!/_{19.24} \approx 4 \qquad (6.6)$$

And the coordinate of the area locates at (17-0, 9-0)/2 = (9, 5) related to the start point. Then the local concentration of solid phase can be calculated too, which will be introduced in the next section for applying the above discussed algorithms for extracting particle features on a whole pipe cross-section.

6.4 RESULTS & DISCUSSION

The experiments were conducted over a pipe cross-section which was 240mm upstream of the elbow inlet or the 3.60m downstream of the particle injection position in the rig (shown in Figure 6.1). Glass beads of size 180~300μm and density 2550 kg/m^3 (manufacturer's specification) were conveyed in ϕ75mm glass pipes by an air superficial velocity of 10m/s. For each fluid condition, we actually recorded two minutes video in which 30s data were cut for particle image analysis. Therefore, a total number of 25×30=750 frames will be used for extracting particle information, according to the sample rate of JVC GZ-HD7 (25 frames per second). In section 6.3.2, we have displayed a group of four sample frames (5th, 10th, 15th and 20th frame) in Figure 6.4. These four frames were extracted from a one-second MPEG-2 video which was also one thirtieth of the video data. Observing these four frames, we can clearly and directly see some qualitative features such as gravity settling, which results in a higher particle number density in the pipe lower half of the pipe and a more dilute suspension in the upper half. Moreover, particles are distributed over the whole pipe section rather than only in the pipe bottom, which indicates that the particles are in a state of dynamic suspension rather than irreversibly depositing on the pipe bottom due to gravity settling after running a 3.75 m distance from the particle feed position (which would happen if the particles were simply settling under gravity). On the other hand, the total number of particles differs from frame to frame and the shape of the particle spatial distribution over a whole section is also different. These kinds of variation of particle distribution demonstrate the heterogeneous and unsteady characteristics of gas-solid pipe flow in a dilute pneumatic conveying system.

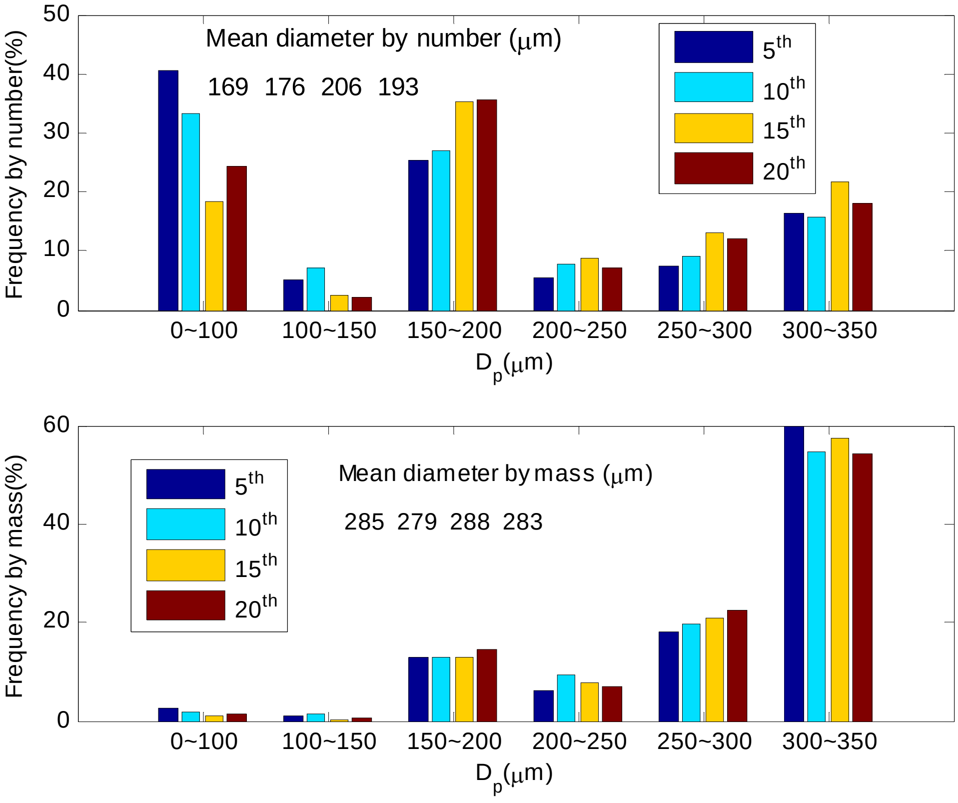

Figure 6.10 Particle diameter frequencies by number and by mass on four example frames

With regard to particle quantitative properties over the whole cross-section, Figure 6.10 shows the measured diameter distribution (the normalized particle number vs. particle diameter and the normalized particle mass vs. particle diameter) in the four frames (5th, 10th, 15th and 20th) as shown in Figure 6.4. These results have been analyzed by using the algorithms of video & image processing discussed in the previous sections. On the whole, we can observe that the shape of the particle diameter distribution curve is approximately conserved over the four example frames, and close to the specified particle distribution. But the frequency's absolute value at every size bin varies over the four frames. This denotes the instantaneous unsteady characteristic of gas-solid pipe flow at every moment. From particle diameter distribution by number, it is clear that particle diameter is mainly concentrated within two intervals of less than 100μm and 175~200μm. Their number fractions are more than 20% and the number fractions in the other size intervals are less than 10%. In addition, the mean particle diameter by number on each frame is different within a standard deviation of 16.8μm from the set of particle mean size by number (169, 176, 206, 193) μm. On the contrary, there are three groups of particles whose mass fractions are more than 10%, as shown in Figure 6.10. Comparing these two diagrams, we can see that fine particles less than 100μm only occupy a small mass fraction less than 5%, although their quantity in terms of particle number is more than 20%. Considering particle mean size by mass on each frame, its measured set of (285, 279, 288, 282) μm shows a narrow variation, since the standard deviation of the set is only 3.9μm compared with that by particle number. It denotes an invariance of particle mean size by mass.

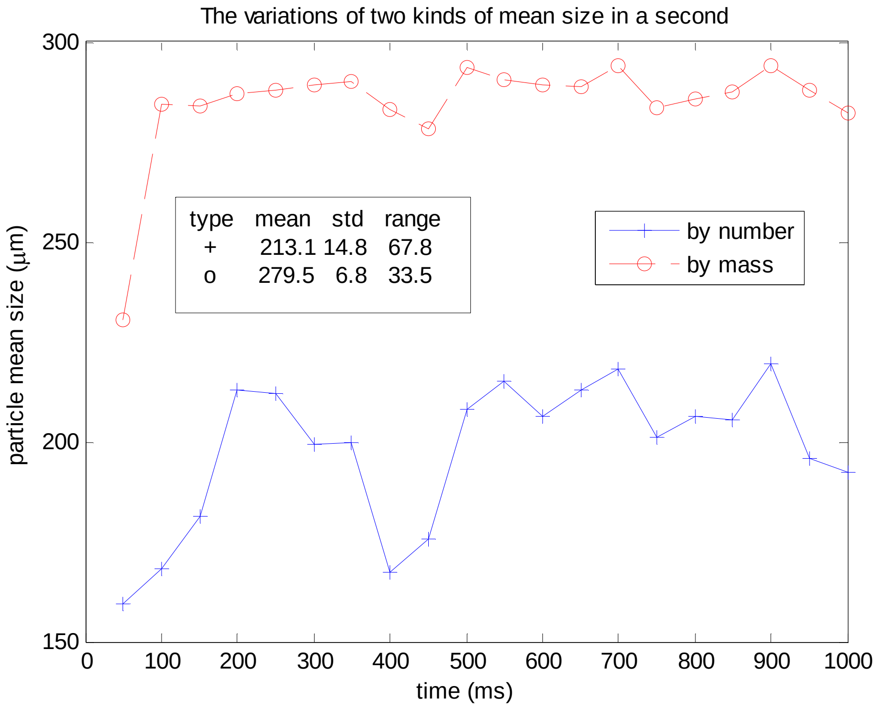

Figure 6.11 The variations of particle number mean size and particle mass mean size over 1s

In order to investigate the temporal variations of particle mean size by number and particle mean size by mass, their temporal variations within one second are plotted in Figure 6.11. A time-averaged value is calculated by averaging the corresponding data on all frames in the specific interval. Obviously, the evolution of particle mean size by mass (the red curve) varies narrowly with a mean value of 279.5μm and a standard variance 6.8μm within a variation range of 33.5μm. Correspondingly, the evolution of particle mean size by number (the blue curve) varies widely with a mean value of 213.1μm and a standard variance 14.8μm within a range of 67.8μm. This is similar to the result shown in Figure 6.10. Therefore, the parameter of particle mass mean size, rather than particle number mean size, is statistically more consistent to describe the steady characteristics of particle diameter in unsteady gas-solid flow, since larger particles have larger weight factors than smaller ones when the mean mass flow rate is calculated over a pipe cross-section. Using particle mean size by mass rather than particle mean size by number is more suitable to describe the statistical properties of unsteady gas-solid flow over a cross-section. For this reason, the following results will focus on the time-averaged property of particle concentration and particle accumulation number (defined as the total number of particles counted in an interval) as well as their cross-sectional distributions.

Figure 6.12 shows two kinds of cross-sectional distributions of particle accumulation number and the normalized values of particle time-averaged concentration over the measurement section at 1s and 30s separately, which are totally counted or time-averaged from the corresponding 25 frames and 750 frames respectively. In general, all of the four diagrams in Figure 6.12 not only clearly display the phenomenon of gravity setting but also show a stratified flow pattern layered by particle number or particle concentration over the cross section. But the contours over 30s show a relatively clear and uniform stratification structure, compared with that over 1s, especially for the diagram of particle concentration distribution. This means that the distribution of particle number or particle concentration requires the averaging of more frames to produce good quality statistical features.

In comparison of Figure 6.12 and Figure 6.13, which is the contour of the dimensionless particle number rate at the section 3D selected from Figure 5.12, both of them demonstrate a similar cross-sectional flow pattern resembling a stratification structure for the spatial distributions of particle number and particle concentration over the cross-section in a horizontal dilute gas-solid pipe flow. However, iso-lines in the two figures have different values and may be located in different positions, especially in the region close to the pipe top wall where the experimental data obtained by LDA still show the dimensionless {N/ln(∑(N)) with a larger value.

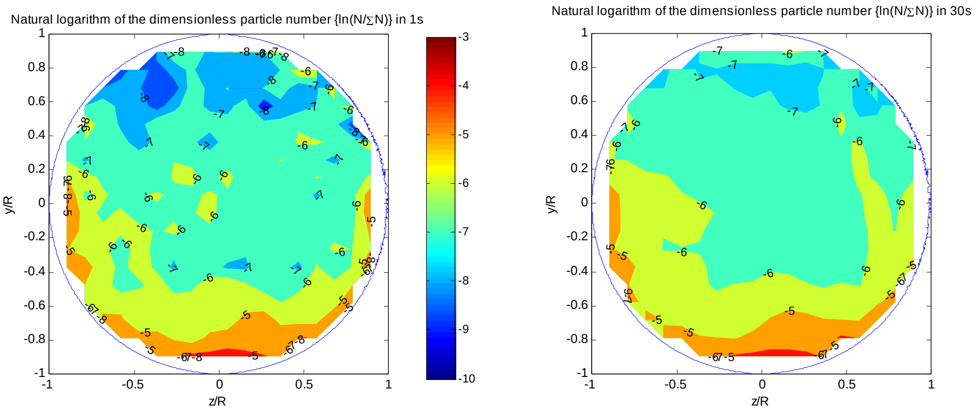

(a) Contours of the dimensionless particle number over 1s and 30s

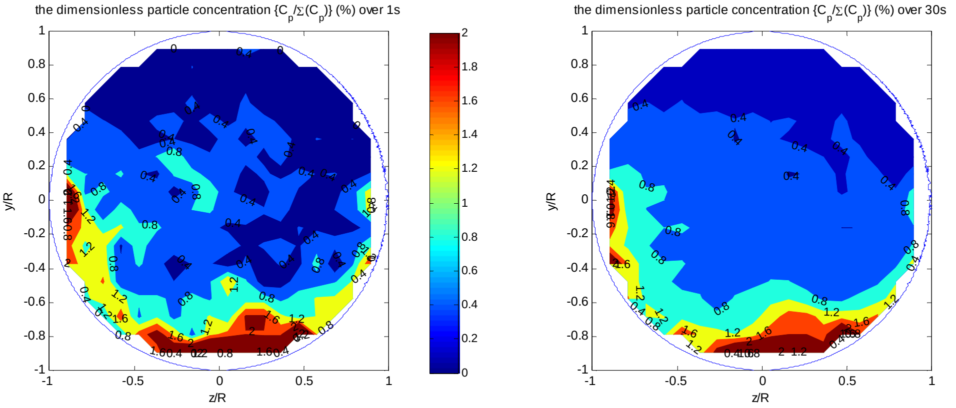

(b) Contours of the dimensionless particle concentration $\{C_p/\mathrm{sum}(C_p)\}$ over 1s and 30s

Figure 6.12 Cross-sectional distributions of the dimensionless particle counting number and the dimensionless particle concentration (N is the particle counting number; R is the pipe radius; $\{C_p\}$ is the local concentration of solid phase)

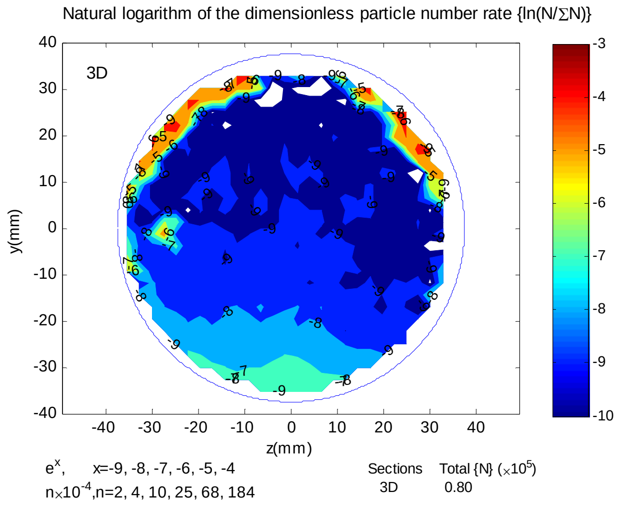

Figure 6.13 The contour of $\{\ln(N/\sum(N))\}$ on the section 3D measured by LDA (selected from Figure 5.12)

6.5 SUMMARY AND CONCLUSIONS

In this chapter, we developed a video & image processing system for measuring particle diameter and analyzing the spatial characteristics of particles over a horizontal pipe cross-section in a dilute pneumatic conveying system. A light sheet produced by a halogen lamp box was used to illuminate and cut a slice of gas-solid flow over a pipe cross-section. Then we used a high definition camcorder to record the particles' behaviour over the highlighted region. A set of video algorithms has been developed to decode the compressed MPEG-2 videos into the AVI format for further image processing. An AVI video, like a database, consists of a series of uncompressed frames. Each pixel on each uncompressed frame is directly mapped to a spatial point in the measurement region. Subsequently, the size and location of each particle can be extracted from every frame by using our developed image algorithms.

As for image processing, firstly, each colour frame which is extracted from an uncompressed AVI video will be converted into the corresponding grey picture according particles luminance information; Second, it will be denoised by Wiener filter; The third step is that a background image will be obtained through removing particle images in the denoised picture by using a 25 × 25 Median Filter. In this way, the feature of background environment can be kept. Subsequently, when the separated background image is subtracted from denoised image, the heterogeneous background will be able to be removed. Then this grey image is to be converted into a binary image by using Otsu's method. Finally, the features of every particle such as shape, size and spatial position can be extracted by applying the Chain Code Technique, which stores the relative co-ordinates between consecutive pixels, achieves the shape of a region by analyzing each point on the boundary in sequence and assigns a code to denote the spatial direction between two adjacent points. Then particle diameter distribution and mean size over a section can be calculated from the set of Chain Code.

The experimental results of particle diameter and size distribution on each frame suggest that gas-solid pipe flow is always heterogeneous in space and unsteady in time. According to their fluctuations in temporal space, using particle mean size by mass is more suitable to statistically describe the unsteady properties of gas-solid pipe flow. On the other hand, both the contours of particle accumulation number and particle time-averaged concentration exhibit a flow pattern resembling a stratified structure over a horizontal pipe cross-section in gas-solid flow. This kind of stratified structure is similar to the results explored by the experimental data of Laser Doppler Anemometry in Chapter 5. But iso-lines may have different values and be located in different positions.

Needless to say, the current developed video & image processing system can be used to measure the size and spatial distribution of particles more than 80μm over a whole cross-section in ϕ75mm pipe. Thus, this visualization system will be suitable for fine particles measurement by using a smaller size of pipeline for experiments. In addition, using coloured granular materials, this system can be developed into a measurement tool for gas-solid pipe flow with a multi-component solid phase by adding the function of discerning particle colour.

Chapter 7

CFD Investigation of Cross-sectional Flow Patterns of Solid phase in Gas-Solid Granular Pipe Flow

This chapter presents numerical predictions of flow patterns on cross-sections along a horizontal pipe using the Discrete Phase Model (DPM) of Fluent 6.3.26 as well as the latter coupled with the Discrete Element Method (DEM) software of EDEM 1.3.1. The simulations are compared to experimental measurements on glass beads (size 70~110μm, solid loading ratio 1.6%) transported by 12m/s air in ϕ75mm glass pipes. Using Laser Doppler Anemometry (LDA), the measured contours of the horizontal particle velocity component show an annular structure over the pipe cross-sections; this flow pattern can also be described as stratified flow over cross-sections, layered by particle number distribution. The comparisons of numerical and experimental cross-sectional flow patterns of solid phase show that there is reasonable agreement at pipe cross-sections located at horizontal positions less than half the product of particle mean velocity and mean free fall time in the pipe from the particle inlet. Further away from the inlet, the numerical results show flow patterns which are increasingly divergent from the experimental results along the pipe in the direction of flow. This discrepancy indicates that particles' spatial distribution in a pipe is not accurately predicted by DPM or Fluent coupled with DEM. Moreover, it is necessary to validate and develop numerical models by using the latest experimental data.

7.1 INTRODUCTION

In Chapter 2, the effects of some macro parameters like the Saffman force and Stokes number on pneumatic transportation have been investigated using the Discrete Phase Model (DPM) in Fluent 6.2.16. In Chapters 4-6, we presented experimental results of solid phase distributions over a series of cross-sections in the horizontal pipe by using an extended Laser Doppler

Anemometry (LDA) technique and developing a visualization system involving video recording and Image processing. These experimental results display two cross-sectional flow patterns of the solid phase, resembling an annular structure and stratification in a horizontal pipe. The annular structure represents the contour of particle velocity and the stratified image represents the contour of particle number rate over a pipe cross-section. These experimental data provide a good tool to validate the availability and limitations of the current numerical models for pneumatic conveying research.

Generally, flow regimes for horizontal conveying of granular materials can be classified into dilute suspension flow, stratified flow, sedimentation dune flow, plug flow and moving bed flow (FAN, 1998). These flow regimes are usually observed along the pipe axis and each is a qualitative term depicting the macro-state of gas-solid flow.

So far, research into solid phase distribution over a pipe cross-section is still scarce. Most numerical and experimental studies only show one-dimensional local information on the solid phase along a line rather than two-dimensional data over a whole cross section. Among these studies, the experimental work of Tsjui (1983), used Laser Doppler Velocimetry to measure the velocity of mixed plastic particles, size 200μm and 3.2mm, density 1000kg/m^3; conveyed by air of velocity 6,10 and 15m/s in a 30.5mm diameter horizontal glass pipe. The vertical profile of the normalized axial particle velocity became flattened with increasing particle size or solid loading ratio, and the profile peak was shifted upwards above the pipe centre line. This is also confirmed by Huber's (1994) experimental data (glass particle size 40μm; air velocity 21m/s and ϕ80mm glass pipe). Huber not only used Phase Doppler Anemometry (PDA) to measure the particle velocity profile, but also applied the light-sheet method to measure particle concentration over the pipe cross-section through analyzing the light densities scattered by particles in images taken by CCD. The contours of particle concentration over pipe cross-sections clearly display an annular structure, but their core regions were located in the lower half of the pipe due to gravitational settling. Using Electrical Capacitance Tomography (ECT), Rao (2001) measured solid phase concentrations over a whole pipe cross-section in various flow regimes. The experimental system was a ϕ40.4mm PVC pipe in which air at superficial velocity 10.4 ~28.6m/s transported three large particle types, which were titanium dioxide (3.01mm, 1683kg/m^3), brown mustard (1.76mm, 879kg/m^3) and polypropylene (2.8mm, 1123 kg/m^3). In the homogeneous flow regime, the contour of time-averaged particle concentration (polypropylene, air velocity 28.6m/s) showed a stratified structure over the cross-section.

Due to the complexity of gas-solid pipe flow, particle transportation is still an area of keen interest in computational fluid dynamics studies. Most numerical simulations in this field have been performed using the Euler/Lagrange approach, which has been developed into the standard Discrete Phase Model (DPM) in the commercial Computational Fluid Dynamics (CFD) software package FLUENT. Among numerical studies of solid phase spatial distribution in horizontal pipes, Huber’s (1998) numerical results show that 40μm glass particles have a good ability to follow the fluid in air of 24m/s superficial velocity in a ϕ80mm smooth glass pipe and that their trajectories are distributed over the whole pipe space. Further, Sommerfeld (2003) investigated the effect of wall roughness on trajectories of 30~700μm particles transported by 18m/s air in a 2D channel with 6m length and 35mm height. The calculated trajectories of 110μm particles without considering the effect of wall roughness indicated that all of them were concentrated in the channel bottom region after 3m forward progress, although they were homogenously injected at the inlet. Although there are some papers on the study of solid phase distribution over cross-sections of pipe bends and vertical pipe runs, their results are not discussed here since it was decided that horizontal pipes provide the best test of the predictions of the two methods.

In the following sections, the numerical models and the corresponding parameters will be introduced firstly. Then the experimental data, which have been measured by the extended technique of Laser Doppler Anemometry, will be summarized. The experimental results include contours of particle velocity and particle number rate on a series of horizontal pipe cross-sections. Basing the inlet condition of numerical simulations on the actual experimental data, theoretical predictions of flow patterns on pipe cross-sections have been explored by using the DPM option of Fluent and Fluent coupled with EDEM respectively. Then we discuss the limitations of current numerical models through analyzing the discrepancy between numerical results and the corresponding experimental data.

7.2 NUMERICAL MODELS AND THEIR PARAMETERS

7.2.1 Mathematical models

In dilute pneumatic conveying, the forces acting on particles may be classified into three groups: (1) forces due to the interface between fluid and particles, (2) forces due to the interactions between particles and collisions of particles with the wall, and (3), forces imposed by external fields such as gravity (Fan, 1998). The forces in the first group normally are the drag force, the Saffman lift force, the thermophoretic force, the Magnus force, the Brownian Force and a force related to the pressure gradient. The forces in the second group are accounted for in the particle-wall collision model and particle-particle interaction models. In the standard DPM of Fluent, which has been introduced in Chapter 2, the standard particle motion equation does not include items corresponding to the Magnus force and the force related to the pressure gradient. It also ignores particle-particle interactions so as to reduce the expense of computation. The concept of parcels, which represents a group of particles with the same properties such as particle size, density and injection position, is introduced in DPM. Thus, DPM in Fluent is modelled to track a set of parcels or particle stream rather than each individual particle in the domain.

An alternative approach different from DPM has been introduced to develop two-fluid continuum models that consider the gas and solid phases as two interpenetrating continua. Then the mechanical behaviour of the solid phase is described by the discrete element method (DEM) and air phase flow structure is solved using the traditional CFD method. Basically, this approach is a coupled DEM-CFD calculation. In the coupled DEM-CFD calculations, conservation equations for the solid phase are no longer required in CFD calculations using the commercial software Fluent. The DEM model directly calculates the solid phase terms in the air phase equations, such as the momentum exchange coefficient between the phases and the mean solid phase velocity. Tracking the motion of individual particles allows a precise calculation of how the solid volume associated with these particles changes with time.

In order to investigate the actual particle-particle influences, Crapper et al. (2005) used a coupled simulation using DEM together with FLUENT to study particle characteristics in elbows of a dilute pneumatic conveying system, since there exist in bends many strong particle interactions. Similarly, Yu et al. (2005) also used the discrete element method coupled with computational fluid dynamics to study the pneumatic transport of polypropylene beads (maximum number 2000, diameter 2.8mm) in both vertical and horizontal one metre long pipes. Their numerical results only focused on solid phase flow along the pipe axis under different operating conditions. Several research workers have applied the method of combining DEM with CFD to simulate plug flow and fluidized beds (Tsuji et al. 1992; Tsuji et al. 1993; Rhodes et al. 2001). Here, we use the commercial DEM software called EDEM which was developed by DEM Solutions Limited of Edinburgh. It can be directly coupled with Fluent for the simulation and analysis of granular material handling and manufacturing operations (Dem-solutions, 2008).

Since both DPM and DEM have been developed to be standard models in commercial software, the detailed equations governing the phase dynamics will not be replicated here. We only focus on selecting the suitable model parameters. Table 7.1 and 7.2 list all the numerical parameters used here for DPM and DEM-Fluent simulations respectively.

Table 7.1 Numerical parameters for DPM simulations

Type	Choices
Solver	✧ Segregated solver with 2^{nd} order discrete scheme ✧ Space: 3D ✧ Unsteady simulation ✧ Time step: 1×10^{-3}s
Turbulence model(k-ε Model)	✧ Model Constants: C_{mu} =0.0845 C_1 = 1.42 C_2=1.68 ✧ RNG options: Differential viscosity model ✧ Near-wall treatment: standard wall functions ✧
Discrete phase option	✧ Interaction with continuous phase ✧ Update DPM sources every 25 fluid phase iterations ✧ Saffman lift force ✧ Two-way turbulence coupling ✧ Developing user-defined-functions (UDF) to control particle number at each position at each injection moment A total of 1047 injection points which produce 53267 parcels within a second.
Gravity	✧ the negative direction of y axis Value: 9.81 m/s^2
Wall collision model	✧ Elastic collision model ✧ Restitution coefficients of normal and tangential directions are 1 ✧ Smooth pipe

Table 7.2 Numerical parameters for DEM-Fluent calculations

Type		Values
Fluent	Solver	Segregated solver with 2^{nd} order discrete scheme Space: 3D Unsteady simulation Time step: 1×10^{-3}s
	Turbulence model(k-ε Model)	Model Constants: C_{mu} =0.0845, C_1 = 1.42, C_2=1.68 RNG options: Differential viscosity model Near-wall treatment: standard wall functions Full buoyancy effects
	Gravity	the negative direction of the y axis, Value: 9.81 m/s^2
EDEM	Particles material	Spherical glass beads
	Particle mean size	90μm
	Number of particles	53267 within a second
	Poisson’s ratio	0.4
	Restitution coefficient	1
	Particle factory (particle injection position)	212
	Time step	1×10^{-6}s
	Shear modulus (Pa)	2.6×10^{8}

7.2.2 Experimental rig and numerical geometry

Figure 7.1 shows the experimental rig and the three meshed sections which schematically display the numerical domain. The domain is the 1m long horizontal glass pipe (ϕ75mm) 90mm upstream of the elbow in order to compare the numerical results with the experimental data without the elbow effect on the upstream fluid. It has been meshed into 76400 triangular cells with a boundary layer of 5 cells thickness. Grid independence has been confirmed by single air phase flow calculations.

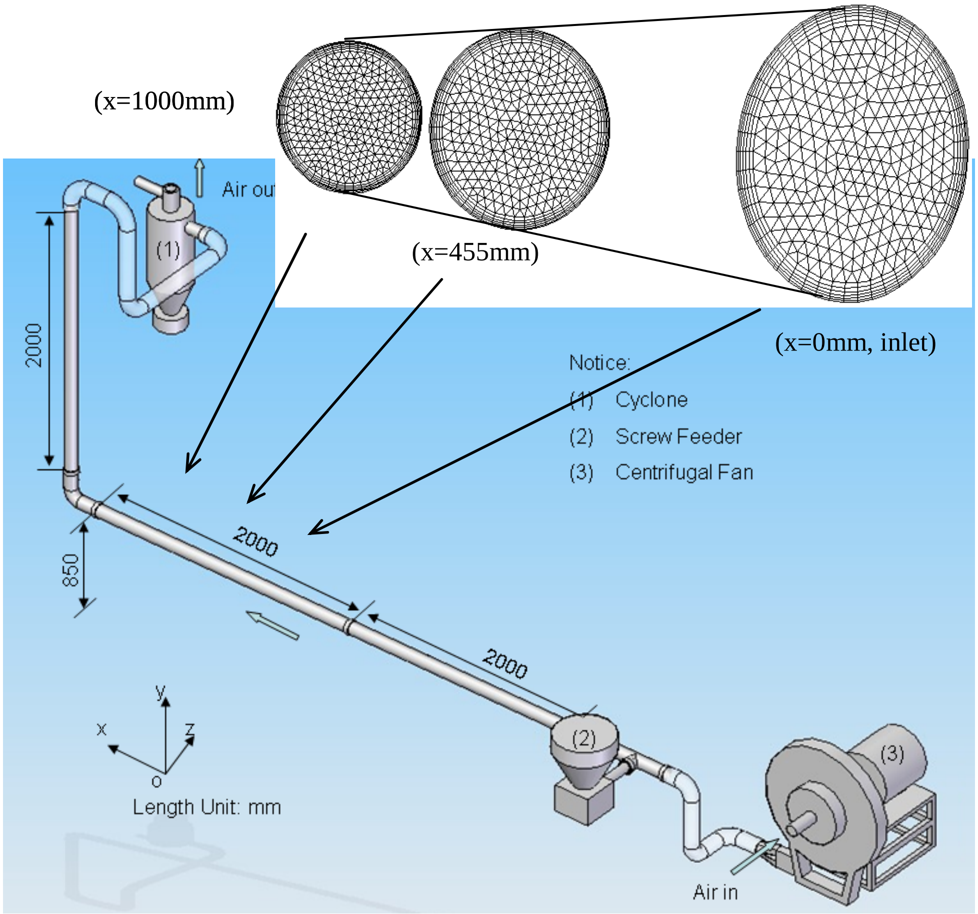

Figure 7.1 Experimental rig and schematic diagram of numerical geometry

7.2.3 Fluid conditions at inlet

The initial conditions at the inlet for numerical simulations are generated following the experimental results. Using the extended LDA technique introduced in Chapter 3, we measured the cross-sectional distributions of air velocity, particle velocity and particle number rate on a series of pipe cross-sections within the numerical domain whose inlet locates 2.9m away from the particle feed position in the horizontal part of the experimental rig (as shown in Figure 7.1). In the experiments, glass beads with mean size 90μm (Stokes number 10.2) and density 2550 kg/m^3 were pneumatically transported by air with a conveying velocity of 12m/s. The experimental results at the inlet of the numerical domain are shown in Figures 7.2 and 7.3 for the air and solid phases respectively.

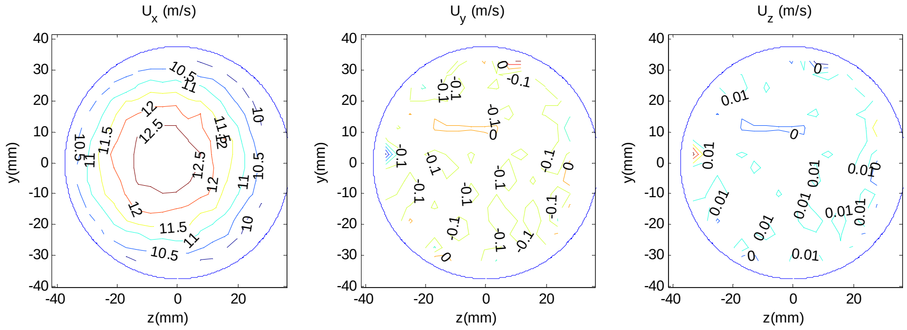

Figure 7.2. Air velocity (U_x, U_y and U_z) at inlet

Figure 7.2 shows the distribution of the three components of air velocity at the section x=0mm (inlet), which were measured by LDA using smoke as seeding particles. The measured turbulence intensity of the air flow is about 3.5%. These experimental data was used as the velocity profile of the air phase at the inlet in the numerical simulations.

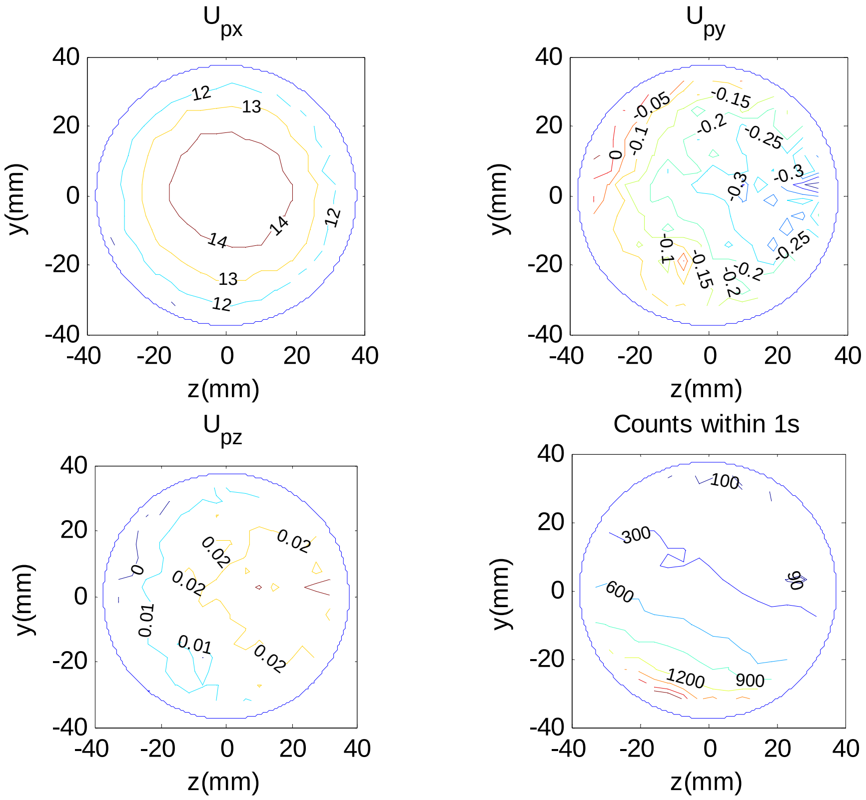

Figure 7.3. Cross sectional distributions of particle velocity and particle number rate at inlet averaged over 1s

With regard to the inlet conditions of the solid phase, the distributions of particle velocity and particle number rate are illustrated in Figure 7.3, as measured under conditions of 1.6% solid loading ratio at 12m/s air conveying velocity in a ϕ75mm pipe. It is clear that solid phase at the inlet is heterogeneous over the section, since particle velocity reduces from the centre to the wall and particle number rate increases from the top to the bottom. Thus the numerical simulations should be performed in the unsteady state.

7.2.4 Experimental cross-sectional flow patterns of solid phase

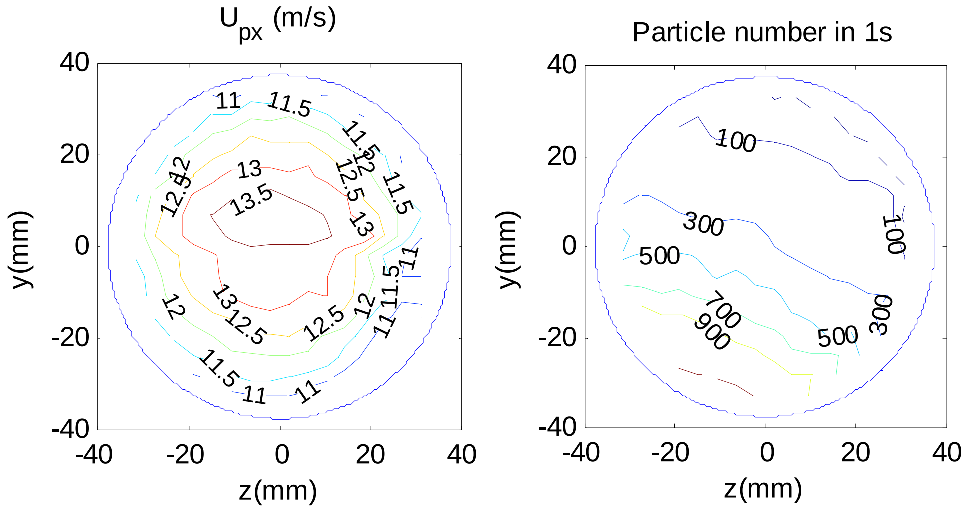

Figure 7.4 The contours of particle velocity U_{px} and particle count over 1s at the section x=455mm

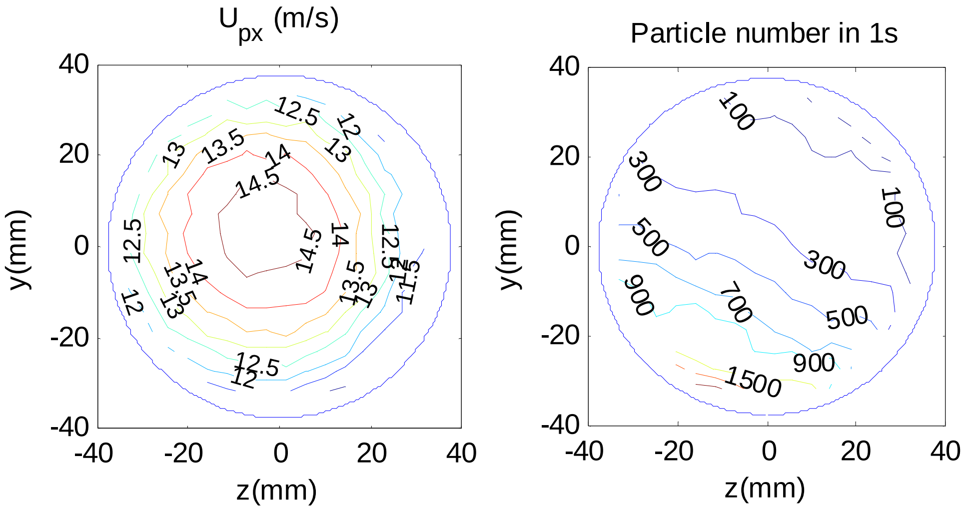

Figure 7.5 The contours of particle velocity U_{px} and particle count over 1s at the section x=1000mm.

In Chapter 5, the experimental cross-sectional flow patterns of solid phase on a series of cross-sections have been displayed under the different fluid conditions. Here two selected samples within the numerical domain are shown in Figure 7.4 and 7.5 which correspond to the mid section and outlet of the numerical domain. They will be used to compare with the numerical results.

As shown in Figures 7.3, 7.4 and 7.5, we notice that the contours of particle horizontal velocity component (U_{px}) at the three sections display a characteristically annular structure, and their annular cores or the fastest U_{px} regions are observed to be displaced upwards above the pipe centre line. The contours of particle number rate on the three sections reveal a characteristically stratified form. Consequently, the flow patterns of gas-solid flow over the pipe cross-sections can be described as an annular pattern in terms of horizontal particle velocity component and a stratified layer pattern in terms of particle number rate.

7.3 RESULTS AND COMPARISONS

7.3.1 Flow patterns of solid phase investigated by DPM

Using DPM in Fluent, we simulated a total of 53267 parcels (the unit of particles in a trajectory at every time interval) passing through the domain from 1047 feeding points over 1s. These feed points were the same as the sampling points in the experiments. Since solid mass flow rates at the feed points were different depending on particle number rate, an injection program utilising a user-defined-function (UDF) by using macros in Fluent was developed and coupled into Fluent. This determined the particle number injected from each point at every numerical time step. For unsteady-state simulations, the time-averaged values of parameters cannot be displayed by Fluent directly. The results were therefore post-processed and statistically analyzed using Matlab7.0. A selection of typical results is shown in Figures 7.6 and 7.7.

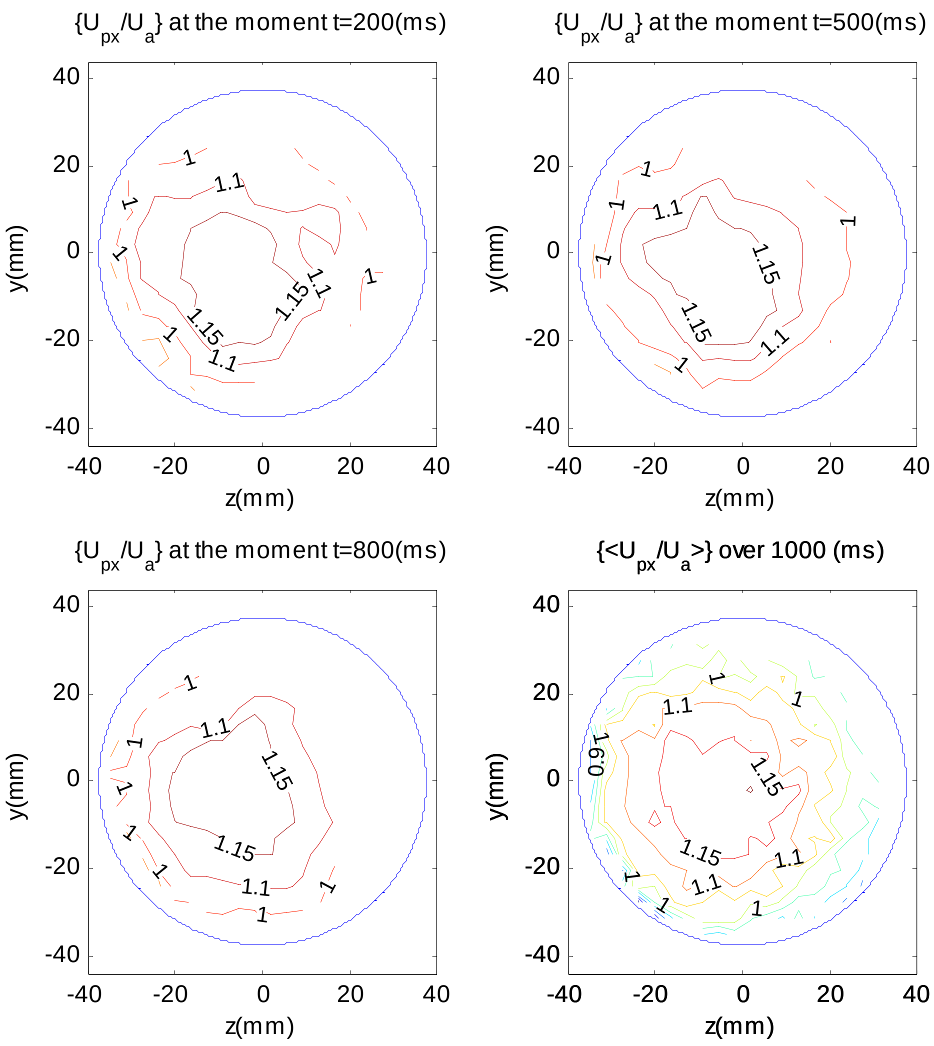

Figure 7.6 Contours of the dimensionless particle instantaneous velocities {U_{px}/U_a} and its time-averaged value {<U_{px}/U_a>} over 1000ms on the section x=455mm obtained from simulation using FLUENT DPM (Ua=12m/s)

Figure 7.6 shows three selected contours of the axial instantaneous particle velocity {U_{px}} and one time-averaged contour {<U_{px}>} over one second on the section x=455mm. Observing the first three contours of particle instantaneous velocity U_{px}, we find that the contour shapes differ from each other. This means that the structure of the U_{px} contour is time-dependent. In addition, we also notice that some fragmented isolines displayed in all four diagrams of Figure 7.6. The time-dependent structure and fragmented isolines indicate that the gas-solid pipe flow is unsteady in time and heterogeneous in space. Compared with the three instantaneous contours, the contour of particle time-averaged velocity over 1s (at the right bottom of Figure 7.6) more clearly shows the annular structure of gas-solid flow over the pipe cross-section. This annular structure is generally similar to the flow pattern portrayed by the experimental data of particle velocity U_{px} in

Figure 7.5 and Figure 7.6. Their difference results from the fact that the fastest region or annular core in Figure 7.6 is displaced downwards below the pipe centre line, while the experimentally located annular core in Figure 7.5 is shifted upwards above the pipe centre line. However, the numerical annular pattern in Figure 7.6 is not uniform like the experimental one in Figure 7.5.

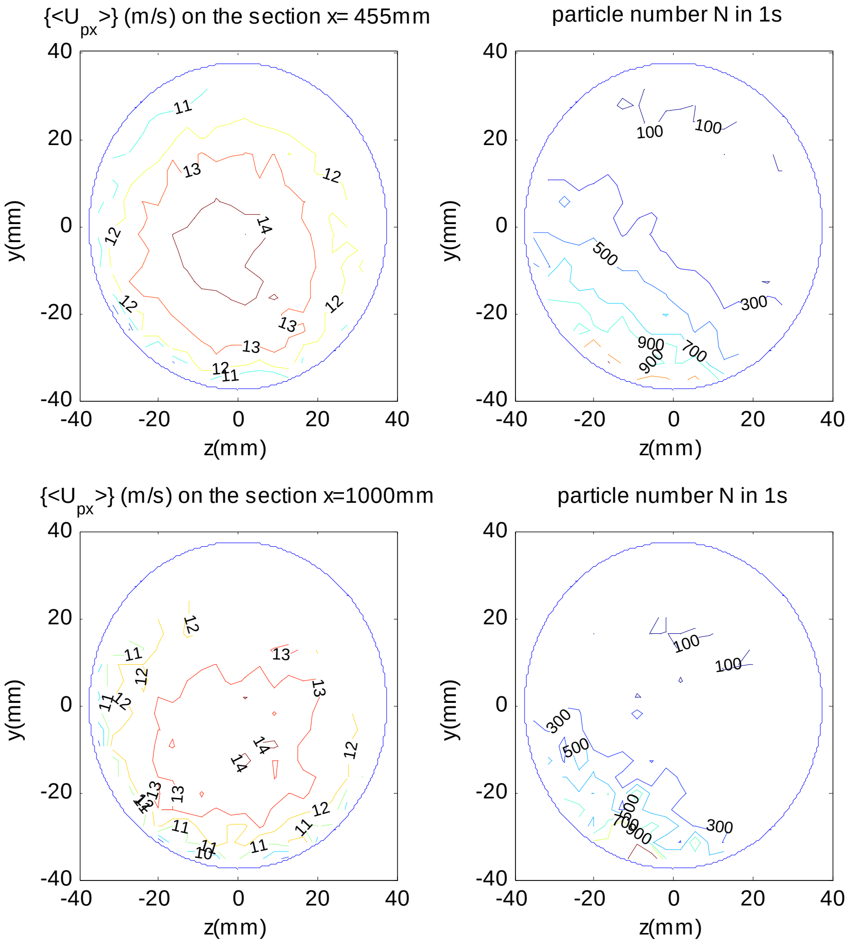

Figure 7.7 Contours of the time-averaged axial particle velocity {<U_{px}>} and particle number {N} over 1s on two sample sections (x=455mm, 1000mm) obtained from FLUENT DPM

Since the contours of time-averaged particle velocity U_{px} are useful to explore some characteristics of gas-solid flow, Figure 7.7 shows contours of time-averaged U_{px} and particle number rate at two sections at x=455mm and 1000mm respectively. Comparing these flow patterns with those at the inlet indicated in Figure 7.3, both the annular structure in terms of U_{px} and the stratified shape layered by particle number rate are still shown in the contours at the x=455mm section, but these two characteristics are distorted to extinction in the contours at the x=1000mm section. This shows that the DPM modelled flow pattern varies along the fluid direction.

7.3.2 Flow patterns of solid phase investigated by Discrete Element Method

In the coupled Fluent & EDEM simulations, all numerical geometry, fluid conditions and boundary conditions were the same as the foregoing ones in the DPM simulations. But for particle injection at the inlet, particles could be automatically injected with a different mass flow rate at every injection point through defining "particle factories" over the inlet rather than using a UDF program to control the process of particle injection. Since the solid phase in the DEM is treated as individual particles dispersed in the fluid rather than as the "parcels" (groups of particles with the same trajectory) used in DPM, the effect of particle-particle interactions and friction due to collisions can be accounted for in detail in the DEM model implemented here by the EDEM software. Due to the need to transfer particle locations back to the fluid domain at each fluid time step, and the large size of domain relative to the particle size and number, the speed of this coupled simulation is rather slow. Typical results of the time-averaged contours of particle velocity U_{px} and particle number rate are shown in Figures 7.8.

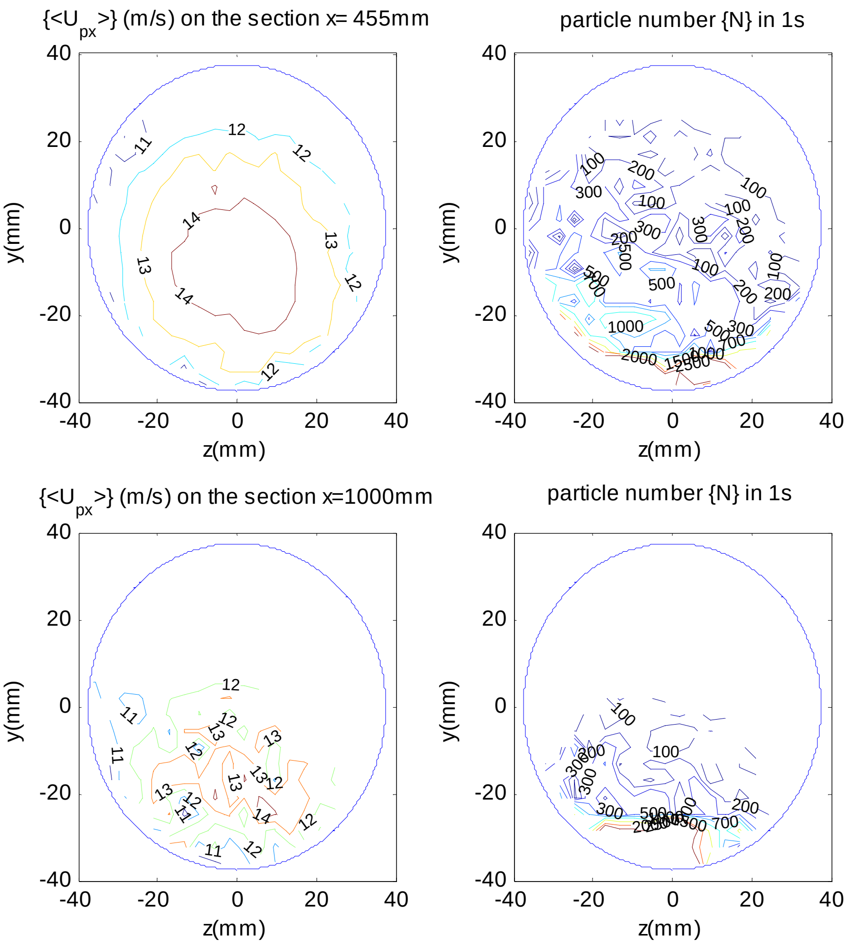

Figure 7.8. The flow patterns of particle mean velocity and particle number on two sample sections (x=455mm, 1000mm) obtained by using FLUENT & EDEM

On the section x=455mm, an annular flow pattern of solid phase in terms of the particle velocity horizontal component (U_{px}) (to be compared with Figures 7.4 and 7.7) is obvious in the upper section of Figure 7.8, and the core region is also displaced downwards below the pipe centre as in the DPM results. However, the stratified flow pattern observed in Figures 7.4 and 7.7 is completely distorted in the upper section of Figure 8. As for flow patterns on the x=1000mm section, both the annular pattern and the stratified pattern are skewed, and no clear pattern can be observed in Figure 7.8.

7.4 DISCUSSION

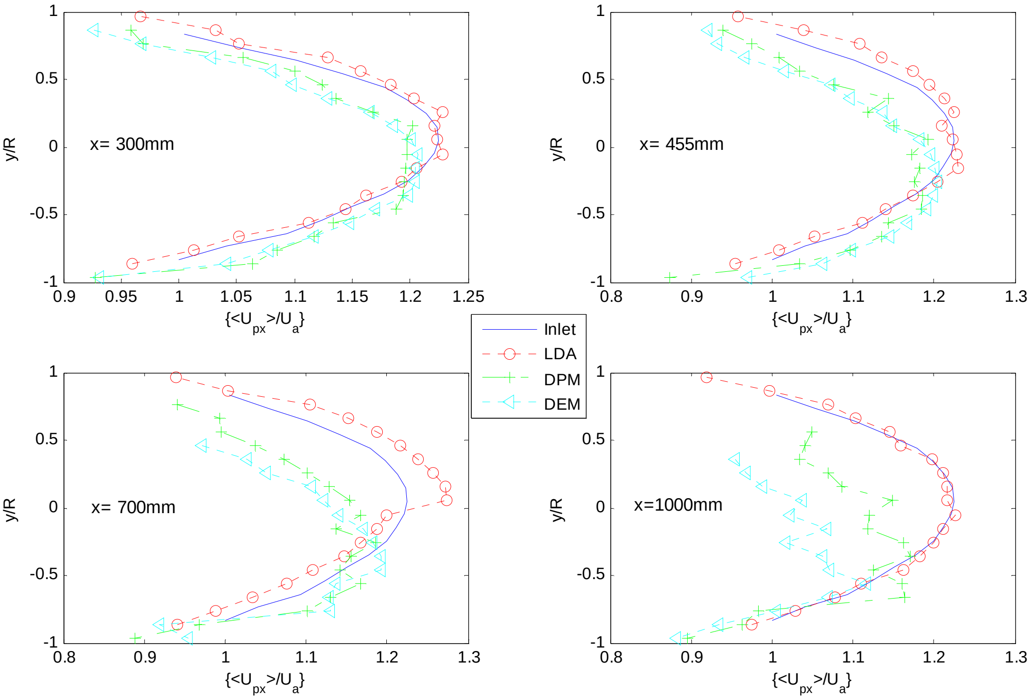

Figure 7.9 Comparison of the numerical and experimental vertical profiles of {<Upx>/Ua} at four different positions along the fluid flow direction (the continuous blue line is the profile at inlet)

In order conveniently to access the evolution of flow patterns along the pipe, the experimental and numerical profiles of the dimensionless $\{<U_{px}>/U_a\}$ and particle number over 1s at the z=0mm lines at several sections (x=300, 455, 7000 and 1000mm) are plotted in Figure 7.9 and Figure 7.10. U_{px} is normalized by the mean air conveying velocity (U_a) which is 12m/s.

In general, profiles at the position of x=300mm have a good agreement with each other as well as similarity to the profile at inlet, although the peaks of both numerical profiles of $\{<U_{px}>/U_a\}$ show a small shift away the pipe centre line. At the further downstream distance of x=455 to

1000mm, there is much discrepancy among these profiles. Especially at the position of x=1000mm, both numerical profiles of {<U_{px}>/U_a} have been distorted, which are completely different from the experimental profile of {<U_{px}>/U_a} as well as the profile at inlet. By contrast, the experimental profiles of {<U_{px}>/U_a} can be observed to be similar at the different positions along the pipe.

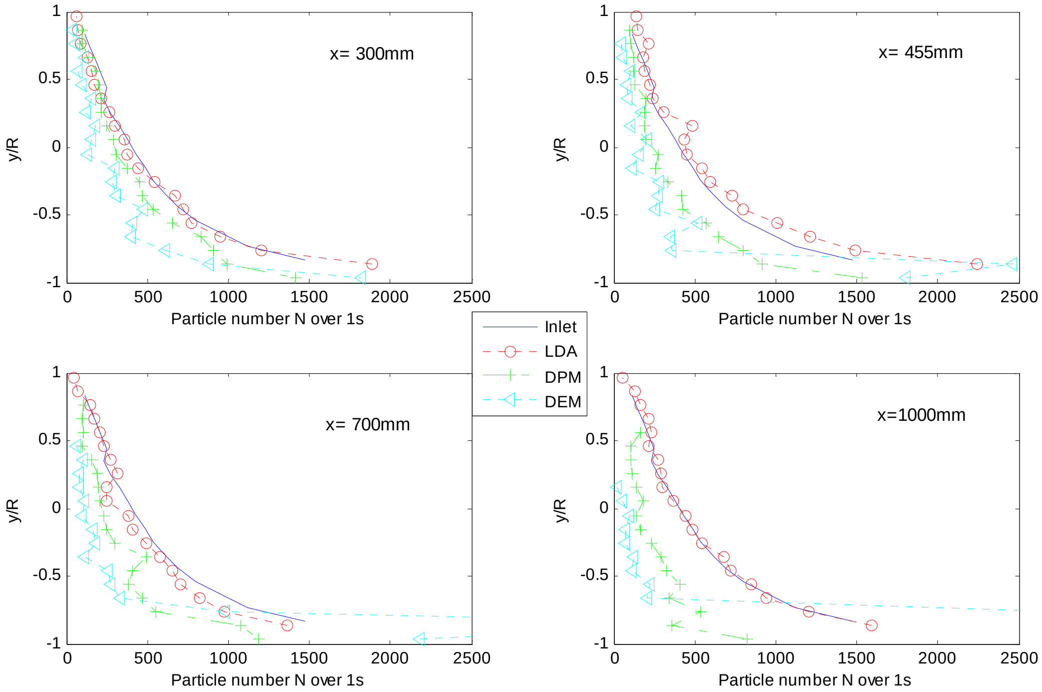

Figure 7.10 Comparison of the numerical and experimental vertical profiles of particle number over 1s at four different positions along the fluid flow direction

As for particle number counted over 1s, Figure 7.10 shows its numerical and experimental profiles at the four different positions along the pipe. On the whole, we can see that the experimental profiles of particle number are identical to each other and they also just vary around the profile of particle number at inlet with a small deviation. With regard to the numerical profiles of particle number over 1s, there is a significant discrepancy among them along the fluid flow direction. Both numerical profiles show that there is an increasing tendency of particle number along the pipe, for particle number gradually increases at pipe bottom and decreases at pipe upper half, even where there is a very dilute or empty space without particles in the pipe upper space at the position x=1000mm.

However, experimental data in Figures 7.3, 7.4 and 7.5 shows that both the annular flow pattern and stratified particle number distribution follow a steady trend along the downstream direction in the whole domain. This indicates that using DPM or DEM can only estimate flow patterns properly within a short domain. In another words, both DPM and DEM have not yielded satisfactory results for predicting some parameters related to particle spatial distribution in the gas-solid pipe flow.

In the previous two sections, the cross-sectional flow patterns and their evolution in the downstream direction, as calculated using two numerical methods, were discussed. Comparisons of the numerical results with the corresponding experimental data indicate that numerically predicted cross-sectional flow patterns show reasonable agreement with experimental ones only at pipe cross-sections located within a specific distance from the inlet. At greater downstream distances, numerical flow patterns become distorted until they are completely different from experimental flow patterns. This discrepancy means that the spatial distribution of 38~110μm particles being transported in the dilute state in a long horizontal pipe is not properly estimated by the current numerical methods.

The numerical results of Huber (1998) showed 40μm glass beads' 2D trajectories on a vertical section of a ϕ80mm horizontal pipe. As would be expected since their Stokes Number was 2.0, the trajectories of these glass beads followed the fluid flow pattern. Furthermore, Sommerfeld (2003) numerically investigated trajectories of four different size glass beads in a 2D horizontal channel with 35mm height and 6m length. Without considering the effect of wall roughness, his numerical results show that all trajectories of 110μm particles end up on the channel bottom by 3m downstream of the inlet. This is similar to our numerical results of particle number in Figures 7 and 9. To allow for the problem of irreversible deposition, Sommerfeld introduced a model of particle-wall collision which assumed particle impact angle composed of the particle trajectory angle and a random normal distributed component due to roughness. The trajectories of 110μm particles were then much widely distributed over the whole channel space and agreed with his experimental data.

In summary, the foregoing discussion reveals that there still exist some effects which have not been accounted for in the current DPM or Fluent & EDEM coupling simulations for investigating gas-solid pipe flow. The model of particle-wall collision introduced by Sommerfeld will be incorporated in future coupling simulations and methods of two-dimensional pattern recognition will replace the current one-dimensional technique to precisely determine the similarity of fluid patterns of the solid phase on a series of pipe cross-sections.

7.5 CONCLUSIONS

Based on experimental data and the geometry of the experimental rig, flow patterns on a series of pipe cross-sections and their vertical profiles along the pipe have been numerically investigated by the standard DPMs of Fluent and Fluent coupled with EDEM. Three conclusions can be deduced from the comparison of numerical and experimental data.

The annular structure of the particle velocity horizontal component and the stratified structure by particle number can be predicted by both Fluent DPM and Fluent & EDEM within a certain distance from the inlet, which can be estimated by the product of particle mean velocity and half the particle free falling time. On pipe cross sections further downstream, the flow patterns modelled are distorted until the annular velocity and stratified particle number characteristics completely disappear. Compared with the contour of particle number and its evolution along the pipe simulated using Fluent DPM, the data achieved by using Fluent & EDEM shows that particles distribute much widely in the pipe space, rather than being located close to the pipe bottom after they have been transported a critical downstream distance. This means that considering the effect of particle-particle interactions in DEM will improve the accuracy of numerical simulations for gas-solid horizontal pipe flow, even though the solid phase is in a dilute state. The distorted flow patterns and their evolution profiles along the pipe indicate that particle spatial characteristics found from experiment are not properly estimated by the current numerical models. Thus, the micro-mechanism of fine particle transport in pipes should be further studied.

Finally, it should be mentioned that work on developing the current numerical model using our experimental data is ongoing.

Chapter 8

Conclusions

Co-firing applications in power stations have been confirmed as being a promising way to reduce CO_2 emissions very considerably while generating enough electricity for energy demand. A demanding task is that of controllably distributing a fuel mixture of pulverized coal blended with biomass particles in a common pipeline, which is likely to save much investment as success would enable existing pulverized fuel boilers to be used for biomass exploitation. Therefore, to address the problem of controllable distribution in co-firing techniques and to gain an improved understanding the mechanism of pneumatic conveying, this research into particle dynamics of pipe flow was undertaken.

The objectives of this research were, firstly, to numerically evaluate the influence of various factors on the behaviour of particles of the different materials in a horizontal pipe flow; secondly, to develop an extended technique of Laser Doppler Anemometry in order to determine cross-sectional characteristics of the solid phase in the horizontal and vertical sections of a pneumatic conveying system; thirdly, to develop a novel imaging system for visualizing particle properties by using a high definition camcorder on a cross-section illuminated by a halogen light sheet; and, finally, to make a comparison of the cross-sectional characteristics revealed by experiment and those simulated by using the Discrete Phase Model of Fluent and the coupling calculations of Fluent & EDEM respectively.

Conclusions of the experimental and numerical investigations are detailed below.

8.1 SUMMARY OF RESULTS

The overall results from this study cover particle dynamics in horizontal pipe flow and in a vertical pipe flow downstream of right-angled elbow. The main results are summarised as follows:

1. ***Critical parameters and particle similarity in a horizontal dilute phase pneumatic conveying system***

   Using the Discrete Phase Model in Fluent 6.2.16, we have explored the influence of air conveying velocity, pipe roughness and particle size on particle trajectories in the boundary region. The numerical results demonstrate that the Saffman Force plays an important role in a dilute pneumatic conveying system, especially for determining whether a particle will be re-suspended from the boundary region. This analysis shows that there exist three critical parameters:

   (1) The critical air conveying velocity. A higher air conveying velocity generally benefits by lifting a particle higher from the boundary region towards the mainstream field of pipe flow, but the height reached is no longer much enhanced when the air velocity is more than 30m/s in our numerical model. This value is defined as the critical air conveying velocity.

   (2) The critical pipe roughness. In the pipe boundary region, increases in pipe roughness result in a particle being able to jump to a much higher position. However, when the pipe relative roughness is more than 1.64%, the trajectories of the particle are the same and the particle is no longer lifted much higher. The value of 1.64% is termed the critical pipe relative roughness for the current fluid conditions of air conveying velocity 24m/s.

   (3) The critical particle size. Basically, the bigger a particle is, the higher it can be suspended if its size is in the range of 10~100μm. However, this phenomenon no longer exists when a particle is larger than 100μm. The value of 100μm is defined as the critical particle size for the current fluid conditions of air conveying velocity 24m/s.

   (4) The characteristics of the dimensionless mean particulate velocity. The numerical results indicate that particle mean velocities of the different materials can be classified into three regions in the horizontal and vertical directions, non-dimensionalising by means of the Stokes Number or divided by the terminal velocity respectively. Particles with a Stokes Number less than 1 have a mean velocity equal to the air conveying velocity in the horizontal direction and a mean vertical velocity equal to the terminal velocity in the fully developed region. Correspondingly, for larger particles with Stokes Number more than 3.5, their mean dimensionless velocity U_{px}/U_a (the horizontal particle velocity divided by air conveying velocity) tends towards 0.6 in the horizontal direction and their mean dimensionless velocity U_{py}/U_a (the vertical particle velocity divided by air conveying velocity) in the vertical direction becomes essentially zero. The mean dimensionless velocities of particles with Stokes number between 1 and 3.6 are in the range of 0.6~1 in the horizontal direction and -1~0 in the vertical direction (as the direction of gravity).

2. ***The extended technique of Laser Doppler Anemometry***

So far, there is still a lack of papers discussing the detailed effect of refraction at the pipe wall and of sample rate in gas-solid flow measurements using Laser Doppler Anemometry. The refraction effect due to the curved surface of the pipe can not be ignored and the sampling rate is related to the statistically accuracy of calculating the time-averaged value of a parameter measured by LDA, we have proposed modifications to the current normal technique of LDA, which has been validated by the comparison of the profiles of air velocity measured by LDA and the corresponding theoretical profile estimated by the empirical one-seventh power law of air velocity in a pipe. This extended technique has been applied to measure the cross-sectional velocity distribution of the air phase in a vertical pipe downstream of a 90° elbow. The contributions of the newly-developed techniques consist of:

(1) Building a mathematical model for calculating the transform matrix of the three pairs of LDA laser beams. The transform matrix is used to map the actual position of the measurement volume of LDA in pipe flow according to probe angle, for any change affected by shifting the three-dimensional traverse system.

(2) Determining a suitable sample rate for LDA experiments. A suitable sample rate (10K Hz) for LDA has been experimentally determined for 70~110μm glass beads conveyed by a 12m/s air velocity with a solid loading ratio of 1.6% in ϕ75mm pipe. This sampling rate applied to the experiments ensures to accurately calculate the local time-averaged particle velocity at any sample point.

(3) Confirming the profile of air velocity in a horizontal pipe. The experimental data show that the profile of air velocity measured by LDA in a horizontal pipe is in good agreement with the empirical one-seventh power law. Similarity among cross-sectional distributions of the axial air velocity on different horizontal cross-sections indicates the stability of fully developed gas pipe flow velocity profile. The axial air velocity shows an annular distribution over a cross-section.

(4) *Cross-sectional characteristics of the air velocity in a vertical pipe downstream of a 90° bend.* On vertical cross-sections, the air velocity distribution at no longer maintains the annular velocity contours in horizontal pipes. The cross-sectional distribution of the axial air velocity shows contours resembling a horseshoe in shape at the elbow outlet, where air flow being faster in the region close to the pipe bend’s outer wall (outside the horseshoe) than in the region inside the horseshoe, in the pipe centre and close to the inner wall of the bend. Further downstream, the differences of axial particle velocity between the horseshoe inside and its outside gradually decrease. A comparison of the experimental data and the numerical results generated by using CFD indicate that both of them show similar results of air velocity evolution in the horizontal pipe after the elbow.

3. ***Cross-sectional characteristics of the solid phase***

By applying the extended LDA technique, we have investigated particle dynamic behaviour of three types of glass beads which are selected to simulate to simulate the pulverised coal and biomass pellets transported in a dilute pneumatic conveying system. Detailed information on the cross-sectional spatial distributions of the axial particle velocity and particle number rate is reported.

(1) A*nnular cross-sectional flow pattern of solid phase by the axial particle velocity*. In a horizontal pipe at the minimum air conveying velocity 10m/s, the experimental data on a series of cross-sections clearly illustrate that the axial particle velocity distribution over a horizontal cross-section is annular, resembling that of the air phase, for particles with Stokes number less than 16. For particles with a Stokes numbers greater than 16, the characteristics of this annular structure become weak.

(2) *Stratified cross-sectional fluid pattern of solid phase by particle number rate*. In a horizontal pipe at the minimum air conveying velocity 10m/s, the experimental contour of particle number rate (counting in one second) over a horizontal cross-section displays a stratified configuration, especially for glass beads with Stokes number less than 16.

(3) *Evolution of the two cross-sectional fluid patterns*. These two types of cross-sectional flow patterns (for the axial particle velocity and particle number rate) can be observed at a number of positions along the pipe axis, but the position of the annular core and the values of iso-lines are dependent on particle size and vary along the fluid direction.

(4) *Cross-sectional characteristics of particle velocity in a vertical pipe downstream of a 90° bend*. In the vertical pipe after an elbow (R/D=1.3, R being the bend radius and D the pipe diameter), a horseshoe-shaped feature has been observed in the cross-sectional distributions of the dimensionless axial particle velocity for all three types of glass beads (less than 50μm; 70~110 μm and 180~300 μm) on the section 0D close to the elbow outlet. Further downstream, the horseshoe feature is gradually distorted until it completely disappears and the axial particle velocity is fairly uniform. This degradation distance is about 4D for the first type of glass beads, 2D for the second type and 1D for the third.

(5) *Cross-sectional characteristics of particle number rate in a vertical pipe downstream of a 90° bend*. The cross-sectional distribution of the dimensionless particle number rate on the section 0D shows that the rope is formed at the pipe outer wall where the maximum particle number rate occurs. On the whole, the rope formed by the first type of glass beads (less than 50 μm diameter) can still be observed at the section 6D. For the second type of glass beads (70~110μm), its rope is re-distributed across the pipe cross-section from the section 4D according to the similarities between cross-sectional distributions of the dimensionless axial particle velocity and the dimensionless particle number rate. Overall, roping is not obviously shown in the gas-solid flow of the third type of glass beads (180~300 µm) downstream of the section 0D. This suggests that larger particles are less prone to form ropes and dissipate more easily when they do, perhaps due to the greater inertial influence on their behaviour.

4. ***Visualization of particle dynamics on a cross-section***

In order to visualize particle dynamics on a cross-section, a video & image processing system for measuring particle size and analyzing particle spatial characteristics over a horizontal pipe cross-section in a dilute pneumatic conveying system was developed. A light sheet produced from a halogen lamp box was used to illuminate and section the gas-solid flow over a pipe cross-section. A high definition camcorder (1900i×1008i pixels, 25 frames per second) was utilized to record particle behaviour over the highlighted region.

(1) *Decoding algorithms for uncompressed MPEG-2 videos*. A set of video algorithms was developed to decode the compressed MPEG-2 videos into AVI format for further image processing. An AVI video, like a database, consists of a series of uncompressed frames. Each pixel on each uncompressed frame is directly mapped to a spatial point in the measurement region for further image processing.

(2) *Image processing algorithms for making each colour frame binary*. First, each color frame extracted from an uncompressed AVI video is converted into the corresponding gray-scale picture according to the particles' luminance information. Secondly, this picture is denoised by a Wiener filter. The third step is that a background image is obtained through removing the particle images in the denoised picture using a 25 × 25 Median Filter. In this way, the features of the background environment can be preserved. Subsequently, when a separated background image is subtracted from the denoised image, the heterogeneous background is removed. The subtraction result of a gray image is then converted into a binary image using Otsu's method.

(3) *Extraction of particle characteristics from a binary image.* The features of every particle such as shape, size and spatial position can then be extracted by applying the Chain Code Technique, which stores the relative co-ordinates between consecutive pixels, and records the shape of a region by analyzing each point on the boundary in sequence and assigns a code to denote the spatial direction between two adjacent points. Then the particle size distribution and the mean size over a section can be calculated from the set of Chain Code.

(4) *Cross-sectional characteristics of particle size distribution.* Experimental results of particle size and size distribution on each frame suggest that gas-solid pipe flow is always heterogeneous in space and unsteady in time. The particle mean size by mass fluctuates less with time and is thus more suitable for statistical descriptions of the unsteady properties of gas-solid pipe. Both the contours of particle number rate and particle time-averaged concentration exhibit the stratified structure characteristic of particle flow in a horizontal pipe cross-section. This kind of stratified structure is similar to the results revealed by Laser Doppler Anemometry

5. ***Discrepancies between experimental data and numerical results in respect of particle cross-sectional distribution***

   Based on experimental data and the geometry of the experimental rig, flow patterns on a series of pipe cross-sections and their vertical profiles along the horizontal pipe have been numerically investigated by the standard Discrete Phase Mode of Fluent and Fluent coupled with EDEM to account for the effects of particle-particle collision. Three conclusions can be deduced from the comparison of numerical and experimental data.

   (1) ***Region with a good agreement between the numerical results and the experimental data***. The annular structure of the particle velocity horizontal component and the stratified structure by particle number can be predicted by both Fluent DPM and Fluent & EDEM within a certain distance of the inlet, which can be estimated by the product of particle mean velocity and half the particle free falling time. On pipe cross sections further downstream, the flow patterns modelled are distorted until the annular velocity and stratified particle number characteristics completely disappear.

   (2) ***Advantages of considering particle-particle interaction in numerical simulations.*** The comparisons of numerical and experimental cross-sectional flow patterns of solid phase show that there is reasonable agreement at pipe cross-sections located at horizontal positions less than half the product of particle mean velocity and mean free fall time in the pipe from the particle inlet. Further away from the inlet, the numerical results show flow patterns which are increasingly divergent from the experimental results along the pipe in the direction of flow. This discrepancy indicates that particles' spatial distribution in a pipe is not accurately predicted by DPM or Fluent coupled with DEM. Thus, the micro-mechanism of fine particle transport in pipes should be further studied.

8.2 RECOMMENDATIONS FOR FUTURE WORK

The findings that arise from this project relating to the experimental and numerical analysis of particle behaviour have explored some fundamental characteristics of particle dynamics in a dilute pneumatic conveying system. Due to the complexity of the phenomena involved, research into gas-solid pipe flow is still an ongoing area of interest, especially for a multiple-component solid phases. Three possible extensions of the current work should be carried out in further studies.

First, in order to obtain empirical equations for particle dynamics in pipe flow, especially in a vertical pipe downstream of a 90° bend, more experimental work using the extended technique of Laser Doppler Anemometry should be carried out to determine the behaviour of different granular materials under a wide range of fluid conditions. Our current work only focused on low air conveying velocities.

Second, the video & image processing system developed in this work should be used to measure the size and spatial distribution of particles more than 80μm in diameter over a whole cross-section of ϕ75mm pipe. This visualization system can be made suitable for fine particle measurements using a smaller diameter of pipeline for experiment. In addition, using coloured granular materials, this system can be developed into a measurement tool for gas-solid pipe flow with a multi-component solid phase through adding a function capable of discerning particle colour.

Third, existing models of particle-particle interaction and particle-wall collision should be investigated in detail and modified to explain and eliminate the discrepancies between the current numerical results and the experimental data.

Fourth, statistical analysis and further experimentation should be undertaken to quantify the reliability of the LDA results and to estimate the error in the final values.

8.3 PUBLICATIONS ARISING FROM THE PROJECT

Lu Y., Glass H. D., Easson J. W., (2009). An investigation of particle behaviour in gas-solid horizontal pipe flow by an extended LDA Technique. Fuel. Accepted (JFUE-D-08-00741).

Lu Y., Glass D. H., Easson W. J., (2008a). Investigating particles behavior in gas-solid horizontal pipe flow by an extended Laser Doppler Anemometry Technique. In: Proceedings of 7th European Conference on Coal Research and its Applications, September 2nd – 5th, Cardiff, UK.

Lu Y., Glass D. H., Easson W. J., Crapper M., (2008b). Investigation of the Flow Patterns of Gas-solid granular flow in a horizontal pipe by FLUENT & EDEM. In: Proceedings of Particle Systems Analysis 2008, September 1st – 3rd, Stratford, UK.

Lu Y., Glass D. H., Easson W. J., (2007). Investigating Flow Properties of Coal Biomass Blends in Pneumatic Conveying Systems by Computational Fluid Dynamics. In: Proceedings of 2007 international conference on Coal Science and Technology, August 28th- 31th, Nottingham, UK.

References

AEA, (2006). The sustainability of biomass in co-firing (Final report). http://www.berr.gov.uk/files/file36485.pdf

Azzopardi B.J., Jackson K., Robinson J., Kaji R., Byars M., Hunt A., (2008). Fluctuations in dense phase pneumatic conveying of pulverised coal measured using electrical capacitance tomography. Chemical Engineering Science. 63: 2548-2558.

Bao J. and Soo S.L., (1995). Measurement of particle flow properties in a suspension by a laser system. Power Technology. 85, 261-268.

Barrent et al. (1995). Use of Laser Doppler Anemometry in the investigation of roughness particle induced transition on suction surfaces. CH34827-95/0000-52.1-10. IEEE.

Baxter Larry, (2005). Biomass-coal co-combustion: opportunity for affordable renewable energy. Fuel 84, 1295-1302.

BERR, (2008). UK renewable energy strategy. http://renewableconsultation.berr.gov.uk/consultation/consultation_summary. BERR: Department for Business Enterprise & Regulatory Reform.

Biagini E., Cioni M., Tognotti L., (2005). Development and characterization of a lab-scale entrained flow reactor for testing biomass fuels. Fuel 84, 1524-1534.

Birchenough A. and Mason J.S., (1976). Local particle velocity measurements with a Laser Anemometer in an upward flowing gas-solid suspension. Powder technology. 14, 139-152.

Bovik Al. Handbook of Image & Video Processing. Academic press London, UK. 10-11.

Brown G.J., Reilly D., Mills D., (1996). Development of an ultrasonic tomography system for application in pneumatic conveying. Measurement Science and Technology. 7(3): 396–405.

Buchhave P. and George K. W., (1979). The measurement of turbulence with the laser-Doppler anemometer. Annual Reviews Fluid Mechanics, 11, 443-503.

Caicedo R.G., Marques P.J., Ruiz G.M., Soler G.J., (2003). A study on the behaviour of bubbles of a 2D gas-solid fluidized bed using digital image analysis. Chemical Engineering and Processing. 42: 9-14.

Campbell S.C., (1990). Rapid granular flow. Annual Review of Fluid Mechanics. 22:57-92.

Carter M. R., Yan Y., Cameron D. S., (2005), On-line measurement of particle size distribution and mass flow rate of particles in a pneumatic suspension using combined imaging and electrostatic sensors. Flow Measurement and Instrumentation. 16: 309-314.

Chao Y.C. and Leu J. H., (1992). A fractal reconstruction method for LDV spectral analysis. Experiments in fluids. 13, 91-97.

Chen R.C. and Kadambi J.R., (1995). Discrimination between solid and liquid velocities in slurry flow using Laser Doppler Velocimeter. Powder Technology. 85, 127-134.

Chu K.W. and Yu A.B., (2007). Numerical simulation of complex particle-fluid flows. Powder Technology (179), 104-114.

Clarke R J. (1995). Digital Compression of Still images and Video. Academic press London, UK. 294-299.

Crapper, M., Ooi, J. Y., Favier, J. and Golz, P., (2005). Coupled Continuum-Discrete Modelling of Solid-Fluid Phase Flow. In: 7th World Congress of Chemical Engineering, Glasgow, UK.

Cui H. and Grace R.J, (2006). Pneumatic conveying of biomass particles: a review. China Particuology. 4(3-4), 183-188.

DANTEC, (2001). Laser Doppler Anemometry: Supplement of the user's manual. DANTEC Measurement Technology, Skovlunde, Denmark.

DANTEC, (2008). Integrated solutions in laser Doppler anemometry. http://www.dantecdynamics.com/Default.aspx?ID=653

Datta U., Dyakowski T. and Mylvaganam S., (2007). Estimation of particulate velocity components in pneumatic transport using pixel based correlation with dual plane ECT. Chemical Engineering Journal. 130, 87-99.

Dem-solutions, (2008), EDEM 1.2 user guide. http://www.dem-solutions.com/

Digital TV Group, (2008). MPEG Encoding. http://www.dtg.org.uk/reference/tutorial_mpeg.html

Drake M., Hoffmann H., Rabbah R., Amarasinglhe S., (2005). MPEG-2 in a stream programming language. Computer Science and Artificial Intelligence Laboratory Technical Report. http://hdl.handle.net/1721.1/30578

DTI. (2003). Multiphase flow in coal-fired power plant (Report No. Coal R252 DTI/Pub URN 03/1635; By A Malmgren, G Oluwande and G Riley; RWE Innogy plc). http://www.berr.gov.uk/files/file20553.pdf

DTI, (2006). Evaluating the sustainability of co-firing in the UK (Report Number: URN 06/1960; Authors: Jeremy Woods, Richard Tipper, Gareth Brow, Peter De Groot. Themba Technology Ltd.). http://www.berr.gov.uk/files/file34448.pdf

DTI, (2007). Best Practice Brochure: Co-firing of biomass (Report No. COAL R287 DTI/Pub URN 05/1160; By Mike Colechin, E.ON UK). http://www.berr.gov.uk/files/file20737.pdf

Dupont P., (1991). Spectral analysis with a LDA in high speed flow. In: Proceedings of International Congress on Instrumentation in Aerospace Simulation Facilities, 14th, Rockville, MD, Oct. 27-31, 1991, Record (A92-54301 23-35). New York, Institute of Electrical and Electronics Engineers, Inc., 1991, p. 329-335.

Durst, F. 1982: Review-combined measurements of particle velocities, size distributions, and concentration. J. Fluids Eng. 104, 284–296

Dyakowski T. and Williams R.A., (1993). Measurement of particle velocity distribution in a vertical channel. Powder technology. 77, 135-142.

Dyakowski T., Jeanmeure L., Jaworski A. J. (2000) Applications of electrical tomography for gas–solids and liquid–solids flows—a review. Powder Technology. 112: 174–192.

Fan J., Zhao H. and Jin J., (1996). Two-phase velocity measurements in particle-laden coaxial jets. The Chemical Engineering Journal. 63, 11-17.

Fan Liang-shih, Zhu Chao, (1998), Principles of Gas-solid Flow, Cambridge University Press, London, UK, pp.464-465.

Fang G.C, Chang C.N. and Wua Y.S., (2002). Suspended particulate variations and mass size distributions of incense burning at Tzu Yun Yen temple in Taiwan, Taichung. Science of The Total Environment 299, 79-87

Fincke R.J., Swank W.D., Jeffery C.L., (1990). Simultaneous measurement of particle size, velocity, and temperature in thermal plasma. IEEE Transcations on Plasma Science. 18 (6), 948-957.

Fitzpatrick J. and Simon L., (2005). Estimation of cross-power spectra using sample-and-hold reconstruction of laser Doppler anemometry data. Experiments in Fluids. 39, 954-965.

Fluent Inc., (2006). Fluent 6.3 user’s guide. p834-836.

Fokeer S., Kingman S., Lowndes I. and Reynolds A., (2004). Characterization of the cross sectional particle concentration distribution in horizontal dilute flow conveying: a review. Chemical Engineering and Processing. 43, 667-691.

Frank S., Heilman C. and Siekmann H.E., (1996). Point-velocity methods for flow-rate measurements in asymmetric pipe flow. Flow Measurement Instrument. 7 (3), 201-209.

Fuchs A., Zangl H., Wypych P., (2007). Signal modeling and algorithms for parameter estimation in pneumatic conveying. Powder Technology. 173: 126-139.

Furuichi N., Hachiga T., Hishida K. and Kumada M., (2002). A development of a two-component velocity profiler using a fiber multi-point LDV and a CCD area image sensor. SICE 2002, Osaka. 1710-1715

Gore, R.A. and Crowe, C.T., (1989). Effect of particle size on modulating turbulent intensity. International Journal of Multiphase Flow 15, 279-285.

Granadaa E., Lareo G., Mígue J.L. Moran Z, J., Porteiro J. and Ortiz L., (2006). Feasibility study of forest residue use as fuel through co-firing with pellets. Biomass and Bioenergy. 30, 238–246

Grechikhin V.A. and Rinkevichyus B.S., (1993). Errors of digital methods of measuring the frequency of the single-frequency signal of a laser Doppler anemometer. Measurement Techniques. 36(10), 1140-1146.

Harris F.R., (2008). Hard bargaining. Current Biology 18(2), 44-45.

Hart C.R., (2001). Seedless laser Velocimetry using heterodyne laser-induced thermal acoustics. 0-7803-7022-8, IEEE.

Huber N. and Sommerfeld M., (1994). Characterization of the cross-sectional particle concentration distribution in a pneumatic conveying system. Powder Technology. 79, 191-210.

Huber N., Sommerfeld M., (1998). Modeling and numerical calculation of dilute-phase pneumatic conveying in pipe systems. Powder Technology, Vol.99, 90-101

Hesselink Lambertus. (1998). Digital image processing in flow visualization. Annual Review of Fluid Mechanics. 20: 421-5.

Hussainov M., Kartushinsky A., Rudi U., Shcheglov I. and Kohnen G., (2000). Experimental investigation of turbulence modulation by solid particles in a grid-generated vertical flow. International Journal of Heat and Fluid Flow. 21, 265-373.

IEA, (2006). World Energy Outlook 2006. http://www.iea.org/textbase/nppdf/free/2006/weo2006.pdf

IPA, (2006). Final Report: The economics of Co-firing to Department of Trade and Industry (Final Report: URN 06/1959). www.berr.gov.uk/files/file34449.pdf

Ireland S.N., Mcgrellis B., Harper N., (2003). On the technical and economic issues involved in the co-firing of coal and waste in a conventional pf-fired power station. Fuel 83, 905-915.

Joppich A. and Salman H., (1999). Wood powder feeding, difficulties and solutions. Biomass and Bioenergy. 16, 191-198

JVC. (2008). Instruction book for JVC GZ-HD7. http://uk.jvc-service.net/public/document.cfm?prog=InstrBook.cfm & Model=GZ-HD7

Kadambi R.J., Martin T.W., Amirthaganesh S., Wernet P.M., (1998). Particle sizing using particle imaging velocimetry for two-phase flows. Powder Technology. 100: 251-259.

Kohnen G., Ruger M., Sommerfeld M., (1994). Convergence behaviour for numerical calculations by the Euler/Lagrange method for strongly coupled phases, in: Numerical Mehtods in Multiphase Flows 1994, ASME Fluids Engineering Division Summer Meeting, Lake Tahoe, USA, vol.185, 191-202

Koppejan, J., (2004). 2004: Overview of experience with cofiring biomass in coal power plants, IEA Bioenergy Task 32: Biomass Combustion and Cofiring. www.ieabioenergy.com/media/53_Co-firingbiomasswithcoal-asuccessstory.doc

Kussin J., Sommerfeld M., (2002). Experimental studies on particle behaviour and turbulence modification in horizontal channel flow with different wall roughness. Experiments in Fluids. 33:14-159.

Lain S., Sommerfeld M. and Kussin J., (2002). Experimental studies and modeling of four-way coupling in particle-laden horizontal channel flow. International Journal of Heat and Fluid Flow. 23, 647-656.

Laurent F.C., Dyakowski T., Zimmerman B.W., Clark W., (2002). Direct flow-pattern identification using electrical capacitance tomography. Experimental Thermal and Fluid Science. 26: 763-773

Li B.E., Xi J., Chicharo F.J., Yao Q.J. and Yu Y.D., (2005). Multi-point laser Doppler Velocimeter. Optics communications. 245, 309-313.

Li Hui and Tomita Yuji, (2000). Particle velocity and concentration characteristics in a horizontal dilute swirling flow pneumatic conveying. Powder Technology. 107: 144-152.

Lijegren M.L. and Vlachos S.N., (1990). Laser velocimetry measurements in a horizontal gas-solid pipe flow. Experiments in fluids. 9, 205-212.

Lim, Jae S., (1990). Two-Dimensional Signal and Image Processing. Englewood Cliffs, NJ, Prentice Hall. pp. 536-540

Lim W.E., Wang C.H., Yu A.B., (2005). Discrete Element Simulation for pneumatic conveying of granular material. Particle Technology and Fluidization. 52(2), 496-509.

Livingston W.R., (2006). Overview of the activities of IEA Bioenergy Task 32: Biomass combustion and co-firing. http://www.berr.gov.uk/files/file39294.pdf

Lu G., Yan Y., Cornwell S. et al., (2008). Impact of co-firing coal and biomass on flame characteristics and stability. Fuel 87, 1133-1140.

Lu Y., Glass D. H., Easson W. J., (2007). Investigating Flow Properties of Coal Biomass Blends in Pneumatic Conveying System by Computational Fluid Dynamics. In: Proceedings of 2007 international conference on Coal Science and Technology, August 28th- 31th, Nottingham, UK.

Lu Y., Glass D. H., Easson W. J., (2008a). Investigating particles behavior in gas-solid horizontal pipe flow by an extended Laser Doppler Anemometry Technique. In: Proceedings of 7th European Conference on Coal Research and its Applications, September 2nd – 5th, Cardiff, UK.

Lu Y., Glass D. H., Easson W. J., Crapper M., (2008b). Investigation of the Flow Patterns of Gas-solid granular flow in a horizontal pipe by FLUENT & EDEM. In: Proceedings of Particle Systems Analysis 2008, September 1st – 3rd, Stratford, UK.

Lu Y., Glass D.H., Easson W. J., (2008c). Visualizing particle characteristics in a horizontal pneumatic conveying system, In: 21st Annual Scottish Fluid Mechanics Meeting, May 22nd, Edinburgh, UK. (Poster)

Lu Y., Glass D. H., Easson W. J., Crapper M., (2008d). A comparison of the Numerical Results Investigated by EDEM & Fluent and the Experimental Data in a Gas-solid Horizontal Pipe Flow. In: Proceedings of EDEM User Group Meeting 2008, April 28th – 30th, Edinburgh, UK. (Poster)

Lu Y., Glass H. D., Easson J. W., (2009). An investigation of particle behaviour in gas-solid horizontal pipe flow by an extended LDA Technique. Fuel. Accepted.

Mathiesen V. and Solberg T., (1999). Experimental and computational study of multiphase gas/particle flow in a CFB riser. Particle technology and fluidization. 45(12), 2503-2518

Matsuo Naoki, (1998). Key elements related to the emissions trading for the Kyoto Protocol. Energy Policy 26 (3), 263-273.

Mckee L.S., Dyakowski T., Williams A.R., Bell A.T. and Allen T., (1995). Solid flow imaging and attrition studies in a pneumatic conveyor. Powder Technology 82: 105-113

Mills D., (2004). Pneumatic conveying design guide. Oxford: Elsevier Butterworth-Heinemann. 6-7, 20-25, 29-53, 46-47, 417, 429.

Miyazaki K., Chen G., Yamamoto F., Ohta J., Murai Y., Horii K., (1999). PIV measurement of particle motion in spiral gas-solid two-phase flow. Experimental Thermal and Fluid Science. 19: 194-203.

Mohammad Zulfiqar, Behdad Moghtaderi and Terry F. Wall. (2006). Flow properties of biomass and coal blends. Fuel Processing Technology. 87, 281 – 288

Morsi S.Y., Tu Y.J., Yeoh H.G. and Yang W., (2004). Principal characteristics of turbulent gas-particulate flow in the vincinity of single tube and tube bundle structure. Chemical Engineering Science. 59, 3141-3157.

Mundo C., Sommerfeld M. and Tropea C., (1994). Droplet-wall collisions: Experimental studies of the deformation and breakup process. International Journal of Multiphase Flow. 21(2), 151-173.

Mundo C., Tropea C. and Sommerfeld M., (1997). Numerical and experimental investigation of spray characteristics in the vicinity of a rigid wall. Experimental Thermal and Fluid Science. 15, 228-237.

NETBIOCOF (Integrated European Network for Biomass Co-firing), (2006). New and advanced concepts in renewable energy technology biomass. http://netbiocof.net/data/upload/uploads/D14%20STATE%20OF%20THE%20ART%20REPORT%202.pdf

Nixon M, Aguado A. (2002). Feature extraction & image processing. Newnes Press, Oxford, UK. 67-308.

Qiu H.H. and Sommerfeld M., (1992). A reliable method for determining the measurement volume size and particle mass fluxes using phase-Doppler anemometry. Experiments in Fluids. 13, 393-404.

Olof Melander, Anders Rasmuson, (2004). PIV measurements of velocities and concentrations of wood fibres in pneumatic transport. Experiments in Fluids. 37, 293–300.

Ostu N., (1979). A threshold selection method from gray-level histograms. IEEE Transactions on Systems, Man and Cybernetics. 1: 62-66.

Pacific Pneumatic Inc. A short history of pneumatic conveying. http://www.pacpneu.com/page14.html

Pakhmomov M.A., Protasov M.V., TerekHov V.I. and Varaksin A., (2007). Experimental and numerical investigation of downward gas-dispersed turbulent pipe flow. International journal of heat and mass transfer. 50, 2017-2116.

Pedrotti L.F., Pedrotti M.L. and Pedrotti S.L., (2007). Introduction to optics. London: Pearson Press. 396-416.

PAN P. (1994), Material properties and flow modes in pneumatic conveying, Power Technology,104, pp.157-163.

Pronobis M., (2006). The influence of biomass co-combustion on boiler fouling and efficiency. Fuel 85, 474-480.

Rao S M, Zhu K, Wang C, Sundaresan S, (2001). Electrical capacitance tomography measurements on the pneumatic conveying of solids. Industrial & Engineering Chemistry Research. 40: 4126-4226

Rasband, W.S.,(2008). ImageJ. U. S. National Institutes of Health, Bethesda, Maryland, USA. Http://rsb.info.nih.gov/ij/, 1997-2008.

Rhodes M.J. Wang X.S., Nguyen M. Stewart P., Liffman K., (2001). Study of mixing in gas-fluidized beds using a DEM model. Chemical Engineering Science. 56: 2859-2866.

Rober W. Fox, Alan T. McDonal, Philip J. Prtichard, (2004). Introduction to fluid mechanics. 6th Edition. New York: John Wiley & Sons. 332-335

Sabersky H.R., Acosta J.A., Hauptmann G.E., Gates M.E., (1999). Fluid flow: a first course in fluid mechanics. Prentice Hall Press, Upper Saddle River, New Jersey. 267-269.

Sami M., Annamalai K., Wooldridge M., (2001). Co-firing of coal and biomass fuel blends. Progress in Energy and combustion science 27, 171-214

Salman A. D., Gorham D. A., Szabo M., Hounshow M.J., (2005), Spherical particle movement in dilute pneumatic conveying, Power Technology, 153, pp.45-50.

Schena G., Santoro L., Favretto S., (2007). Conceiving a high resolution and fast X-ray CT system for imaging fine multi-phase mineral particles and retrieving mineral liberation spectra. International Journal of Mineral Processing. 84: 327-336

Schlichting Hermann, (1995). Boundary Layer Theory. London: Pergamon Press LTD. P402-405.

Seeger A., Kertzscher U., Affeld K., Wellnhofer E., (2003). Measurement of the local velocity of the solid phase and the local solid hold-up in a three-phase flow by X-ray based particle tracking Velocimetry (XPTV). Chemical Engineering Science. 58: 1721-1729.

Seville J.P.K, Tuzun U. and Clift R., (1997). Processing of particulate solids. London: Blackie Academic & Professional Press. 57-62, 82-83, 99-199.

Shiavi R., (1999). Introduction to applied statistical signal analysis. Academic Press: New York. pp. 131-135.

Smith, Steven W. Digital signal processing: a practical guide for engineers and scientists. Elsevier Publications. (2003) 39-43

Sondreal A.E., Benson A. S. et al., (2001). Review of advances in combustion technology and biomass cofiring. Fuel Processing Technology 71, 7-38.

Sommerfeld M., Huber N., (1999). Experimental analysis and modeling of particle-wall collisions. International Journal of Multiphase Flow. 25: 1457-1489.

Sommerfeld M. and Qiu H.H., (1998). Experimental studies of spray evaporation in turbulent flow. International Journal of Heat and Fluid Flow. 19, 10-22.

Sommerfeld M., (2003). Analysis of collision effects for turbulent gas-particle flow in a horizontal channel: Part I. Particle transport. International Journal of Multiphase Flow 29, 675-699.

Sommerfeld M. and Kussin J., (2004). Wall roughness effects on pneumatic conveying of spherical particles in a narrow horizontal channel. Powder Technology. 142, 180-192.

Takei M., Ochi M., Saito Y., (2004). Image extraction of particle concentration at the plug front using 3D wavelets and comparison with LDV. Powder Technology. 142: 70-78.

Tsuji Y., Kawaguchi T., Tanaka T., (1993). Discrete particle simulation of two-dimensional fluidized bed. Powder Technology. 77: 79-87.

Tsuji Y. and Morikawa Y., (1982). LDV measurements of an air-solid two-phase flow in a horizontal pipe. Journal Fluid Mechanics. 120, 385-400.

Tsuji Y., Morikawa Y. and Shiomi H., (1984). LDV measurements of an air-solid two-phase flow in a vertical pipe. Journal Fluid Mechanics. 139, 417-434.

Tsuji Y., Tanaka T., Ishida T., (1992). Lagrangian numerical simulation of plug flow of cohesion less particles in a horizontal pipe. Powder Technology. 71: 239-250.

Tu Y.J., Fletcher J.C., Morsi S.Y., Yang W. and Behnia M., (1997). Numerical and experimental studies of turbulent particle-laden gas flow in an in-line tube bank. Chemical Engineering Science. 53(2), 225-238.

Tudor N. P., (1995). MPEG-2 Video compression. Electronics & Communication Engineering Journal. 7(6): 257-264.

Utomo B. M., Warsito W., Sakai T., Uchida S., (2001). Analysis of distributions of gas and TiO2 particles in slurry bubble column using ultrasonic computed tomography. Chemical Engineering Science. 56: 6073-6078.

Van de wall R.E. and Soo S.L., (1994). Measurement of particle cloud density and velocity using laser devices. Powder Technology. 81, 269-278.

Vasquez N., Jacob K., Cocco R., Dhodapkar S., Klinzing E. G., (2008). Visual analysis of particle bouncing and its effect on pressure drop in dilute phase pneumatic conveying. Powder Technology. 179: 170-175.

Wallace M.J., (1995). The measurement of vorticity in turbulent flows. Annual review of Fluid Mechanics. 27, 469-514.

Wang S.X., Valero V., Soria J. and Rhodes J.M., (2006). Laser-based planar imaging of nano-particle fluidization: Part I – determination of aggregate size and shape. Chemical Engineering Science. 61: 5476-5486.

Warsito W., Ohkawa M., Kawata N., Uchida S., (1999). Cross-sectional distributions of gas and solid holdups in slurry bubble column investigated by ultrasonic computed tomography. Chemical Engineering Science. 54: 4711-4728.

Werther J., Hage B. and Rudnick C., (1996). A comparison of laser Doppler and single-fibre reflection probes for the measurement of the velocity of solids in a gas-solid circulating fluidized bed. Chemical Engineering and Processing. 35, 381-391.

Worf Glaskugeln, (2008). The data sheet of glass beads. http://www.worf.de/en/index.html

Worf Glaskugeln GmbH, (2008). Precision glass beads. http://www.worf.de

Yang Q.W., Liu S., (2000). Role of tomography in gas/solids flow measurements. Flow Measurement and Instrumentation. 11: 237-244.

Yilmaz Ali and Levy K. Edward, (2001). Formation and dispersion of ropes in pneumatic conveying. Powder Technology. 144:168-185.